

In presenting this dissertation as a partial fulfillment of the requirements of an advanced degree from Emory University, I agree that the Library of the University shall make it available for inspection and circulation in accordance with its regulations, governing materials of this type. I agree that permission to copy from, or to publish, this dissertation may be granted by the professor under whose direction it was written, or, in his/her absence, by the Dean of the Graduate School when such copying or publication is solely for scholarly purposes and does not involve potential financial gain. It is understood that any copying from, or publication of, this dissertation which involves potential financial gain will not be allowed without written permission.

Wan-Hee Goh

Single Molecule Study of Fluorescence from Organic Dyes at Interfaces

By

Wan-Hee Goh
Doctor of Philosophy

Department of Chemistry

Dr. Tianquan Lian
Advisor

Dr. Keiji Morokuma
Committee Member

Dr. Michael C. Heaven
Committee Member

Accepted:

Dean of Graduate School

Date

Single Molecule Study of Fluorescence from Organic Dyes at Interfaces

By

Wan-Hee Goh

B.S. Korea University, 1994

M.S. Pohang University of Science and Technology, 1996

Advisor: Tianquan Lian, Ph.D.

An Abstract of

A dissertation submitted to the Faculty of the Graduate

School of Emory University in partial fulfillment

of the requirements for the degree of

Doctor of Philosophy

Department of Chemistry

2007

Abstract

Single molecule study has been performed on the fluorescence emitted from organic dyes adsorbed on nanocrystalline films. The basic configuration of the study was rhodamine B (RB) and PDI derivative (PDI-P1) [*N*-octyl-1,7(3',5' di-*tert*-butylphenoxy)perylene-3,4:4,10-bis(di-carboximide)-benzoic acid] dyes adsorbed on the surfaces of various nanocrystalline substrates at extremely low surface number density ~ 0.06 molecule/ μm^2 : nanocrystalline Antimony doped Tin Oxide (ATO, Sb:SnO₂), glass, and nanocrystalline ZrO₂ film. The nanocrystalline ATO substrate accepted an electron from the excited state of the single RB or PDI-P1 dye. Electron transfer (ET) to the glass and the nanocrystalline ZrO₂ is not allowed energetically. Properly sampled single RB molecules on ATO had fluorescence lifetime distribution with average 0.7 ns. Typical average of single molecule fluorescence lifetime (SMFL) distribution of RB on glass or on ZrO₂ ranged from 3.0 to 3.4 ns. The significant reduction of lifetime by more than 2 ns is ascribed to the electron transfer from RB to ATO. Similarly, the average of SMFL distribution of PDI-P1 on ATO was 1.2 ns, while those on glass and on ZrO₂ were 2.9 ns and 3.7 ns respectively. The lower limit of our SMFL detection was about 100 ps. Therefore, many molecules that had electron transfer channel in less than tens of picosecond time scale were not detectable due to their low quantum yields. The SMFLs of detected molecules in nanoporous film were controlled by not only the ET process but also nearby optical and dielectric environment. Local field correction and effective medium approximation theories were applied to the interpretation of the measured SMFL distributions. The glass was an ET-inactive substrate but it interacted with adsorbed dye in a peculiar way. There was a power loss through the air-glass surface depending on the

orientation of emission dipole of a single molecule, which resulted in the finite lifetime distributions of RB and PDI-P1 dispersed on glass. The most probable dipole orientation of the dyes on glass was estimated to be about 65° from surface normal. The unique intensity fluctuations of RB on glass has been observed. We have accumulated new evidences and proposed a tentative conclusion that RB on glass forms multiple long lived dark states dynamically. We have occasionally seen interesting correlations between intensity trajectory and fluorescence lifetime trajectory mostly for PDI-P1 single molecules adsorbed on the substrates. The correlations were ascribed to the conformation fluctuation pivoted on the rigid surfaces.

Single Molecule Study of Fluorescence from Organic Dyes at Interfaces

By

Wan-Hee Goh

B.S. Korea University, 1994

M.S. Pohang University of Science and Technology, 1996

Advisor: Tianquan Lian, Ph.D.

A dissertation submitted to the Faculty of the Graduate

School of Emory University in partial fulfillment

of the requirements for the degree of

Doctor of Philosophy

Department of Chemistry

2007

Acknowledgments

I would like to express my deepest gratitude to my advisor, Professor Tianquan Lian, for his consistent support to my graduate study. He has always encouraged me to pursue the joy of understanding nature and to develop the critical reasoning. Through the days of his training, I have come to be able to have confidence in learning scientific knowledge in the right way.

I would like to extend my gratitude to my committee members, Prof. Keiji Morokuma and Prof. Michael Heaven, for their advice that was crucial to my progress.

I am grateful to group members, J. Guo, C. She, D. Stockwell, J. Huang, and new members. They have been important collaborators and the good friends. I am grateful to Dr. A. Issac for discussions on my thesis. A special thanks goes to Dr. N. Anderson who has helped me in every part of my laboratory work.

I am grateful to the members of Prof. R. M. Dickson's group for exchanging ideas and laboratory tools, which were invaluable in the beginning of my single molecule study.

I am grateful to my housemates, a large family. I remember every single day as a pleasant and wonderful time with them.

I owe many people in Korea a debt of gratitude for help and wishing me well. Dr. K. Kim and other members of our team in LG Chem. Ltd. have given me a great help in settling down to my new work and life. I would like to express my gratitude to Prof. M. Ree for his continued interest in my studies.

Finally, I would like to acknowledge my mother, sister, and father of blessed memory. Their encouragement and support has been the source of energy during my graduate study.

Single Molecule Study of Fluorescence from Organic Dyes at Interfaces

Abstract

Acknowledgments

List of Illustrations

List of Tables

Chapter 1. Overview of Single Molecule Study of Fluorescence from ----- 1

Organic Dyes at Interfaces

Chapter 2. Theory of Fluorescence Lifetime in Single Molecule Detection

I. Introduction -----	13
II. Elements of Fluorescence -----	13
III. Radiative Lifetime Dependence on Optical Environment -----	19
III.A. Local Field Effect -----	20
III.B. Orientation of Dipole on a Dielectric Flat Surface -----	23
IV. Criterion of Goodness of Fit -----	32
V. Conclusion -----	34
References -----	35

Chapter 3. Microscopy and Sample Preparation for Single Molecule Detection

I. Sample Preparation -----	39
I.A. Cleaning -----	39
I.B. Nanoporous Film Preparation -----	41
I.C. Sensitizing the Nanoporous Film with Organic Dye in Single -----	44

Molecule Level	
II. Single Molecule Microscopy -----	47
II.A. Time-Correlated Single Photon Counting -----	47
II.B. Experimental Setup for Single Molecule Lifetime -----	59
Measurement by TCSPC	
III. Single Molecule Detection Method -----	70
III.A. General Procedure -----	70
III.B. Proper Number Density for SM Detection -----	78
III.C. Statistical Fluctuation of Virtual SMFL Source -----	86
IV. Conclusion -----	95
References -----	97

Chapter 4. Single Molecule Detection of Rhodamine B on the Surface of

Nanocrystalline Thin Film and Glass

I. Introduction -----	101
II. Results -----	106
II.A. Bulk Fluorescence Lifetime Measurement of RB on ATO -----	106
II.B. Single Molecule Detection -----	111
II.B.1. Single Molecule Imaging -----	111
II.B.2. Single Molecule Intensity Trajectory -----	113
II.B.3. Experimental Evidences of Single Molecule -----	115
Detection	
II.C. Single Molecule Lifetime Measurement -----	119

II.C.1. SMFL of RB on ATO -----	120
II.C.2. SMFL of RB on ZrO ₂ -----	131
III. Discussion -----	132
III.A. Fluorescence Lifetime of RB on ATO -----	132
III.A.1 General Description -----	132
III.A.2. Features of the Electron Transfer Observation -----	137
in Single Molecule Level	
III.A.3 Origin of Radiative Lifetime Dispersion -----	143
IV. Conclusion -----	155
Appendix A: Polarization Dependence of Fluorescence Intensity -----	157
Appendix B: Solubility of Oxygen in Water and Alcohol -----	160
References -----	161

Chapter 5. Surface Induced Fluorescence Lifetime Distribution of

Rhodamine B on Glass Measured by Single Molecule Detection

I. Introduction -----	169
II. Results -----	171
II.A. Bulk Fluorescence Lifetime of RB on Glass -----	171
II.B. Single Molecule Fluorescence Lifetime of RB -----	174
on Glass Surface	
III. Discussion -----	179
III.A. Single Molecule Fluorescence Intensity Trajectory -----	179
III.B. Single Molecule Fluorescence Lifetime -----	190

IV. Conclusion -----	195
References -----	196

Chapter 6. Single Molecule Detection of PDI-P1 on Nanocrystalline Thin films

I. Introduction -----	201
II. Results -----	206
II.A. Bulk Test of PDI-P1 on ATO -----	206
II.B. Bulk Test of PDI-P1 on Glass -----	207
II.C. Bulk Test of PDI-P1 on ZrO ₂ -----	210
II.D. SMFL Test of PDI-P1 on ATO -----	212
II.E. Single Molecule Fluorescence Lifetime of PDI-P1 on Glass -----	215
II.F. SMFL of PDI-P1 on ZrO ₂ -----	219
III. Discussion -----	220
III.A. SM and Bulk Lifetimes of PDI-P1 on ATO -----	220
III.B. Single Molecule and Bulk Lifetime of PDI-P1 -----	226
on Glass Surface	
III.C. Single Molecule and Bulk Lifetime of PDI-P1 on ZrO ₂ -----	229
IV. Conclusion -----	231
References -----	235

Illustrations

Figure 2.1. Perrin-Jablonski diagram

Figure 2.2. Schematic diagram of single dipole in front of a planar interface

Figure 2.3. Schematic illustration of experimental configuration of a single dipole near glass-air interface

Figure 3.1. AFM image of glass cover slip surface

Figure 3.2. AFM images of nanoporous films

Figure 3.3. Schematic diagram of micro-view of surface being sensitized by dropping scheme

Figure 3.4. Schematic diagram of sensitization procedure by soaking scheme

Figure 3.5. Principle of decay curve generation

Figure 3.6. Schematic diagram of basic components of reversed start-stop mode time-correlation single photon counting (TCSPC) system

Figure 3.7. Schematic diagram of pile-up error and a graph of probability of missing photons by the pile-up error with various photon arrival rates

Figure 3.8. Magnitude of distortion function $D(t)$ after excitation

Figure 3.9. Actual and correct decay curves in terms of the pile-up error

Figure 3.10. Schematic diagram of optical alignment of home-built oscillator

Figure 3.11. Kerr-lensing effect

Figure 3.12. Simplified schematic diagram of the whole microscopic system

Figure 3.13. The structure of TCSPC data of a tested area

Figure 3.14. Search-Optimization-Record procedure

Figure 3.15. The optimization procedure of real experimental data

Figure 3.16. Other examples of optimization procedure

Figure 3.17. $P_{\leq m}$ vs. total number of pixels

Figure 3.18. $P_{\leq m}$ vs. total number of deposited molecules with $tp=12,000$ and $tp=40,000$

Figure 3.19. Experimental configuration of virtual SMFL test around an excitation laser focus

Figure 3.20. An example of the fluctuation of virtual constant lifetime source

Figure 3.21. Distribution of virtual SMFLs prepared from 77 sections of full TCSPC data divided by 0.57 s unit time

Figure 3.22. Standard deviation depending on the integrated photon counts of virtual SMFL sources

Figure 3.23. Plots of lifetime fluctuation vs. average lifetime for various integrated counts

Figure 3.24. Comparison of the lifetime fluctuation vs. counts of virtual SMFL source curves of two solutions of two different solutes having similar lifetimes

Figure 4.1. Schematic diagram of redox potential energies of valance and conduction bands of ATO, ZrO_2 , and ground and excited states of rhodamine B referenced to the NHE standard

Figure 4.2. Absorption (solid) and emission (dotted) spectra of RB in water

Figure 4.3. Stage-scanned two-photon fluorescence image of RB molecules adsorbed on a nanoporous ATO film

Figure 4.4. Decay curves of the fluorescence detected in the imaging of RB on ATO in linear scale

Figure 4.5. Decay curves of the fluorescence detected in the imaging of RB on ATO in log scale

Figure 4.6. Raster-scanned two-photon fluorescence image of single RB molecules dispersed on ATO film

Figure 4.7. Intensity trajectory along the scanned positions of the image of single RB on ATO film shown in Figure 4.6

Figure 4.8. Trajectories of fluorescence intensity as a function of time for RB on ATO thin nanoporous film and glass cover slip

Figure 4.9. Configuration of single absorption dipole moment and plane polarization direction of excitation beam

Figure 4.10. Polarization dependence of a RB molecule deposited on a glass substrate

Figure 4.11. Comparison of fluorescence spectra of a single RB molecule (thick solid line) and an ensemble (thin solid line) of RB molecules on a glass cover slip

Figure 4.12. Two representative intensity trajectories of single RB molecule on a nanoporous ATO film

Figure 4.13. Single exponential decay model fitted to the measured single molecule fluorescence decay curves

Figure 4.14. Distribution of 114 single molecule fluorescence lifetimes of RB on ATO

Figure 4.15. Average photon emission power of molecules in various lifetime ranges of the single molecule fluorescence lifetime (SMFL) test of RB on ATO with high sampling threshold (1,200 cps)

Figure 4.16. Stage-scanned two-photon fluorescence image of RB molecules adsorbed on a nanoporous ATO film

Figure 4.17. Intensity trajectory along the scanned positions of the image of single RB molecules dispersed on ATO film shown in Figure 4.16

Figure 4.18. SMFL distributions of RB on glass surface and RB on ATO with sampling threshold of 500 and 1,200 cps

Figure 4.19. Average photon emission power of molecules in various lifetime ranges of the SMFL test of RB on ATO with low sampling threshold (500 cps)

Figure 4.20. Distribution of 129 SMFLs of RB on ZrO₂

Figure 4.21. Fluorescence intensity of single molecule with varying ET rate

Figure 4.22. Distribution of the characteristic lifetime of ET in the SMFL test of RB on ATO with low threshold 500 cps

Figure 4.23. Fluorescence image of RB on glass and ATO thin film acquired with CCD detector

Figure 4.24. Intensity trajectory drawn in 5 ms unit time

Figure 4.25. Three models of effective medium approximation represented by dielectric constant as a function of filling factor of ATO nanoparticle

Figure 4.26. Chemical Structure of rhodamine 101

Figure 4.27. Three local field correction models fitted to experimental data published in Ref. 38

Figure 4.28. Plot of radiative lifetime as a function of filling factor based on three combinations of effective medium approximation and local field correction

Figure 4.29. AFM image of ATO nanoporous film divided into two kinds of spaces

Figure 4.30. Schematic diagram of ATO absorption and RB emission spectra

Figure 4.31. Absorption spectrum of nanocrystalline ATO film

Figure 4.32. Schematic diagram of the coordinates in lab frame and laser beam frame in microscope

Figure 5.1. Schematic resonance structures of rhodamine B in zwitterion form

Figure 5.2. Stage-scanned two-photon fluorescence image of RB molecules adsorbed on a glass surface

Figure 5.3. Fluorescence decay curve of bulk RB on a cover slip measured in the test shown in Figure 5.2 and fitted to single exponential model

Figure 5.4. Information of single photons of TCSPC data for the construction of decay curve and intensity trajectory

Figure 5.5. Two pairs of representative fluorescence intensity trajectory and decay of single molecules on glass

Figure 5.6. Two sets of SMFL experiments of RB on glass

Figure 5.7. Measured intensity autocorrelation function of single RB on glass drawn in two different unit times, 5 ms and 2 μ s

Figure 5.8. Measured intensity autocorrelation function of single RB on ATO drawn in 2 μ s unit time

Figure 5.9. Intensity trajectory of RB on glass drawn in 50 ms unit time

Figure 5.10. Fluorescence decay data of high and low intensity times fitted to single exponential decay model

Figure 5.11. Time series of eight fluorescence images of two single RB molecules on glass surface illuminated by TIR method and recorded by CCD camera

Figure 5.12. Total counts vs. lifetime plot of SMFL test of RB on glass

Figure 5.13. Polar angle dependence of fluorescence lifetime of RB on glass

Figure 6.1. Chemical structure of PDI-P1 [*N*-octyl-1,7(3',5' di-*tert*-butylphenoxy)perylene-3,4:4',10-bis(dicarboximide)-benzoic acid]

Figure 6.2. Absorption (thick, 10^{-5} M) and emission (thin, 10^{-6} M) spectra of PDI-P1 in MeOH

Figure 6.3. Schematic diagram of redox potential energies of valance and conduction bands of ATO, ZrO₂, and ground and excited states of PDI-P1

Figure 6.4. Fluorescence image and lifetime of bulk PDI-P1 on ATO

Figure 6.5. Fluorescence decay profile of bulk PDI-P1 on ATO fitted with triple exponential model

Figure 6.6. Fluorescence image and lifetime of bulk PDI-P1 on glass

Figure 6.7. Artificial SMFL distributions having different standard deviations σ and their decay curves

Figure 6.8. Fluorescence image and lifetime of bulk PDI-P1 on ZrO₂

Figure 6.9. Three single molecule fluorescence decays fitted with single exponential decay model

Figure 6.10. Four sets of SMFL distribution measurements done with various sampling threshold

Figure 6.11. Fluorescence images of blank and sample for SMD of PDI-P1 on glass

Figure 6.12. SMFL distribution of PDI-P1 on glass

Figure 6.13. Dual plots of fluorescence intensity and lifetime trajectories of three SMDs of PDI-P1 on glass

Figure 6.14. Duration of emission of PDI-P1 on ATO and glass

Figure 6.15. SMFL distribution of PDI-P1 on ZrO₂

Figure 6.16. Average emission power vs. range of lifetime

Figure 6.17. Distribution of characteristic electron transfer

Figure 6.18. Single molecule fluorescence intensity and lifetime trajectories drawn in a graph

Figure 6.19. Schematic diagram of ATO--PDI-P1 single junction

Figure 6.20. Polar angle dependence of fluorescence lifetime of PDI-P1 on glass

Figure 6.21. Schematically diagram of the configurations of dipole orientation change in the case of the simultaneous lifetime change

Figure 6.22. Plot of radiative lifetime as a function of filling factor based on three combinations of effective medium approximation and local field correction

Figure 6.23. Average emission power vs. range of lifetime without any proportionality between them

Figure 6.24. SMFL distribution of PDI-P1 on ATO, glass, and ZrO_2

Figure 6.25. Diagram of lifetime fluctuation mechanisms suggested in this work

Tables

Table 3.1. Basic specification of home-built and commercial oscillator

Table 3.2. Five bulk solutions used in the virtual SMFL test

Table 4.1. Quantum yields of RB in Water and Methanol

Table 6.1. Fitting result of bulk fluorescence lifetime decay shown in Figure 6.4. τ_i and A_i are the lifetime and amplitude of exponential decay model

Chapter 1. Overview of Single Molecule Study of Fluorescence from Organic Dyes at Interfaces

Lineage of Single Molecule Detection

Single molecule detection (SMD) is a unique method of probing the spectroscopic nature of a chromophore with ultimately high spatial resolution¹⁻¹⁵. It is regarded as the only technique that can eliminate ensemble averaging completely¹⁶. In the early stage of the SMD, people implemented the SMD as a method complementary to other line narrowing techniques, *e.g.* hole burning¹⁷ and photon echo^{18,19}, to understand the fundamental dynamics of an amorphous solid in cryogenic temperature. Both the hole burning and photon echo could eliminate the inhomogeneous broadening of probe chromophores and measured homogeneous broadening resulting from the intrinsic dynamics of the interaction between chromophore and glassy environment. However, both techniques still measured the ensemble averages, which could be overcome by SMD. The first detection of single molecule was achieved by Moerner and Kador in 1989. They took the absorption spectrum of single pentacene molecule embedded in p-terphenyl single crystal⁶. In 1990, Orrit and Bernard took a fluorescence excitation spectrum of the same system²⁰. Betzig and Chichester first addressed the single molecules individually in room temperature by near-field scanning optical microscopy (NSOM) in 1993²¹. Their milestone work contributed to the shaping into modern SMD despite the perturbation of fluorescence by NSOM tip²². In 1994, Nie et al. first made the far-field observation of single molecules flowing through a diffraction limited excitation volume using confocal microscope²³. The current SMD setups are not so different from their framework. The

wide-field SMD microscopy has evolved extensively in many ultra-sensitive and high-resolution experiments: fluorescence correlation spectroscopy^{10,24-26}, fluorescence resonance energy transfer²⁷⁻³², surface enhanced raman spectroscopy³³⁻³⁵, etc. In 1997, Lu and Xie published an important study on the interfacial electron transfer by the SMD of fluorescence emitted from the electron donating Cresyl Violet molecules adsorbed on an electron accepting indium tin oxide film¹. In the conventional ways, the interfacial ET dynamics has been observed as a multi-component dynamics due to the strong surface heterogeneity³⁶⁻³⁸. Including the interfacial ET, not much is known and observed about the nature of single molecules adsorbed on a rigid surface. The goal of our study in this thesis is to elucidate the single molecule phenomena in several selected optical environments.

Theoretical Background

Conventional theories about molecular radiation will be presented in Chapter 2. The concepts of fluorescence lifetime, radiative, non-radiative lifetime, and quantum yield are useful in understanding the observations made in this study. Special attention is paid to the radiative decay lifetime. The non-radiative decay rates of the dyes used in this study, rhodamine B and PDI-P1, were much slower than the radiative decay rates in our experimental conditions; the quantum yield of them were assumed to be close to 1 without extra de-activation channels of electronic excited state³⁹⁻⁴². As a result, the measured fluorescence decay rate was the sum of the rates of the radiative decay and the extra decay channels such as electron transfer; or the measured fluorescence was just the radiative decay in the inert environment. The radiative decay rate of any dye is known to

change depending on the optical and dielectric properties of surrounding medium^{39,43-46}. Several theoretical models have been applied to the estimation of the radiative lifetime: local field correction⁴³⁻⁴⁵, effective medium approximation^{47,48}, and dipole orientation effect at interface^{46,49}. Those theories correct the radiative lifetime in vacuum for the refractive index (local field correction), filling factor of nanoparticles (effective medium approximation), and geometry (dipole orientation effect at interface) of surrounding medium of a single dye molecule. The radiative decay rate of the dye in vacuum can be calculated using the absorption and emission spectra of its solution⁵⁰, or can be experimentally obtained by measuring quantum yield and fluorescence lifetime. It is necessary to apply the theoretical models to the single molecule study, because the single molecule fluorescence lifetime is sensitive to the microscopic heterogeneity of its environment.

Methodology of Single Molecule Detection

Careful cleaning, maintaining, and impurity-checking of substrate are required in SMD⁵¹. Burning, ozone-purging⁵² or wet-cleaning methods⁵¹ have been used depending on the substrates. Dye solution and its container have to be as clean as possible. Experimental setup for SMD was composed of laser, microscope, and detection parts. Home-built and commercial Femtosecond Ti:sapphire oscillators were used to implement the virtual delta-function excitation pulse. Two-photon^{2,53} or one-photon⁵³ excitation were adapted depending on the signal sizes of the single molecules, background, and impurity. Because the detection of single molecule on a quenching substrate is usually limited by the number of photons recorded, a reliable fluorescence imaging and an automatic position-

optimization of laser focus⁵⁴ were implemented in our SMD system. In Chapter 3, several topics will be examined to understand and to confirm the high and reliable performance of time-correlated single photon counting technique of our SMD. Statistical consideration will be given to the verification of observing the single molecule, because the experimental verification is practically hard for daily experiments. As a result, surface number density of about 100 bright spots on $40\ \mu\text{m} \times 40\ \mu\text{m}$ is considered to be a maximum number density allowed for qualified observation of individual molecules in this study. Due to the shortage of data amount of the SMD, the calculated single molecule fluorescence lifetime (SMFL) should be different from its true value. To quantify such a statistical fluctuation of SMFL, we prepared a series of never-bleaching virtual SMFL source, and built two plots: SMFL fluctuation vs. the magnitude of lifetime and SMFL vs. number of photons constituting a decay curve. We will show how those plots are referred to in verifying that a measured comparatively narrow SMFL distribution of RB on glass is not just a statistical broadening but a real one reflecting heterogeneity of dipole orientation of RB.

SMD of RB on ATO

Electron transfer from S_1 state of rhodamine B to nanocrystalline ATO is energetically allowed^{37,55-57}. The electron transfer competes with fluorescence reducing the lifetime of the fluorescence decay. The fluorescence decay contributed from many RB molecules adsorbed on ATO, so-called bulk decay, showed clear deviation from the single exponential decay dynamics. The non-exponential decay could be resolved into many individual single exponential decays originated from the single molecule junctions with

ATO surface¹. The rate of each single molecule fluorescence decay depended primarily on its interfacial ET rate because the quenching effect of ET overwhelmed all the other factors that modified the fluorescence lifetime. The SMD of them has shown that the single exponential dynamics of fluorescence decay was going on at almost all the individual junctions; it means that the individual interfacial ET components followed the first order kinetics^{1,58,59}.

The single molecule electron transfer rates are considered to be widely distributed from several picoseconds confirmed by transient IR absorption experiment. Given the fluorescence lifetime of nanoseconds without ET, our SMD could not see the single RB molecules injecting electron in picosecond timescale due to low quantum yield ~ 0.001 . The observed RBs on ATO had slow ET rates around ~ 1 ns, which means that the observed SMFL distribution was a part of total distribution. As was mentioned in the previous paragraph, SMFL distribution could also be influenced by heterogeneous optical environment through the modification of radiative lifetime. To filter out all the non-ET effect and to see only the effect of ET on fluorescence lifetime of RB on ATO, we performed SMD of RB on nanocrystalline ZrO₂ film. The ZrO₂ was expected to work as a blank sample for ATO in terms of ET, because (1) the ET from RB excited state to ZrO₂ conduction band is not energetically allowed^{37,56,60} and (2) its microscopic morphology and refractive index were similar to the ATO⁶¹. Surprisingly, we found that the SMFL distribution of RB on ET-inactive ZrO₂ was much wider than instrument- and statistical fluctuation-limited lifetime dispersion. It was interpreted resultantly that the measured SMFL of the dye on ET-active nanoporous surface is the convolution of heterogeneous ET dynamics and the lifetime dispersion originated from the local field

correction as a function of heterogeneous effective refractive index. However, a definite comparison with theoretical model was not achieved due to the notion of possible contributions from (1) slow back electron transfer from the electron-filled conduction band or trap states to the unpaired HOMO during the excited state⁶² or (2) energy transfer to the surface plasmon of ATO nanoparticles^{63,64}.

SMD of RB on Glass

The RB was deposited on glass surface and the SMD has been performed. Glass was an ET-inactive substrate. Being different from other nanoporous films, the glass surface is a comparatively flat and lossless dielectric surface. The satisfaction of the boundary condition between electromagnetic fields on both side of the air-glass interface allowed power loss through the evanescent field emitted from RB^{46,49,65}. As a result, the radiative lifetime of single RB on glass changed depending on the emission dipole orientation, distance to the surface, and refractive indices near the interface. The RB is considered to have quantum yield 1 on glass surface and so the measured fluorescence lifetime was equal to its radiative lifetime. We measured the lifetime distribution of RB on glass surface and compared successfully with the predicted lifetime distribution with the help of local field correction.

SMD of PDI-P1 on ATO and glass

Similar results were obtained in the tests of PDI-P1 to those of RB. The quantum yield of the dye was measured and has been known to be 1, because its non-radiative decay channel would hardly be generated in normal condition. Therefore, the fluorescence

lifetime of PDI-P1 is considered to be the same as the radiative lifetime without extra quenching channels like ET. The modification of radiative lifetime of PDI-P1 is explained in the same way as the case of RB because the dependence of radiative lifetime on environment is assumed to be a purely optical process. The SMFL distribution of PDI-P1 on ATO was a part of its total distribution because the molecules injecting electron in picosecond time scale was hard to be detected due to its low quantum yield. The shape of the measured distribution may depend on the intensity threshold of sampling in SMD: the lower the quantum yields of detected single molecules are, the shorter the SMFL distribution shifts to. The SMD experiments with various sampling thresholds of PDI-P1 molecules on ATO showed clear shift of lifetime distribution. The nanoporous ZrO₂ was used as an ET-inactive matrix and the lifetime distribution of PDI-P1 was interpreted with the local field correction and effective medium approximation. PDI-P1 on glass showed single molecule lifetime distribution that could be explained with the dipole orientation effect but non-negligible number of molecules of long lifetime were also detected. We compared bulk and SMD data more systematically. From the comparison, we confirmed the correspondence between the bulk measurement and SMD and the resolving power of SMD. The PDI was discerned from RB by the frequent observations of time-dependent SMFL fluctuations of single PDI-P1 on ATO and glass. The fluctuations were ascribed to the time-dependent conformational change of the adsorbed PDI-P1.

References

- (1) Lu, H. P.; Xie, X. S. *J. Phys. Chem. B* **1997**, *101*, 2753.
- (2) Sanchez, E. J.; Novotny, L.; Holtom, G. R.; Xie, X. S. *Journal of Physical Chemistry A* **1997**, *101*, 7019.
- (3) Macklin, J. J.; Trautman, J. K.; Harris, T. D.; Brus, L. E. *Science* **1996**, *272*, 255.
- (4) Liu, R.; Holman, M. W.; Zang, L.; Adams, D. M. *J. Phys. Chem. A* **2003**, *107*, 6522.
- (5) Moerner, W. E.; Fromm, D. P. *Review of Scientific Instruments* **2003**, *74*, 3597.
- (6) Moerner, W. E.; Kador, L. *Physical Review Letters* **1989**, *62*, 2535.
- (7) Xie, X. S. *Accounts of Chemical Research* **1996**, *29*, 598.
- (8) English, D. S.; Furube, A.; Barbara, P. F. *Chem. Phys. Lett.* **2000**, *324*, 15.
- (9) Ha, T.; Chemla, D. S.; Enderle, T.; Weiss, S. *Bioimaging* **1997**, *5*, 99.
- (10) Zander, C.; Sauer, M.; Drexhage, K. H.; Ko, D.-S.; Schulz, A.; Wolfrum, J.; Brand, L.; Eggeling, C.; Seidel, C. A. M. *Appl. Phys. B* **1996**, *63*, 517.
- (11) Edman, L.; Mets, U.; Rigler, R. *PNAS* **1996**, *93*, 6710.
- (12) Ha, T.; Rasnik, I.; Cheng, W.; Babcock, H. P.; Gauss, G. H.; Lhoman, T. M.; Chu, S. *Nature* **2002**, *419*, 638.
- (13) Chu, S. *Phil. Trans.R. Soc. Lond. A* **2003**, *361*, 689.
- (14) Yang, H.; Luo, G.; Karnchanaphanurach, P.; Louie, T.-M.; Rech, I.; Cova, S.; Xun, L.; Xie, X. S. *Science* **2003**, *302*, 262.

- (15) Shimizu, K. T.; Neuhauser, R. G.; Leatherdale, C. A.; Empedocles, S. A.; Woo, W. K.; Bawendi, M. G. *Physical Review B* **2001**, *63*, 205316.
- (16) Zilker, S. J.; Kador, L.; Friebel, J.; Vainer, Y. G.; Kol'chenko, M. A.; Personov, R. I. *Journal of Chemical Physics* **1998**, *109*, 6780.
- (17) Kozankiewicz, B.; Bernard, J.; Orrit, M. *Journal of Chemical Physics* **1994**, *101*, 9377.
- (18) Molenkamp, L. W.; Wiersma, D. A. *Journal of Chemical Physics* **1985**, *83*, 1.
- (19) Berg, M.; Walsh, C. A.; Narasimhan, L. R.; Littau, K. A.; Fayer, M. D. *Journal of Chemical Physics* **1994**, *101*, 1564.
- (20) Orrit, M.; Bernard, J. *Physical Review Letters* **1990**, *65*, 2716.
- (21) Betzig, E.; Chichester, R. J. *Science* **1993**, *262*, 1422.
- (22) Ambrose, W. P.; Goodwin, P. M.; Martin, J. C.; Keller, R. A. *Science* **1994**, *265*, 364.
- (23) Nie, S.; Chiu, D. T.; Zare, R. N. *Science* **1994**, *266*, 1018.
- (24) Widengren, J.; Mets, U.; Rigler, R. *Journal of Physical Chemistry* **1995**, *99*, 13368.
- (25) Enderlein, J.; Kollner, M. *Bioimaging* **1998**, *6*, 3.
- (26) Borsch, M.; Diez, M.; Graber, P. *Single Mol.* **2000**, *1*, 180.
- (27) Ha, T.; Ting, A. Y.; Liang, J.; Caldwell, W. B.; Deniz, A. A.; Chemla, D. S.; Schultz, P. G.; Weiss, S. *Proc. Natl. Acad. Sci. USA* **1999**, *96*, 893.
- (28) Zhuang, X.; Bartley, L. E.; Babcock, H. P.; Russell, R.; Ha, T.; Herschlag, D.; Chu, S. *Science* **2000**, *288*, 2048.

- (29) Deniz, A. A.; Dahan, M.; Grunwell, J. R.; Ha, T.; Faulhaber, A. E.; Chemla, D. S.; Weiss, S.; Schultz, P. G. *PNAS* **1999**, *96*, 3670.
- (30) Murphy, M. C.; Rasnik, I.; Cheng, W.; Lohman, T. M.; Ha, T. *Biophysical Journal* **2004**, *86*, 2530.
- (31) Kuhnemuth, R.; Seidel, C. A. M. *Single Mol.* **2001**, *2*, 251.
- (32) Haustein, E.; Schwille, P. *Methods* **2003**, *29*, 153.
- (33) Kneipp, K.; Wang, Y.; Kneipp, H.; Perelman, L. T.; Itzkan, I.; Dasari, R. R.; Feld, M. S. *Physical Review Letters* **1997**, *78*, 1667.
- (34) Nie, S.; Emory, S. R. *Science* **1997**, *275*, 1102.
- (35) Futamata, M. *Faraday Discussions* **2006**, *132*, 45.
- (36) Liu, D.; Kamat, P. V. *Journal of Chemical Physics* **1996**, *105*, 965.
- (37) Hashimoto, K.; Hiramoto, M.; Sakata, T. *The Journal of Physical Chemistry* **1988**, *92*, 4272.
- (38) Rehm, J. M.; McLendon, G. L.; Nagasawa, Y.; Yoshihara, K.; Moser, J.; Gratzel, M. *J. Phys. Chem.* **1996**, *100*, 9577-9578.
- (39) Magde, D.; Rojas, G. E.; Seybold, P. G. *Photochemistry and Photobiology* **1999**, *70*, 737.
- (40) Snare, M. J.; Treloar, F. E.; Ghiggino, K. P.; Thistlethwaite, P. J. *Journal of Photochemistry* **1982**, *18*, 335.
- (41) Kircher, T.; Lohmannsroben, H.-G. *Phys. Chem. Chem. Phys.* **1999**, *1*, 3987.
- (42) Lee, S. K.; Zu, Y.; Herrmann, A.; Geerts, Y.; Mullen, K.; Bard, A. J. *J. Am. Chem. Soc.* **1999**, *121*, 3513.

- (43) Glauber, R. J.; Lewenstein, M. *Physical Review A* **1991**, *43*, 467.
- (44) Barnett, S. M.; Huttner, B.; Loudon, R. *Physical Review Letters* **1992**, *68*, 3698.
- (45) Crenshaw, M. E.; Bowden, C. M. *Physical Review Letters* **2000**, *85*, 1851.
- (46) Lukosz, W.; Kunz, R. E. *J. Opt. Soc. Am.* **1977**, *67*, 1607.
- (47) Vallee, R. A. L.; Tomczak, N.; Vancso, G. J.; Kuipers, L.; Hulst, N. F. v. *Journal of Chemical Physics* **2005**, *122*, 114704.
- (48) Aspnes, D. E. *Am. J. Phys.* **1982**, *50*, 704.
- (49) Lukosz, W.; Kunz, R. E. *Optics Communications* **1977**, *20*, 195.
- (50) Birks, J. B. *Photophysics of Aromatic Molecules*; Wiley-Interscience: London, New York, 1970.
- (51) Ha, T. *Methods* **2001**, *25*, 78.
- (52) Ip, K.; Gila, B. P.; Onstine, A. H.; Lambers, E. S.; Heo, Y. W.; Baik, K. H.; Norton, D. P.; Pearton, S. J.; Kim, S.; LaRoche, J. R.; Ren, F. *Applied Physics Letters* **2004**, *84*, 5133.
- (53) Brand, L.; Eggeling, C.; Zander, C.; Drexhage, K. H.; Seidel, C. A. M. *J. Phys. Chem. A* **1997**, *101*, 4313.
- (54) Ha, T.; Chemla, D. S.; Enderle, T.; Weiss, S. *Appl. Phys. Lett.* **1997**, *70*, 782.
- (55) Hagfeldt, A.; Gratzel, M. *Chem. Rev.* **1995**, *95*, 49.
- (56) Kung, H. H.; Jarrett, H. S.; Sleight, A. W.; Ferretti, A. *Journal of Applied Physics* **1977**, *48*, 2463.
- (57) Kim, H.; Pique, A. *Applied Physics Letters* **2004**, *84*, 218.

- (58) Asbury, J. B.; Hao, E.; Wang, Y.; Ghosh, H. N.; Lian, T. *Journal of Physical Chemistry B* **2001**, *105*, 4545.
- (59) Moser, J. E.; Gratzel, M. *Chemical Physics* **1993**, *176*, 493-500.
- (60) Pant, D.; Levinger, N. E. *Chem. Phys. Lett.* **1998**, *292*, 200.
- (61) Venkataraj, S.; Kappertz, O.; Weis, H.; Drese, R.; Jayavel, R.; Wuttig, M. *Journal of Applied Physics* **2002**, *92*, 3599.
- (62) Guo, J.; She, C.; Lian, T. *Journal of Physical Chemistry B* **2005**, *109*, 7095.
- (63) Nutz, T.; Felde, U. z.; Haase, M. *Journal of Chemical Physics* **1999**, *110*, 12142.
- (64) Andrew, P.; Barnes, W. L. *Science* **2004**, *306*, 1002.
- (65) Arnoldus, H. F.; Foley, J. T. *OPTICS LETTERS* **2003**, *28*, 1299.

Chapter 2. Theory of Fluorescence Lifetime in Single Molecule Detection

I. Introduction

Fluorescence was first brought into scientific realm in 1852 by Sir George Stokes¹. Since then, people have understood molecular photophysical and photochemical processes probed by the fluorescence that has high sensitivity and universality. Historically, single molecule detection had begun from detecting fluorescence of single molecule probably due to the overwhelmingly higher sensitivity of the fluorescence than other spectroscopic tools. The objective of SMD is to resolve the ensemble-averaged spatial heterogeneity of the characteristics of fluorescence. This point requires the new knowledge of the relation between the fluorescence of a probe molecule and the optical and geometrical property of environment.

In the beginning, an elementary introduction to the various aspects of fluorescence is presented: definitions of the processes involved in the electronic transitions and their relations in the presence of electron transfer. Next, the local field correction and dipole orientation effect on the fluorescence decay rate are briefly introduced for their applications in later discussion sections about the unexpectedly broad distributions of measured SMFLs in several experimental situations. In the last section, a brief explanation of fitting method in this study is presented.

II. Elements of Fluorescence

Kinetics

The fluorescence is a part of energy release from a molecule after its electronic transition from ground state to excited state. The other de-excitation pathways and the fluorescence compete among themselves with their rates depending on the intrinsic property of the molecules and their environment^{1,2}. Figure 2.1 is a well-known Perrin-Jablonski diagram showing the possible processes¹. The electronic excitation, E, can be made by any kind of perturbation having energy corresponding to the energy gap between ground and excited states. In this work, the electronic excitation is induced only by the absorption of light. The efficiency of electronic transition is determined by the magnitude of transition dipole moment and Frank-Condon overlap. Upon excitation to the vibronic manifold of the first electronic excited state (S_1), the molecule quickly relaxes to the lowest vibrational level of the first excited state ($S_{1,v=0}$; v , vibrational quantum number) through vibration relaxation (VR), in the air or solution medium by the collision with bath molecules. Illuminated with shorter wavelength than that for excitation to S_1 , the molecules can be excited to S_n ($n>1$) states and again quickly relax to the $S_{1,v=0}$ via internal conversion (IC) and VR non-radiatively. Therefore, the excitation wavelength dependence of the subsequent photo-physical processes after relaxation to $S_{1,v=0}$ is negligible because they are much slower than the IC and the VR on excitation.

The molecule in $S_{1,v=0}$ state relaxes to their ground state either radiatively or non-radiatively. The fluorescence decay rate is the rate of population decay of the $S_{1,v=0}$ state. Therefore, the fluorescence decay rate constant k_f is the sum of radiative (k_r) and non-radiative (k_{nr}) decay rate constants:

$$k_f = k_r + k_{nr} \quad (2.1)$$

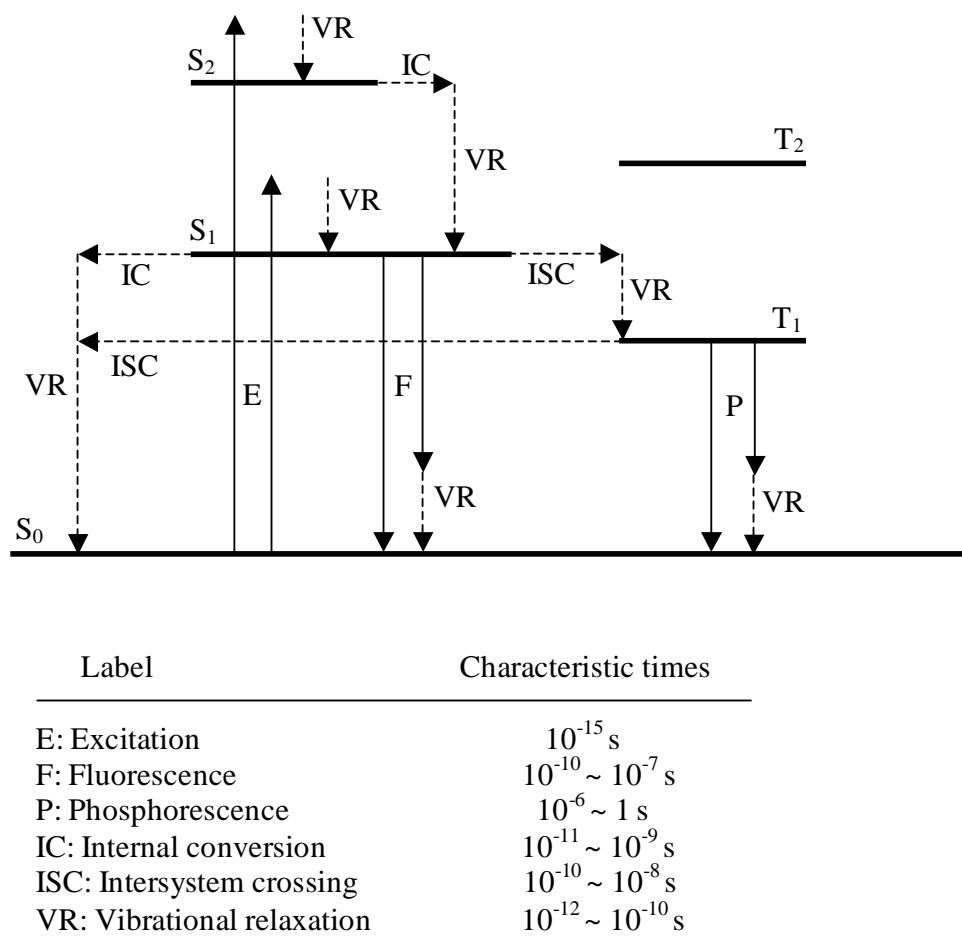


Figure 2.1. Perrin-Jablonski diagram¹. Most of photophysical pathways to the ground state after an electronic excitation E are shown schematically. S_0 , S_1 , S_2 , T_1 , and T_2 are singlet ground state, singlet first and second excited state, triplet first and second excited state, respectively. Typical time scales of individual pathways are tabulated behind the diagram.

The non-radiative decay rate from $S_{1,v=0}$ is a sum of the internal conversion (k_{IC}) into high vibronic levels of S_0 and intersystem crossing (k_{ISC}) into low-energy-lying triplet state.

Then, Equation (2.1) becomes:

$$k_f = k_r + k_{IC} + k_{ISC} \quad (2.2)$$

Equation 2.2 is quite general for the chromophore interacting with surrounding medium thermally and statically without proton³ or electron transfer. However, the electron transfer from the electronic excited state to electron acceptor provides an additional non-radiative de-excitation channel of $S_{1,v=0}$ when the chromophore is in close proximity to the electron acceptor as follows:

$$\begin{aligned} k_{fE} &= k_r + k_{IC} + k_{ISC} + k_{ET} \\ &= k_r + k_{nr} + k_{ET} \\ &= k_f + k_{ET} \end{aligned} \quad (2.3)$$

where the k_{fE} and k_f represent the fluorescence decay rate constants with and without electron transfer, respectively. The basic idea of fluorescence technique in electron transfer study is to find the k_{ET} by measuring k_{fE} with the separately acquired knowledge of fluorescence decay rate of non-interacting system k_f . Often, the lifetime τ ($=1/k$) of corresponding process is mentioned more than its rate constant k . The relation equivalent to Equation 2.3 in terms of lifetime is:

$$\tau_{fE} = \frac{\tau_f \tau_{ET}}{\tau_f + \tau_{ET}} \quad (2.4)$$

where τ_{fE} is the measured fluorescence lifetime, τ_f is the fluorescence lifetime of non-interacting system that may be measured from blank sample for the ET process, and τ_{ET} is the characteristic time of ET.

Quantum Yield

Quantum yield is one of the most important photophysical data of a chromophore. It is not only the characteristic of a photon emitter but also a good indication showing the properties of environment and chromophore-environment interaction. The quantum yield (Φ_F) is defined as the ratio of the number of emitted photons to the number of absorbed photons. It can be expressed in a variety of forms using photophysical parameters as shown in Equation 2.5a and 2.5b¹:

$$\Phi_F = \frac{k_r}{k_r + k_{nr}} = k_r \tau_f = \frac{\tau_f}{\tau_r} \quad (2.5a)$$

$$= \frac{n^2}{SI_0(\lambda_E)(1 - 10^{-A(\lambda_E)})} \int_0^\infty I_F(\lambda_E, \lambda_F) d\lambda_F \quad (2.5b)$$

where n is the refractive index of medium, S is the sensitivity constant of instrument, $I_0(\lambda_E)$ is the excitation intensity at wavelength λ_E , $A(\lambda_E)$ is the absorbance, and $I_F(\lambda_E, \lambda_F)$ is the emission intensity measured at λ_F when the excitation wavelength is λ_E . The n^2 term is from the “ $\frac{1}{n^2}$ correction” for the refraction of light due to the difference of refractive index of sample medium and detector medium^{4,5}. The quantum

yield data is usually used in the quantitative estimation of non-radiative decay rate constant as a function of optical environment. ET rate constant is included in the non-radiative decay rate constant for simplicity. In this study, it is especially informative in equating the fluorescence lifetime to the radiative lifetime because the yield of non-radiative decay is frequently negligible in the dye system studied.

The quantum yield can be estimated by the comparison with the reference sample of known quantum yield^{6,7} or by the direct measurement of absolute quantum yield^{8,9}. The first method is more popular for the sake of convenience and readiness. The detailed method of quantum yield measurement is different from one to the next. The following simple comparison method can be used, if the detection system is well corrected for the wavelength dependence of sensitivity, is free of polarization effect, and the concentration of the solution is low enough (<0.1 OD) not to have inner filter effect¹. The quantum yield expression in Equation 2.5b includes S and $I_0(\lambda_E)$ values, which are inaccurate and not readily measurable, disappear by dividing the same equation of reference of known quantum yield, and we get a relation that has terms that are available from UV-Vis and fluorescence emission test.

$$\Phi_F = \frac{n^2(1 - 10^{-A_R(\lambda_E)}) \int_0^\infty I_F(\lambda_E, \lambda_F) d\lambda_F}{n_R^2(1 - 10^{-A(\lambda_E)}) \int_0^\infty I_{FR}(\lambda_E, \lambda_F) d\lambda_F} \Phi_{FR} \quad (2.7)$$

Here n_R is the refractive index of the reference medium, $A_R(\lambda_E)$ is the absorbance of reference, $I_{FR}(\lambda_E, \lambda_F)$ is the emission intensity of reference measured at λ_F when the excitation wavelength is λ_E , and Φ_{FR} is the known quantum yield of reference.

As an alternative way, we can find the quantum yield by measuring fluorescence lifetime and calculating the radiative lifetime using Equation 2.5a and the Strickler-Berg equation in Equation 2.7^{10,11}. The inverse of radiative decay lifetime is:

$$\frac{1}{\tau_R} = 2.88 \times 10^{-9} n^2 \frac{\int F(\tilde{\nu}) d\tilde{\nu}}{\int F(\tilde{\nu}) \tilde{\nu}^{-3} d\tilde{\nu}} \int \varepsilon(\tilde{\nu}) \tilde{\nu}^{-1} d\tilde{\nu} \quad (2.7)$$

where , $F(\tilde{\nu})$ is the emission spectrum in arbitrary unit as a function of wave number. $\varepsilon(\tilde{\nu})$ is the molar absorption coefficient spectrum as a function of wave number. n is the refractive index of solvent used when measuring emission and absorption spectrum. This method was used in the past and the expression in Equation 2.7 does not include the modern treatment of the interaction between chromophore and medium. However, it has been reported that the quantum yield measured by this method is in good agreement with the reference comparison method in our and previous works^{7,12}.

III. Radiative Lifetime Dependence on Optical Environment

The fluorescence decay rate constant k_{fE} in Equation 2.3 changes when the chromophore or its surrounding medium changes. Each term in the right side of Equation 2.3 depends on both chromophore and medium. In other words, no term in Equation 2.3 depends only on either chromophore or medium. Therefore, when the fluorescence lifetime measurement is performed in different conditions, it is often not clear what kind of process is involved with what extent unless one of the possible processes dominates the de-excitation of the excited state. To correctly interpret the change of fluorescence lifetime, it is necessary to understand and to determine quantitatively all the possible

sources of lifetime change. The non-radiative decay rate k_{nr} is often much slower than radiative decay rate in the organic dyes that are used in the single molecule experiments. In that case, the non-radiative decay rate can be safely approximated to zero, and the radiative lifetime becomes an important parameter to know and to be compared with the electron transfer rate. There are a couple of theoretical models that are applicable to the estimation of radiative lifetime under the influence of optical properties of surrounding medium, which are introduced in Section III.A and III.B.

III.A. Local Field Effect

The notion that the spontaneous emission (radiative decay) rate is dependent on the refractive index or dielectric constant of surrounding medium has formed for decades¹³⁻²⁰. Early knowledge of the relation is that the radiative lifetime of an embedded two level system decreases by a factor of refractive index of surrounding medium from its value in vacuum^{15,19,21}.

$$\tau_{rad}(n) = \frac{\tau_{vac}}{n} \quad (2.8)$$

where $\tau_{rad}(n)$ is the radiative lifetime of emission in a medium with refractive index n and τ_{vac} is the radiative lifetime in vacuum. The simple relation results from the theoretical model of homogeneous dielectric constant over space with the application of quantized macroscopic Maxwell equations. In 1946, Purcell predicted the necessity of local field correction for the local interaction between the radiating two level system and nearby

medium dipoles¹⁴. Since then, three models - empty-cavity²², virtual-cavity^{16,17,23}, and fully microscopic model^{18,19} - have been studied theoretically and experimentally:

$$\text{Empty-cavity} \quad \tau_{rad}(n) = \left(\frac{3n^2}{2n^2 + 1} \right)^{-2} \frac{\tau_{vac}}{n} \quad (2.9)$$

$$\text{Virtual-cavity} \quad \tau_{rad}(n) = \left(\frac{n^2 + 2}{3} \right)^{-2} \frac{\tau_{vac}}{n} \quad (2.10)$$

$$\text{Fully Microscopic} \quad \tau_{rad}(n) = \left(\frac{n^2 + 2}{3} \right)^{-1} \tau_{vac} \quad (2.11)$$

The n^2 terms in brackets are equivalent to the dielectric constant of non-absorbing material. Both the empty-cavity and virtual-cavity model describe macroscopically the radiative lifetime dependence of an oscillator inside a cavity on the local field from the medium of refractive index n outside the cavity. The cavity is filled with empty space in the empty-cavity model and its dipoles at the same refractive index as its surrounding medium in the virtual cavity model. The dipoles inside the virtual cavity are assumed not to contribute to the local field. The virtual cavity model has been favored but experimental results indicated that the empty-cavity model should be employed²⁴. Most recently, Crenshaw et al.¹⁸ developed a fully microscopic quantum-electrodynamical, many-body derivation of Langevin-Bloch operator equations of motion for a radiating two-level system embedded in a dielectric medium which is also treated as a polarizable collection of two-level systems. The two kinds of two-level systems interact to each other via quantized electromagnetic field. In the single molecule detection limit, the authors

derived the local field enhancement factor shown in Equation 2.11. In general, the enhancement effect without local field interaction in Equation 2.7 is due to the higher density of states for photons in higher refractive index medium, which is reminiscent of radiation density dependence on n^3 in blackbody radiation¹⁰. That is to say, the relation between radiative lifetime and medium refractive index arises from the density of optical modes and radiation-induced polarization of neighboring medium atoms.

In the past, the experimental studies concerning those theories^{15,17,25,26} involved non-trivial boundary conditions like the capping material of embedded emitter, and therefore, they might have not measured the true relation between radiative emission rate and medium refractive index¹⁸. In 2004, Wuister et al. designed a more reasonable experimental model than previous ones and demonstrated that the local field correction term in 2.11 was consistent with experimental data¹⁹. The previous experimental systems had been a small radiating atom within much larger low-dielectric capping material^{15,17,25,26}, through which the medium oscillators influenced on the embedded atom and the atom did not on medium. As a result, empty-cavity and virtual-cavity model had explained the experimental results well. However, because the true medium refractive index dependence of the radiative lifetime is the result of interaction between the radiating dipole and nearby dipoles, Wuister et al¹⁹ used organically capped CdSe and CdTe quantum dots of which diameters were much bigger than the thickness of organic capping material. Such an experimental model resembled the radiating system in polarizable medium interacting via local electric field and had refractive index dependence in accordance with Equation 2.11.

The optical structures of the samples studied in this thesis have not been as simple as the model studied in those theoretical studies. Therefore, it may be hard to think any one of the presented theories is a cure-all for interpreting experimental results, and it should even be doubted that the local field correction worked in the dye-adsorbed ATO nanoparticle system. However, many previous studies have shown that the effective medium approximation of dielectric property worked in the studies of radiative lifetime fluctuation in a glassy medium^{27,28}, optical properties of nanocrystal aggregates^{17,29} and, specifically, nanocrystalline ATO film^{30,31}; the effective medium approximation (EMA) stems from the notion of local field correction³². Therefore, the previous experimental and theoretical studies hint that those theories are pertinent to the understanding the optical phenomena of fluorescing dyes adsorbed on the nanocrystalline material. The most important ability of the theoretical models of the local field correction is that they, jointly with the EMA, are apt to explaining the spatial heterogeneity of fluorescence lifetime that is uniquely observed in single molecule detection. In this work, the convolution of local field correction and effective medium approximation will explain the observed magnitudes and distributions of single molecule lifetimes in several applicable situations.

III.B. Orientation of Dipole on a Dielectric Flat Surface

The dependence of the radiative decay lifetime on the microscopic interaction between a chromophore and surrounding medium was introduced in the previous section. Another effect has been known to change the radiative lifetime of a molecule that is close to an object of finite geometry³³⁻³⁵. The near field effect is determined by the geometrical

variables and macroscopic optical parameters. The coupling of evanescent wave to its substrate or interference between traveling waves inhibits or enhances the power emission of the chromophore. To be more rigorous, coupled dipole method should be adopted to account for the interaction with the dielectric response of substrate in case of an adsorbed molecule^{36,37}. In the coupled dipole method, the substrate is modeled to be a three dimensional lattice consisted of many polarizable units. The molecule experiences additional field from the units induced by itself. In this section, a summary of classical theoretical works published by Lukosz et al.^{33,34} and Arnoldus et al.³⁵ are presented for its application to the experimental results in later discussion. Quantum electrodynamical formalism can also describe the phenomenon but it is known that there is little difference in their results³⁶.

Reciprocal Relation between Radiative lifetime and Emission Power

The radiative decay rate constant is the sum of the Einstein A coefficients, the transition probabilities of spontaneous emission from the lowest vibrational level of S₁ state down to the manifold of vibrational levels of S₀ state³⁸:

$$\frac{1}{\tau_r} = k_r = \sum_{\nu} A_{1,0 \rightarrow 0,\nu} \quad (2.13)$$

where $A_{1,0 \rightarrow 0,\nu}$ is the Einstein A coefficients from the lowest vibrational level of S₁ state down to a vibrational level ν of S₀ state. In fact, the Strickler-Berg equation in Equation 2.7 can be derived from Equation 2.13³⁸. Power L emitted by N number of molecules in state S_{1,0} is:

$$L = N \sum_{\nu} A_{1,0 \rightarrow 0,\nu} \hbar \omega_{\nu} \quad (2.14)$$

where, ω_{ν} is the frequency of transition from $S_{1,0}$ to $S_{0,\nu}$. Then, the power emitted by a single molecule is:

$$L = \sum_{\nu} A_{1,0 \rightarrow 0,\nu} \hbar \omega_{\nu} \quad (2.15)$$

Let us assume that we could substitute average transition frequency ω_a of detection frequency window for the ω_{ν} :

$$L = \hbar \omega_a \sum_{\nu} A_{1,0 \rightarrow 0,\nu} \quad (2.16)$$

Then, the following important relation can be drawn from Equation 2.13 and 2.16:

$$\tau = \frac{\hbar \omega_a}{L} \quad (2.17)$$

The theoretical work had been done based on two-level system without the assumption in Equation 2.16 and started with a relation, $\tau = \hbar \omega / L$ ³⁴. The assumption is valid if the Einstein $A(\omega)$ coefficient is symmetric around the average transition frequency ω_a . It should be good because the $A(\omega)$ is proportional to the fluorescence intensity and the measured fluorescence spectrum of RB was roughly symmetric around the center of detection window. Now we bring the single molecule close to the interface as shown in Figure 2.2. The single molecule is represented with and treated as a classical dipole (\mathbf{d}_0) corresponding to the electronic transition dipole moment³³. The azimuthal angle is set to zero because of the symmetry of the rotation about the z axis. Both sides of Equation 2.17 is scaled by their values when $z_0 \rightarrow \infty$, τ_{∞} and L_{∞} :

$$\frac{\tau_{z_0}}{\tau_\infty} = \frac{L_\infty}{L(z_0)} \quad (2.18)$$

By the scaling, the right-hand side term becomes a function of z_0 , relative refractive index $n = n_2/n_1$, and dipole orientation angle θ shown in Figure 2.2. The analytical form of it will be shown in the next section.

Dipole Orientation Dependence

The power radiated by an electric dipole is given by the following expression³³:

$$L = \frac{1}{2} \omega \mathbf{d}_0 \cdot \text{Im}\{\mathbf{E}(z_0)\} \quad (2.19)$$

where, \mathbf{d}_0 is an amplitude vector of dipole oscillation making angle θ in Figure 2.2. $\text{Im}\{\}$ denotes the imaginary part of $\{\}$. $\mathbf{E}(z_0)$ is the electric field radiated from dipole at position z_0 . The imaginary part of the amplitude vector of $\mathbf{E}(z_0)$ is decomposed to z and

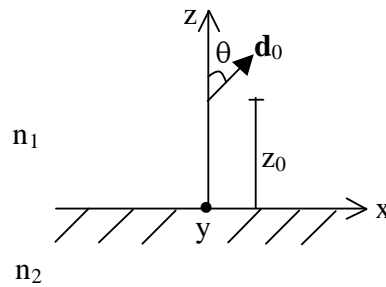


Figure 2.2. Schematic diagram of a dipole (\mathbf{d}_0) in front of a planar interface between medium 1 and 2 with refractive indices n_1 and n_2 respectively. The distance of the dipole from the interface is z_0 of which magnitude is less than the wavelength of emitted light for the lifetime modification effect to work³⁵. θ is the angle between the dipole and z axis.

x-y plane; the projection on x-y plane is symmetric on the plane and we fix it to x axis. The $\text{Im}\{\mathbf{E}(z_0)\}$ can be represented as $F(z_0)\cos\theta \hat{\mathbf{z}} + F'(z_0)\sin\theta \hat{\mathbf{x}}$. The analytical expression of $F(z_0)$ and $F'(z_0)$ can be found in Ref. 33. Then, we obtain an expression of the power L expanded to the contributions of the dipoles perpendicular and parallel to the interface:

$$L = \frac{1}{2}\omega(d_0 \cos\theta \hat{\mathbf{z}} + d_0 \sin\theta \hat{\mathbf{x}}) \cdot \{F(z_0)\cos\theta \hat{\mathbf{z}} + F'(z_0)\sin\theta \hat{\mathbf{x}}\} \quad (2.20a)$$

$$= \cos^2\theta \frac{1}{2}\omega d_0 F(z_0) + \sin^2\theta \frac{1}{2}\omega d_0 F'(z_0) \quad (2.20b)$$

The $1/2\omega d_0 F(z_0)$ and the $1/2\omega d_0 F'(z_0)$ in the first and second terms of the right side of 2.20b is the power radiated by the vertical and horizontal dipoles, respectively. In other words, the emission power of the dipole of arbitrary orientation θ is the sum of its powers when it were vertical and horizontal to the interface weighted by $\cos^2\theta$ and $\sin^2\theta$, respectively³³:

$$\frac{L(z_0)}{L_\infty} = \cos^2\theta \left[\frac{L_\perp(z_0)}{L_\infty} \right] + \sin^2\theta \left[\frac{L_\parallel(z_0)}{L_\infty} \right] \quad (2.21)$$

where the suffixes \perp and \parallel denote that the dipole were vertical and horizontal to the interface. Again, we scaled with L_∞ that is isotropic. Analytical expressions of the powers of the vertical and horizontal dipoles in the right side of Equation 2.21 are presented in Ref. 34. Given those expressions for the two directions of the dipole, the radiative lifetime is determined only by the angle with the z axis.

Power Loss through the Evanescent Field

Lastly, the origin of the power change near the interface of lossless dielectric media is explained in this section³³⁻³⁵. In Equation 2.21, the relative lifetime τ_r/τ_∞ was derived to a function of θ with n_1 , n_2 , and z_0 as its experimental parameters. In the experimental setup where n_2 is greater than n_1 , the relative lifetime function is less than 1 whatever the orientation of dipole θ is. The reason can be explained as follows: the radiation field from the dipole consists of superposition of plane waves in all direction and imaginary evanescent field. When the dipole is away from the interface far enough ($z_0 \gg \lambda_1$), there is no power transport through the evanescent field while the traveling plane waves transport energy from the source (dipole) into space spherically. Therefore, the radiative lifetime of the dipole far away from the interface is related only to the power emission through the traveling waves. When the dipole is brought to the interface close enough ($z_0 < \lambda_1$), power emission through the traveling waves does not change but additional power emission through the evanescent wave is turned on. As a result, the relative power emission increases and relative radiative lifetime decreases according to Equation 2.18, when the dipole gets close to the interface.

Let us look at a detailed schematic diagram of the configuration and ray optics in the real experiment in Figure 2.3. All the notation and symbols in this paragraph pertain to Figure 2.3. The radiation field of the single dipole consists of two different waves: traveling waves in all directions and evanescent waves that decay exponentially in both negative and positive z directions and travel along the xy plane. The two kinds of waves have different z -components of wave vector \mathbf{k}_1 in medium 1³⁵:

$$\mathbf{k}_1 = \mathbf{k}_x + \beta \operatorname{sgn}(z - z_0) \mathbf{e}_z \quad (2.22)$$

$$\beta = \begin{cases} \sqrt{k_1^2 - k_x^2} & k_x < k_1 & ; \text{traveling wave} \\ i\sqrt{k_x^2 - k_1^2} & k_x > k_1 & ; \text{evanescent wave} \end{cases} \quad (2.23)$$

where, \mathbf{k}_x is the wave vector of \mathbf{k}_1 projected on x axis. $\text{sgn}(z-z_0)$ is a sign function defined to be 1 ($z > z_0$), 0 ($z = z_0$), or -1 ($z < z_0$). \mathbf{e}_z is a unit vector of z axis. We can see that the wave number along the z direction of the evanescent field is imaginary. Because $n_2 > n_1$, all the traveling waves propagating downwards between the two planes $z = z_0$ and $z = 0$ (ray II for $0 < \theta_i < 90^\circ$) are reflected (ray II_r) and transmit (ray II_t) partially at the interface. The reflected ray II_r interferes with the ray I constructively or destructively. The sum of the powers of all the emission interference patterns in the upper half-space ($\text{I} + \text{II}_r$ for $z > z_0$) and transmitted light (II_t) are the same as the total emission power of the dipole when $z_0 \gg \lambda_1$ because all the traveling waves from the dipole are integrated at both distances. According to the Snell's law $\sin\theta_1 = n_2 \sin\theta_t$, the θ_t is limited from 0 to $\sin^{-1}(1/n_2)$ for $0 < \theta_i < 90^\circ$. The angle $\sin^{-1}(1/n_2)$ is defined as critical angle θ_c . If the medium 1 and 2 are air and glass respectively, θ_c is about 41° . In other words, all the traveling waves propagating downwards in medium 1 (ray II) transmit the interface with the angle of refraction limited to the θ_c . How about the traveling waves (I_e and I_e') of which direction makes angle with the z axis higher than the θ_c ? They also transport energy from the dipole. Because the energy transported by the rays within the critical angle θ_c is the same as the total energy emitted by the dipole at $z_0 \gg \lambda_1$, the energy transported by the rays outside the θ_c contributes to extra power radiation and results in the decrease of radiative lifetime (Equation 2.18). The wave number of the horizontal component of the ray outside the θ_c (I_e or I_e') is:

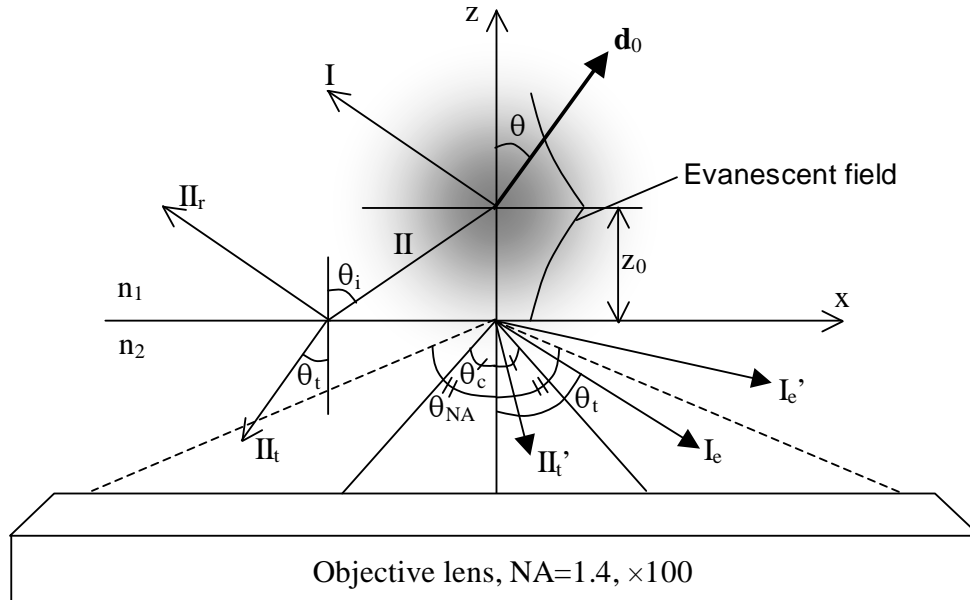


Figure 2.3. Schematic illustration of experimental configuration of a single dipole \mathbf{d}_0 near glass-air interface. The position of dipole is $(0, 0, z_0)$. The dipole makes the angle θ with z axis. The refractive indices of air (n_1) and glass (n_2) are 1.0 and 1.52 respectively. The specifications of rays: I, traveling wave radiated to the upper half-space; II, traveling wave radiated to the bottom half-space; II_r and II_t, reflected and refracted traveling waves of II; θ_i and θ_t , incidence and refraction (or transmission) angles; θ_c , critical angle; θ_{NA} , half of angular aperture; I_e, traveling wave of which transmission angle is greater than the critical angle and source is evanescent field in medium 1; I_e', traveling wave of which transmission angle is greater than the θ_{NA} and source is evanescent field in medium 1; II_t', another refracted traveling wave. The object in the bottom of the figure is an objective lens used in experiment having numerical aperture 1.4 and multiplication factor 100.

$$k_2 \sin \theta > k_2 \sin \theta_c = k_1 \quad (2.24)$$

where, the definition of critical angle and $n_1=1$ are used. To satisfy the boundary condition, the wave number of horizontal component in medium 2 has to be the same as k_x :

$$k_2 \sin \theta = k_x > k_1 \quad (2.25)$$

Comparing Equation (2.25) and (2.23), we can find that the source of the rays propagating with angle θ , higher than θ_c in the medium 2 is the evanescent field in the medium 1. A brief conclusion is that the radiative lifetime is reduced through the evanescent field by approaching the dipole to the interface between two dielectric lossless media of different refractive indices. As shown in Figure 2.3, the traveling waves in medium 2, which is converted from evanescent field in medium 1, makes wide angle with z axis ($>41^\circ$) at a glance. Depending on the numerical aperture of objective lens, we may lose significant portion of rays outside the angular aperture marked by dotted lines it may be hard to detect such an adsorbed single molecule due to (1) the low photon flux which is the intrinsic property of single molecule compared to bulk detection, and (2) the fact that, because $z_0 \ll \lambda_1$, the highest portion of power is transported through the evanescent field with limited angular aperture of the objective lens. In fact, 68.7% and 56.5% of the total power from the vertical dipole and horizontal dipole, respectively, are transported through the evanescent field. The half of angular aperture, θ_{NA} , is:

$$\theta_{NA} = \sin^{-1}\left(\frac{1.4}{1.52}\right) = 67.1^\circ \quad (2.26)$$

where, 1.4 is the numerical aperture of the objective lens used in experiment, and 1.52 is the refractive index of glass. If the radiation power per unit solid angle in medium 2 is homogeneous, the lost photon flux is about 30%, which may not a critical cause of low sensitivity that disables SMD in certain experiment.

IV. Criterion of Goodness of Fit

Least square fit method has been used for the calculation of fluorescence lifetime extensively in this work. It is a popular data analysis method but there are a couple of points to comment on the justification of applying the method because of the special characteristics of single molecule detection.

The reduced chi square χ_r^2 was chosen as a criterion of goodness of fit to an assumed model³⁹⁻⁴³:

$$\chi_r^2 = \frac{1}{N - n - 1} \sum_{i=1}^N \frac{(I_i^e - I_i^m)^2}{s_i^2} \quad (2.27)$$

where N is the number of data points, n is the number of fitting parameters, I_i^e and I_i^m are the experimental and model function intensities at the i th time bin, and s_i is the standard deviation at the i th time bin⁴³. It is a chi square normalized by the degree of freedom, $N - n - 1$. The minimization of the χ_r^2 by systematically changing the parameters (amplitudes and lifetimes of model decay) included in the I_i^m results in the best fit of the assumed model to the experimental data. The minimization procedure is implemented by nonlinear least square fit based on Marquardt algorithm⁴⁴. It is not possible to find the standard deviation s_i experimentally because the SM test cannot be repeated because of

irreversible bleaching. However, the theoretical standard deviation is $\sqrt{I_i^e}$, and we could use I_i^e instead of experimental s_i^2 . Another problems specific in SMFL test is that the decay data is low in size down to zero in many points, highly noisy, and can be negative when background subtraction is done; thus, the I_i^e can not substitute for s_i^2 . To circumvent the problem, the I_i^m is used instead because it is smooth, always positive, and as valid as I_i^e in simulating s_i^2 after the completion of fitting.

Minimizing χ_r^2 is equivalent to maximizing likelihood or log likelihood function of a probability model of which error has gaussian distribution centered at the I_i^m :

$$L = A \prod_{i=1}^N e^{-\frac{(I_i^e - I_i^m)^2}{I_i^m}} \quad (2.28)$$

$$\log_e L = A' - \sum_{i=1}^N \frac{(I_i^e - I_i^m)^2}{I_i^m} \quad (2.29)$$

where L is the likelihood function and A and A' are constants. The L means the likelihood or the probability of observing the experimental data, given with fitting parameters of assumed model. Actually, the error of time-correlated single photon counting (light detection method to be introduced in Chapter 3) observes the poisson distribution, while the gaussian error is an approximation of poisson error of large data size. Fitting data using the likelihood function of poisson error is conventionally called Maximum Likelihood Estimation (MLE)^{42,45-49}. The decay lifetime calculated by least square is reported to be ~5% lower than that by MLE below ~20,000 total counts⁴². The highest level of total counts from a single molecule on ATO film is about 20,000.

However, the systematic ~5% underestimation of lifetime is not considered to be significant compared to the accuracy decreased by the low amount of photon counts, the background subtraction, and the instrument response.

V. Conclusion

We have reviewed several theoretical ingredients for this work. The conventional concepts and definitions about fluorescence study were introduced. The dependence of the radiative decay lifetime on local field correction convoluted with effective medium approximation was reviewed. The detailed description of the dipole orientation effect on the radiative decay lifetime was presented. The two theoretical tools will be applied to the analysis of the SMFL results of the two different forms of sample: nanoporous film and flat glass surface respectively. Least square fitting method to be used throughout this study was discussed in terms of the characteristics of single molecule detection.

References

- (1) Valeur, B. *Molecular Fluorescence*; Wiley-VCH: Weinheim, 2002.
- (2) Becker, R. S. *Theory and Interpretation of Fluorescence and Phosphorescence*; Wiley Interscience: New York, 1969.
- (3) Agmon, N.; Huppert, D.; Masad, A.; Pines, E. *Journal of Physical Chemistry* **1991**, *95*, 10407.
- (4) Demas, J. N.; Crosby, G. A. *Journal of Physical Chemistry* **1971**, *75*, 991.
- (5) Ediger, M. D.; Moog, R. S.; Boxer, S. G.; Fayer, M. D. *Chemical Physics Letters* **1982**, *88*, 123.
- (6) Fery-Forgues, S.; Lavabre, D. *Journal of Chemical Education* **1999**, *76*, 1260.
- (7) Langhals, H.; Karolin, J.; Johansson, L. B.-A. *J. Chem. Soc., Faraday Trans.* **1998**, *94*, 2919.
- (8) Bindhu, C. V.; Harilal, S. S.; Varier, G. K.; Issac, R. C.; Nampoory, V. P. N.; Vallabhan, C. P. G. *J. Phys. D: Appl. Phys.* **1996**, *29*, 1074.
- (9) Brannon, J. H.; Magde, D. *The Journal of Physical Chemistry* **1978**, *82*, 705.
- (10) Birks, J. B. *Photophysics of Aromatic Molecules*; Wiley-Interscience: London, New York, 1970.
- (11) Bolton, J. R.; Archer, M. D. *The Journal of Physical Chemistry* **1991**, *95*, 8453.
- (12) Strickler, S. J.; Berg, R. A. *Journal of Chemical Physics* **1962**, *37*, 814.
- (13) Nienhuis, G.; Alkemade, C. T. J. *Physica B & C* **1976**, *81C*, 181.

- (14) Purcell, E. M. *Phys. Rev.* **1946**, *69*, 681.
- (15) Christensen, H. P.; Gabbe, D. R.; Jenssen, H. P. *Physical Review B* **1982**, *25*, 1467.
- (16) Barnett, S. M.; Huttner, B.; Loudon, R. *Physical Review Letters* **1992**, *68*, 3698.
- (17) Meltzer, R. S.; Feofilov, S. P.; Tissue, B.; Yuan, H. B. *Physical Review B* **1999**, *60*, R14012.
- (18) Crenshaw, M. E.; Bowden, C. M. *Physical Review Letters* **2000**, *85*, 1851.
- (19) Wuister, S. F.; Donega, C. d. M.; Meijerink, A. *Journal of Chemical Physics* **2004**, *121*, 4310.
- (20) Hulet, R. G.; Hilfer, E. S.; Kleppner, D. *Physical Review Letters* **1985**, *55*, 2137.
- (21) Nienhuis, G.; Alkemade, C. T. J. *Physica B+C* **1976**, *81*, 181.
- (22) Glauber, R. J.; Lewenstein, M. *Physical Review A* **1991**, *43*, 467.
- (23) Henderson, B.; Imbusch, G. F. *Optical spectroscopy of inorganic solids*; Clarendon Press: Oxford, 1989.
- (24) Schuurmans, F. J. P.; Vries, P. d.; Lagendijk, A. *Physics Letters A* **2000**, *264*, 472.
- (25) Rikken, G. L. J. A.; Kessener, Y. A. R. R. *Physical Review Letters* **1995**, *74*, 880.
- (26) Schuurmans, F. J. P.; Lang, D. T. N. d.; Wegdam, G. H.; Sprik, R.; Lagendijk, A. *Physical Review Letters* **1998**, *80*, 5077.

- (27) Vallee, R. A. L.; Tomczak, N.; Vancso, G. J.; Kuipers, L.; Hulst, N. F. v. *Journal of Chemical Physics* **2005**, *122*, 114704.
- (28) Vallee, R. A. L.; Tomczak, N.; Kuipers, L.; Vancso, G. J.; Hulst, N. F. v. *Physical Review Letters* **2003**, *91*, 038301.
- (29) Granqvist, C. G.; Hunderi, O. *Physical Review B* **1977**, *16*, 3513.
- (30) Nutz, T.; Felde, U. z.; Haase, M. *Journal of Chemical Physics* **1999**, *110*, 12142.
- (31) Guo, J.; She, C.; Lian, T. *Journal of Physical Chemistry B* **2005**, *109*, 7095.
- (32) Aspnes, D. E. *Am. J. Phys.* **1982**, *50*, 704.
- (33) Lukosz, W.; Kunz, R. E. *J. Opt. Soc. Am.* **1977**, *67*, 1607.
- (34) Lukosz, W.; Kunz, R. E. *Optics Communications* **1977**, *20*, 195.
- (35) Arnoldus, H. F.; Foley, J. T. *OPTICS LETTERS* **2003**, *28*, 1299.
- (36) Rahmani, A.; Chaumet, P. C.; Fornel, F. d. *Physical Review A* **2001**, *63*, 023819.
- (37) Chaumet, P. C.; Rahmani, A.; Fornel, F. d.; Dufour, J.-P. *Physical Review B* **1998**, *58*, 2310.
- (38) Birks, J. B. In *Photophysics of Aromatic Molecules*; Wiley: New York, 1969, p 44.
- (39) Bevington, P. R. *Data Reduction and Error Analysis for the Physical Sciences*; McGraw-Hill: New York, 1969.
- (40) Robbins, R. J.; Fleming, G. R.; Beddard, G. S.; Robinson, G. W.; Thistlethwaite, P. J.; Woolfe, G. J. *J. Am. Chem. Soc.* **1980**, *102*, 6271.

- (41) Baumler, W.; Schmalzl, A. X.; Gosl, G.; Penzkoler, A. *Meas. Sci. Technol.* **1992**, *3*, 384.
- (42) Maus, M.; Cotlet, M.; Hofkens, J.; Gensch, T.; Schryver, F. C. D.; Seidel, J. S. C. A. M. *Anal. Chem.* **2001**, *73*, 2078.
- (43) James, D. R.; Siemiarczuk, A.; Ware, W. R. *Rev. Sci. Instrum.* **1992**, *63*, 1710.
- (44) Marquardt, D. W. *Journal of Society for Industrial and Applied Mathematics* **1963**, *11*, 431.
- (45) Yang, H.; Xie, X. S. *Chemical Physics* **2002**, *284*, 423.
- (46) Brand, L.; Eggeling, C.; Zander, C.; Drexhage, K. H.; Seidel, C. A. M. *J. Phys. Chem. A* **1997**, *101*, 4313.
- (47) Hall, P.; Selinger, B. *The Journal of Physical Chemistry* **1981**, *85*, 2941.
- (48) Emery, A. F.; Nenarokomov, A. V. *Meas. Sci. Technol.* **1998**, *9*, 864.
- (49) Enderlein, J.; Sauer, M. *Journal of Physical Chemistry A* **2001**, *105*, 48.

Chapter 3. Microscopy and Sample Preparation for Single Molecule

Detection

I. Sample Preparation

For the sample preparation of SMD, great care has to be taken because of the extremely low surface number density of dye molecules, overwhelming number of impurities from the experimental tools and solvent if not treated carefully, and the bleaching of dye molecules if the substrate is an efficient electron acceptor. In the following sections, the methods of sample preparation are described observing the high level of requirements for the proper single molecule detection.

I.A. Cleaning

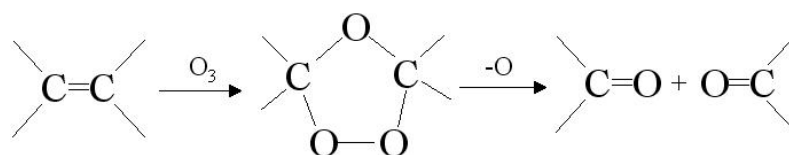
Both the dye solution and all the glassware must be as clean as possible to minimize the number of impurities. Normal cleaning methods commonly used in bulk measurement make the sample dominated by the impurity molecules. The typical procedure of cleaning a glass bottle that stores dye solution is:

1. A glass bottle with metal-coated cap is prepared. The caps are stored separately.
2. Dissolve about 30g of oxidant reagent that decomposes organic material (Aldrich NOCHROMIX) in 1L of pure sulfuric acid.
3. Immerse the glass bottles in the sulfuric acid at least for 4 hours.
4. Rinse the glass bottles with de-ionized water.
5. Store the rinsed glass in an ozone-chamber at least 6 hours. (optional)

6. Burn the glass bottle with a propane torch or Bunsen burner for a couple of minutes.

In addition, all the tools such as a glass pipet and tweezers that were in contact with the dye solution during the sample preparation were also burned before use. The cleaning method may differ depending on the rigor of experiment in terms of impurity contribution. Ha suggested a different wet-cleaning method¹.

The most important surface to be cleaned was the top surface of the cover slip and nanoporous film where sample molecules resided. The cover slip was first washed with solvent like MeOH and next was burned by the torch. The cover slip shuttled through the flame from torch about 20 times. The nanoporous film was not clean enough to use for single molecule detection even right after baking at 400°C. Burning method was not used because of uncertain heat treatment effect at higher than 1000°C. Instead, the film was treated with flowing ozone gas at least 24 hours, which turned out to be sufficiently effective for all the used nanoporous films ATO, ZrO₂, etc. The ozone treatment is a well known cleaning method of semiconductor²⁻⁴. Ozone is a powerful oxidizing reagent. It is believed that ozone was especially effective in eliminating fluorescing impurity because ozone broke the C=C bond^{5,6} that should be abundant in the impurity forming π -conjugation:



Ozonolysis

The side effect of ozone cleaning of ATO is to fill the oxygen vacant sites at surface layer; the oxygen vacant sites donate free electrons⁷. The influence of ozone purging on ATO has not been studied much although extensive studies on thin indium-tin oxide (ITO) film have been done. The ITO is also a transparent n-type conducting material where Sn⁴⁺ and oxygen vacancy are free electron donors. Those studies confirmed that ozone fills oxygen vacant sites at ITO surface with oxygen atoms raising work function and current density^{4,8-11}. Density of states in conduction band of electron accepting ATO nanocrystalline film^{12,13}, electronic coupling between adsorbed molecule and ATO surface metal ion¹³, energy difference between conduction band edge and redox potential of adsorbate excited state^{13,14} are considered as the main factors that determine the forward electron transfer rate at (doped) semiconductor surface. Filling oxygen vacancy doesn't seem to change above factors significantly. The phenomena other than decomposition of organic contaminant and increase of oxygen composition on ATO surface are not known.

I.B. Nanoporous Film Preparation

Colloidal ATO was synthesized according to a published procedure¹⁵. Briefly, 30 g (~85 mmol.) of SnCl₄·5H₂O (98%, from Aldrich) was dissolved in 500 ml of H₂O (Millipore, 18.3 MΩ/cm), to which a solution of SbCl₃ (98%, from Aldrich) dissolved in 20 ml of HCl (37 wt.%) was added dropwise in an ice bath under rapid stirring. The doping level is controlled by the amount of SbCl₃ solution added. Sb to Sn molar ratio of 0.1:1 is referred to as 10% ATO. The resulting clear colorless solution was stirred for 30 minutes before aqueous ammonia (25%) was added to adjust the pH to 3.5-4.0, which led to the

precipitation of nanoparticles. The solution was allowed to settle over night in the dark, during which, the color of the white precipitate changed to yellow or dark blue depending on the antimony doping level. The precipitate was washed at least three times with water and then dissolved in 300 ml of water. The solution was adjusted to pH value of 9.5-10, stirred for more than 8 hours, and dialyzed against 10 L of aqueous ammonia at pH 10 to produce clear ATO solution.

The ATO colloidal solution was refluxed for 4 hours. A 120 ml of this colloid was poured into an autoclave and heated at 150 °C for 1 hour and at 270 °C for 16 hours. The colloid was then concentrated to 60 ml. Then 5 ml of the solution and 2 drops of TritonX-100 (from Aldrich) was mixed and stirred for 1 day. The resulting solution was cast onto a cover slip, dried in air, and then baked at 400 °C for 1 hour in an oven to produce nanoporous crystalline thin films.

SnO₂ nanocrystalline thin films were prepared by a previously published method¹⁶ which is similar to ATO film preparation procedure.

ZrO₂ nanoparticles were obtained from Degussa Corporation, and the thin films were prepared according to the published procedure¹⁷. ZrO₂ powder (2g) was ground in a mortar with distilled water (4 mL), acetylacetone (10 µl) and 5 drops of Triton X-100 to break up the aggregate into a dispersed paste. After being dried in air, the film was baked at 400°C for 1 h in air.

The morphologies of the glass cover slip and nanocrystalline films mentioned above are shown in Figure 3.1 and 3.2. The brighter points are higher than the darker points in the direction of surface normal. In Figure 3.1, an AFM image of cleaned cover slip surface shows that the surface was comparatively flat, but has lots of bumps¹⁸. Their

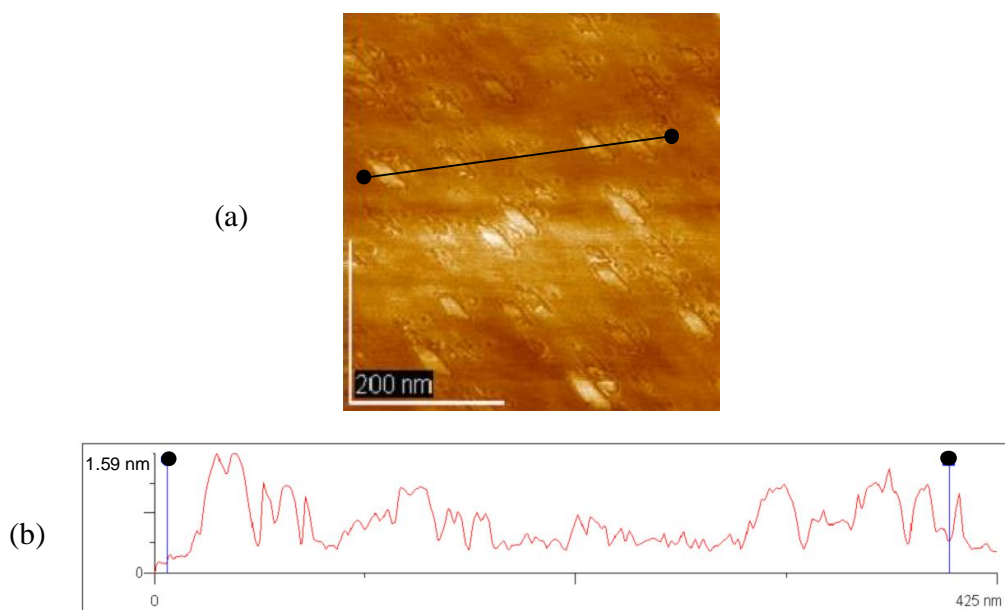


Figure 3.1. AFM image of glass cover slip surface. (a) $500\text{nm} \times 500\text{nm}$ area; many ~ 20 nm-wide and $\sim 70\text{nm}$ -long bumps are observed. (b) Height profile along the black line on (a). The bumps are about 1 nm-high.

sizes were about 20 nm-wide, 70nm-long, and 1nm-high¹⁸. The ATO and ZrO_2 nanoporous films were shown in Figure 3.2. The sizes of ATO nanoparticles were about 20nm in diameter (Figure 3.2a), and those of ZrO_2 were about 30 ~50nm in diameter (Figure 3.2b). In both films, the nanoparticles were sintered during the 400 °C baking process to make ohmic contacts with surrounding nanoparticles that allowed the flow of charge carriers. There is as much empty space as that occupied by the irregular structure of nanoparticles. When the nanoporous film was wet with a dye solution, the dye molecules could penetrate the nanoparticle film through the empty space. Therefore, most of the dye molecules adsorbed on the nanoparticle surface had common nanoscopic

irregular environment, and such a point was important idea of understanding some of optical properties of adsorbate-substrate system.

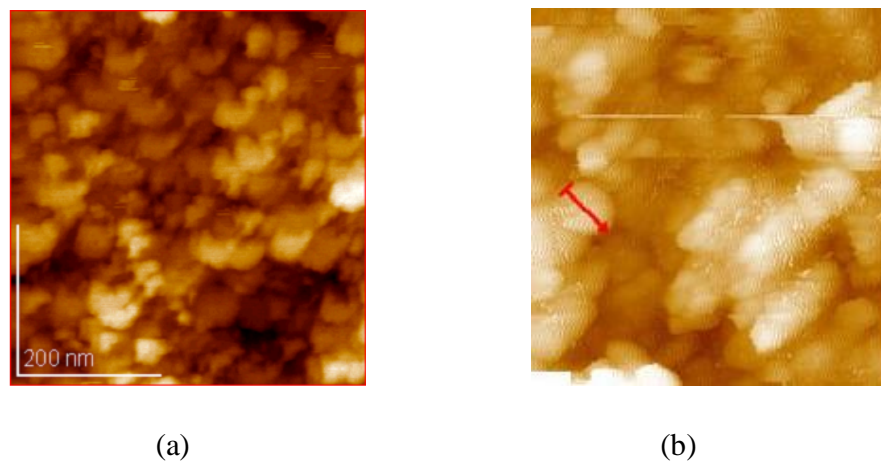


Figure 3.2. AFM images of nanoporous films. (a) Nanocrystalline ATO film: size of the nanoparticles are about 20~30 nm in diameter. (b) Nanocrystalline ZrO_2 film: size of the nanoparticles are about 30~50 nm in diameter. Brighter round regions are nanoparticles and dark points are empty spaces.

I.C. Sensitizing the Nanoporous Film with Organic Dye in Single Molecule Level

There are two ways of sensitizing nanoporous film with dye molecules: dropping and soaking. The dropping scheme was chosen when it was necessary to make samples of the same surface number densities. The number density test was frequently performed to check how well a substrate quenched the adsorbed dyes compared with a reference substrate that usually was not active in quenching. However, dropping scheme might tend to make aggregates or heterogeneous distribution of dye molecules. Figure 3.3 is a schematic diagram of the formation of unwanted product by the dropping scheme. The

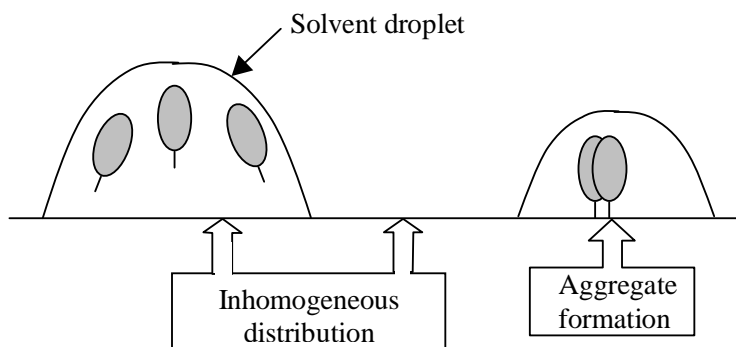


Figure 3.3. Schematic diagram of micro-view of surface being sensitized by dropping scheme. Global inhomogeneous distribution and aggregate formation due to high local concentration of dye are supposed to occur.

solvated dye molecules would tend to remain in solvent until the last moment of evaporation unless the van der Waals or electrostatic force between dye and substrate was so high that the adsorption of the dye is done before solvent evaporates. Actually, the formation of aggregates or inhomogeneous distribution has not been clearly observed in the sample prepared by dropping scheme. However, the dropping scheme was not preferred unless there was any reason to choose it. The soaking scheme is considered to be a proper way of making the single molecule junction.

A schematic diagram of sensitization procedure of soaking method is shown in Figure 3.4. After the ozone purging, only nanoporous film side of substrate was soaked in dye solution. After the soaking, the sample was washed with the same solvent as the one in the sensitizing solution to get rid of physisorbed molecules. The number density of the dye molecules on a substrate was controlled by either the concentration of dye solution or soaking time. Because the adsorption of the molecules on the substrate

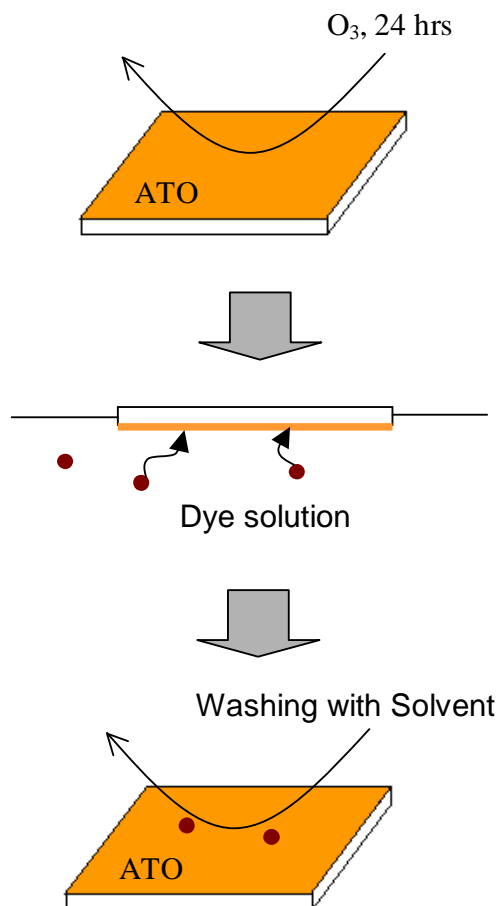


Figure 3.4. Schematic diagram of sensitization procedure by soaking scheme. Dye molecules reacted with ATO substrate at random position to make homogeneous distribution of adsorbed single molecules. The bottom side of the ATO substrate did not contact with dye solution to prevent contamination in the second step. The product of the second step was washed with the same solvent as the one in dye solution to wash out physisorbed dyes in the third step. The second and third steps were done in dark environment to prevent bleaching of dyes on ATO surface before the laser illumination.

occurred randomly, the spatial distribution of dye molecules was homogeneous and no anomalous formation of aggregates was assumed.

II. Single Molecule Microscopy

The single molecule detection is based on the time-correlated single photon counting (TCSPC). In this section, the basic principle and the experimental devices of the TCSPC are described. Not only the SMD, bulk measurement is also shown to be available using the TCSPC. Home-built femtosecond laser as a light source for the SMD was built in this work and pulse generation mechanism of it is briefly described.

II.A. Time-Correlated Single Photon Counting

TCSPC as a Method of Single Molecule Fluorescence Lifetime Measurement

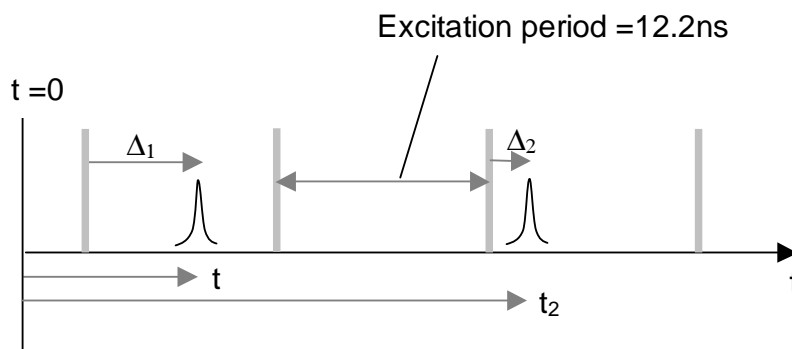
The fluorescence lifetime can be measured either in time domain or frequency domain. In the frequency domain technique, the phase and modulation of fluorescence is measured with respect to the sinusoidally modulated CW excitation light^{19,20}. The frequency domain technique is an expensive technique; and it is seldom applied to SMFL measurement because it does not work with weak light. The time domain technique records a decay profile of fluorescence intensity as time after excitation. There are many ways to implement the technique depending on their detection methods: Streak camera²¹, boxcar integrator²², up-conversion^{23,24}, and time-correlated single photon counting²⁴⁻²⁶. Above all, only the TCSPC is applicable to our single molecule detection although other techniques can have faster timing limit than the TCSPC. The reason is that the total number and emission rate of photons from organic single emitter are low and limited.

The other techniques require high intensity fluorescence or time-gating, so that many molecules have to be excited at the same time with low detection sensitivity. In contrast, the TCSPC records information of all the detected photons and fully utilizes the TCSPC data resulting in the highest detection sensitivity.

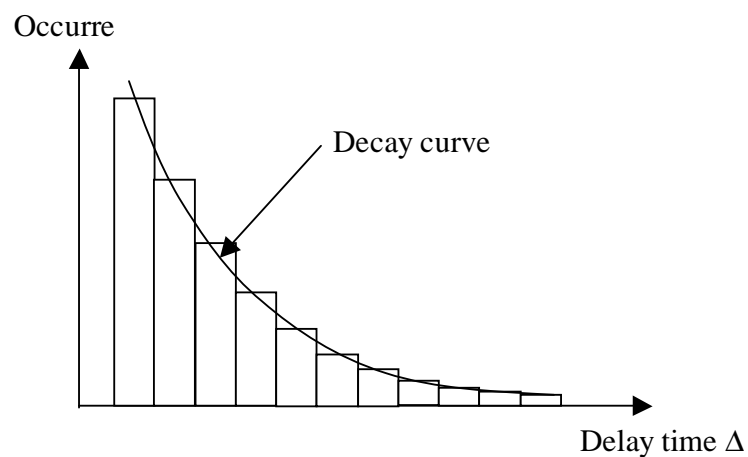
One interesting point is that the weaker the fluorescence is, the more accurately the TCSPC technique performs, if it were not for background photons. The TCSPC is based on poisson statistics of photon detection, which requires that the time differences between adjacent detected photons have to be much longer than their excitation pulse period. Single molecule emitter satisfies naturally this requirement because the single molecule does not emit multi photons during one excitation period, and weak fluorescence intensity from single molecule is not difficulty but helps increase accuracy. Multi-photon emission from single emitter is possible but negligible using femtosecond pulsed excitation²⁷.

Principles of TCSPC

Figure 3.5 illustrates how the TCSPC works in the fluorescence decay curve measurement²⁸. In Figure 3.5a, the time when a photon is detected by a detector is correlated with two reference times, the excitation time and the start time of experiment. The time referred to the former is called delay time and the latter is called chronological time. The delay time means how long a sample has been in its excited state after the excitation. Electronic transition occurs in sub-femtosecond time scale, so that it is considered to be instantaneous compared to the nanosecond time scale fluorescence decay. After collecting the delay time data of the detected photons, we can build a



(a)



(b)

Figure 3.5. Principle of decay curve generation. (a) Timing of photon detection relative to two reference times, excitaiton time and chronological time. Δ_i : Delay time of i^{th} detected photon; t_i : Chronological time of i^{th} detected photon. (b) Histogram of delay time that is equivalent to decay profile.

histogram of which abscissa is the delay time, and then the curve connecting the occurrence values is identical with the real-time trace of the S_1 population decay of the sample. The identity is based the ergodic hypothesis^{29,30}, which states that an ensemble-averaged observable is the same as a time-averaged one. According to the hypothesis, the intensity decay of the ensemble sample after just one excitation is the same as the delay time histogram of a single molecule accumulated for a long time. The sample for the time-averaged observation does not have to be the single emitter only if no more than one photon is detected during any excitation pulse cycle, because the single emitters are the replica of the same property and the photons from different emitters are indistinguishable. The TCSPC of a bulk mixture still makes the same result as the real-time decay trace of the bulk mixture because the TCSPC can be considered as the tracing of an imaginary single emitter that changes steadily and randomly among the components of the mixture.

Figure 3.6 shows a schematic diagram of the basic components of the TCSPC experimental setup. A Mode-locked laser outputs the pulsed excitation light. Fluorescence from the sample is collected by an objective lens and is detected by a detector, single photon counter. The detector outputs an electrical pulse to signal the arrival of a photon to a photon counting board (Becker & Hickl GmbH, SPC-600) installed in PC. The excitation reference time is supplied by a fast photodiode detecting the pulsed laser light inside the laser. The time difference between the excitation reference time and the time registered by the signal from detector is the delay time in Figure 3.5. The time difference measurement starts by the signal from the single photon counter and stops by the signal from the fast photodiode as labeled in Figure 3.6, which is called “Reversed Start-stop” mode. It is conceptually natural to have the excitation time

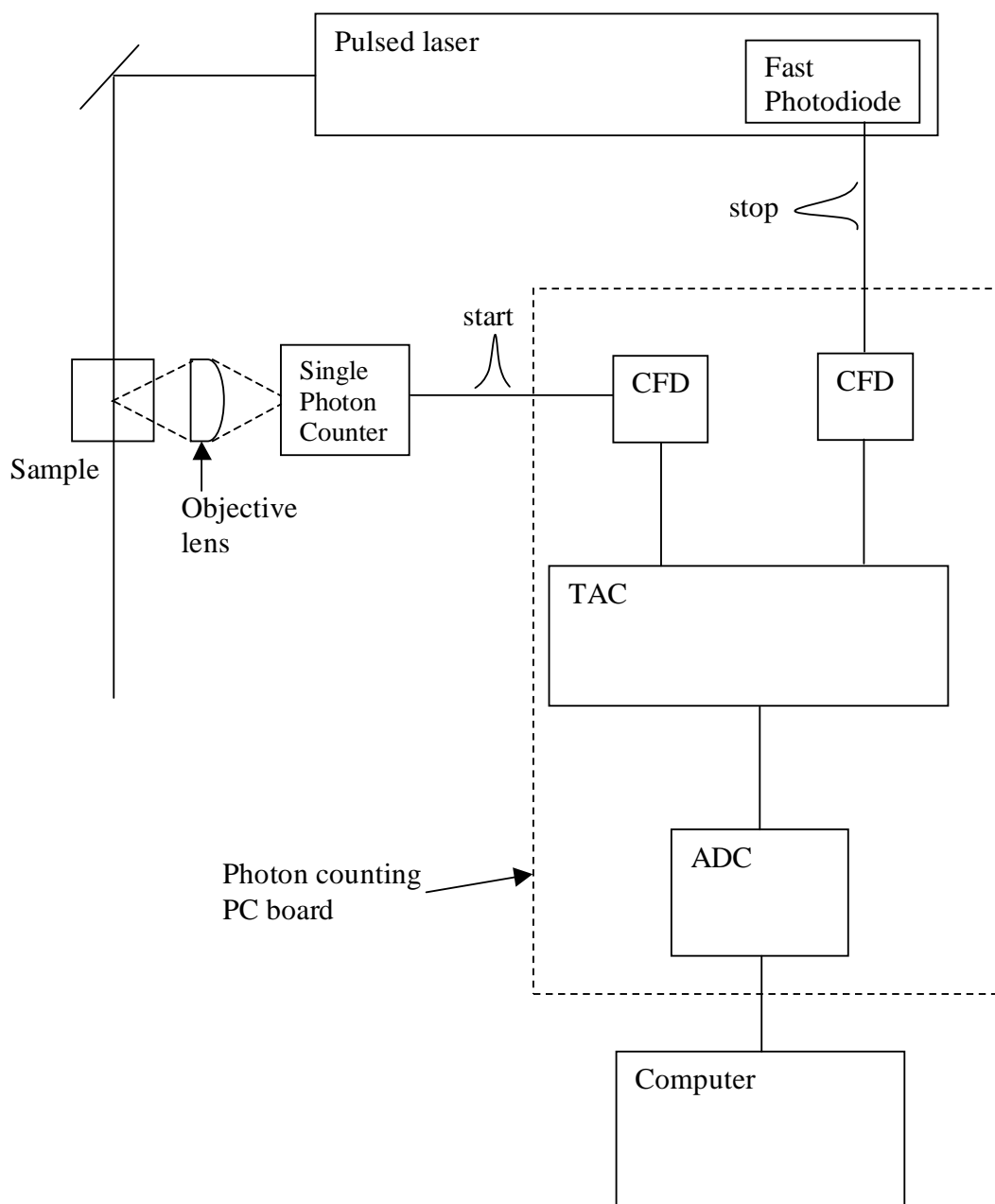


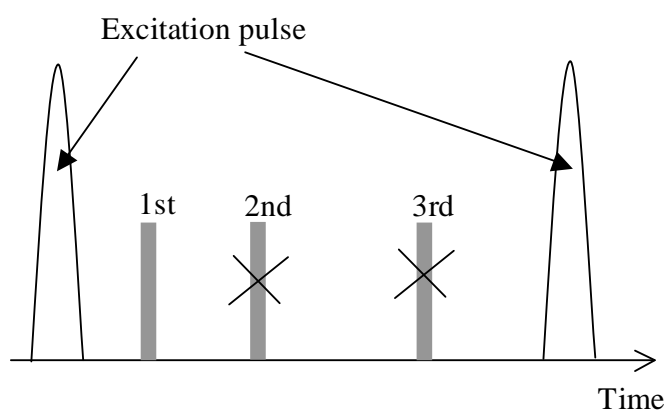
Figure 3.6. Schematic diagram of the basic components of reversed start-stop mode TCSPC system. CFD (Constant Fraction Discriminator), TAC (Time-to-Amplitude Converter), and ADC (Analog-Digital Converter) are integrated in a TCSPC PC board.

signal as the “start” and photon detection time signal as “stop”. However, such a method is unrealizable because it makes the photon counting system so busy in starting delay time measurement at typically tens of MHz frequency of mode-locking -- 82MHz in this work. Use of low frequency excitation results in a long observation time and missing a possible fast intensity change. In the reversed mode, the delay time measurement occurs at the same frequency of photon detection of which frequency is usually less than 1MHz with practically unrestricted excitation rate.

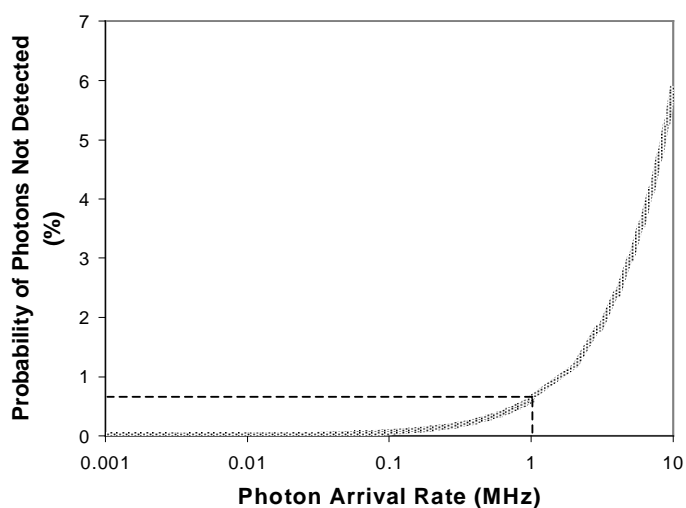
Those start and stop signals pass through the Constant Fraction Discriminator (CFD) to get rid of timing jitter²⁶ and are fed to Time-to-Amplitude Converter (TAC). TAC converts the time difference between the start and stop signals into voltage which is linear to the time difference. The voltage of TAC is read by Analog-Digital Converter (ADC) and written in the memory banks. The ADC resolution is 12bit so that there can be 4096 ($=2^{12}$) channels in the TAC window.

Pile-up Error

When the TCSPC technique is used to measure the decay profile of a bulk sample, it is probable that more than one photon will arrive at a detector during one period of excitation pulse. In this case, only the first photon is timed and registered. The rest of photons are neither detected nor recorded due to the dead times of detector and TCSPC board. The missing of subsequent photons during an excitation distorts its fluorescence decay profile, so called “pile-up error”²⁴. The pile-up error exists only in the bulk fluorescence measurement not in the SMD because a single molecule can emit at most one photon unless its excitation and radiative de-excitation cycle occurs twice during an



(a)



(b)

Figure 3.7. Pile-up error and its probability as a function of photon arrival rate. (a) Schematic diagram of pile-up error between adjacent excitation pulses: The second and third arrived photons are missed. (b) The probability of missing photons by pile-up error with various photon arrival rates.

excitation pulse duration²⁷. Figure 3.7a illustrates what is going on in pile-up error. Three photons arrive at the detector between two subsequent excitations, but second and third photons are neither detected nor recorded.

The probability of pile-up error has to be sufficiently low not to distort the decay profile based on a criterion. Let's first see the number of photons not detected for the error. The photon counting event is governed by poisson statistics^{24,31} at such a low intensity level that enables single photon counting. The probability of the arrival of n number of photons on detector, $P(n)$, is:

$$P(n) = \frac{(\lambda t)^n e^{-\lambda t}}{n!} \quad (3.1)$$

where, λ is an average arrival rate, and t is an integration time, the laser excitation period.

The probability of arrival of more than two photons, $P(n \geq 2)$, is:

$$P(n \geq 2) = 1 - P(0) - P(1) \quad (3.2)$$

During one excitation period 12.2ns, at photon arrival rate of 1MHz:

$$P(n \geq 2) = 0.000074 \quad (3.3)$$

For one second, the pile-up error happens 6068 ($= 0.000074 \times 82 \text{ MHz}$) times, and 988,269 ($=P(1) \times 82 \text{ MHz}$) number of photons arrived alone, and 994,337 ($= 988,269 + 6068$) number of photons are registered into the photon counting board. The probability of photons not registered out of the total photons arriving at detector is 0.57%

[=100×(1,000,000 - 994,337)/1,000,000]. Figure 3.7b shows the probability of missing photons by pile-up error with various photon arrival rates.

Still, it is not clear what the “sufficiently” low pile-up error is. In each channel of the delay time, actually recorded photon count suffering the pile-up error is less than the value of perfect experiment done without pile-up error. The relation of the correct and actual count is^{24,32}:

$$N_i^c = \frac{N_i}{1 - \frac{1}{N_e} \sum_{j=1}^{i-1} N_j^c} \quad (3.4)$$

where N_i^c is the correct count in i th channel, N_i is the actual count in i th channel, and N_e is the number of excitation pulses. Assuming that the ADC resolution is so high that the delay time histogram is equivalent to the continuous decay curve, Equation 3.4 can be transformed to an equation with continuous variables:

$$N_c(t) = \frac{N(t)}{1 - \frac{\int_0^t N_c(t) dt}{N_e}} \quad (3.5)$$

where $N_c(t)$ is the correct count at time t , $N(t)$ is the actual count at time t . The correct count $N_c(t)$ decays as time with a correct decay rate k :

$$N_c(t) = Ae^{-kt} \quad (3.6)$$

Equation 3.5 becomes:

$$f(t)N_c(t) = N(t) \quad (3.7)$$

$$f(t) \equiv \left(1 - \frac{A}{kN_e} + \frac{A}{kN_e} e^{-kt} \right) = \left(1 - F_A + F_A e^{-kt} \right) \quad (3.8)$$

where the term $\frac{A}{kN_e}$ is the ratio of total number of photons arrived at the detector to the

total number of excitation pulses and is represented by F_A . Differentiating Equation 3.7 with respect to t :

$$f \frac{dN_c}{dt} = \frac{dN}{dt} - N_c \frac{df}{dt} \quad (3.9)$$

Substituting the derivative of Equation 3.6 into Equation 3.9:

$$-kfN_c(t) = \frac{dN}{dt} - N_c \frac{df}{dt} \quad (3.10)$$

Rearranging Equation 3.10 and using Equation 3.7:

$$\frac{dN(t)}{dt} = - \left(k - \frac{f'(t)}{f(t)} \right) N(t) \quad (3.11)$$

Substituting the expression of $f(t)$ and $f'(t)$, we get finally:

$$\frac{dN(t)}{dt} = -k \left(1 + \frac{F_A e^{-kt}}{1 - F_A + F_A e^{-kt}} \right) N(t) \quad (3.12)$$

$$= -k [1 + D(t)] N(t) \quad (3.13)$$

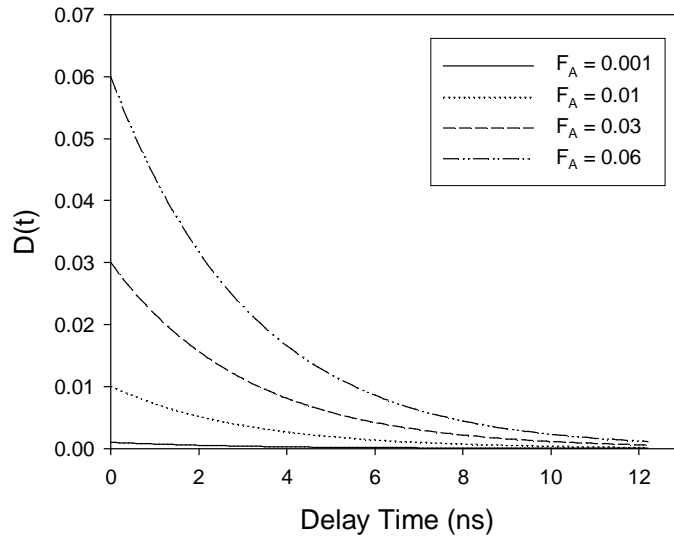


Figure 3.8. Magnitude of distortion function $D(t)$ after excitation.

The second term inside the bracket in Equation 3.12 is represented by $D(t)$ in Equation 3.13. The $D(t)$ is named ‘distortion function’ because it distorts the curvature of decay curve at time t due to the pile-up error. Four $D(t)$ s parameterized by the F_A with $k = 3.3 \times 10^8 \text{ s}^{-1}$ are plotted in Figure 3.8. It is interesting that the decay slope distortion is higher in early delay time than later delay time although the pile-up error is more likely in the later delay time. A plot of missed photon along the delay time is shown in Figure 3.9. The correct [$N_c(t)$, dotted line] and actual [$N(t)$, solid line] decay curves are drawn in Figure 3.9 with $F_A = 0.03$ and $k = 3.3 \times 10^8 \text{ s}^{-1}$. The number of photons missed peaks around 2ns despite the $D(t)$ decreases from time zero in Figure 3.8. The analytical expression of the number of missed photons, $N_c(t) - N(t)$ is given to be:

$$N_c(t) - N(t) = A e^{-kt} \cdot \left\{ 1 - \exp \left[-k \int_0^t D(t') dt' \right] \right\} \quad (3.15)$$

Or simply using Equation 3.7 and 3.8:

$$N_c(t) - N(t) = Ae^{-kt} \cdot [F_A(1 - e^{-kt})] \quad (3.16)$$

The functions in the braces and the brackets in Equation 3.15 and 3.16 increase from zero to one monotonically as the delay time t . It may be concluded that the missed photon curve is a multiplication of the decay signal intensity and a function that may mean the probability of not being recorded at delay time t , just as the 2nd and 3rd photons in Figure 3.7a.

What is important is in Figure 3.8. It may be assumed that the error of a fitted

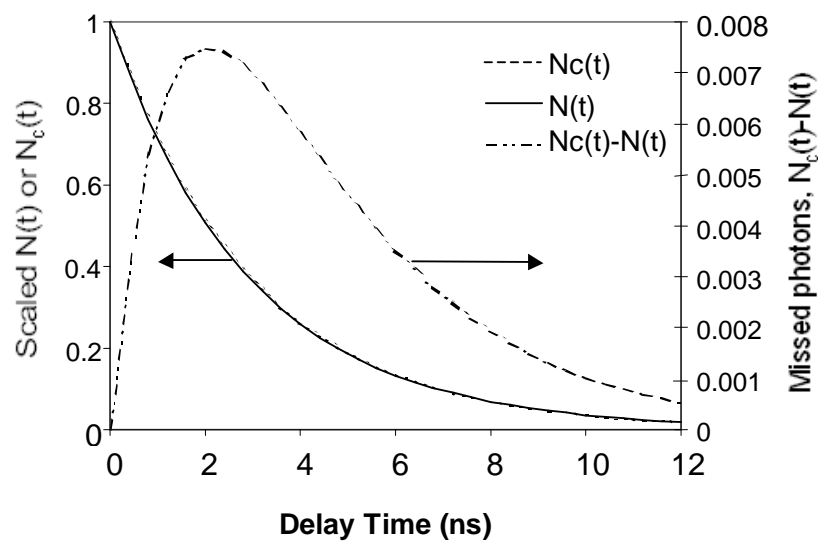


Figure 3.9. Actual and correct decay curves in terms of the pile-up error. $N(t)$ (solid line) and $N_c(t)$ (dashed line) are actual and correct decay curves with delay time t , respectively. The Y axis of their difference (alternating dashed and dotted line) is in the right side. The distortion from single exponential decay by pile-up error is biggest near the 2 ns delay time.

decay lifetime is roughly about the average $D(t)$, so that the error may be just a few % from its correct decay lifetime for all the F_A parameters selected in Figure 3.8. The photon arrival rate corresponding to the highest value 0.06 is about 5MHz. The 5MHz is redundantly high counting rate in most of experiments and suffers the dead time of photon counting board, 200ns. Typical bulk experiments are done at 0.01~0.1MHz of photon counting rate corresponding to $F_A = 0.0001\sim 0.001$. The $D(t)$ curve of $F_A = 0.001$ is lower than 0.1% through the delay time in Figure 3.8. The effective number of lifetime value is usually placed in the tenth number place when the unit of lifetime is nanosecond, which means a few percent of error always exists from other sources like background, instrument response function and statistical noise. The 0.1% distortion from pile-up error can be regarded to be negligible compared to other sources of error. In conclusion, the pile-up error is quantitatively proved not to be significant in TCSPC experiment in the condition of this work.

II.B. Experimental Setup for Single Molecule Lifetime Measurement by TCSPC

Light Source

Fluorescence lifetime measurement in time domain requires the pulsed excitation and records the decay of intensity as a function of time after the excitation. The shape of decay curve is determined by the population dynamics. However, the measured fluorescence decay data is not exactly the same as the intrinsic or true decay. The true decay is distorted by the finite excitation pulse duration and δ -function response of apparatus. In fact, the measured decay is the convolution integral of the excitation pulse

shape $E(t)$, the instrument response function $IRF(t)$, and the decay dynamics model $M(t)$ ²⁴:

$$I(t) = E(t) \otimes IRF(t) \otimes M(t) \quad (3.17)$$

If any of the convoluted term is δ -function, the $I(t)$ is simply the convolution of the rest of the terms not including the δ -function. In this work, 50 ~ 100 femtosecond FWHM pulse was used to excite the dye molecules of which lifetime ranged from tens of picoseconds to a few nanoseconds. Therefore, the excitation laser pulse could be regarded as the δ -function and the $I(t)$ is simplified to be $IRF(t) \otimes M(t)$.

To generate the femtosecond pulse, two mode-locked Ti:Sapphire oscillators have been used. One was a home-built oscillator (parts from Washington State University) and the other was a commercial oscillator (Tsunami 3941-M1BB, Spectra-Physics). Both of them had the standard configurations. The basic specifications of the two lasers are tabulated in Table 3.1. They were generally similar but different to each other in tunability and mode-locking method. Wavelength tuning was available in the Tsunami oscillator because it was composed of broad band (700~1000nm) optical parts and gain profile of Ti:Sapphire crystal. Wavelength selection was achieved by adjusting slit position located between two group velocity dispersion (GVD) compensation prisms. Pulse width could also be tuned by changing the width of the slit. The methods of mode-locking of the two oscillators were popular ones for the modern ultrashort pulse source. A couple of next paragraphs describe the mode-locking mechanism in general and of particular devices.

A schematic diagram of the home-built oscillator is shown in Figure 3.10. Laser

	Home Built	Tsunami
Gain Medium	Ti:Sapphire	Ti:Sapphire
Repetition Period (rate)	11.4ns (88MHz)	12.4ns (80.8MHz)
Pulse Width	~50fs	<100fs
Pump Laser	Nd:YVO ₄	Nd:YVO ₄
Pump Power	4W	5W
Mode-locking	Self-mode-locking	AOM initiated self-mode-locking
Wavelength Tunability	NA	700 – 1000 nm

Table 3.1. Basic specifications of home-built and commercial oscillator.

cavity is the optical path between the end mirror (E) and output coupler (O). Different longitudinal modes inside the cavity are superposed and interfere with themselves. When no control is imposed on the phases of modes, they are random so that the constructive and destructive interferences are temporally and spatially random. Such an incoherent superposition makes structureless noisy temporal intensity profile at a detector, which is called CW laser. If the initial phases of the cavity modes are kept equal coherently in some way or other, the sharply peaked constructive interference travels with period $2L/c$, where L is cavity length and c is the speed of light:

$$\begin{aligned}
 E_1(t) &= E_1 \cos(\omega_1 t + \varphi) \\
 E_2(t) &= E_2 \cos(\omega_2 t + \varphi) \\
 &\dots
 \end{aligned}
 \tag{3.18}$$

$$E_i(t) = E_i \cos(\omega_i t + \varphi)$$

...

$$E_n(t) = E_n \cos(\omega_n t + \varphi)$$

where $E_i(t)$ is the electric field of i th mode of total n number of modes in gain bandwidth, E_i is the amplitude of the field, ω_i is the frequency of i th mode with $\omega_i - \omega_{i-1} = c/2L$, and φ is the initial phase. Keeping the initial phases equal results in short width pulse in time

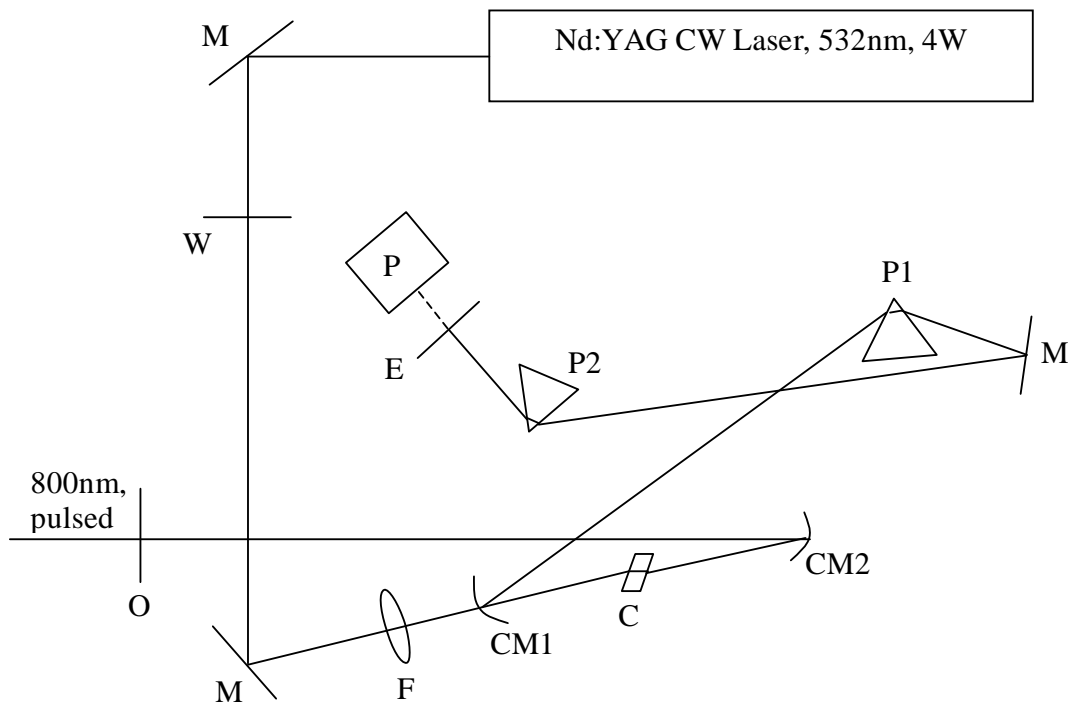


Figure 3.10. Schematic diagram of optical alignment of home-built oscillator. M, aluminum mirror; W, halfwave plate; F, focusing lens; CM1 and CM2, curved mirrors; C, Ti:sapphire crystal; P1 and P2, prisms; E, end mirror; P, fast photodiode; O, output mirror.

domain and Fourier-transform-limited spectrum in frequency domain, which is called Mode-locking and the pulse is the coherent superposition of the allowed cavity modes. Because the period is $2L/c$, there is only one intensity spike inside the cavity. Whenever the spike bounces back at the output coupler, 10% of its intensity transmits through and it is our excitation pulse.

Then, how can the mode-locking be implemented in real world? There are lots of ways of describing the mode-locking mechanism depending on its practical technique, but they are essentially the same: application of periodic loss (or gain) modulation to the intra-cavity radiation whose period is matched to the cavity round trip time³³. It can be further explained in frequency and time domain. In frequency domain, when a longitudinal mode of ω_i is amplitude-modulated with a modulation signal, sidebands form with frequency $\omega_i \pm \Omega$: Ω is the angular frequency of the modulation. In fact, the sidebands originate from the beating of the cavity mode and modulation that is in phase with the longitudinal mode. As the $\Omega/2\pi$ approaches the inter-mode frequency separation $c/2L$, the frequency of the sidebands coincides with the frequency of adjacent modes $\omega_{i\pm 1}$; and they come to be able to resonate inside the cavity coherently with the original longitudinal mode. Such energy shifts are done further to the next modes with $\omega_{i\pm 2}$, and so on. As a result, all the possible modes exchanges energy with their phases locked. In the time domain, the mode-locking operation is more straightforward. Let's imagine that there is an optical shutter inside the laser cavity, which operates at the cavity trip frequency. Then, the net gain is modulated at the frequency and only a coherence spike that passes the shutter is selectively amplified. The cavity energy gets concentrated on the

developing coherent peak through the loss of energy of other modes of different initial phase.

The home-built oscillator was mode-locked by Kerr-lens mode-locking (KLM) method³³⁻³⁵. It is a kind of passive and self mode-locking mechanism, which simulates a saturable absorber. Kerr-lens effect has its origin in the third-order nonlinearity. The refractive index experienced by the light propagating through the Kerr-medium is linearly dependent on the intensity of the light with response time of about 4fs. The wavefront of gaussian beam inside laser cavity does not have homogeneous intensity but decreases radially from the central maximum along the gaussian profile, and so does the refractive index. As a result, the peripheral rays passing through the low refractive index region bend toward the center according to Fermat's principle³⁶. This is exactly the same operation as a lens, and the Kerr-medium is called Kerr-lens. The higher the intensity is, the tighter the focusing is. Therefore, the optimum cavity for high intensity light is different from low intensity light. Then, the high intensity light is amplified selectively while loss of low intensity light occurs, if the cavity is adjusted for the high intensity light. Figure 3.11 shows a schematic diagram of Kerr-lensing. Weak intensity beam diverges while the high intensity beam is collimated after reflection on the curved mirror. The cavity energy gets concentrated on the highest spike during many cavity trips; and eventually the spike becomes an intense and short-duration Fourier-transform-limited coherence superposition of cavity modes of which phases are all locked. This is one way of attaining the differential gain/loss and there is another way named gain-guiding as follows. The waist of pump beam in the Kerr-medium is designed to be smaller than cavity mode. Therefore, the more focused higher intensity light has better overlap with

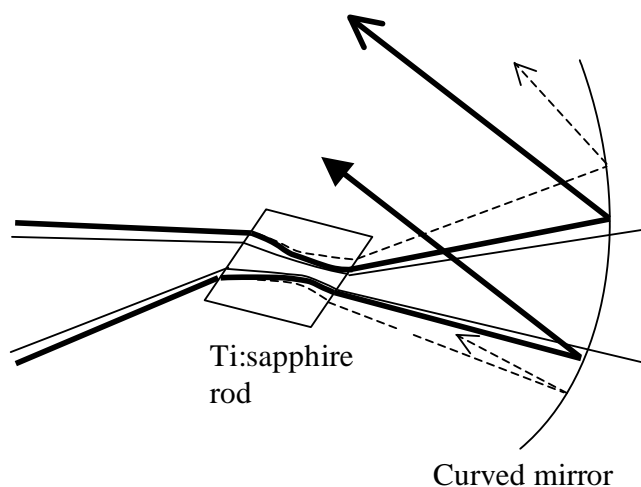


Figure 3.11. Kerr-lensing effect. The thin solid line is the pump beam. The thick solid line is the high intensity beam. The dashed line is the low intensity beam. The Kerr-lens effect preserves the high intensity beam more effectively.

the pump beam; and the differential gain/loss is made. The two mechanisms of KLM are going on simultaneously. Unfortunately, the home-built KLM laser does not have strong enough intensity fluctuation for the sufficient Kerr-lensing to form in continuous regime; thus it does not self-start. There are many ways to initiate the KLM laser: acousto-optical modulator³⁷, saturable absorber³⁸, moving a mirror in external cavity³⁹, simply tapping a mirror^{33,35}, translating a GVD compensation prism^{33,35}, and so forth. The common feature of the methods is to make sufficiently short and high intensity pulses that can initiate KLM. In this work, the prism P2 in Figure 3.10 was translated. It temporarily turns off lasing and makes the high-energy pulse instantaneously when the prism moves back to its lasing position.

The KLM starts and the temporal spike is amplified. However, the laser cavity is still optimized for continuous regime. When the intense light passes through the gain medium experiencing the differential gain, the Kerr-lensing shifts the position of the focus of the amplified intense light. To compensate for the focus shifts, the two curved mirrors (CM1 and CM2) are slightly recessed by about 0.1 mm. By doing so, the loosely focused weak light diverges after reflection on the curved mirrors, which helps developing and maintaining the mode-locking regime. A slit could be put in front of the end mirror E as a “hard aperture”³³ to block the diffuse low intensity light.

The gain medium of the commercial oscillator Tsunami is also Ti:sapphire crystal. The KLM of the oscillator is initiated by regenerative acousto-optical modulator (AOM) that prepares ps pulses inside the cavity. The ps pulse has sufficient energy for effective differential gain, and then fs pulse forms by KLM. The AOM is the most common active mode-locking method. The AOM module is placed in front of end mirror. Time-dependent refractive index grating perpendicular to the beam forms inside the quartz of which one side is attached with RF frequency (half the cavity trip frequency) driven piezoelectric transducer. Diffraction and loss of initially long pulse is sinusoidally modulated by the RF signal. Amplitude is shaped sharp in time very effectively after many trips in the cavity. However, the pulse shaping is slow and stops eventually as the pulse width gets much shorter than modulation period. Typically ps pulse is formed by the AOM. Any drift in the cavity length will impair the stability and shape of pulsing. This can be overcome by the regenerative mode-locking technique. RF driver gets feedback from a photodiode that detects the output pulse train. By doing so, AOM

operates at the same RF frequency as that of the pulse trip within laser cavity whatever the cavity trip frequency is.

Two-Photon and Confocal Microscope

Microscope system for single molecule detection is implemented in a standard way⁴⁰⁻⁴³. A simplified schematic diagram of the whole microscopic system is shown in Figure 3.12. The laser in Figure 3.12 is the tunable commercial oscillator. Its specification and principle of operation explained in the previous section. The wavelength of the output from the home-built oscillator was fixed to 800nm and the power is 200mW. The wavelength of output from commercial Tsunami oscillator was tunable ranging from 700nm to 1000nm. The power of Tsunami oscillator is 400mW(at 700nm), 1W(at 800nm), and 150mW(at 995nm). The near IR outputs from both oscillators were sent through a frequency doubling BBO crystal when the excitation mode was one-photon excitation. For two-photon excitation, the BBO crystal was taken out and the near IR was used directly. The excitation beam was sent to an inverted microscope (IX70, Olympus Optical Co.); and it was reflected by a beam splitter that reflected excitation beam and passed fluorescence from sample with ~90% transmission. The excitation beam reflected from the beam splitter was focused down to $\sim 300\text{nm } 1/e^2$ diameter and attenuated to a typical excitation intensity of $\sim 0.3 \text{ MW/cm}^2$ at the sample through an objective lens (100X, 1.4 NA, oil immersion, Olympus Optical Co.) in case of two-photon excitation. In the case of one-photon excitation the focus size and excitation intensity were $\sim 450\text{nm}$ in diameter and $13 \sim 63 \text{ W/cm}^2$, respectively. Sample position was controlled by a XYZ-nanopositioning stage (Mad City Labs Inc. $\sim 10 \text{ nm}$ resolution). The epi-fluorescence

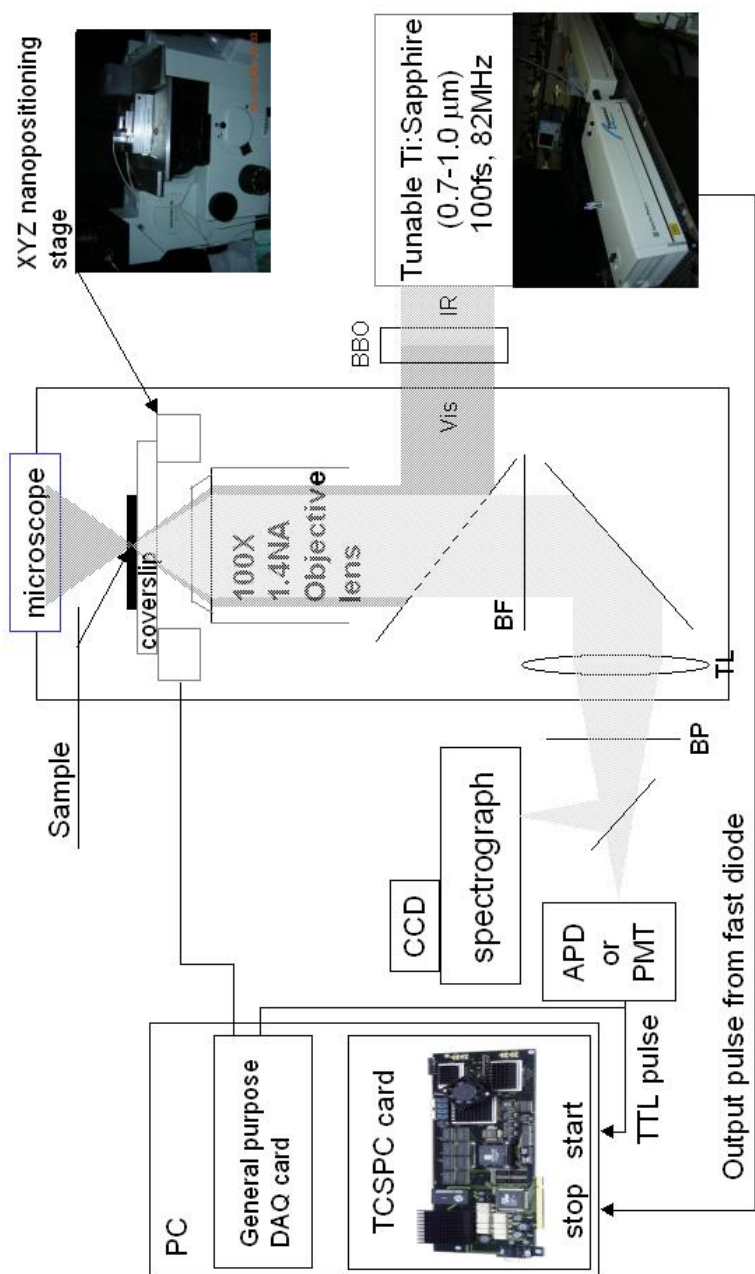


Figure 3.12. Simplified schematic diagram of the whole microscopic system

from the focus was sent through the beam splitter mentioned above and an excitation beam-blocking filter next to it. Because the IX70 microscope is infinity-corrected, the collected fluorescence emerging from the back-aperture of objective lens was collimated. The collimated light was focused on the image plane outside the microscope by a tube lens (TL). A band pass filter specific to a fluorescent dye was placed before the image plane to increase signal to background ratio. An avalanche photodiode (APD, EG&G model SPCM-14) was placed at the image plane. The dead time of the APD was 50 ns, and photon detection efficiency was 50~70% depending on the wavelength of the fluorescence. Each time of single photon detection, a TTL pulses from APD was sent to the TCSPC PC card (SPC-600, Becker & Hickl GmbH, 60 ps time resolution, 125 ns dead time) operating in the photon-stamping mode, in which both the chronological time and delay time of each detected photon were recorded. The chronological time data were used to make intensity trajectory with 60 ns time-resolution; and fluorescence decay curve was constructed from the delay time histogram. The instrument response function for the fluorescence decay was obtained by measuring glass scattering at 800 nm, which shows a full-width-at-half maximum of about 400ps. To record the fluorescence spectra, a spectrograph (Acton Research Corp. SpectraPro-300i) with a CCD camera (Roper Scientific, VersArray 515B) is used in place of or simultaneously with the APD.

III. Single Molecule Detection Method

III.A. General Procedure

Imaging

The next step after the sample preparation is to take the fluorescence images. The purposes of imaging are:

1. Impurity and background test
2. Fluorescence intensity level
3. Sharpness of intensity
4. Number and distribution of bright spots.

In many single molecule tests, fluorescence or scattering from impurity interfered spatially with the fluorescence from sample molecules. Such interference could be clearly observed by taking an image of a blank sample that was prepared in exactly the same manner and condition as a single molecule sample except for the existence of dye molecules. The comparative number and intensity of bright spots of the sample and blank were used as the barometer of the interference. The sharpness and intensity of the bright spots were referred to when we wanted to check if the focus of laser was on the sample plane. The number and distribution of bright spots were very important information in characterizing single molecule sample. The number density of spots enabled us to estimate the probability of observing multiple molecules (not single molecule) in a pixel and on a whole area scanned. The details of the statistical estimation of multiple molecule detection error will be explained in the Section III.B. The fluorescence imaging was

implemented by controlling the motion of the XYZ nanopositioning stage and the photon counting board simultaneously. As was mentioned before, the photon counting data included not only the chronological data but also the delay time. Therefore, the various ways of analysis were feasible from the single molecule fluorescence imaging experiment: intensity map, fluorescence lifetime of whole area, and fluorescence lifetime image. The structure of TCSPC data of a tested area is shown in Figure 3.13. One image

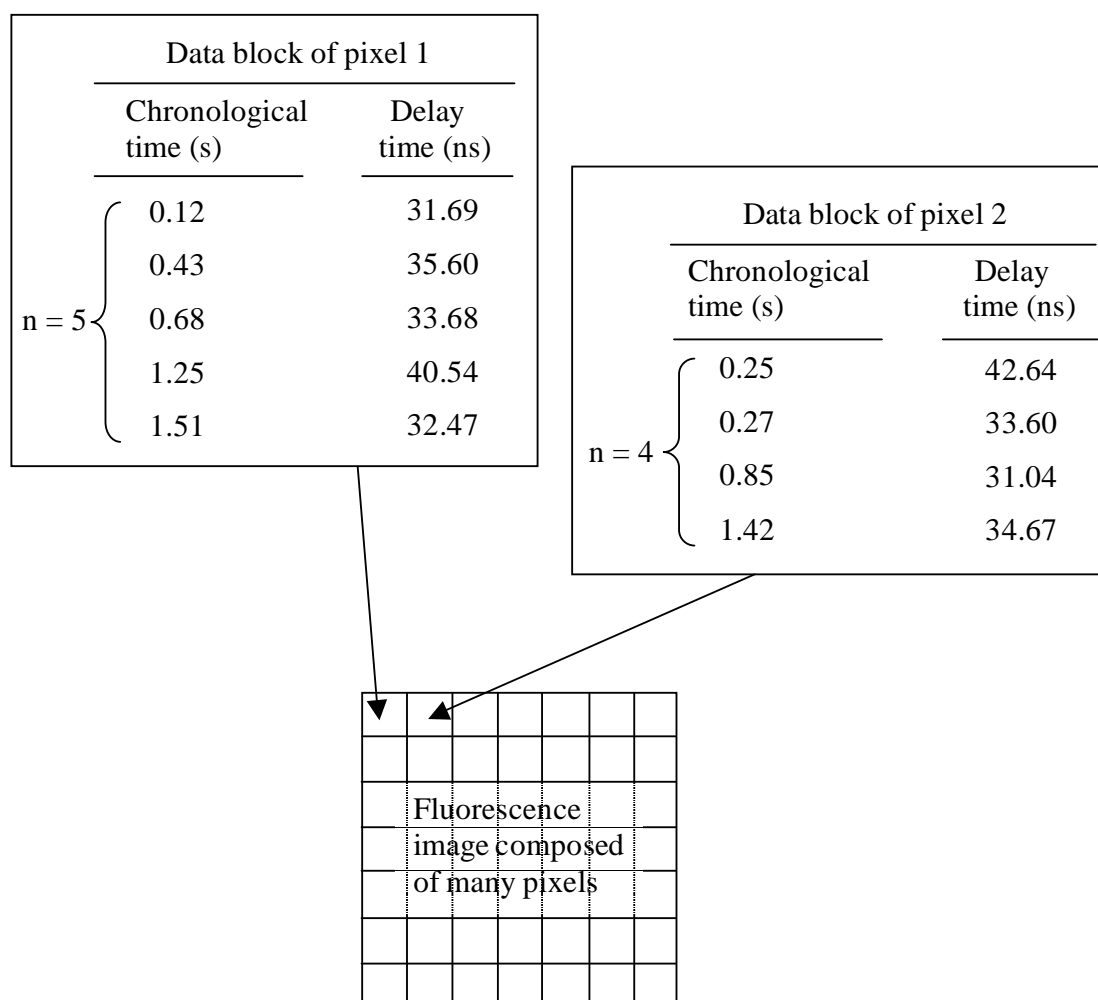


Figure 3.13. The structure of TCSPC data of a tested area.

was composed of pixels on a 2D area. The laser focus stayed on each pixel for a finite time acquiring both chronological and delay time data, or only chronological time data. As manifested in Figure 3.13, the chronological time always increases and delay time is not time-ordered. A block of photon counting data is registered to a pixel. The image is a set of the block of the pixel data. The intensity map is simply the map of the total number of counted photons on a pixel, n in Figure 3.13. The fluorescence decay curve of the whole area is meaningful because it includes the spatial heterogeneity of fluorescence lifetime. It can be built from the collection of delay time data of all the blocks. The individual pixel data can be a complete photon counting data from which an intensity trajectory and decay curve can be made. The decay lifetimes of individual blocks can constitute a map called the lifetime image. The imaging may be the end of an experiment in bulk fluorescence test. For single molecule detection, it was necessary to collect data with the laser focus fixed on individual light sources. In this work, it has been performed by a subsequent “search and optimization” method described in the next section.

Searching and Optimization

A single dye molecule lives for a finite duration under the illumination with its total number of photons being limited⁴⁴. Such limited amount and low flux of photons really influences and determines the quality and reliability of data analysis. Moreover, compared to the dye molecule in an inert environment, the total number and flux of the emitted photons reduces in a system where electron transfer from the excited state of dye molecule to an acceptor is going on; and irreversible bleach is much faster than the intrinsic molecule on the ET-active nanocrystalline film. As a result, significant portions

of single molecules on the electron accepting nanocrystalline film stop emitting light in one second – a practical minimum duration of emission for the reliable SMFL calculation - and/or have intensity comparable to the background signal. Locating single molecules by taking image before the detection of individual molecules did not work because the irreversible bleach had gone in many molecules during the imaging step itself. Manual positioning of the laser focus at a single molecule also did not work because it was very laborious and an illuminated molecule bleached during the positioning; and sampling was likely to have bias. To maximize the measurement time and proper sampling of quickly bleaching and weakly emitting single molecules, a fully automatic search and position optimization method has been implemented.

Figure 3.14 shows a schematic diagram of the search-optimization-record procedure. LabView based PC program controlled the procedure giving instruction to XYZ nano-positioning state and reading signal from APD. In the search mode, the laser focus moved (actually sample moved with the laser focus stationary) on a sample area in X and Y direction just the same way as the standard imaging. On the photon counts being over “Start threshold”, scanning stopped and the program proceeded to the optimization mode. The goal of the optimization was to put a molecule at the center of the laser focus where the power of the excitation light was highest. It adjusted the position of the laser focus with a finer step distance than the search mode while monitoring the fluorescence intensity. The algorithm of the optimization procedure was similar to Ha’s⁴⁵. In the beginning, the laser focus moved by a step size (60nm) in the positive direction along X axis, and next it moved in the positive direction along Y axis by the same step size. The step size was chosen to be 60nm because the optimization has been known to be fastest

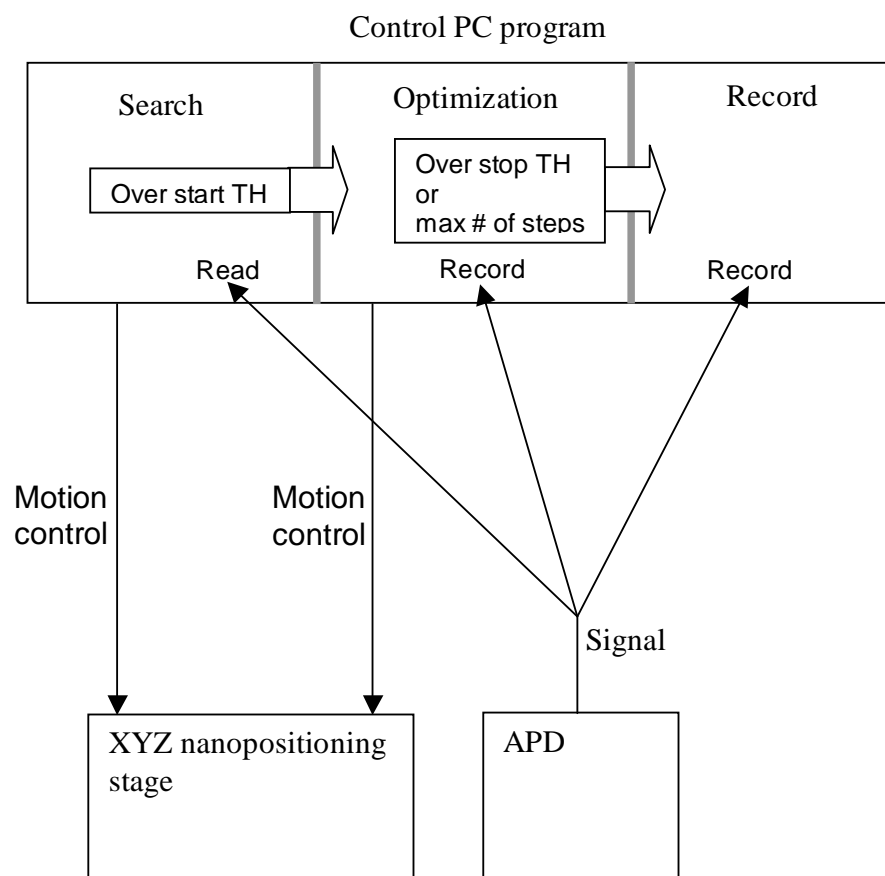


Figure 3.14. Search-Optimization-Record procedure. The direction of arrow line indicate the direction of data or instruction flow.

when the step size is $\sim 0.15 \times \text{focus waist}^{45}$. The direction of the second motion along X axis was determined by the change of intensity during the first motion along X axis. If the intensity increased during the first motion, the direction of second motion was positive direction and vice versa. The direction of second Y motion was determined in the same way. This procedure repeated. The focus moved along the X and Y axis alternatively by the fixed step size. The direction of i^{th} motion in X axis was determined by the direction

and intensity changes during the $i-1^{\text{th}}$ motion in X axis; and so was in Y axis. If the intensity had got higher than a “Stop threshold”, the optimization procedure stopped right away and the control program moved to “Record mode”. If the intensity had not been over the stop threshold through the preset maximum number of optimization steps, the control program moved to the record mode after the maximum number of steps; and the laser focus was put at the position where the intensity was highest during the optimization. In the record mode, photon counting and data recording were done with the laser focus fixed at the optimized position.

Figure 3.15 shows the optimization procedure of real experimental data. The parameters for the test were:

Start threshold: 30 counts/30ms

Step size: 60nm

Stop threshold: 200 counts/30ms

Maximum # of steps: 24

The laser focus has scanned sample from right side in the search mode before the optimization. The search procedure stopped and the optimization began when the intensity at the position marked by ① was 34 counts/30ms because the start threshold was 30 counts/30ms. The photon count has never been over 100 counts/30ms up to the maximum # of steps, 24 steps: therefore the laser focus was set back to the 21th step position where the highest count was recorded and the optimization ended. In the beginning of optimization, convergence to the molecule was slow; and then it became

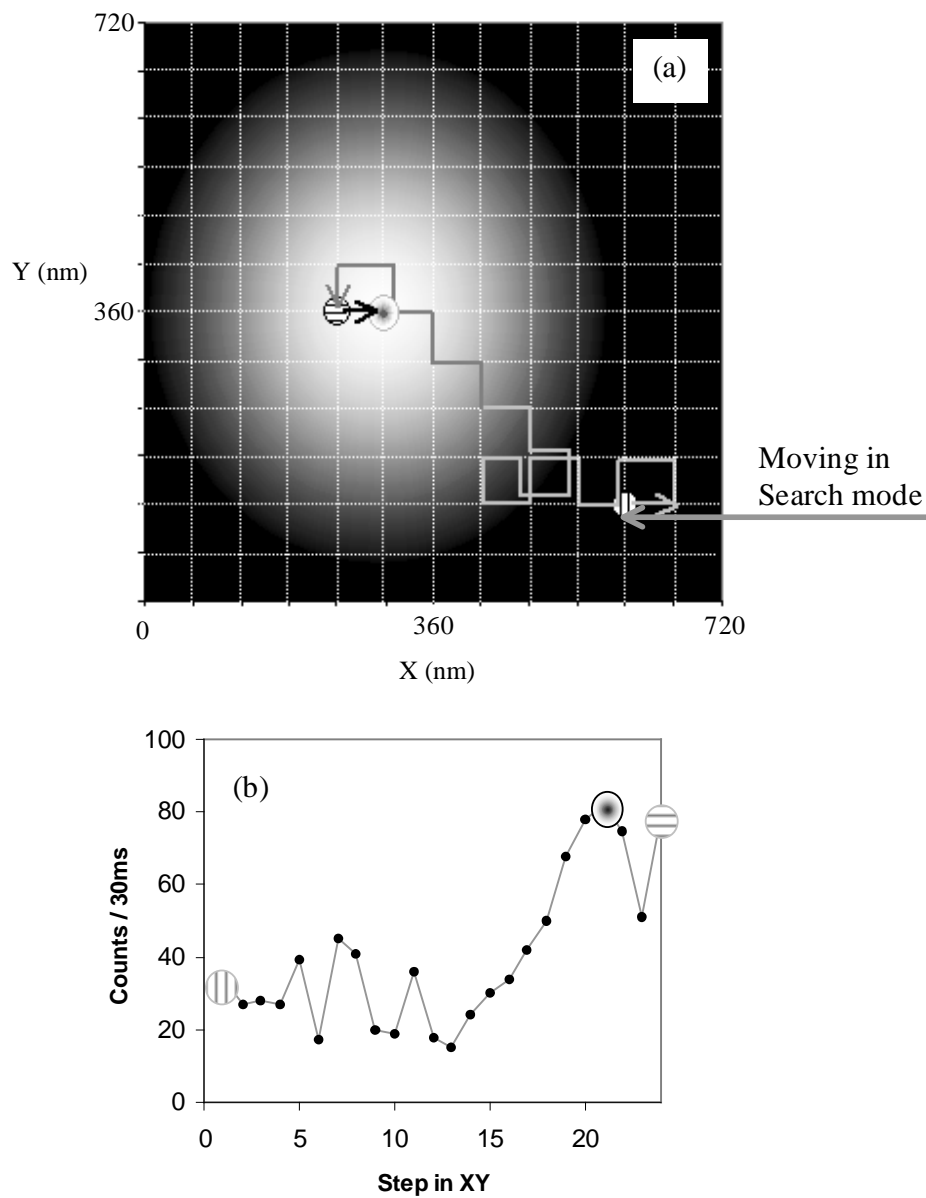


Figure 3.15. The optimization procedure of real experimental data. (a) A walk of laser focus to the top of a single molecule marked by \odot . (b) Intensity trajectory along the path of laser focus in (a). The initial and final positions are marked by \perp and \ominus respectively.

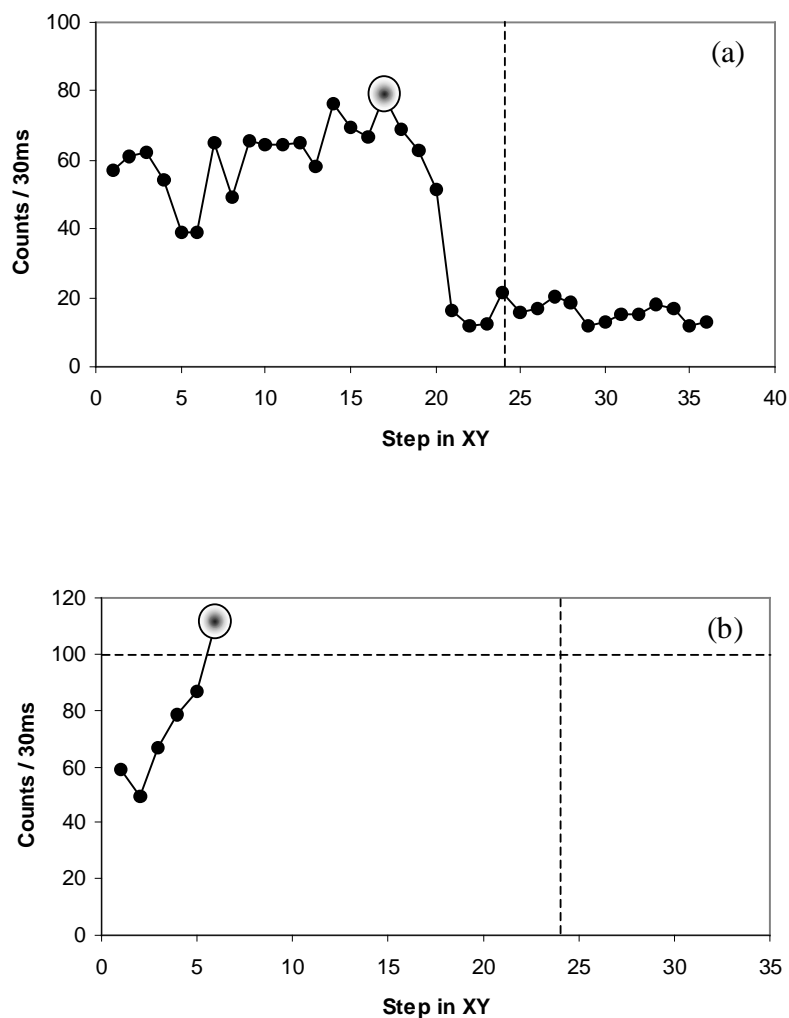




Figure 3.16. Other examples of the optimization procedure that terminated before the preset maximum number of steps 24 marked by vertical dashed line. (a) The aimed molecule bleached during the optimization at about 20th step. The subsequent record procedure would detect only background signal. SMFL was calculated using the TCSPC data acquired during the optimization. (b) Fluorescence intensity went over the stop threshold (100 counts/30ms) and record procedure started right away. The position of laser focus is optimized to the position marked by  in both cases.

fast from 220nm away from the molecule. 220nm corresponds to the $1/e$ radius of the laser focus. Two other examples of optimization are shown in Figure 3.16. An aimed molecule bleached during the optimization as shown in Figure 3.16a. The intensity of another molecule in Figure 3.16b increased over the stop threshold (here, 100 counts/30ms) at 6th step and the optimization procedure stopped. The position of laser focus was optimized to the position marked by  in both cases.

The optimization procedure enabled the use of low start threshold slightly over the background level. Without the optimization, the search procedure had to use the high stop threshold for high enough signal/background ratio for SMFL calculation, and consequently, the molecules having low quantum yield would not have been sampled. The TCSPC data during the optimization were stored, because the optimization time was typically 0.7s and significant number of molecules could bleach in 1s where electron transfer was going on. The duration of data loss was only a couple of millisecond corresponding to the transition time from the search to optimization mode.

III.B. Proper Number Density for the SMD

Questions always arise in the single molecule observation about identity and single molecularity. In other words, we need to confirm that each bright spot is really from a single molecule of interest. There is no one perfect method to answer the questions because the amount of data is very limited and observation time is short. Otherwise, we can talk about only probability of identity and single molecularity. The identity of sample molecule was ensured relatively easily by performing blank test, taking single molecule emission spectrum, and the purity of reagent. Being a single molecule or not could be

tested by integrating the information of the response to the rotation of linear polarization of excitation light, intensity and shape of fluorescence intensity trajectory. However, the single molecularity of a molecule was tested usually until the molecule was bleached and we measured new unknown molecules believing the probability of being single molecule found from the repeated experiences. If the dye molecules do not form aggregates noticeably, we could estimate roughly how many bright spots per area should be observed in single molecule detection.

The distribution of SMFL in a condition has been built by measuring usually about 100 molecules in about $40\mu\text{m} \times 40\mu\text{m}$. Then, we could prepare 11937 cells of which areas are the same as the effective excitation area of our laser focus in the $40\mu\text{m} \times 40\mu\text{m}$ area. Let's suppose that we are depositing 100 molecules on a substrate of the $40\mu\text{m} \times 40\mu\text{m}$ area. Depositing 100 dye molecules is equivalent to picking i ($1 \leq i \leq 100$) number of cells and putting the 100 molecules into them because more than one molecules can occupy one cell. The number of ways to pick the i number of cells is ${}_{11937}C_i$. Next, putting the 100 molecules into the i cells is equivalent to dividing the 100 molecules into i number of parts. The number of doing that is ${}_{99}C_{i-1}$. The total possible number of ways to put 100 molecules into the 11937 cells, T , is:

$$T = \sum_{i=1}^{100} {}_{11937}C_i \cdot {}_{99}C_{i-1} \quad (3.19)$$

Then, the probability of each cell has only one molecule, P_1 , is:

$$P_1 = \frac{{}_{11937}C_{100}}{T} = 0.436 \quad (3.20)$$

The probability of only one cell has two molecules and all the other cells have only one molecule, P_2 , is:

$$P_2 = \frac{11937 C_{99} \cdot 99 C_{98}}{T} = 0.365 \quad (3.21)$$

The probability of each of two cells have two molecules or one cell has three molecules, and all the other cells has only one molecule, P_3 , is:

$$P_3 = \frac{11937 C_{98} \cdot 99 C_{97}}{T} = 0.15 \quad (3.22)$$

$P_1+P_2+P_3=0.951$. Therefore, we can say that 96 of 100 molecules on the $40\mu\text{m} \times 40\mu\text{m}$ area are illuminated alone with 95% probability.

Above simple statistics has an impractical assumption of square-shaped laser focus. For the analysis to be more realistic and versatile, poisson statistics can be applied. The poisson statistics is valid because the depositing process of such a low concentrated dye solution meets the assumption of poisson process^{31,46}. However, the influence of overlap between subsequent illuminated areas on the result is not taken into account. The probability of having n number of molecules within a laser focus is:

$$P(n) = \frac{\mu^n e^{-\mu}}{n!} \quad (3.23)$$

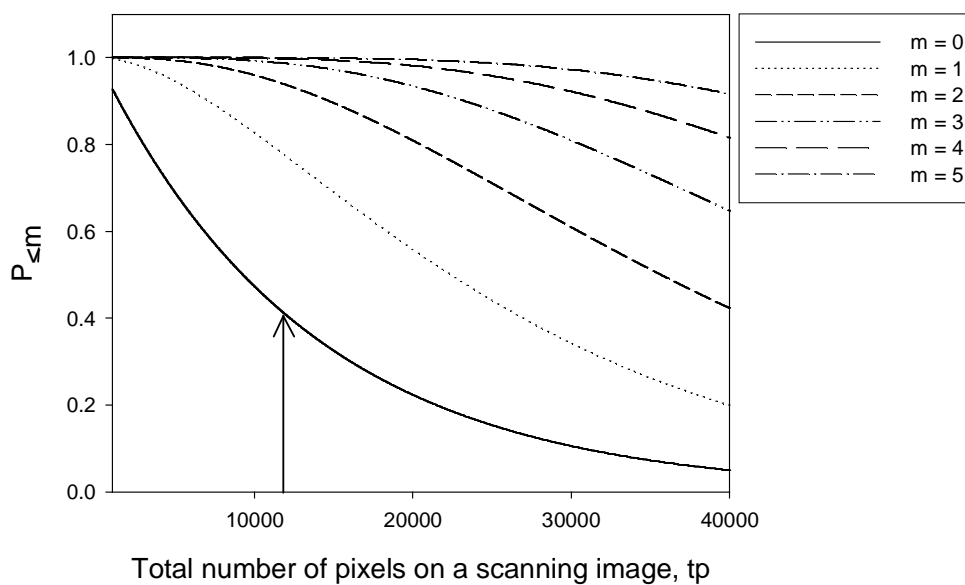
The average number of molecules on the laser focus, μ , is 0.012 when 100 molecules are deposited on the $40\mu\text{m} \times 40\mu\text{m}$ area. The probability of detecting single or no molecule at an arbitrary position of laser P is the sum of $P(0)$ and $P(1)$.

$$P = P(0) + P(1) = 1 - P(n \geq 2) = 0.999925 \quad (3.24)$$

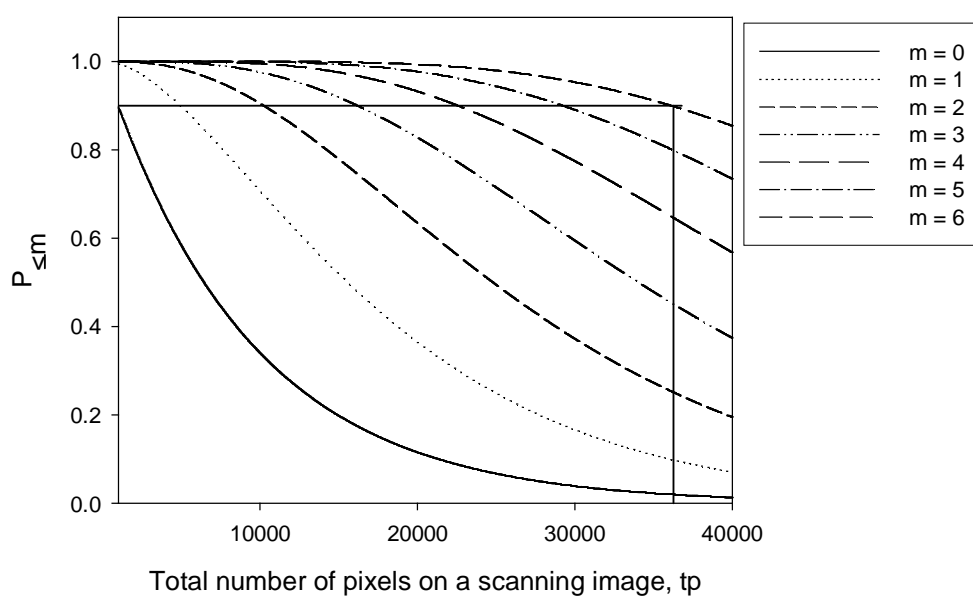
As shown above, the probability of detecting multi-molecules when you put laser focus at arbitrary position is negligible. However, there are typically tens of thousands of statistically equivalent one-pixel detections as the laser scans through the sample of the $40\mu\text{m} \times 40\mu\text{m}$ area. The probability of observing multi-molecules at a pixel equal to or less than m times over the whole scanned area, $P_{\leq m}$, is a binomial distribution:

$$P_{\leq m} = \sum_{i=0}^m {}_{tp}C_i P^{tp-i} (1-P)^i \quad (3.25)$$

Where, tp is the total number of pixels in the $40\mu\text{m} \times 40\mu\text{m}$ area. i is the occurrence of multi-molecule detection. Figure 3.17a ~ 3.17f show the $P_{\leq m}$ values with increasing number of pixels. Typical total number of pixels in the $40\mu\text{m} \times 40\mu\text{m}$ area is from 10,000 to 40,000. Different graphs are different in the number of molecules on $40\mu\text{m} \times 40\mu\text{m}$ area, changing from 100 to 200 molecules by the step of 20 molecules. In each graph, various lines are drawn corresponding to the m values. In Figure 3.17a, the probability of observing only zero or single molecules out of total 11,937 pixels, $P_{\leq 0}|_{tp=11937}$, is 0.408 that is similar to the value in Equation 3.20. Obviously, the $P_{\leq m}$ decreases as the number of scanned spots or pixels increases. We can see that the probability of detecting only zero or single molecules over the whole area, $P_{\leq 0}$, is about 20% even at the practically lower limit of number density, $0.0625 \text{ molecule}/\mu\text{m}^2$ ($100 \text{ molecule}/40 \times 40 \mu\text{m}^2$), in Figure 3.17a. At higher number density, the $P_{\leq 0}$ levels drop to negligible value quickly. That is, we cannot expect pure single molecule observation in the typical condition and

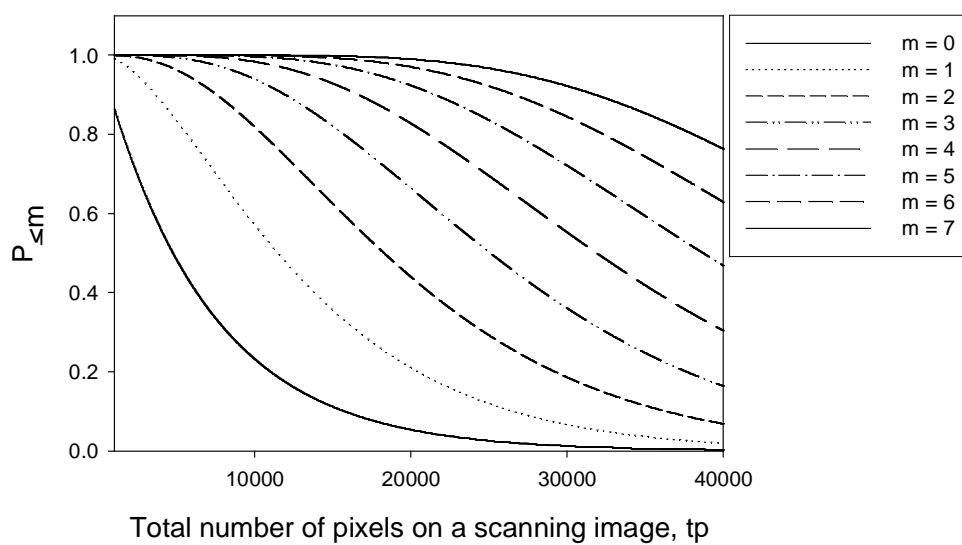


(a)

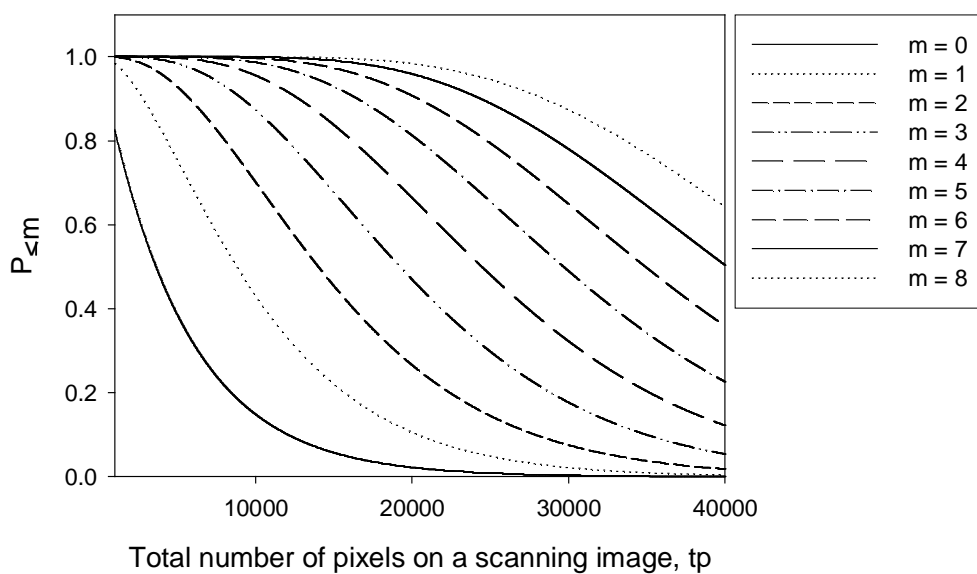


(b)

Figure 3.17. $P_{\leq m}$ vs. total number of pixels. The numbers of molecules deposited are 100 and 120 in (a) and (b), respectively.

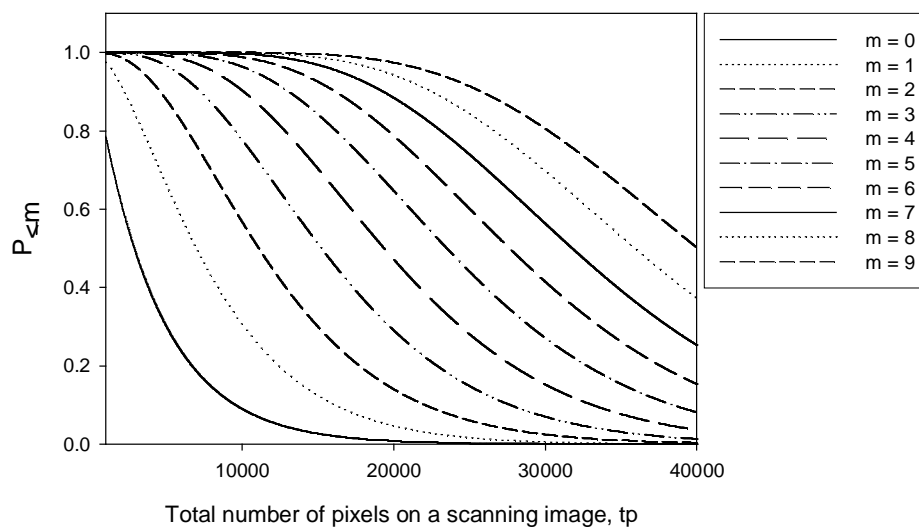


(c)

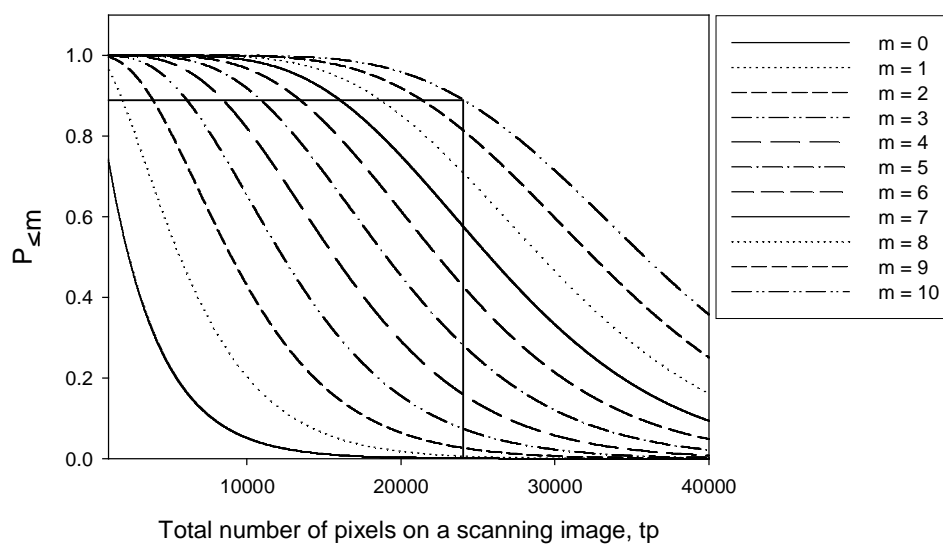


(d)

Figure 3.17. (continued). $P_{\leq m}$ vs. total number of pixels. The numbers of molecules deposited are 140 and 160 in (c) and (d), respectively.



(e)



(f)

Figure 3.17. (continued). $P_{\leq m}$ vs. total number of pixels. The numbers of molecules deposited are 180 and 200 in (e) and (f), respectively.

have to allow the multi-molecule detection at a reasonable sampling rate or number density of dye molecules.

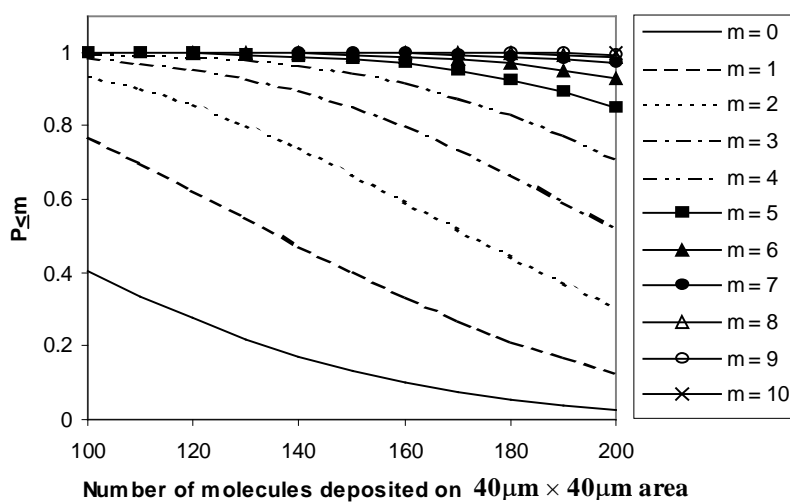
Then, what is the satisfactory number of detecting multiple molecules at a pixel? It may depend on the purpose of single molecule test. In this study, let's define the satisfactory experiment as detecting multiple molecules equal to or less than 5% times of the total number of deposited molecules. That is, it is regarded as a good single molecule test to detect equal to or more than two molecules at a pixel once, twice, three, four, or five times on a $40\mu\text{m} \times 40\mu\text{m}$ area deposited with 100 molecules. A test that detects multi-molecules at a time less than three times is better than the "good" test, but the "better" test is less likely than the "good" test ($P_{\leq} < P_{\leq 5}$). The better a test is, the harder to achieve it and we are satisfied with the "good" test. Our goal is to find in what condition we can do the good test. There is no way to prepare a condition that makes the good test for sure. Here, we define another probability of achieving the "good" test. It is an element with m ($= 5\%$ of the total number of molecules) of the set $\{P_{\leq m}\}$ and labeled $P_{5\%}$. The $P_{5\%}$ curves in Figure 3.17a through 3.17f are the uppermost lines. As above, what is the satisfactory probability of having the $P_{5\%}$ over the whole area? It may depend on the purpose of the test and can be arbitrarily chosen. In this study, $P_{5\%}$ higher than 90% is defined to be satisfactory and the test is the proper single molecule detection. In Figure 3.17a, $P_{5\%}$ ($=P_{\leq 5}$) is higher than 90% regardless of tp . Therefore, all the tests done at the number density 100 molecule/ $40 \times 40\mu\text{m}^2$ are valid. The number density, 120 molecule/ $40 \times 40\mu\text{m}^2$, shows the tail of $P_{5\%}$ less than 90% at high resolution imaging ($tp > 36,000$). The $tp|_{P_{5\%}=90\%}$ keeps decreasing down to 24,000 pixels at the number density 200 molecule/ $40 \times 40\mu\text{m}^2$. Figure 3.18 shows the plots of $P_{\leq m}$ ($0 \leq m \leq 10$) versus

total number of deposited molecules. Figure 3.18a and 3.18b are of the low-resolution ($tp=12,000$) and high-resolution ($tp=40,000$) detection, respectively. Obviously, the $P_{\leq n}$ s decrease as the number of deposited molecules increases. The perfect single molecule detection (solid line) could be expected with 40% probability in the low resolution detection of 100 deposited molecules in Figure 3.18a; but it looks not likely in the high resolution scanning in Figure 3.18b. You can do the “satisfactory” single molecule test ($P_{5\%}$ higher than 90%) regardless of the number density from 100 to 200 molecules on $40\mu\text{m} \times 40\mu\text{m}$ area in the low-resolution detection in Figure 3.18a. On the contrary, the “satisfactory high resolution detection is allowed only for the sample with 100 molecules on $40\mu\text{m} \times 40\mu\text{m}$ area in Figure 3.18b. The thick gray line in Figure 3.18b connecting the top ends of $P_{\leq n}$ lines is the $P_{5\%}$ line. It is over 90% only at the points of near 100 molecules.

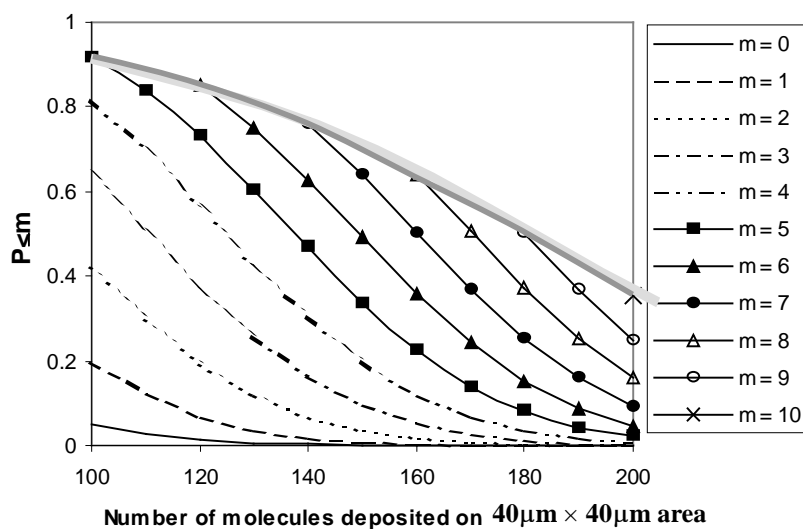
In conclusion, it is important to convince oneself that the measurement is done on single molecules. The direct experimental verification of single molecularity for routine tests is usually impractical for the small amount of data from single molecule. Instead, the statistical estimation gives quantitative reliability of observing single molecules based on the number density and resolution of detection. In the analysis, it is concluded that detecting total $\sim 30,000$ pixels with 100~140 molecules deposited on $40\mu\text{m} \times 40\mu\text{m}$ area is a practically acceptable condition.

III.C. Statistical Fluctuation of Virtual SMFL Source

The single molecule lifetime measurement is usually subject to the shortage of data – photon counts. The limited amount of data in SMFL measurement entails statistical error



(a)



(b)

Figure 3.18. $P_{\leq m}$ vs. total number of deposited molecules with (a) $t_p = 12,000$ and (b) $t_p = 40,000$.

in calculating lifetimes. The uncertainty of the calculated lifetime is not negligible and need to be clarified quantitatively. For example, you may want to know the credibility of the shape and width of a SMFL distribution built from many molecules, especially if the distribution could be compared with one that is predicted by theoretical models. To quantify such a distortion or broadening of SMFL distribution by the statistical error, a virtual SMFL experiment had been performed. It was analogous to an experiment that measured SMFL distribution of imaginary molecules that had a completely identical lifetime; thus, the measured SMFL distribution was a pure lifetime broadening resulting from the instrument response plus the statistical fluctuation. The reason for the virtual SMFL test was that (1) preparing real collection of single molecules of an exactly identical lifetime was difficult because they are not free from spatial inhomogeneity, and (2) detecting a single molecule for a long time is practically not allowed for photo-bleach and SMFL may change dynamically. The fluorescence source of the virtual SMFL test must have a constant fluorescence lifetime and must be stable enough to be detected repeatedly or for a long time for the statistical analysis of the lifetime fluctuation. As the virtual SMFL source, bulk dye solutions were used. The bulk solutions have a constant fluorescence lifetime and can be detected for a long time without change. The virtual SM data are prepared by slicing the full TCSPC data of the virtual SM fluorescence into the chunks of data, of which photon counts correspond to the total counts of the full trajectory of a molecule till its irreversible photo-bleaching.

Five bulk solutions were chosen for the virtual SMFL test. Their concentrations and fluorescence lifetimes are listed in Table 2. The fluorescence lifetimes of the five solutions covered the range in which most of the single molecule lifetimes that have been

observed in this work were distributed. For each solution, nine identical samples were prepared and their TCSPC tests were performed as depicted in Figure 3.19. The excitation laser was focused in the dye solution about 10 μ m above the cover glass. The 10 μ m was deep enough to avoid the influence of the glass surface on the fluorescence lifetime. Each cell in the fluorescence lifetime column in Table 2 contained an average and standard deviation of the nine lifetime values of full trajectories of the nine samples. The full TCSPC data of each sample had huge amount (0.5 million) of counts and they were divided into tens or hundreds of virtual SM TCSPC data.

The dye molecules in a solution were identical and in homogeneous environment in terms of fluorescence lifetime. If the lifetimes of individual molecules in the laser focus ever changed (*e.g.* due to spectral diffusion), the standard deviation of the lifetime fluctuation of the bulk sample was $\sqrt{\text{number of molecules in the laser focus}}$ times smaller than single molecule lifetime change according to the central limit theorem⁴⁷. In applying the central limit theorem, the fluorescence lifetime of bulk solution was assumed to be the average of SMFLs in the focus. The effective excitation volume of the laser focus was about 1 fL and the concentrations of the solutions in Table 2 ranged from 2.0 to 5.0 μ M; therefore about 1,200~3,000 molecules were considered to exist in the focus. Therefore, the lifetime fluctuations of the bulk solutions had at least $\sqrt{1200} = 35$ times smaller than the lifetime fluctuation of single molecule in solution, if ever existed. As a result, the bulk solution could be used as a constant and stable lifetime source.

Figure 3.20 shows an example of the lifetime fluctuation of the virtual constant lifetime source, 2.0 μ M RB solution in 2-Propanol listed in Table 2. The solid line is the

	Concentration (10^{-6} M)	Fluorescence lifetime (ns)* Average (stand. dev.)
RB in DI water	5.0	1.7 (0.01)
RB in mixture of DI water and glycerol (5:1 v/v)	4.2	2.1 (0.01 ₄)
RB in MeOH	2.0	2.5 (0.01)
RB in 2-PrOH	2.0	3.2 (0.008)
R101 in DI water	2.0	4.2 (0.01 ₅)

* Average and stand. dev. of nine fluorescence lifetimes of full trajectories

Table 3.2. Five bulk solutions used in the virtual SMFL test. The solutions were selected to cover the range of fluorescence lifetime in which most of the SMFL observed in this work were distributed. The averages and standard deviations are calculated from nine full TCSPC data of the nine samples.

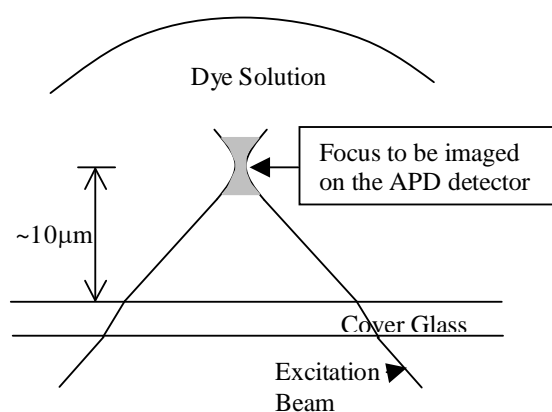


Figure 3.19. Experimental configuration of virtual SMFL test around an excitation laser focus. 30µL of dye solution was dropped on a cover glass. Laser focus is located about 10µm deep into the dye solution to be devoid of the effect of surface on lifetime.

intensity trajectory and the dotted line is the lifetime fluctuation. The two trajectories are 10 second parts of full TCSPC data of one of nine RB in 2-Propanol samples. For the lifetime fluctuation, the TCSPC data was divided into 77 sections of 0.57s unit time duration. 77 fluorescence decay curves were prepared from the 77 TCSPC data sections (5673 photons on average). The standard deviation of the lifetimes of 77 sections was 0.08 ns with average 3.2 ns – same as the lifetime of full TCSPC in Table 2. In other words, the statistical lifetime fluctuation of the virtual SMFL source was 0.08 ns in terms of standard deviation. The histogram of the lifetimes of the 77 divisions is shown in Figure 3.21. We can use this data to find the probability of true SMFL when a measured SMFL is 3.2 ns and the number of photon counts used in making SM decay curve is 5673.

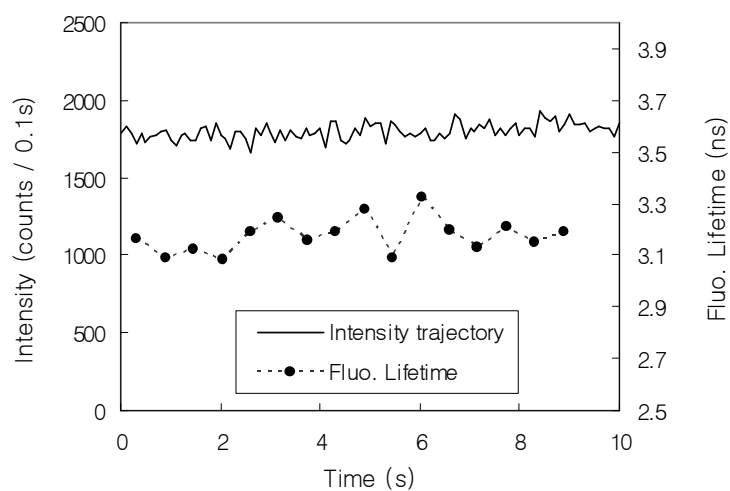


Figure 3.20. An example of the fluctuation of virtual constant lifetime source. Solid line is the intensity trajectory of the bulk solution, 2.00 μM RB solution in 2-Propanol listed in Table 2. Dotted line is a lifetime curve of chunks of TCSPC data divided by 0.57s unit time.

Here, the probability for the true lifetime being in [3.12, 3.28] range is 68% assuming that the distribution in Figure 3.21 is gaussian.

The dependence of the standard deviation of the lifetime fluctuation on the integrated photon counts of decay curve could be obtained by drawing the lifetime trajectory by various unit times out of the same TCSPC data as presented above. In addition, it was found that the lifetime fluctuation was dependent on the magnitude of lifetime, too. The five solutions with different lifetimes were tested to include the dependence on the magnitude of lifetime. Figure 3.22 is the graph of the standard deviation vs. integrated photon counts of the virtual SMFL source. The value on Y axis is the average standard deviation of nine samples. The error bar means the range of data within 95% confidence. The standard deviations of all five solutions decrease monotonically as the number of integrated photon counts. The virtual SMFL sources

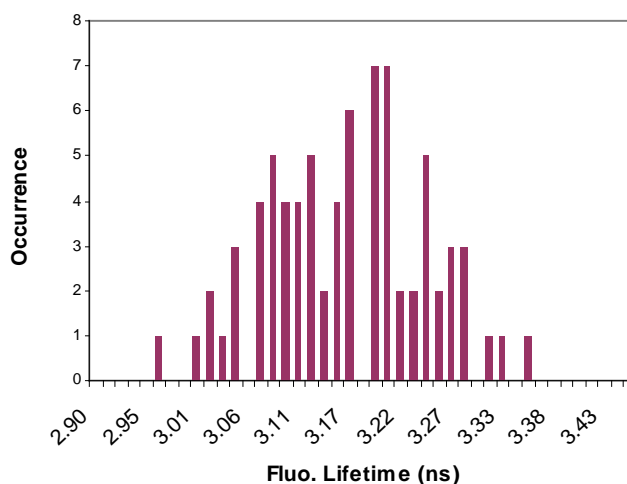


Figure 3.21. Distribution of virtual SMFLs prepared from 77 sections of full TCSPC data divided by 0.57 s unit time. Average and standard deviation are 3.2 ns and 0.08 ns respectively.

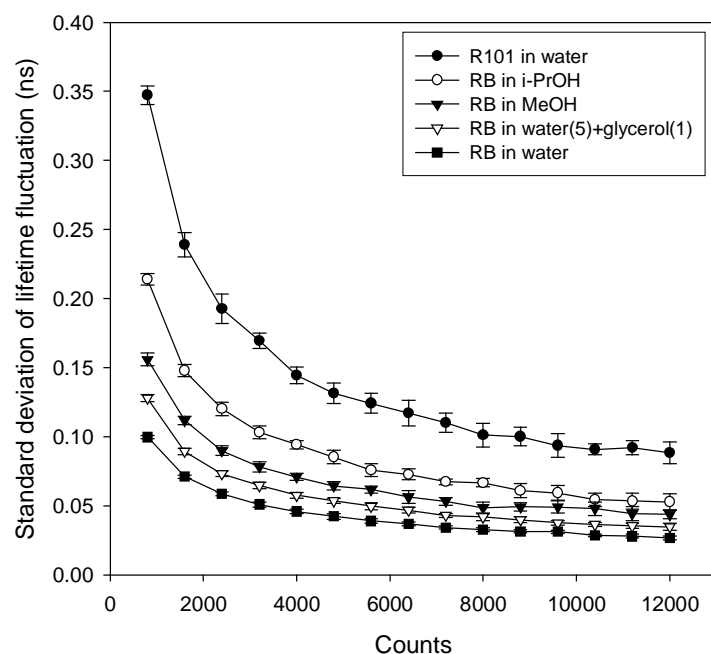


Figure 3.22. Standard deviation depending on the integrated photon counts of virtual SMFL sources. Five different solutions have different curves but decreasing monotonically as the number of integrated photon counts.

along the line have different size of the number of integrated photons but have the same average lifetime. Different lines obviously have different lifetimes. The longer the lifetime is, the higher the fluctuation is in all integrated counts. The heights of the error bars manifest that the curves are well separated. The standard deviation of the lifetime fluctuation vs. average lifetime is plotted in Figure 3.23. It shows that the fluctuation increases with the magnitude of lifetime monotonically and curved a little bit. To apply the result of the experimental estimation of the lifetime and photon counts dependence of lifetime fluctuation to any kind of SMFL data, the values in Figure 3.22 and 3.23 have not to depend on chemical species. For the purpose, 3.5 μM R6G solution in DI water

was tested and compared with the result of R101 in DI water of 4.2ns lifetime in Figure 3.24. The R6G in waster also had 4.2 ns fluorescence lifetime. The curve of R101 is borrowed from Figure 3.22. Though the curve of R6G was made from only one sample, it

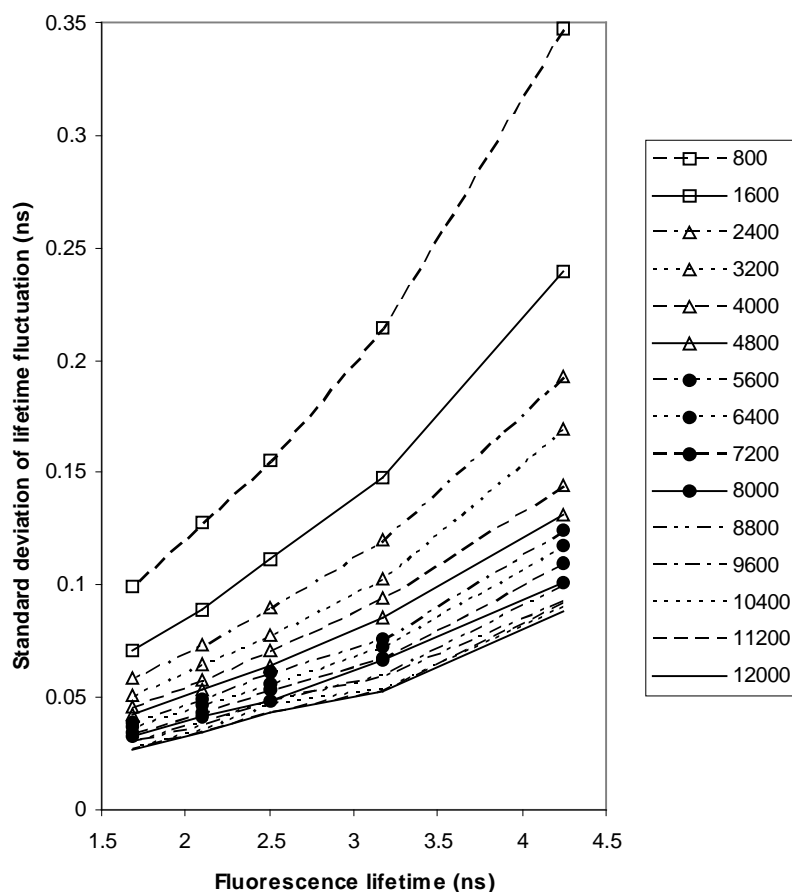


Figure 3.23. Plots of lifetime fluctuation vs. average lifetime for various integrated counts. The different lines correspond to the different integrated counts marked in the legend. The higher the fluorescence lifetime is the higher the statistical fluctuation of calculated lifetime value is. The statistical fluctuation increases monotonically as the increase of lifetime.

fit reasonably well to the curve of R101. Figure 3.22 and 3.23 are the gist of the analysis and will be used in justifying the reliability of SMFL distribution. They are mostly determined by pure statistics of photon counting but may need to be set up for new different photon counting devices, such as the detector, the photon-counting board, etc.

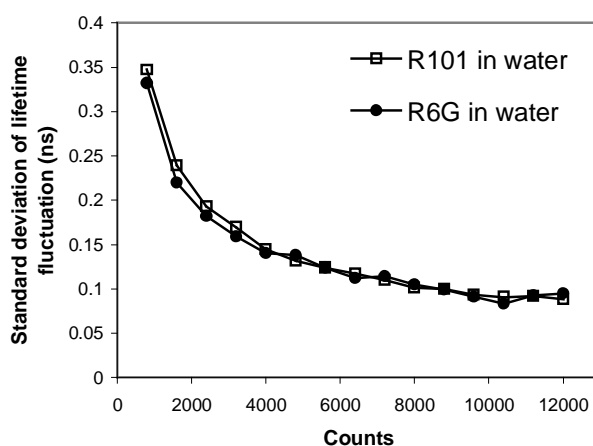


Figure 3.24. Comparison of the lifetime fluctuation vs. counts of virtual SMFL source curves of two solutions of two different solutes having similar lifetimes. Therefore, the relations in Figure 3.22 and 3.23 could be used in any kinds of test done in our SMD tools.

IV. Conclusion

In the above sections, the various parts of the single molecule detection technique were described in detail. The complete cleaning, suppression of impurity, and the careful control of sensitization are necessary to prepare the reliable single molecule junctions. The experimental setup for the time-domain measurement of the fluorescence lifetime

was implemented by applying the time-correlated single photon counting technique. We have developed the most sensitive single molecule detection method. The search-optimization-record procedure has enabled us to sample the single molecules having very weak quantum yield due to quenching by electron transfer. Instead of testing the single molecularity experimentally, we have prepared the single molecule samples of known probability of error by referring to the statistical analysis of observing single molecule, provided with the surface number density of molecules. The quantitative relations of the statistical fluctuation of lifetime vs. photon counts and vs. lifetime have been established by the control experiment of the virtual lifetime source - the solutions of adequately high concentration. Those relations are necessary in estimating the probability of the true lifetime of a single molecule, because the single molecule lifetime calculation usually suffers from the shortage of the data amount and the true lifetime value could be quite different from its calculated value.

References

- (1) Ha, T. *Methods* **2001**, 25, 78.
- (2) Ridge, P. *Handbook of Semiconductor Wafer Cleaning Technology: Science, Technology, and Applications*; Noyes Publications: Park Ridge, NJ, USA, 1993.
- (3) Ip, K.; Gila, B. P.; Onstine, A. H.; Lambers, E. S.; Heo, Y. W.; Baik, K. H.; Norton, D. P.; Pearton, S. J.; Kim, S.; LaRoche, J. R.; Ren, F. *Applied Physics Letters* **2004**, 84, 5133.
- (4) So, S. K.; Choi, W. K.; Cheng, C. H.; Leung, L. M.; Kwong, C. F. *Appl. Phys. A* **1999**, 68, 447.
- (5) Louis, L., Jr. *Chem. Rev.* **1940**, 27, 437.
- (6) Morrison, R. T.; Boyd, R. N. *Organic Chemistry*; Allyn and Bacon: Boston, 1987.
- (7) Dyshel, D. E.; Maksimovich, N. P.; Blizhnyuk, S. A.; Eremina, L. E.; Kaskevich, O. K. *Powder Metallurgy and Metal Ceramics* **1993**, 32, 913.
- (8) Chen, S.-H. *J. Appl. Phys.* **2005**, 97, 073713.
- (9) Low, B. L.; Zhu, F. R.; Zhang, K. R.; Chua, S. J. *Thin Solid Films* **2002**, 417, 116.
- (10) Mori, N.; Ooki, S.; Masubuchi, N.; Tanaka, A.; Kogoma, M.; Ito, T. *Thin Solid Films* **2002**, 411, 6.
- (11) Donley, C.; Dunphy, D.; Paine, D.; Carter, C.; Nebesny, K.; Lee, P.; Alloway, D.; Armstrong, N. R. *Langmuir* **2002**, 18, 450.
- (12) Asbury, J. B.; Hao, E.; Wang, Y.; Ghosh, H. N.; Lian, T. *Journal of Physical Chemistry B* **2001**, 105, 4545.

- (13) Gosavi, S.; Marcus, R. A. *Journal of Physical Chemistry B* **2000**, *104*, 2067.
- (14) Hashimoto, K.; Hiramoto, M.; Sakata, T. *Chem. Phys. Lett.* **1988**, *148*, 215.
- (15) Rockenberger, J.; Felde, U. z.; Tischer, M.; Troger, L.; Haase, M.; Weller, H. *Journal of Chemical Physics* **2000**, *112*, 4296.
- (16) Anderson, N. A.; Hao, E.; Ai, X.; Hastings, G.; Lian, T. *Chem. Phys. Lett.* **2001**, *347*, 304-310.
- (17) Nazeeruddin, M. K.; Kay, A.; Rodicio, I.; Humphrybaker, R.; Muller, E.; Liska, P.; Vlachopoulos, N.; Gratzel, M. *J. Am. Chem. Soc.* **1993**, *115*, 6382-6390.
- (18) Pelling, A. E.; Li, Y.; Cross, S. E.; Castaneda, S.; Shi, W.; Gimzewski, J. K. *Cell Mobility and the Cytoskeleton* **2006**, *63*, 141.
- (19) Pouget, J.; Mugnier, J.; Valeur, B. *J. Phys. E: Sci. Instrum.* **1989**, *22*, 855.
- (20) Klein, U. K. A.; Mastromarino, J.; Yamani, Z. H.; Suwaiyan, A. *Chem. Phys. Lett.* **1994**, *217*, 80.
- (21) Kusumi, A.; Tsuji, A.; Murata, M.; Sako, Y.; Yoshizawa, A. C.; Kagiwada, S.; Hayakawa, T.; Ohnishi, S.-i. *Biochemistry* **1991**, *30*, 6517.
- (22) James, D. R.; Siemiarczuk, A.; Ware, W. R. *Rev. Sci. Instrum.* **1992**, *63*, 1710.
- (23) Pancur, T.; Schwalb, N. K.; Renth, F.; Temps, F. *Chemical Physics* **2005**, *313*, 199.
- (24) O'Connor, D. V. *Time-correlated Single Photon Counting*; Academic Press: Orlando, 1984.

- (25) Legendre, B. L. J.; Williams, D. C.; Soper, S. A.; Erdmann, R.; Ortmann, U.; Enderlein, J. *Rev. Sci. Instrum.* **1996**, *67*, 3984.
- (26) Knight, A. E. W.; Selinger, B. K. *Aust. J. Chem.* **1973**, *26*, 1.
- (27) Moerner, W. E. *New Journal of Physics* **2004**, *6*, 88.
- (28) Felekyan, S.; Kuhnemuth, R.; Kudryavtsev, V.; Sandhagen, C.; Becker, W.; Seidel, C. A. M. *Review of Scientific Instruments* **2005**, *76*, 083104.
- (29) McHale, J. L. *Molecular Spectroscopy*; Prentice Hall: Upper Saddle River, N.J., 1999.
- (30) McQuarrie, D. A. *Statistical Mechanics*; University Science Books: Sausalito, Calif., 2000.
- (31) Kalbfleisch, J. G. *Probability and Statistical Inference*; Springer-Verlag: New York, 1985; Vol. 1.
- (32) Yguerabide, J. *Methods in Enzymology* **1972**, *26*, 498.
- (33) French, P. M. W. *Contemporary Physics* **1996**, *37*, 283.
- (34) Backus, S.; III, C. G. D.; Murnane, M. M.; Kapteyn, H. C. *Rev. Sci. Instrum.* **1998**, *69*, 1207.
- (35) Rulliere, C. *Femtosecond laser pulses: principles and experiments*; Springer: Berlin: New York, 1998.
- (36) Hecht, E. *Optics*; Addison-Wesley: San Francisco, CA 2002.
- (37) Curley, P. F.; Ferguson, A. I. *OPTICS LETTERS* **1991**, *16*, 1016.
- (38) Keller, U.; Knox, W. H.; Roskos, H. *OPTICS LETTERS* **1990**, *15*, 1377.
- (39) Rizvi, N. H.; French, P. M. W.; Taylor, J. R. *OPTICS LETTERS* **1992**, *17*, 279.

- (40) Lu, H. P.; Xie, X. S. *J. Phys. Chem. B* **1997**, *101*, 2753.
- (41) Ha, T.; Chemla, D. S.; Enderle, T.; Weiss, S. *Bioimaging* **1997**, *5*, 99.
- (42) Sanchez, E. J.; Novotny, L.; Holtom, G. R.; Xie, X. S. *Journal of Physical Chemistry A* **1997**, *101*, 7019.
- (43) Brand, L.; Eggeling, C.; Zander, C.; Drexhage, K. H.; Seidel, C. A. M. *J. Phys. Chem. A* **1997**, *101*, 4313.
- (44) Maiti, S.; Haupts, U.; Webb, W. W. *PNAS* **1997**, *94*, 11753.
- (45) Ha, T.; Chemla, D. S.; Enderle, T.; Weiss, S. *Appl. Phys. Lett.* **1997**, *70*, 782.
- (46) Bevington, P. R. *Data Reduction and Error Analysis for the Physical Sciences*; McGraw-Hill: New York, 1969.
- (47) Mathews, J.; Walker, R. L. *Mathematical Methods of Physics*; W. A. Benjamin: New York, 1964.

Chapter 4. Single Molecule Detection of Rhodamine B on Nanocrystalline Thin film

I. Introduction

Electron transfer across the molecule-nanoparticle junction has drawn attention from many researchers for its fundamental interest¹⁻⁴ and its role as a key process involved in many applications of nanoparticles, such as molecular electronics^{2,5,6}, photovoltaics^{2,7,8}. Previous studies of ET in an ensemble of junctions often showed non-single exponential electron transfer kinetics⁹⁻¹⁴, implying the heterogeneous distributions of electron transfer processes. Dynamic heterogeneity has also been implicated in the studies of interfacial ET through the self-assembly monolayers of alkanethiol on bulk Au electrodes¹⁵. A detailed understanding of the heterogeneities can be best achieved by probing each junction individually, an approach that is also of significant technical interest. Much insight on the molecule-nanoparticle junction has been obtained by measuring single molecule conductance using scanning probe techniques¹⁶⁻¹⁸. In addition to the molecule-nanoparticle (or bulk electrode) junction, these approaches require an additional contact between a molecule and the measuring probe tip. The stability and reproducibility of the latter contact can often be difficult to control¹⁷. On the other hand, photoinduced electron transfer rate across a single molecule-nanoparticle junction can be measured without the establishment of additional contact^{1,2,19-22}. For this reason, single molecule fluorescence spectroscopy²³ may provide a valuable approach to study the molecular/nanoparticle junction. There have been three reports of the single molecule interfacial electron transfer in recent years²⁴⁻²⁶. While cresyl violet on Sn:In₂O₃ (ITO) exhibited a static

heterogeneous distribution of lifetimes^{24,26}, it was found to undergo intermittent ET activity on TiO_2 ²⁶. The reason for the dramatically different behavior remains unclear and requires further examinations. In this work, we report a single molecule fluorescence study of rhodamine-B (RB) on antimony doped tin oxide (ATO, $\text{Sb}:\text{SnO}_2$) nanoparticles by two-photon excitation. Unlike the previous single molecule interfacial ET studies, which utilize single photon excitation, the two-photon excitation and non-contact approach reported here can potentially be used to address a single molecule-nanoparticle junction embedded in three-dimensional arrays.

Our prime interest is the fluorescence lifetime of a single RB molecule adsorbed on nanocrystalline ATO thin film. The indication of the ET process from S_1 state into the conduction band is the reduction of fluorescence decay lifetime because the ET and the fluorescence emission compete and sum to a constant energy release from the excited state of RB. Figure 4.1 is a schematic diagram of the redox potential energies of valence and conduction bands of ATO, ZrO_2 , and ground and excited states of rhodamine B referenced to the NHE standard²⁷⁻³². The excited state of RB is about 1.3 eV higher (0.5 eV lower) than the conduction band edge of ATO (ZrO_2). Trap states and bottom levels of the conduction band of ATO nanocrystal are filled with excess electrons by n-type doping, which shifts up Fermi level (E_f) by $\sim 0.09\text{eV}$ above the conduction band edge³³. An electron is transferred from the discrete level in the electronic excited state of RB to the high-density states in the conduction band of ATO in picosecond and femtosecond time scale. The dynamics of the interfacial electron transfer from molecular adsorbate to the nanocrystalline semiconductor is well described in previous works^{2,34}. It has been known that the ultrafast ET in dye-sensitized (doped or undoped) semiconductor

nanoparticle is driven by the continuous high-density acceptor levels in the conduction band of acceptor nanoparticles. Guo et al. has recently published a study on the ultrafast electron transfer and recombination of dye-adsorbed ATO nanoparticle³³. Their adsorbate was $\text{Re}(\text{dpbpy})(\text{CO})_3\text{Cl}$ (dpbpy = 4,4'-($\text{CH}_2\text{PO}(\text{OH})_2$)₂-2,2'-bipyridine) but nanocrystalline ATO was prepared by the same method. In their work, the doping did not change the characteristic time scale and the yield of electron injection. The rate of

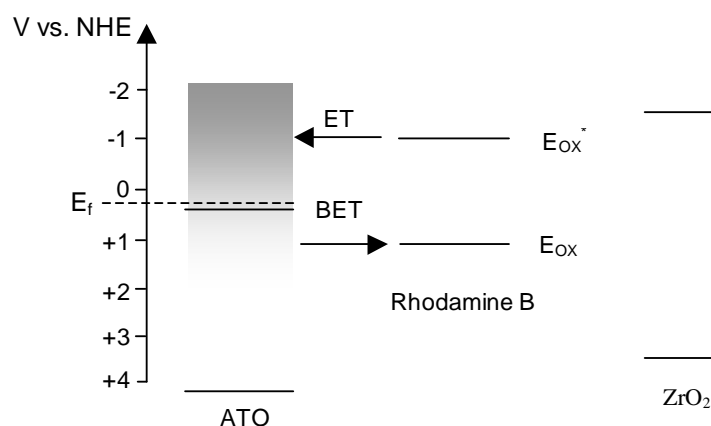


Figure 4.1. Schematic diagram of redox potential energies of valence and conduction bands of ATO, ZrO₂, and ground and excited states of rhodamine B referenced to the NHE standard²⁷⁻³². E_f is the Fermi energy level of ATO of 10% doping level³³. Excited state of RB is about 1.3 eV higher (0.5 eV lower) than the conduction band edge of ATO (ZrO₂). An electron is transferred from the discrete level in the electronic excited state of RB to the high-density states in the conduction band of ATO. The constant population of electrons in the trap states and bottom of conduction band secures back electron transfer. Electron transfer to the conduction band of ZrO₂ is not allowed energetically.

recombination of the injected electron and oxidized adsorbate was determined by the concentration of electrons in ATO particle, which was modeled with pseudo-first order kinetics. The recombination obeyed the electron transfer kinetics, not the electron transport by trapping/detrapping. Similar phenomena have been observed by Guo in our RB/ATO system. In our single molecule tests, those points were more critical. The number density of the adsorbed RB molecules in single molecule test was many orders lower than in the bulk test. During the illumination of RB/undoped SnO₂, only one electron cycled around its related orbitals in the simplest picture. Once the 'single' injected electron escaped the site of adsorbed RB, the concentration of electron available for the back electron transfer became negligible around the oxidized RB because no other RB injects electron. In addition, the ohmic contacts between SnO₂ particles makes the bleach almost irreversible. As a result, no single molecule has been detected reliably for the RB/SnO₂ due to the highly effective and almost irreversible fluorescence bleach. On the contrary, the electrons populated in the trap state and conduction band of ATO were the constant sources of recombination regardless of the escape of the single injected electron. In short, the n-doping has enabled our single molecule detection of RB/ATO.

The RB dye studied in this chapter is a well-known laser dye and its spectroscopic property has been studied extensively. Its high photostability³⁵, low triplet yield 0.006³⁶, highest level of two-photon absorption cross-section ($\sim 150 \text{ GM}^{37}$), high molar absorption coefficient (max. $\sim 100,000 \text{ Lmol}^{-1}\text{cm}^{-1}$), and high quantum yield (~ 1 in a non-polar or rigid medium)³⁸⁻⁴³ has made the RB suitable for our two-photon SMD. The absorption and emission spectra are shown in Figure 4.2. Due to the parity selection rule^{44,45}, the absorption spectrum in two-photon excitation (TPE) is quite different from that in one-

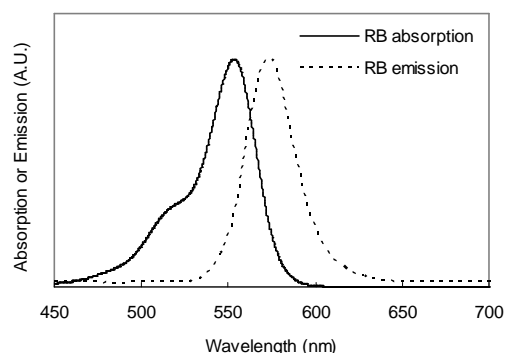


Figure 4.2. One-photon absorption (solid) and emission (dotted) spectra of RB in water. Absorption spectrum of two-photon excitation is quite different from the solid line.

photon excitation (OPE). There is negligible absorbance at 400 nm in OPE while 800 nm - used in this work for the TPE - is near the two-photon absorption peak. The ATO is considered to be one of the most appropriate material for solar cell and electrode in molecular electronics because the ATO is chemically and thermally stable and mechanically hard compared to widely used ITO^{27,28} in addition to its conductivity and transparency.

In single molecule level, the electron transfer is observed most effectively when the ET rate from the electronic excited state is similar to that of radiataion. If a single molecule's ET rate is much faster than the fluorescence devoid of ET, quantum yield becomes too low to measure its actual fluorescence lifetime. The ET rate of RB/ATO falls in the ultrafast ET regime like other dye-semiconductor nanocrystal junctions. As a result, the ET rate conjugated with measured SMFL ranged from intermediate ET rate to unrealistically slow ET rate. Therefore, we doubted that the origin of the distribution of the measured slow SMFLs was conjugated only to the ET; we rather

considered it to be governed by other mechanism than the interfacial ET. In this study, we suggest that the unexpectedly long lifetimes measured in RB on nanoporous ATO be explained by a completely different language: a combination of local field correction and effective medium approximation. Those theories have been applied very recently to the study of lifetime fluctuation of single dye in glassy medium⁴⁶. The local field correction has been an important theory in understanding the relation between spontaneous emission rate and optical refractive index or dielectric property of medium. Given the three theoretical models introduced in Section III.A of Chapter 2, empty-cavity^{47,48}, virtual-cavity^{48,49}, and fully microscopic^{50,51} models, we interpret the measured slow SMFL distribution as a consequence of spatially heterogeneous refractive index of ATO film.

In Section II, starting from the results of bulk tests of RB/ATO and RB/ZrO₂, the comparative observations of RB/ATO and RB/ZrO₂ in single molecule level will be presented. In Section III, the results presented in Section II will be discussed to search for the origin of SMFL distributions applying the theoretical tools introduced in Chapter 2.

II. Results

II.A. Bulk Fluorescence Lifetime Measurement of RB on ATO

The TCSPC data of a fluorescence image are composed of the TCSPC data of individual pixels including not only fluorescence intensity but also delay times of individual photons detected. The data structure is shown schematically in Figure 3.13 in Chapter 3. By summing up the delay time data of all the pixels, we can make a fluorescence decay curve of the scanned area. The decay curve is equivalent to a snapshot of decay curve that could be taken by wide-field illumination using a detector having large enough active

area that can cover the illuminated region. We define the bulk fluorescence lifetime as the lifetime of fluorescence decay curve built out of the sum of delay time data of all the pixels of a scanned area. Here, the results of the bulk tests of RB on ATO are presented. Those tests raised the main motivation of the SM experiments that will be presented from Section II.B.

Sensitization of the ATO film was done following the standard sensitization method explained in Section I.C of Chapter 3. The ozone-cleaned ATO film was soaked in 10 μ M RB in DI water solution for 80s and was washed with the DI water. A stage-scanned 10 \times 10 μ m²-wide two-photon-excited fluorescence image is shown in Figure 4.3. X and Y axis define the scanned area, and Z axis represents the fluorescence intensity. The 3D fluorescence image was made by recording the fluorescence TCSPC data while the sample stage moved with the laser beam fixed. Excitation wavelength and power were 800nm and 40kW/cm² respectively. The average number of RB molecules at one pixel is estimated to be about 50 by comparing the excitation power and fluorescence intensity of this test with those of typical single molecule detection experiments. Average distance to the closest molecule was roughly 100 nm, which was far enough to prevent intermolecular interactions (*e.g.* electron transfer, energy transfer, re-absorption, exciton formation⁵²⁻⁵⁴). The 10 \times 10 μ m² area was wide enough for bulk test with respect to the number of molecules on it and reproducibility. Figure 4.4a and 4.4b are the decay curves of the total fluorescence photons detected in the experiment shown in Figure 4.3, fitted with different decay models. In Figure 4.4a, a single exponential model convoluted with an instrument response function was fitted to the measured decay curve, whereas a double exponential model was used in Figure 4.4b. The instrument response function is

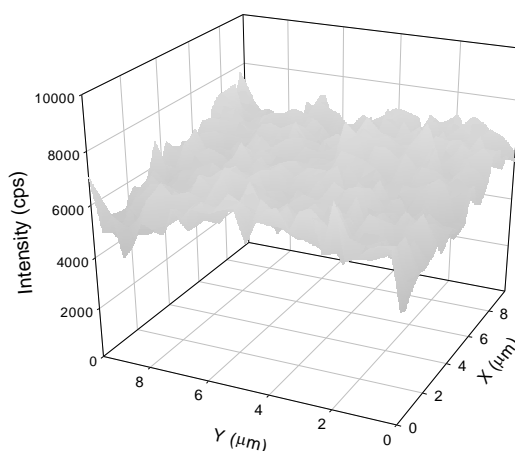


Figure 4.3. Stage-scanned two-photon fluorescence image of RB molecules adsorbed on a nanoporous ATO film. Total scanned area is $10 \times 10 \mu\text{m}^2$ (30 pixels by 30 pixels). Excitation wavelength and power were 800nm and $40\text{kW}/\text{cm}^2$ respectively. The X and Y axis define the scanned area, and Z axis represents the fluorescence intensity in unit of cps (counts per second). There are approximately 50 molecules at a pixel on average; thus, fluorescence from the individual molecules is not resolved, and such a test is called “bulk test”.

marked by the dotted line.

The best fit of lifetime parameter is 1.0 ns with reduced chi square χ^2_r being 11.9 in Figure 4.4a. We can easily conclude that the single exponential model was not fitted to the decay data by looking at the significant deviations marked by two dotted circles. The value of reduced chi square, 11.9, was way bigger than the practical range of good fitting (1 ~ 1.5) implying that the decay dynamics was not single exponential. In Figure 4.4b, the double exponential model decay curve does not show significant deviation from its

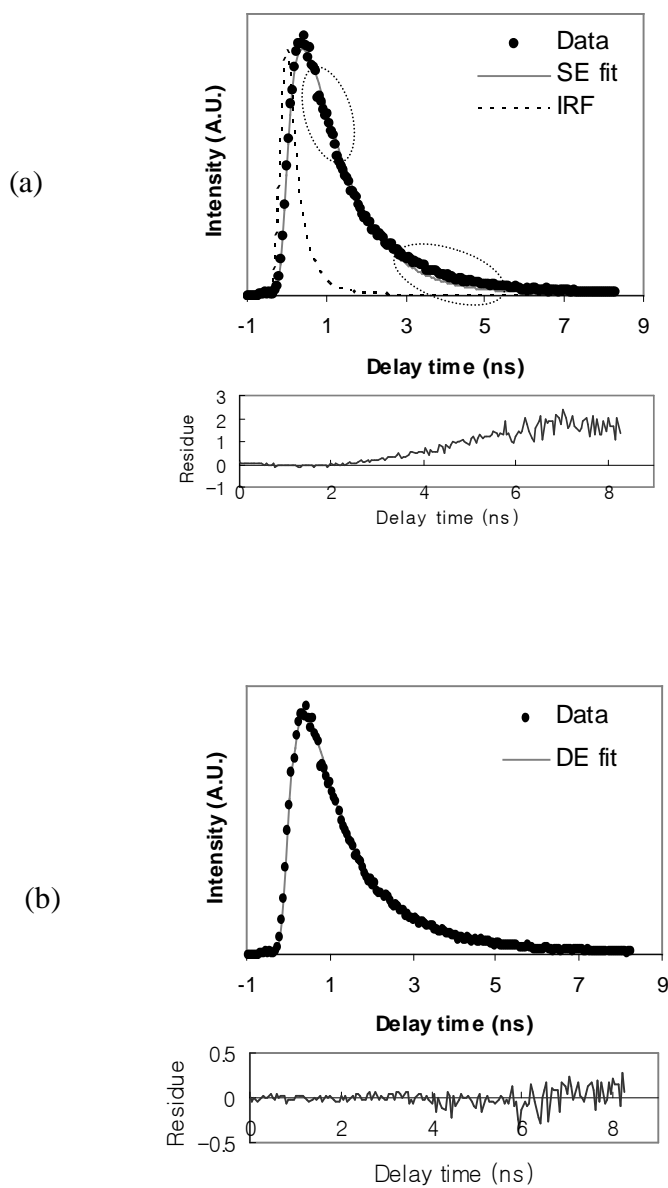


Figure 4.4. Decay curves of the fluorescence detected in the experiment shown in Figure 4.3. (a) Fit to single exponential (SE) decay model: τ and χ^2_{τ} are 1.0 ns and 11.9 respectively. (b) Fit to double exponential (DE) model: τ (slow component) and τ (fast component) are 0.7 (74%) and 2.4 ns (26%) respectively. χ^2_{τ} is 1.1.

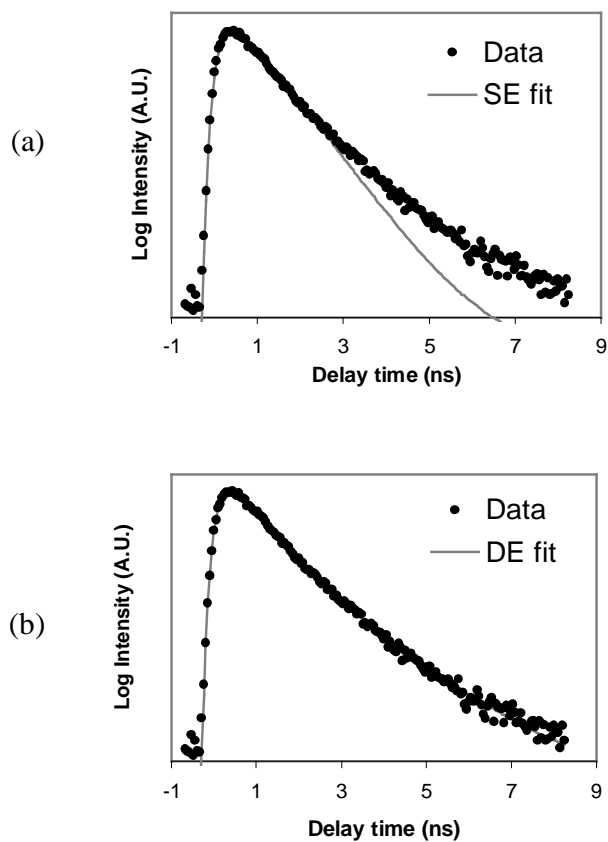


Figure 4.5. Decay curves same as those in Figure 4.4 except for being re-drawn in log Y scale. The log Y scale magnifies the deviation in fitting in the low intensity region. (a) Single exponential model does not fit to data after 3ns. (b) Double exponential model does not show any significant the deviation down to the baseline.

decay data. The best fit lifetimes were 0.7 ns (74%) and 2.0 ns (26%) with χ^2_r being 1.1, which means that the fitting with the two components was satisfactory regardless of its true dynamics. The multi-exponential characteristic is attributed to multi-component electron transfer dynamics. In addition, the feature of bulk fluorescence lifetime was influenced by other microscopic electrodynamics, which will be explained in the

Discussion section in detail. The two graphs in Figure 4.4 are re-drawn in Figure 4.5 in log scale of Y axis. The log Y scale magnifies the deviation in fitting in the low intensity region. The model decay curve (gray solid) in Figure 4.5a deviates from straight linear line after 5ns delay time due to the baseline of IRF, while single exponential decay not convoluted with IRF is linear in the log Y-linear X scale. We can see clearly that the measured decay data deviate from single exponential model in Figure 4.5a. Fitting to the double exponential in Figure 4.5b does not show the deviation down to baseline as confirmed by the reduced chi square value, 1.1.

II.B. Single Molecule Detection

II.B.1. Single Molecule Imaging

Bulk fluorescence images were shown in Figure 4.3. At every single spot, similar level of fluorescence intensity was recorded because multiple molecules sat within a laser focus; we call it bulk test. To detect fluorescence from a single molecule, we need to see a bright spot surrounded by a dark region with the photon counting rate of baseline level. After confirming that most of the bright spots are surrounded by the dark region, we count the number of bright spots and judge whether the sample is valid single molecule sample or not according to the method introduced in Section III.B of Chapter 3.

5×10^{-11} M RB in MeOH was prepared and dropped on an ATO nanocrystalline film. After drying, a fluorescence image was taken. Figure 4.6 is an example of 3D fluorescence intensity graph of RB/ATO nanoparticle junctions drawn by the same method as shown in Figure 4.3. It shows well-separated single molecules. The FWHM of the peaks are about 400nm. It means that the fluorescence was emitted from a point

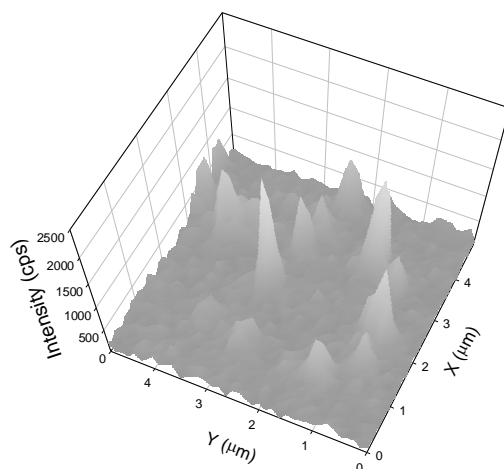
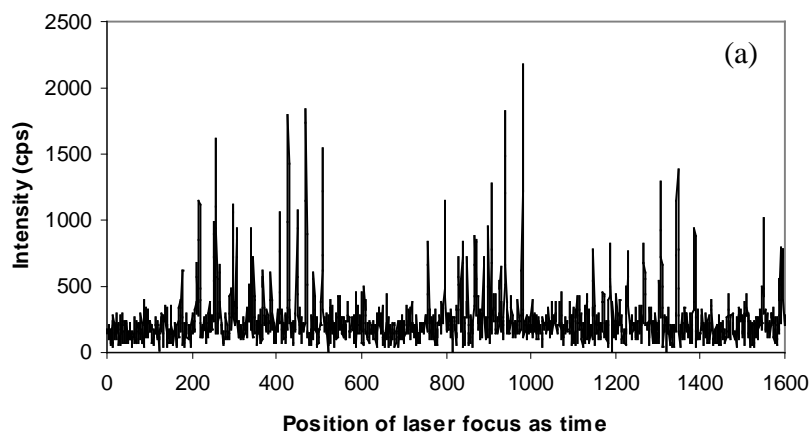


Figure 4.6. Raster scanned two-photon fluorescence image of single RB molecules dispersed on ATO film. $5 \times 5 \mu\text{m}^2$ area (40 pixels by 40 pixels). Acquisition time was 12s. Excitation wavelength and power were 800nm and 0.12 MW/cm^2 respectively.

source because the displacement (400nm) along the diameter of the bright spots corresponds to the diameter of the laser focus. Around the bright spots, relatively dark regions indicate the absence of RB molecules by comparing with the photon count level of a blank sample. One-dimensional plot of intensity along the scanned positions of the test in Figure 4.6 is shown in Figure 4.7a, and Figure 4.7b is a schematic diagram of numerical sequence of illumination in terms of the pixel position. The laser focus moved in zigzags. The indices of X axis in Figure 4.7a correspond to the position number in Figure 4.7b. There are more peaks in Figure 4.7a than in Figure 4.6 because a single molecule was illuminated multiple times due to the smaller pixel size than the diameter of laser focus. In Figure 4.7a, background level was about 160 cps and single molecule signals are identified when they were over about 300 cps.



(b)

1599	1598	1561	1560
79	78	41	40
0				38	39

Figure 4.7. (a) Intensity trajectory along the scanned positions of the test shown in Figure 4.6. (b) Schematic diagram of numerical sequence of illumination in terms of the pixel position. The laser focus moves in zigzags.

II.B.2. Single Molecule Intensity Trajectory

After confirming the proper surface number density (100 ~ 150 molecules on $40\mu\text{m}\times 40\mu\text{m}$) and the fluorescence intensity level, fluorescence photons from the individual single molecules were collected by the search-optimization-record method explained in Section III.A of Chapter 3 until it bleached irreversibly. The chronological

time data of TCSPC were converted to the fluorescence intensity trajectory. Typical fluorescence intensity trajectories of RB single molecules on ATO and glass are shown in Figure 4.8a and 4.8b, respectively. The intensity trajectory of RB highly fluctuated on glass surface from millisecond to second time scale while it was constant on ATO surface within the noise level. The highly fluctuating intensity of rhodamine dyes in inert polymer matrixes^{55,56} and silicate⁵⁷ has been observed by others, too. In fact, 90% of molecules on ATO film had the static intensity trajectory and 90% of molecules on glass had the fluctuating intensity trajectory in this work. On ATO, there were still noticeable counts from the sample due to scattering from the ATO film after irreversible bleach.

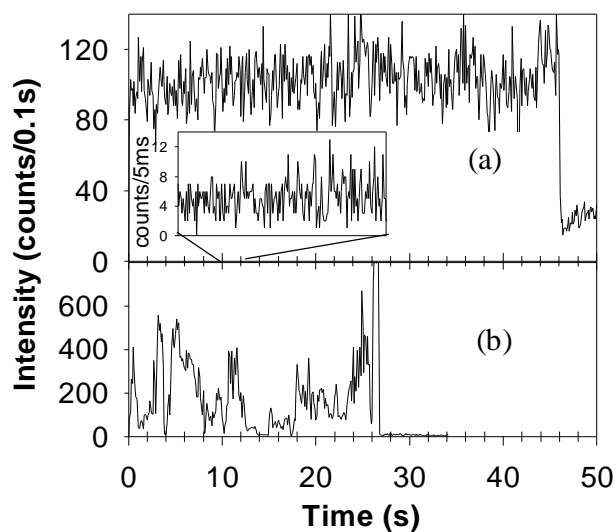


Figure 4.8. Trajectories of fluorescence intensity as a function of time for RB on (a) ATO thin nanoporous film and (b) glass cover slip. The inset in graph (a) shows an expanded view with shorter binning time.

II.B.3. Experimental Evidences of Single Molecule Detection

Polarization Dependence

The sudden photobleach observed in all the intensity trajectories is indicative of fluorescence from a single emitter. This notion is further confirmed by their polarization dependence of single molecule. The probability of transition per unit time of transition $i \rightarrow f$ is given by Fermi Golden rule⁵⁸:

$$\omega_{if} = \frac{\pi}{2\hbar^2} \left| \langle f | \boldsymbol{\mu} \cdot \mathbf{E}_0 | i \rangle \right|^2 \left\{ \delta(\omega_{fi} - \omega) + \delta(\omega_{fi} + \omega) \right\} \quad (4.1)$$

where $\boldsymbol{\mu}$ and \mathbf{E}_0 are the dipole moment of the single emitter and perturbing electric field amplitude, and ω_{fi} is the frequency corresponding to the energy gap of the two states (i and f), and ω is the frequency of the perturbing electric field. The orientation of $\boldsymbol{\mu}$ is assumed to be constant during the polarization dependence test, and a single molecule was identified by changing the polarization direction of linearly polarized excitation laser beam⁵⁹⁻⁶². However, it has been reported that the direction of absorption dipole moment of rhodamine dyes bound to DNA on a glass surface tethered with aminopropylsilane could change⁶³. The $\langle f | \boldsymbol{\mu} \cdot \mathbf{E}_0 | i \rangle$ in Equation 4.1 is simplified to be $\boldsymbol{\mu}_{if} \cdot \mathbf{E}_0$ because the \mathbf{E}_0 is just a constant vector. The quantum mechanical transition dipole moment $\boldsymbol{\mu}_{if}$ is treated as a classical oscillator $\boldsymbol{\mu}$ here. Only the inner product $\boldsymbol{\mu} \cdot \mathbf{E}_0$ changes during the polarization dependence test. A geometric relation of the dipole, electric field, and laser propagation directions are shown in Figure 4.9. Detailed analysis of polarization response test is in Appendix A. When the single molecule is positioned well enough to be within

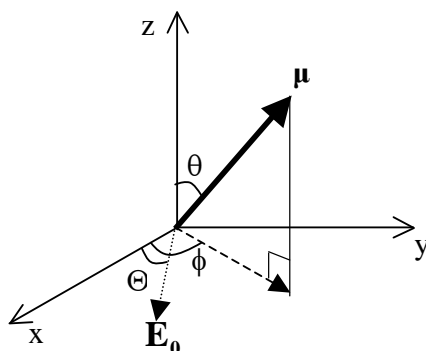


Figure 4.9. Configuration of single absorption dipole moment and plane polarization direction of excitation beam. The direction of laser propagation is along z axis and the surface of substrate is on x-y plane. θ and ϕ are the polar and azimuthal angles of a dipole moment. Θ is the rotation angle of the plane of polarization. x, y, and z are arbitrary lab coordinates.

about 100 nm radially from the center of the laser focus (see Appendix A), the explicit expression of $|\boldsymbol{\mu} \cdot \mathbf{E}_0|^2$ is:

$$|\boldsymbol{\mu} \cdot \mathbf{E}_0|^2 \propto \cos^2 \Theta \quad (4.2)$$

where the θ and ϕ are fixed, and Θ changes. For the two-photon excitation, absorption efficiency is determined by two-photon tensor:

$$|\mathbf{T} : \mathbf{E}_0 \mathbf{E}_0|^2 \propto \cos^4 \Theta \quad (4.3)$$

As a result, fluorescence recorded with varying Θ makes a cosine square and quartic curves in one-photon and two-photon excitation, respectively. If the laser focus is not positioned well for the single molecule to be outside the circle of about 100 nm radius

concentric with the laser focus, the total electric field amplitude can be the sum of all three components. As a result, the fluorescence response to the rotating total electric field will show a complicated curve obviously. Figure 4.10 shows an example of the polarization dependence test. Linearly polarized input beam passed through a half waveplate, and the plane of polarization rotated by turning the half waveplate. Detected fluorescence intensity changed making the distinct curve and was fit to the cosine quartic function. The test manifests that the emitter was a single dipole, and that the dipole is considered to have positioned within the circle inside which the polarization state in lab frame is the same as the input beam. Such a cosine quartic responses have been observed in about 90% of bright spots after the preparation of the RB on glass sample for single molecule detection.

The surface of glass cover slip is not flat but has lots of bumps of ~ 1 nm height as shown in Figure 3.1. Therefore, a significant number of molecules should have the

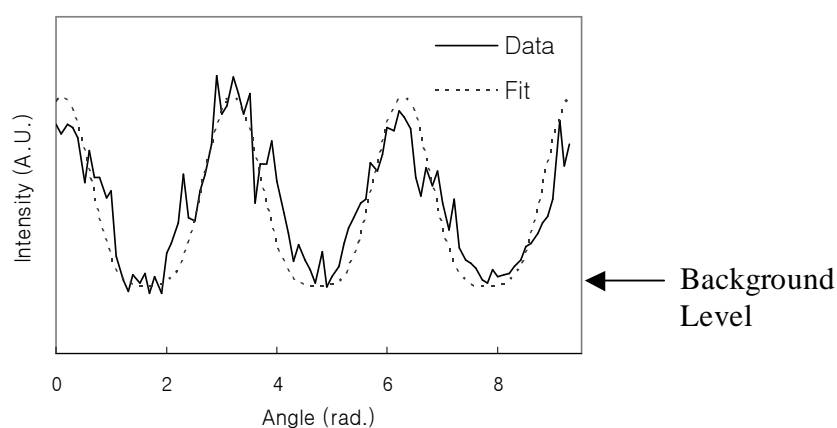


Figure 4.10. Polarization dependence of a RB molecule deposited on a glass substrate. By rotating the plane of polarization of linearly polarized input laser beam, cosine quartic response was detected.

vertical dipole component $\mu_z(\mathbf{r})$. At the very center of the focus, however, E_z is negligible⁶⁰, and the absorption through the vertical component of dipole moment does not occur when the sample is positioned close to the center of the focus. As a result, the minimum of the curve in Figure 4.10 was on the background intensity level.

In case that there are multiple number of molecule at a focus, the response to the rotating linear polarization is not of vector sum of the dipoles but the sum of responses of individual dipoles: the response of the vector sum is not distinguishable from a single molecule. Therefore, the observed response curve would not be able to decrease down to the background level and will be the sum of cosine quartic curves with phase differences corresponding to the differences between the azimuthal angles. Therefore, the response like that shown in Figure 4.10 proves that the fluorescence emitter at the focus was highly likely a single molecule. However, if all the molecules align in parallel, or the dipole moments of all the other molecules except for one molecule direct in parallel to the optic axis of microscope (z axis), the same curve will be observed even though there are multiple number of molecules at the focus.

Such a cosine square and quartic response is possible only when the absorption dipole moment is linear in one-photon and the 2nd rank two-photon absorption tensor has only one dominant diagonal component in the two-photon excitation⁶⁴⁻⁶⁶. The RB is known to have the diagonal two-photon absorption tensor with one dominant element in molecular frame like most of dye molecules⁶⁷.

Single Molecule Emission Spectrum

In addition to the blank tests, which showed that the photon signal over the background level originated only from sample solutions containing the RB, we directly confirmed the identity of the emitters by recording their emission spectra. As shown in Figure 4.11, the emission spectrum of a single RB molecule on a glass cover slip (thick solid line) was similar to the ensemble-averaged spectrum of RB molecules (thin solid line).

From the practical point of view, the experimental verification of SMD discussed so far could not be done routinely because of the difficulty and time for single molecule verification test itself. In addition, when the dyes were on a substrate that was an efficient quencher of excited state, such verification was even more difficult. Instead, the careful blank test and the statistical estimation of the probability of single molecule observation discussed in Chapter 3 was a practically preferred way to confirm the SMD.

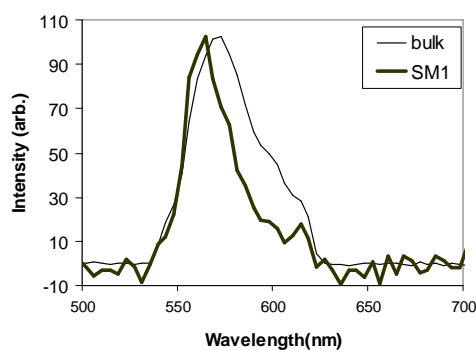


Figure 4.11. Comparison of fluorescence spectra of a single RB molecule (thick solid line) and an ensemble (thin solid line) of RB molecules on a glass cover slip.

II.C. Single Molecule Lifetime Measurement

The bulk fluorescence lifetime measurements, such as those in Section II.A, have shown that it was normal to see the deviation of bulk fluorescence decay from the single

exponential decay when the sample molecules were distributed on a substrate surface. The deviation should be the result of summing up the single exponential decays of individual molecules sitting on their different environments surrounding the individual molecules in short-range. The single exponential decay has been observed for individual molecules whatever the bulk decay dynamics is, in most cases. The multi-exponential fluorescence decay may be unlikely energetically in electronic excitation of single dye molecule. Once a molecule is shelved to its S_1 state, all the other channels to ground state contribute to the increase of decay rate not changing the decay dynamics – single exponential. In occasional cases, however, unexpected multi-exponential decay of a molecule has been observed on a glass surface. The temporal heterogeneity is treated in Chapter 6 separately. In order to decompose and understand the spatial heterogeneity that was responsible for the deviation from the single exponential decay in bulk tests, the single molecule lifetimes of RB molecules deposited on ATO nanocrystalline film, ZrO_2 nanocrystalline film, and glass were investigated. They could be termed as a nanoporous electron acceptor (ATO), a non-interacting nanoporous substrate (ZrO_2), and a non-interacting flat surface (glass). In this Section, the result of SMD of RB on ATO and ZrO_2 are presented. The SMD of RB on glass will be treated in Chapter 5.

II.C.1. SMFL of RB on ATO

The typical fluorescence intensity trajectories of single RB on ATO are shown in figure 4.12. Contrary to the intensity trajectory of RB on glass shown in Figure 4.8b, 106 molecules out of 114 molecules had the static trajectories similar to that in Figure 4.12a. The other 8 molecules had partial fluctuations similar to that in Figure 4.12b. The

dominant static trajectories and the absence of high fluctuation suggest that those RB molecules were in contact with only ATO film not on the glass surface beneath the ATO film. Figure 4.13 shows the fluorescence decay profiles in log scale (4.13a) and linear scale (4.13b) corresponding to the trajectories in Figure 4.12a. The solid lines in Figure 4.13 are the sum of background signal and the convolutions of single exponential decay function with instrument response function represented by dotted line:

$$I(t) = A \cdot \text{background}(t) + \int_0^{\infty} B e^{-t'/\tau} \cdot \text{IRF}(t-t') dt' \quad (4.4)$$

where the $\text{background}(t)$ was the scattering from ATO measured in the same condition as the sample molecules, and the $\text{IRF}(t)$ was prepared by measuring the scattered light from a bare cover glass without laser blocking filter⁶⁸. The A , B , and τ are the parameters of fitting of the calculated $I(t)$ to the experimental data. The decay curve was fitted to the

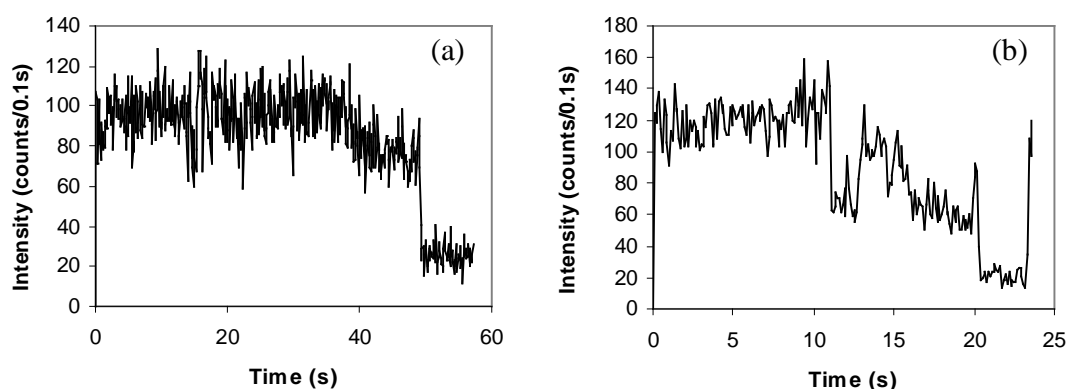


Figure 4.12. Two representative intensity trajectory of single RB molecule on nanoporous ATO film. (a) 106 out of 114 molecules had constant intensity level. (b) 8 out of 114 molecules had partial fluctuation.

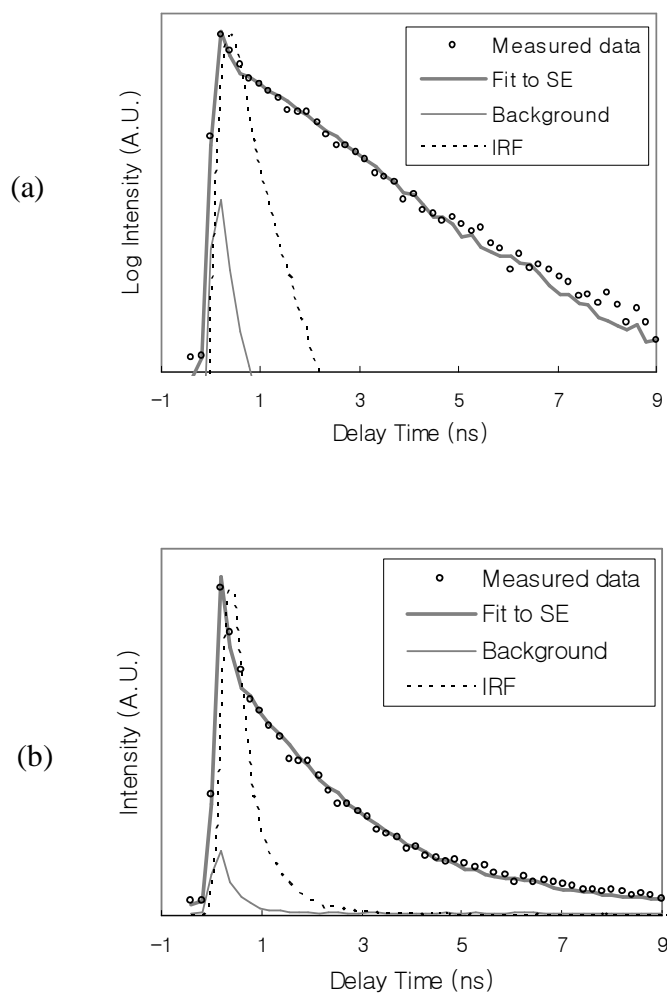


Figure 4.13. Single exponential decay model fitted to the measured single molecule fluorescence decay curves. The hollow dots are measured data. The thick solid line is the calculated signal fitted to the measured data. The thin solid line is the background scattering from ATO film. The dotted line is the instrument response function (FWHM, 400 ps). The calculated signal includes the background scattering with adjustable coefficient. The IRF (wavelength, centered at 560 nm) arrives at detector later than background (~ 800 nm) due to the dispersion of light.

single exponential satisfactorily with lifetime 2.6 ns and reduced chi-square 1.3. Similar single exponential decays were observed for most of single molecules on ATO.

The distribution of 114 SMFLs is shown in Figure 4.14. Also shown for comparison is a typical SMFL distribution of RB on glass surface, which will be shown in Figure 5.6a with detailed discussion. It is clear from the comparison that the average lifetime (2.4 ns) of SMFL of RB on ATO was shorter than on glass (3.4 ns) that was an ET-inactive substrate. The standard deviation of RB on ATO film was 0.64 ns that was bigger than on glass (0.35 ns).

Herein, the optimization step of the search-optimization-record method was not implemented (Section III.A of Chapter 3) but only search-record procedure was used. The search-record method required much higher threshold for stopping search (about half of highest count known from the imaging procedure) than search-optimization-record method (slightly higher than background level). Using the low threshold in the search-record method would have resulted in a low signal to background ratio because the search-record method did not optimize molecule's position to the center of laser focus. The threshold of stopping the search procedure was 1,200 cps in the measurement of SMFL distribution of RB on ATO shown in Figure 4.14. In Figure 4.7a, 1,200 cps was about the half of maximum count. Many weakly emitting molecules were not detected by the high threshold. According to Equations 2.3 and 2.5a, electron transfer reduces the quantum yield of adsorbate. Proportionality of quantum yield to fluorescence lifetime should exist if a lifetime distribution originated from the electron transfer rate distribution. To check the proportionality, the RB single molecules on ATO, of which fluorescence lifetimes constituted the SMFL distribution marked by darker bars in Figure 4.14, were

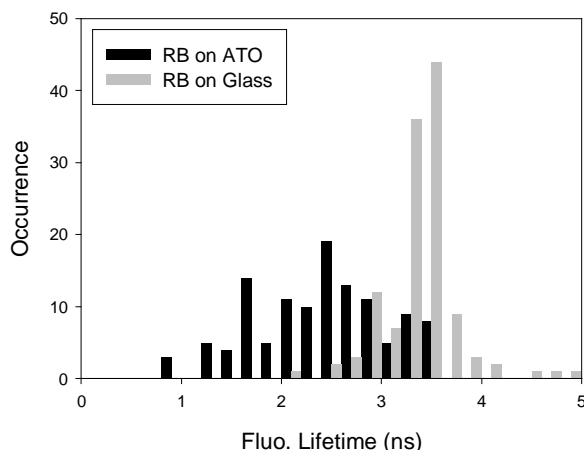


Figure 4.14. Distribution of 114 SMFLs of RB on ATO represented by dark bars ranging from 0.8 ns to 3.6 ns. Also shown for comparison is the distribution of SMFLs of RB on glass, at which no interfacial electron transfer is expected.

classified into five lifetime ranges. Average photon emission power of molecules in each range was calculated and plotted in Figure 4.15. Shorter lifetime range (e.g. 0.5 ~ 1.0ns) does not seem to have low quantum yield compared to longer lifetime range. If a quenching process like the electron transfer was effective, the fluorescence lifetime and the quantum yield had to decrease together. The reason for the absence of relation between lifetime and emission power is that the threshold of the search-stopping procedure was so high that it detected only high quantum yield molecules that might not inject electrons into ATO film. Moreover, the laser focus, which had a gaussian intensity profile across its cross-section, stopped moving on the moment of the fluorescence intensity just being over the threshold; thus, the center of the laser focus was not right above a single molecule but at a random distance from the single molecule, so that the magnitude of recorded emission power was controlled not by the property of the

adsorbates but, trivially, by the distance between the single molecule and the center of focus. Therefore, it was necessary to lower the threshold to detect the low quantum yield molecules that were missed when using the high threshold. And, the optimization procedure ought to be adapted not only to increase the S/B ratio but also to see the dependence of lifetime on the emission power.

Another set of SM test of RB on ATO was performed with a lowered threshold. Ozone purged ATO film on a cover slip was soaked in 7×10^{-9} M RB in MeOH solution for 1 minute (sensitization scheme) and was washed with the same MeOH solvent. Fluorescence images of arbitrary areas of the sample were taken before the Search-Optimization-Record (SOR) procedures. As was explained, the purpose of the

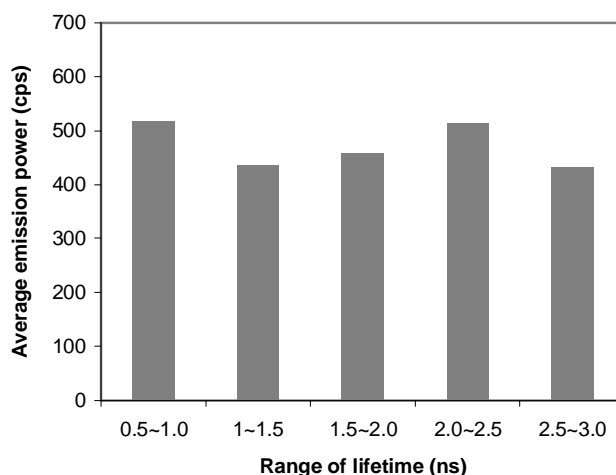


Figure 4.15. Average photon emission power of molecules in various lifetime ranges of the SMFL test of RB on ATO with TH = 1,200 cps. There is no lifetime dependence of emission power. Only single molecules having high fluorescence quantum yield and very low injection yield were detected due to the use of high threshold and lack of optimization procedure.

fluorescence imaging was just to check the status of the sample. The imaging and SOR procedures were performed in two different areas due to the bleaching during the imaging test: the bleaching will obviously change the SMFL distribution especially reducing the occurrence of short lifetime. The SOR procedure collected the SM TCSPC data, which were subsequently converted to the SMFLs. The threshold for stopping the search procedure was 500 cps, which was 2.4 times lower than 1,200 cps used in the high threshold test shown above.

A stage-scanned fluorescence image of the sample is shown in Figure 4.16a together with an image of blank sample in Figure 4.16b. The only difference of the blank sample from the single molecule sample was the absence of RB molecules in the sensitizing solution. The baseline of the graphs in Figure 4.16 was chosen to be 500 cps to clarify the signals at which the search procedure would have stopped: actually, the SOR procedure was done in other fresh areas to avoid the instantaneous bleaching during the imaging procedure. The number of gray-colored intensity peaks of the SM sample and the blank were 105 and 14, respectively. Not all the 105 peaks contributed to their SMFL distribution. About 55% (58 peaks) of the peaks in Figure 4.16a bleached instantaneously (<0.5 s) in the SOR procedure and 45% (47 peaks) of them lived long enough to provide photon counts for the lifetime calculation. The 14 out of 105 peaks should be from impurities if the blank test had been done ideally. It has been routinely observed that a large portion of impurities of the blank sample were bleached very quickly, in about 0.5s. Therefore, assuming that the number of impurity peaks having less than 0.5s duration in Figure 4.16a was 7 (about half of 14), it could be inferred that the contribution of impurities to the SMFL test was 7 out of 47. The number 7 may or may

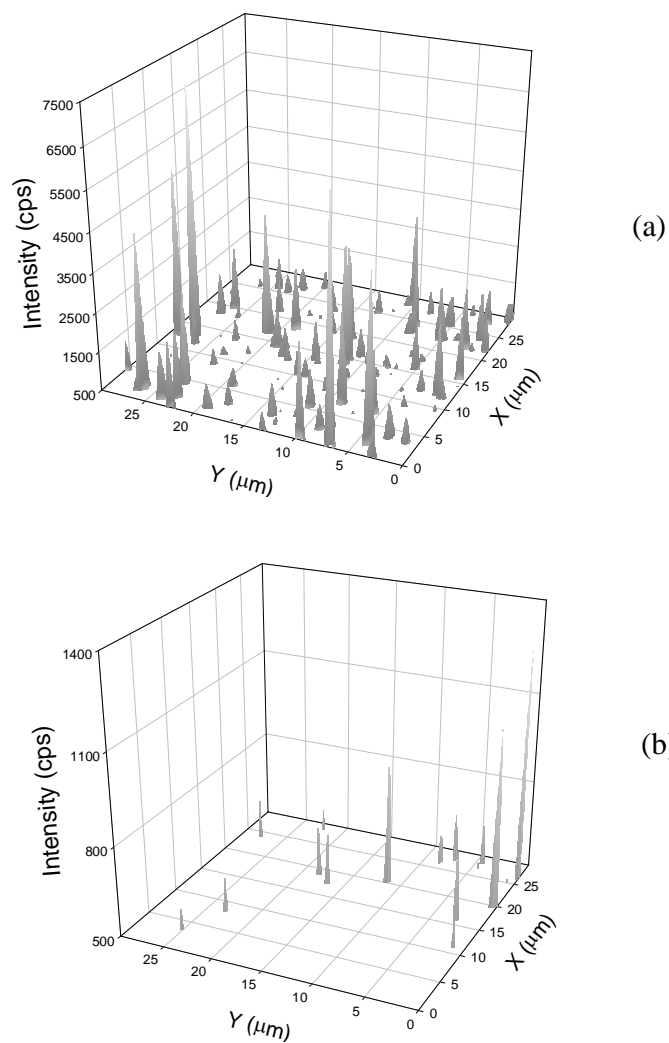


Figure 4.16. Stage-scanned two-photon fluorescence image of single RB molecules on ATO. Excitation wavelength and power were 800nm and 0.16 MW/cm^2 respectively. $30 \times 30 \mu\text{m}^2$ area (150 pixels by 150 pixels) was stage-scanned. The baseline of both graphs was 500 cps. (a) sample fluorescence image with 105 spots over the baseline. (b) blank fluorescence image with 14 spots over the baseline. The SOR procedure in the next step used the lowest possible threshold 500 cps to sample the molecules of fast lifetime that were missed in the high threshold test shown in Figure 4.14 through 4.15.

not be considered to be large. It has been measured and is believed that the lifetime distribution of the impurities is broad and that the existence of impurities would not change the overall shape of SMFL distribution.

Figure 4.17 shows the intensity trajectories, similar to the one in Figure 4.7a, along the scanned positions of the SM and blank sample shown in Figure 4.16. Figure 4.17 is just a different format of the fluorescence intensity plots of Figure 4.16. The threshold 500 cps slightly touched the highest background intensity in both samples showing that it was the lowest possible value.

The distribution of 78 SMFLs sampled with 500 cps threshold is shown in Figure 4.18 together with the distributions in Figure 4.14. The average of the new distribution is certainly shifted to shorter lifetime (0.7 ns) by choosing the low threshold. It is apparent how much the high threshold (1,200 cps) suppressed the population of short lifetime by comparing the distributions represented by the black and gray bars. The question is whether the black and gray distributions were different just by using different threshold or by their different origins. In Figure 4.15, it was suggested that there was not extra quenching pathway for molecules of shorter lifetimes. In the same way, a plot of average photon emission power of molecules in various lifetime ranges of the low threshold experiment is drawn in Figure 4.19. The average emission power of molecules having lifetimes in the range from 0 to 0.3 ns is less than 50% of that of longer lifetime ranges contrary to the independence of the emission power to the SMFL when using high threshold in Figure 4.15. It implies that the excited state of the molecules was quenched by electron transfer process. Other non-radiative decays and intersystem crossing could also influence both the quantum yield and lifetime. However, transient IR absorption

spectroscopy has confirmed the electron injection from RB into ATO nanoporous film in about 5 ps, which predicted that the distribution in Figure 4.18 should decrease sharply from the first bar (0~200 ps) when the sampling of SM experiment could be done ideally.

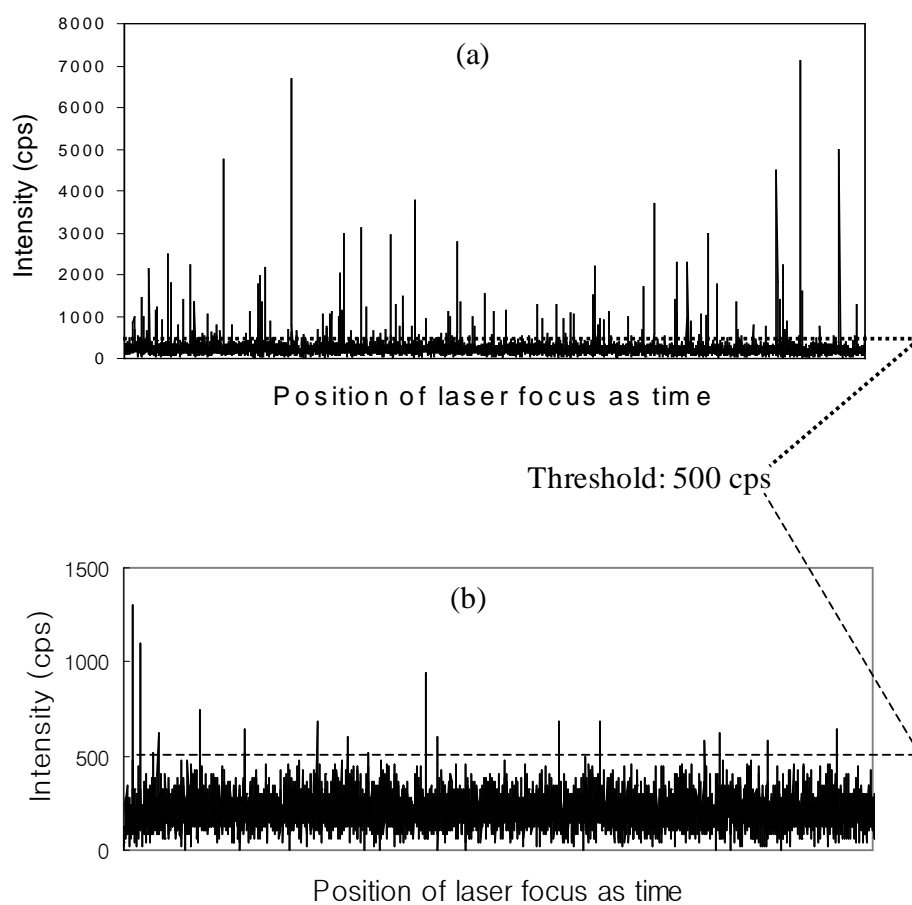


Figure 4.17. Intensity trajectory along the laser-scanned positions of the test in Figure 4.16 for (a) sample and (b) blank. Two or three peaks resulted from a molecule because the size of the laser focus was bigger than the size of pixel and passed through the molecule several times. 500 cps was slightly higher than the higher level of background noise.

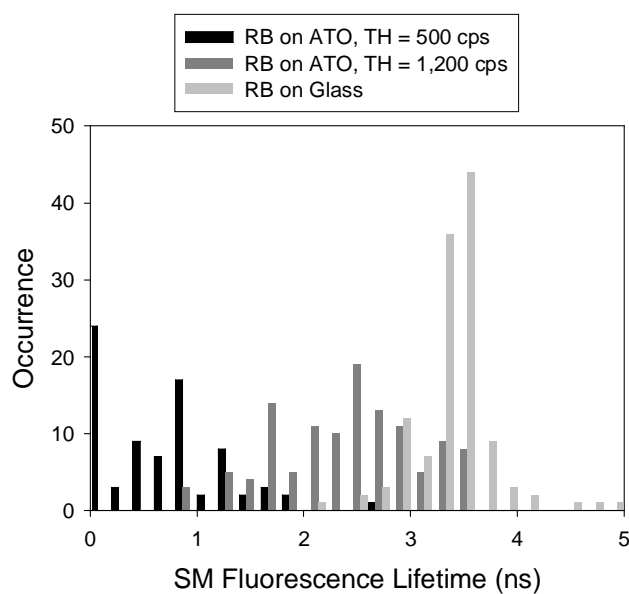


Figure 4.18. SMFL distribution of three different samples: black bar, RB on ATO sampled with TH = 500 cps; gray bar, RB on ATO sampled with TH = 1,200 cps; pale gray bar, RB on glass surface.

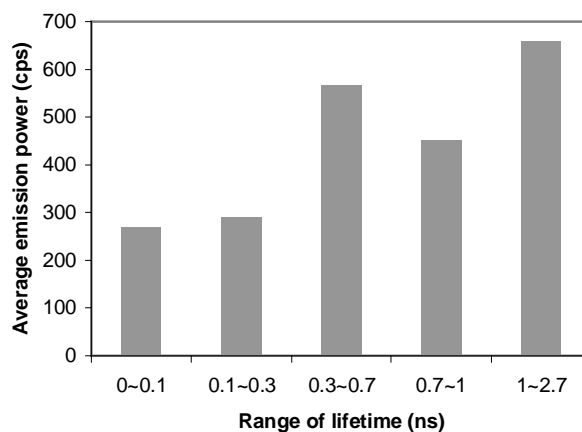


Figure 4.19. Average photon emission power of molecules in various lifetime ranges of the SMFL test of RB on ATO with TH = 500 cps.

On both the ATO and glass, RB would have negligible non-radiative decay yield and intersystem crossing yield. Therefore, the large differences in the distributions are ascribed to the interfacial electron transfer. The detailed interpretation on the SMFL distribution will be presented in the Discussion sections.

II.C.2. SMFL of RB on ZrO₂

The nanoporous ZrO₂ film has similar refractive index ~ 2.1 for the wavelength of fluorescence of RB⁶⁹ to ATO (~ 2) and morphology to the nanoporous ATO, which makes the ZrO₂ an effective reference substrate for nanoporous ATO film. The single molecule test of RB deposited on the nanocrystalline ZrO₂ film has been performed in the same method as the previously described RB on ATO: film preparation-ozone cleaning-sensitization-imaging-SOR procedure with low threshold. The ZrO₂ was chosen as a non-interacting (ET-inactive) blank sample. A nanoporous ZrO₂ film was soaked in 7×10^{-10} M RB solution in MeOH for 1 min and washed with 5 ml of MeOH. The two-photon excitation was done with the pulsed 800 nm laser of 0.16 MW/cm^2 intensity. Figure 4.20 is a resultant distribution of the SMFLs of the RB on ZrO₂ (gray bars) compared with that of RB on ATO already shown in Figure 4.18. The average and standard deviation of the SMFL distribution of RB on ZrO₂ were 3.0 ns and 0.78 ns, respectively. The two distributions are clearly separated because the electron injection into the conduction band of ZrO₂ is not energetically allowed.

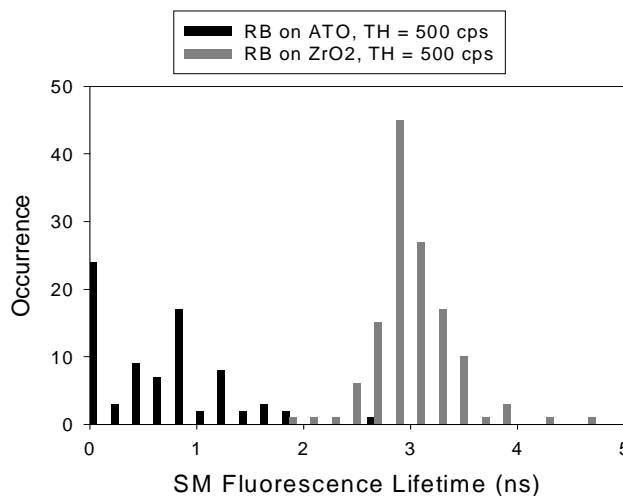


Figure 4.20. Distribution of 129 SMFLs of RB on ZrO₂ (gray bars). Also shown for comparison is the distribution of SMFLs of RB on glass (black bars). Both tests were done with low (500 cps) threshold.

III. Discussion

III.A. Fluorescence Lifetime of RB on ATO

III.A.1. General Description

The fluorescence decay curve of many RB molecules on the 10 μm by 10 μm area of ATO nanoporous film was measured in Section II.A. It was certain that the bulk decay was fitted not to the single exponential ($\chi^2_r = 11.9$) but to the double exponential satisfactorily ($\chi^2_r = 1.1$). The fast and slow components of bulk fluorescence decay were 0.7 ns (74%) and 2.0 ns (26%). Both components were clearly shorter than typical lifetime $\sim 3\text{ns}$ measured in both the bulk and single molecule RB on ZrO₂ which were believed to be an ET-inactive references. As we shall see in the later sections, the lifetime of RB on ATO is governed by a combination of electron transfer and dielectric property

of surrounding medium. The decay dynamics of the bulk fluorescence, however, should have a broad and continuous distribution of single exponential decay components. The number of single exponential decay components of a fitting model was a matter of representation. Fitting of more than three components was not helpful: it did not converge easily and its accuracy was doubtful. The individual components constituting the bulk decay was foreseen to be single exponential because (1) the Franck-Condon excited state may relax to one fluorescent excited state evidenced by the emission spectrum in Figure 4.11 (thick line) that does not have multiple peaks⁴⁰ and (2) constant lifetime has been observed for most of single RBs on ATO: the relaxation into the multiple fluorescent excited states and time-varying lifetime of single exponential decay result in multi-component fluorescence decay.

Comparing the SMFL distributions of RB on ATO measured by the high and low thresholds shown in Figure 4.18 with the bulk result in Section II.A, we could connect the populations lower than 1 ns and around 2.5 ns to the fast and slow components of bulk decay, respectively. It was mentioned that ET governed the lifetime distribution lower than 1 ns and did not work in the distribution over 0.8 ns in Section II.C.1. The existence of the significant amount of ET-inactive RB on TiO₂ nanocrystalline film has been observed in previous work⁷⁰. The authors showed that the incident photon to current efficiency (IPCE) of RB and N3 [Ru(dcbpy)₂(NCS)₂ dcbpy=(4,4'-dicarboxy-2,2'-bipyridine)] on nanocrystalline TiO₂ film were 8% and 75%, respectively. It was not surprising to observe the inactive RB dyes on ATO because the energetics and morphology of the systems are similar. Takeshita et al.⁷⁰ suggested that the origin of the inactive dyes was site heterogeneity^{71,72} or aggregate formation⁷³. It has been known that

thiazine, oxazine, and R6G dyes forms H-aggregate on nanocrystalline SnO₂ surface^{74,75}; and RB forms both H- and J-aggregate in silica matrix prepared by sol-gel process^{76,77}. The H-aggregate is non-fluorescent and usually has low (~1% IPCE⁷⁵) injection efficiency; and J-aggregate is fluorescent but injection efficiency of RB on semiconductor film is not known to my knowledge^{53,54}. In brief, if the J-aggregate of RB had particularly low injection rate than other monomers around it, though it does not have a background, the distribution measured with the high threshold could have been assigned to J-aggregates of RB. However, the concentration of dye solution in sensitizing nanocrystalline oxide films in above previous studies^{70,74,75} were in the range 10⁻⁴ ~ 10⁻⁵ M. On the contrary, the concentration of RB solution used in our SMD with high threshold was 5×10⁻¹¹ M, which was about five orders lower than the previous bulk study, 10⁻⁴ ~ 10⁻⁵ M. The aggregate formation has been considered to be unlikely in such a low concentration^{57,75,76} because the factor of decrease of dimer is the square of that of monomer. Therefore, the molecules comprising the distribution sampled with the high threshold had the electron transfer rate much slower than their fluorescence lifetime to be called inactive dyes. The inactivity may come from the negligible electronic coupling due to the following possible phenomena. (1) Amplitude at the diethylamino group of π* orbital of RB is so low because of the charge-transfer characteristics of electronic excitation from the diethylamino group to xanthene ring. RB is considered to anchor on the negatively charge ATO nanocrystalline surface by strong electrostatic attraction⁷⁴ with the diethylamino groups which have net positive charge in resonance structures as will be described in Section II.A in Chapter 5. The electronic coupling decays by 1/e factor for every 0.4 ~ 1 Å increase of acceptor- donor distance^{2,4,71,78}. (2) The site of a

single RB happened to be a small anomalously thick insulating domain or a defect site. A new description of the origin of the wide distribution around 2.5 ns will be presented later in Section III.A.3 based on the notion that those RB molecules constituting the distribution were inactive in ET. Otherwise, the measured nanosecond time scale SM injection rates might have to be ascribed to the coupling of excited state of RB with discrete or low-density defect states. However, this possibility contradicts to the direct proportionality of quenched fluorescence lifetime with quantum yield in Equation 2.5a.

The distribution measured with the low threshold also does not seem to have the contribution of aggregate. The concentration of sensitizing solution used in the low threshold measurement was 7×10^{-9} M. The concentration of RB dimer in the solution was about 7×10^{-14} M because the dissociation constant of RB dimer in water is 6.8×10^{-4} M⁷⁹, even though MeOH was solvent in this study, and has twice higher solubility for RB than water⁸⁰. Therefore, the five order difference in the monomer and dimer populations allows us to neglect the dimer formation in the sample. In conclusion, the two distributions were of single molecules; one was composed of very slowly electron injecting or inactive molecules, and the other was of the electron injecting molecules.

The proportionality between the lifetime and emission power in Figure 4.19 does not sufficiently explain the existence of ET in the SMFL distribution (black bars) in Figure 4.18. The reason is that there are generally other non-radiative decay channels, and there could be the lifetime-emission power proportionality resulting from a broad non-radiative decay distribution. It is considered that the non-radiative decay could be neglected with respect to the following argument.

The interesting property of RB is that its quantum yield is highly influenced by

the polarity, rigidity, and concentration of medium³⁸⁻⁴³. The concentration dependence is just a matter of dimer formation, so it is not considered here. pH is another source of quantum yield variation because acid or base (zwitterionic) forms have different quantum yield of RB⁸¹⁻⁸³. However, as stated in Section II.A in Chapter 5, the base form is dominant in neutral solutions, and the pH dependence is also not considered, too. Other variables that influence on the change of quantum yield are often related with the formation of twisted intramolecular charge-transfer (TICT) excited state. The TICT state is a result of stabilization of twisted excited state of RB after the charge-transfer transition. The 90° twisted diethylamino group with respect to the xanthene ring is favored in polar solvent, and the rotation of the diethylamino group is in picosecond timescale. The twisted form relaxes to S₀ state non-radiatively. Therefore, the better the TICT state forms, the faster the non-radiative decay is. The quantum yield of RB in common protic solvents ranges from 0.3 to 0.7 in room temperature³⁹. The various quantum yields are due to the large differences in non-radiative decay rates with similar radiative decay rates; the non-radiative decay rate may depend on the viscosity and polarity of solvents in terms of the stabilization and formation of TICT state^{40-42,84}. The radiative and non-radiative decay rates of RB in water and methanol are listed in Table 4.1 as an example³⁹. The radiative decay rates in both solvents is about 2×10^8 (s⁻¹), but the non-radiative decay rates are different twice times. The quantum yield of RB in a solvent is also dependent on the temperature^{42,85,86} because the viscosity of the solvent determines quantum yield effectively^{39,42}. It has been known that the quantum yield approaches 1 as the viscosity of medium increases⁴². The polarity is important in that the TICT state of RB is not stabilized and quantum yield should be high in a non-polar

	$k_r \times 10^8 \text{ (s}^{-1}\text{)}$	$k_{nr} \times 10^8 \text{ (s}^{-1}\text{)}$	Quantum Yield
H ₂ O	1.9	4.0	0.32
MeOH	2.2	2.0	0.53

Table 4.1. Quantum yields of RB in Water and Methanol. The different non-radiative decay rates are responsible for the different quantum yields.

medium^{39,87}. In conclusion, the RB single molecules adsorbed on solid substrate-air interface are very likely to have quantum yield close to 1. The relatively wide distribution around 2.5 ns is, therefore, not due to non-radiative decay rate distribution because it is too slow to compete with radiative decay. What we have come to know is that the measured fluorescence lifetime is equivalent to the radiative lifetime of RB on the substrates ATO and glass that we have used, when we sample strongly emitting molecules by a high threshold.

III.A.2. Features of the Electron Transfer Observation in Single Molecule Level

The SMFL distribution below 1 ns in Figure 4.18 reflects the lifetime reduction due to electron transfer, but it is not complete. Majority of molecules injected electron in picosecond timescale, and the nanosecond time scale fluorescence decay could not compete with the ET rate. As a result, significant portion of the single molecules were not sampled, and the occurrences of the shorter SMFLs in Figure 4.18 were less than it should be in reality. Fluorescence intensity of single molecule with varying ET rate is plotted in Figure 4.21. The thin solid line is the fluorescence intensity vs. ET rate curve.

The thick solid line is a part of the thin line where the ET rate is less than 0.1 ns. The fluorescence intensities of the molecules with ET rate less than 0.1 ns were much less than the background level and those molecules could not be sampled with the threshold 500 cps (black bar). Assuming that the majority of molecules had ET rate less than 0.1 ns, the distribution measured with 500 cps threshold in Figure 4.18 was of only single molecules having very slow ET rates, and was just a wing of its true distribution. The arrow in Figure 4.21 marks the shortest lifetime in the distribution measured by 500 cps threshold in Figure 4.18. The lower the threshold of sampling was, the arrow would shift to shorter lifetime. But, using the low threshold was limited due to the fluctuation of background signal that could reach frequently up to 500 cps (Figure 4.17b). The ET rate

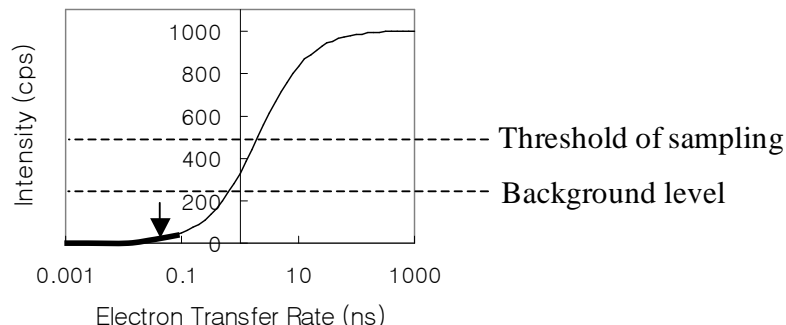


Figure 4.21. Fluorescence intensity of single molecule with varying ET rate. Maximum intensity when the ET rate is infinite is set to 1000 cps. Background level is about 250 cps. Thin solid line is the intensity vs. ET rate curve. Thick solid line is the range of fluorescence intensity with the competing ET rate less than 0.1 ns. The arrow pointing at 0.05 ns represents the shortest lifetime of the distribution measured with 500 cps threshold in Figure 4.18.

distribution calculated from the measured lifetime distribution (Figure 4.18, black bars) is shown in Figure 4.22 according to Equation 2.4 in Chapter 2. The fluorescence lifetime of non-interacting system τ_f in Equation 2.4 is assumed to be 2.5 ns that is the center of the distribution measured with high threshold 1200 cps. The molecules from the second bar centered at 0.5 ns may be the group of most slowly injecting molecules in the whole population. The molecules in the first bar have so called the ultrafast electron injection process. The shortest ET lifetime in the first bar was 50 ps, which is still a long lifetime compared to the transient IR absorption experiment that had showed several ps injection time.

The weak emission of RB due to ET was not the only reason for missing the majority of molecules in SMD. Significant number of single molecules were missed by bleaching fast during the illumination. The evidence of the fast bleaching is that it has been routinely observed that the fluorescence intensity at a spot of a bulk sample on ATO dropped to 1/e intensity in a couple of second while the fluorescence intensity on glass did not change noticeably for minutes. The bleach resulted from the irreversible transport of injected electron through the ohmic contacts that existed at every pair of adjacent nanoparticles (see Figure 3.2). In fact, the decay of intensity due to the bleaching was fitted well to the time-dependent concentration decay of matter (here, electron on surface) following the diffusion kinetics. The notion of the quenching and the bleaching was confirmed by comparing the number of bright molecules in the samples having the same number densities of RB molecules on glass and on ATO, as shown in Figure 4.23. Same concentration (0.1 nM) and same volume (30 μL) of RB solution in MeOH was dropped on glass and ATO. 22 $\mu\text{m} \times 22 \mu\text{m}$ area of each sample was wide-field illuminated by

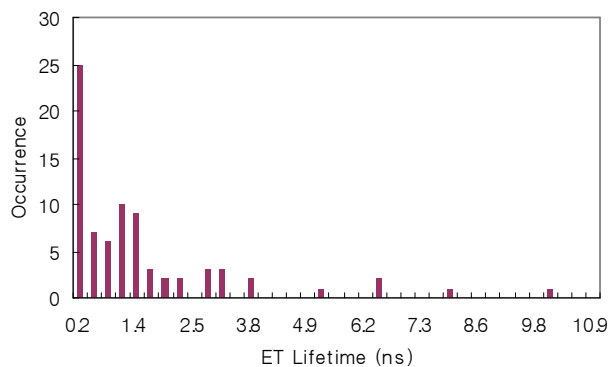


Figure 4.22. ET characteristic lifetime distribution in the SMFL experiment of RB on ATO with low threshold 500 cps shown in Figure 4.18. The shortest SM ET lifetime was 51 ps.

defocusing the excitation laser. CCD images of two samples were taken. Hundreds of molecules were visible in RB on glass sample, while there were less than twenty molecules on ATO. The intensity of molecules on glass is about 3 times higher than on ATO. Majority of RB molecules on ATO were not visible because they emitted photons so weakly for ET or were oxidized for a long time by the diffusion of electron from adsorption sites into the bulk region of the film. The bleaching effect should be much less in the stage-scanning detection with focused laser (normal method of SMFL test) than in the CCD detection. In the stage-scanning detection, all the pixels had been fresh before illumination and recording started on the moment of illumination; but the CCD image was taken after about ten seconds of focusing, during which significant number of RB molecules were bleached. Measurement time on each pixel in the stage-scan imaging were 80 ms (TCSPC data acquisition time was 50 ms, and 30 ms is for stabilization of stage, program execution, etc.), which is not long time for significant bleaching. However,

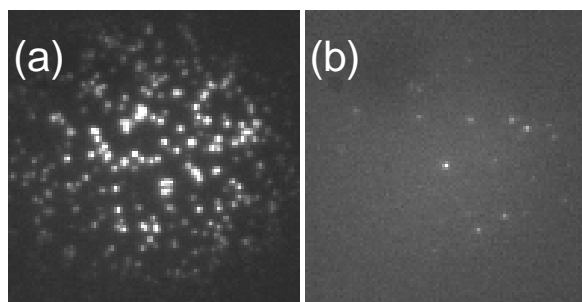


Figure 4.23. Fluorescence image of RB on a) glass and b) an AT0 thin film acquired with CCD detector. Both images were taken by wide-field illumination at 532 nm. The number of bright RB molecules on AT0 is much smaller than that on glass despite similar number of molecules in both samples. The lower number density of (b) is attributed to the quenching by fast electron transfer and the bleaching due to the diffusion of injected electron.

bleaching could have gone far in the 80 ms depending on material.

Since both the chronological and delay times for each photon were recorded, we have also analyzed the fluctuation of lifetime. At first, the whole TCSPC data were divided into a series of pieces of 1 ~ 2 second duration, which was the minimum time range of TCSPC data that could be converted to a decay curve of each piece. No single RB molecules exhibited clear change of lifetime along the series of TCSPC data pieces. Sometimes SMFL seemed to change appreciably after a long dark state or sudden change of intensity. But no change has been observed during the interval of one block of data with constant intensity. Next, we needed to reduce the duration of TCSPC data pieces to check any lifetime fluctuation in faster time scale than second; it could not, however, be done for short of the data amount for the lifetime calculation in any shorter duration.

Instead, the average decay curves of high and low intensity times of a trajectory drawn in a unit time were constructed and the two lifetimes were compared; there should be a lifetime fluctuation in the unit time scale if they were different to each other. A whole SM trajectory was drawn with 5 ~ 10 ms unit time, and a criterion level (6 counts/5ms) was set at about the half of the peak intensity as shown in Figure 4.24. Two decay curves were constructed by gathering the TCSPC data pieces during the time above and below the criterion level, and their lifetimes were calculated. As a result, in all the SMD trajectories, the two decays did not have noticeable difference in lifetime, and both were single exponential. It means that the heterogeneities of electron transfer and radiative lifetime dispersion were static in nature, in agreement with the finding of the previous study of Cresyl Violet on ITO (Sn:In₂O₃)²⁴.

It is interesting to note that the measured SMFLs in the current as well as the previous studies^{24,26} of single molecule interfacial ET are inconsistent with the much faster electron transfer rate measured by ensemble average approaches. In the previous

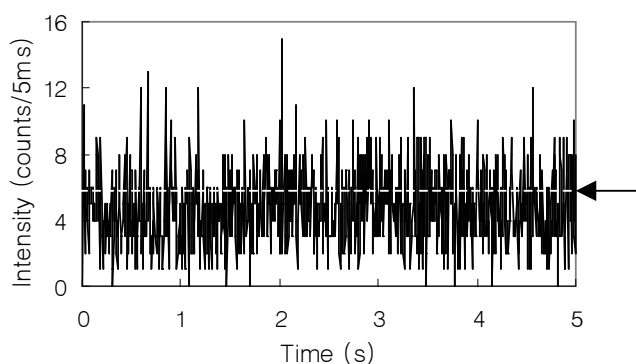


Figure 4.24. Intensity trajectory drawn in 5 ms unit time. The dashed line is a criterion level (6 counts/5ms) for classifying its TCSPC data pieces into high intensity and low intensity groups. Two decay curves were constructed from the two groups.

study of single molecule transfer in coumarin 343 and cresyl violet sensitized TiO₂ nanoparticle, fluorescence lifetimes on the nanosecond timescale was also observed, and the intensity trajectories showed large fluctuations that were not observed for the same molecules on glass, an non-electron acceptor. To account for the reported fast ensemble-averaged electron injection rate from C343 to TiO₂, and pronounced intensity fluctuation, the authors suggested that the molecules underwent significant fluctuation in their redox activity, changing between fast and slow injection states. According to this model, in the fast injecting states, the injection rate was so fast that fluorescence quantum yield was too low to be observed and single molecule fluorescence measurement only captures the molecules in the slow injection states.

Here, we suggest an additional mechanism that is responsible for the apparent long single molecule lifetimes of RB on ATO. We suggest that our single molecule measurement selectively probes slowly injecting portion of the total population. This notion is confirmed by comparing the number of bright molecules in samples containing the same number density of RB molecules on glass and on ATO, as shown in Figure 4.23. For RB on ATO, the majority of molecules undergo fast injection, emitting too few photons to be observed. This model differs from that of Biju et al²⁶, although it is possible that both mechanisms can be present simultaneously.

III.A.3. Origin of Radiative Lifetime Dispersion

The SMFL distribution below 1 ns was assigned to the lifetime dispersion because of the electron transfer. The features of the observations were discussed in Section III.A.2. It was reasoned that the other SMFL distribution over 0.8 ns was influenced by neither ET

nor non-radiative decay lifetime in Section III.A.1. Then, the origin of the factor that governed the spatially heterogeneous SMFL distribution is in question. Triplet state lifetime is usually broadened by spatial heterogeneity^{40,88}; however, the triplet lifetime of RB is 1.6 μs in alcohol³⁶ and even slower on dry surface than in solution⁸⁹. It could be separated almost completely from the nanosecond time scale dynamics. Moreover, the triplet yield of RB was reported to be only 0.006³⁶. Therefore, the only channel left for the decay from S_1 to S_0 is the radiative transition. In other words, the measured single molecule fluorescence lifetimes in the distribution over 0.8 ns were the single molecule radiative lifetimes.

According to Section III.A in Chapter 2, the radiative lifetime depends on the refractive index of surrounding medium by local field correction. We can estimate the radiative lifetime in a particular medium if we know the refractive index of the medium. The refractive index of ATO is about 2, but it cannot be used in applying the local field correction. The RB molecules were not embedded in a large bulk ATO crystal medium, but they were adsorbed on the surface of sub-wavelength scale ATO particles that formed intricate structure as shown in Figure 3.2a in Chapter 3. The nanoporous ATO film is a heterogeneous mixture of the two constituents: nano-granule ATO crystal and air. The dielectric property of the composite medium is a sort of spatial average of the two constituents. In order to apply the local field correction properly, the effective medium approximation (EMA) is necessary. There are several expressions for the EMA^{46,90}. Lorentz-Lorenz effective medium expression is a result of the simple arithmetic averaging of polarizabilities of individual constituents corrected by the virtual-cavity local field correction (Equation 2.10 in Chapter 2). Maxwell Garnett effective-medium

expression takes into account of the dimension of each constituent, which is comparable with the wavelength of electric field; and they found an expression of EMA by applying empty-cavity local field correction:

$$\frac{\varepsilon - \varepsilon_b}{\varepsilon + 2\varepsilon_b} = f_a \frac{\varepsilon_a - \varepsilon_b}{\varepsilon_a + 2\varepsilon_b} \quad (4.5)$$

where ε is the effective dielectric constant, and ε_a and ε_b are dielectric constants of the component a and b in pure form, respectively. f_a is a filling factor with the component b being considered as surrounding medium. Bruggeman suggested another expression choosing the effective medium as surrounding medium of itself^{90,91}:

$$0 = f_a \frac{\varepsilon_a - \varepsilon}{\varepsilon_a + 2\varepsilon} + (1 - f_a) \frac{\varepsilon_b - \varepsilon}{\varepsilon_b + 2\varepsilon} \quad (4.6)$$

Some people use just an average of pure dielectric constants for a polymer matrix with fluctuating free volume⁴⁶:

$$\varepsilon = (1 - f_{pol})\varepsilon_{vac} + f_{pol}\varepsilon_{pol} \quad (4.7)$$

where ε_{pol} and ε_{vac} are the dielectric constants of polymer and vacuum respectively. f_{pol} is the filling factor of the polymer. The dielectric constant curves of three EMA models are drawn in Figure 4.25 as the functions of the filling factor of ATO nanoparticle using Equation 4.5, 4.6, and 4.7.

The Maxwell Garnett expression is suitable for a configuration that the phase a is spherical and completely surrounded by the medium phase b , separate-grain structure^{90,92}.

In the Bruggeman theory, the two constituents are mixed randomly forming aggregate structure^{90,92}. Both theories explain the effective optical property of particles of practically interesting size 3 nm ~ 30 nm. The Bruggeman EMA can be applied over the whole range of filling factor while the filling factor of Maxwell Garnett EMA is limited to less than 0.7⁹². The Bruggeman EMA is more appropriate in applying to the experimental results of nanoporous film, because the structure of the nanoporous film is basically a random aggregate and its filling factor can be close to 1. It has been applied to the studies of electrical and optical properties of ATO nanoporous film^{33,91}. Other studies on gold nanoparticle⁹³ and the SMFL fluctuation of organic dye in polymer matrix⁴⁶ also have been done. By the way, the difference between the curves of Maxwell Garnett and Bruggeman theories in Figure 4.25 may not be significant with respect to other error sources such as screening effect⁹⁰, possible singularity resulting from the dye's position

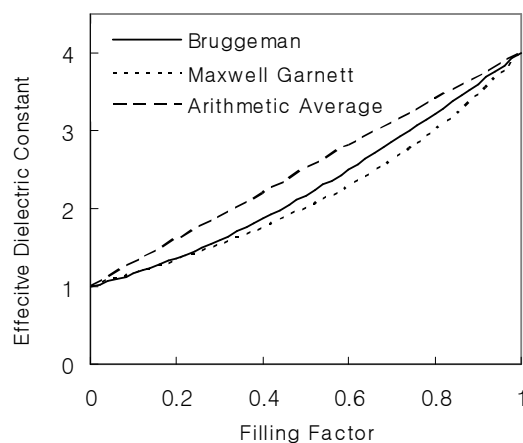


Figure 4.25. Three EMA models represented by dielectric constant as a function of filling factor of ATO nanoparticle. Solid line, Bruggeman model; dotted line, Maxwell Garnett model; dashed line, Arithmetic average.

on ATO nanocrystal surface.

Here are important hypotheses advanced: (1) the radiative lifetime of RB changes depending on the refractive index of surrounding medium according to the local field correction. (2) Single RB molecule feels the local effective refractive index of the nanoporous ATO film. (3) The effective refractive index is directly used in calculating the radiative lifetime of RB following the local field correction. We could expect that RB single molecules on ATO may have fluorescence lifetimes or radiative decay lifetimes that are distributed to a certain degree due to the inhomogeneous filling factor within the film. To find the expected lifetime distribution we need to know the radiative lifetime in vacuum to apply the local field correction. The radiative lifetime in vacuum is calculated in turn by the local field correction of a measured radiative lifetime in a medium of known refractive index. Following the line of method above, we chose EtOH as the medium of known refractive index and calculated the radiative lifetime of RB using Equation 2.7 substituted with the absorption and emission spectra. The refractive index of EtOH, 1.3611⁹⁴ (measured by 598 nm at 20 °C), was substituted in the equation. The calculated radiative decay lifetime of RB in EtOH was 4.23 ns. There is a kind of consistency in the calculated value and photophysical properties of RB and rhodamine 101 (R101). As shown in Figure 4.26, the structure of R101 is the same as RB except for the two julolidyl rings instead of diethyl groups of RB, so that the TICT state does not form in polar solvents such as EtOH and MeOH. R101 really have quantum yield ~1 in EtOH⁴² and MeOH^{95,96}. Fluorescence lifetime of R101 (base form in water) was measured to be 4.27 ns, and the reported values are 4.32 ± 0.1 ns (base form in water)³⁸, 4.46 ± 0.1 ns (base form in EtOH)³⁸, and 4.25 ± 0.2 (acid form in EtOH)⁹⁷. It looks quite

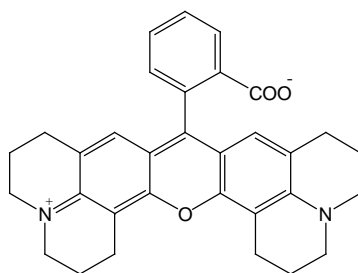


Figure 4.26. Chemical Structure of rhodamine 101. Julolidyl rings prevent the free rotation of amino groups that is responsible for the formation of TICT state in RB.

true that the R101 is an analog of RB that has negligible yield of non-radiative decay in a non-polar or rigid medium. The calculated radiative decay lifetime of RB in EtOH, 4.23 ns, would be reliable to use for further analysis. Cross-checking with another method based on Equation 2.5a would have been helpful.

The three theoretical models in Equation 2.9, 2.10, and 2.11 are applied to the calculation of the radiative lifetime of RB in vacuum using the value in EtOH, 4.23 ns. The radiative decay lifetimes in vacuum were 8.03, 9.50, and 5.43 ns calculated from the empty-cavity, virtual-cavity, and fully microscopic model, respectively. The value from the fully microscopic model is particularly different from the other two values. The three models were compared with a specially designed experiment⁵¹ and were introduced in Section III.A in Chapter 2. In that experiment, the fully microscopic model showed most successful fit to measured data. In this section, we will check the three models once more using the reported data. Figure 4.27 shows the measured fluorescence lifetime data of R101 (base form) in various alcohol solutions reported by Magde et al.³⁸ and best fits of the three models to the measured data. Because the quantum yield of R101 must be ~ 1 ,

we can take the fluorescence lifetime in Y axis as the radiative lifetime of R101 or RB. The fully microscopic model predicts the dependence of radiative lifetime on the refractive index of solvent best again. However, the R101 was surrounded by the polar solvent molecules directly, so it is not known what electrostatic effects interfered with the refractive index dependence of the radiative lifetime. Therefore, the virtual- and empty-cavity model will still be considered. Finally, we show how the filling factor determines the radiative lifetime based on the previous discussion. Three radiative lifetime vs. filling factor curves are drawn in Figure 4.28. The radiative lifetime is a functional of effective refractive index, which is, in turn, a function of the filling factor. The Bruggeman model for effective refractive index is combined with the three local field correction models in Section III.A of Chapter 2. The gray area represents the span of the measured radiative

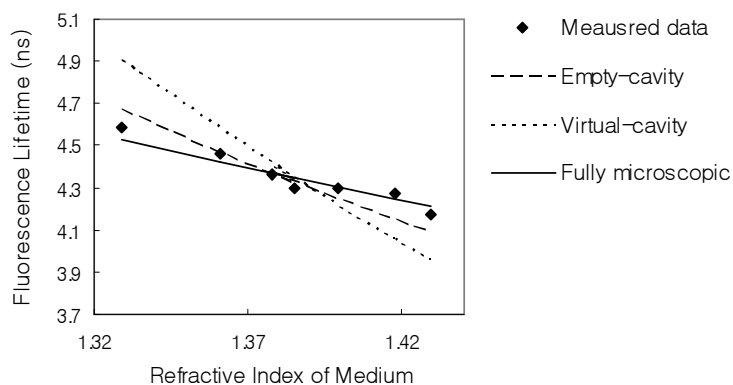


Figure 4.27. Three local field correction models fitted to experimental data published by Magde et al.³⁸. Dots are measured data of R101 (base form) dissolved in MeOH (1.3288), EtOH (1.3611), *i*-Propanol (1.3776), *n*-Propanol (1.3850), *n*-Butanol (1.3992), *n*-Hexanol (1.4178), and *n*-Octanol (1.4293) – the values in the parentheses are refractive indices. The fully microscopic theory fits to the measured data best.

lifetime distribution shown in Figure 4.14 marked by black bars (0.8 ns ~ 3.6 ns). Both the curves of empty-cavity and fully microscopic model could not reach 0.8 ns, the experimentally observed minimum lifetime. The virtual-cavity model can cover almost the full range of the experimental distribution. It is not known for a certainty why the virtual-cavity model alone fits to the experimental result. We could doubt that the lower limit of the expression in Equation 2.10 might just happen to reach the lowest lifetime and that the mechanism of observed dispersion was different from that of virtual-cavity model. It may rather be better to think that the fully microscopic model was distorted by other reasons. There are three explanations: (1) very slow electron transfer longer than 1

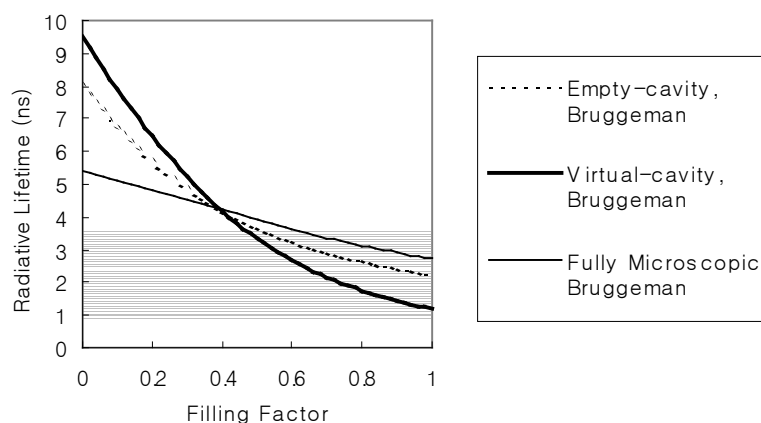


Figure 4.28. Plot of radiative lifetime as a function of filling factor based on three combinations of effective medium approximation and local field correction. Dotted line, empty-cavity and Bruggeman model; Thick solid line, virtual-cavity and Bruggeman model; thin solid line, fully microscopic and Bruggeman model. The gray area represents the span of measured radiative lifetime distribution shown in Figure 4.14 marked by black bars (0.8 ns ~ 3.6 ns).

ns worked. (2) electron transfer from electron-filled trap states to the unpaired HOMO of RB during its excited state. The back ET process was confirmed to exist with bi-exponential model (0.1 ns and 2 ns) by Guo et al³³. The n-doped ATO is ready to transfer electron. If the typical picosecond time scale ET does not work, the back electron transfer could quench the excited state of RB. (3) quenching by surface plasmon (to be discussed later in this section). All three mechanisms give rise to the proportionality in the relation of emission power and lifetime. Therefore, if any one of the three quenching mechanisms was true, the proportionality actually existed and the Figure 4.15 could not reveal it. The range of SMFL distribution of RB on ZrO₂ was from 1.8 ns to 4.7 ns. The ZrO₂ is considered as an ET-inactive reference substrate for RB on ATO. Therefore, the idea of the distortion of fully microscopic model by a quenching mechanism is supported by the SMFL distribution of RB on ZrO₂.

We assume that the true radiative lifetime vs. filling factor curve was not very different from the three curves in Figure 4.28. Then, the filling factor estimated from the experimental lifetime distribution ranged from 0.5 to 1. Typical filling factor of nanoporous film is about 0.2^{33,49,91}. Average filling factor estimated here is ~ 0.63. For the average filling factor to be 0.2, the average SMFL has to be higher than 5 ns. This inconsistency bears contemplation as follows. The effective refractive index was spatially inhomogeneous depending on the concentration of ATO nanoparticle, and the RB adsorbates felt the inhomogeneous effective refractive index. Accordingly, the local field correction of the radiative lifetime of RB depends on its local effective refractive index. The ATO nanoporous film is divided into the void inter-particle space and the filled aggregates space, which is represented schematically in Figure 4.29 on a real AFM image.

If we think only top layer, the region marked by the dotted (solid) loop is the void inter-particle space (filled aggregate space). A RB molecule existing in the aggregate space might feel higher effective refractive index than in inter-particle space if the inhomogeneity of effective medium approximation existed. An important point is that the adsorbates could not float in the void inter-particle space but must be on the surface of ATO particle. Therefore, the effective filling factors around the adsorbed RB molecules was higher than bulk average. As a result, the filling factor traced back from the measured lifetime distribution is over 0.5 even though the inter-particle space looks much bigger than the space occupied by ATO nanoparticles and reported filling factors. Dynamic heterogeneity of the optical environment of a probe molecule in polymer matrix was experimentally observed⁹⁸ and theoretically modelled⁹⁹. Those studies support the idea of static heterogeneity of EMA in the interpretation of our study because the



Figure 4.29. AFM image of ATO nanoporous film divided into two kinds of spaces. In the top layer, the regions marked by dotted loop and solid loop were void inter-particle space and filled aggregate space, respectively. The effective filling factors in the two kinds of spaces were different if the inhomogeneity of effective medium approximation existed.

observation of dynamic heterogeneity implies that the non-homogeneous effective medium approximation was going on.

The distribution measured with the low threshold 500 cps was attributed to the heterogeneous electron transfer rate. The measured single molecule ET rates were not completely consistent with the values of bulk transient IR experiments, but it was due to the limited sensitivity of the SMD. The measured hundreds picosecond SM injection rates in Figure 4.22 may be ascribed to the coupling of excited state RB with discrete or low-density trap states, or weak coupling between surface states of ATO and charge transferred excited state. Another possible mechanism of lifetime reduction accompanied by quantum yield or emission power reduction could be energy transfer from RB to ATO nanoparticle. The band gap of SnO₂ is about 3.5 eV (350 nm)²⁹ and the on-set energy of emission from excited RB is 2.34 eV (530 nm). It has been observed that SnO₂ showed no interband absorption between 3.1 eV (400 nm) and 0.16 eV (8000 nm)⁹¹. As shown in Figure 4.30, there is no overlap between the absorption and emission spectra of ATO and RB respectively, and so the resonance energy transfer would not be feasible. Moreover,

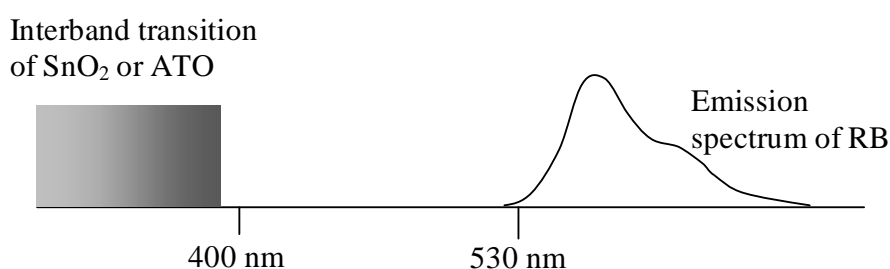


Figure 4.30. Schematic diagram of ATO absorption and RB emission spectra. The two spectra do not overlap and resonance energy transfer is not feasible.

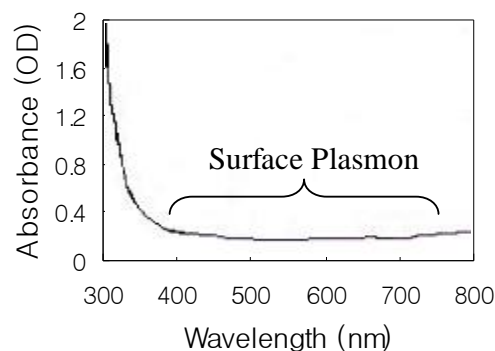


Figure 4.31. Absorption spectrum of nanocrystalline ATO film. Finite absorbance in the visible region is the short-wavelength-side wing of strong surface plasmon band centered at IR ($\sim 3\mu\text{m}^{33}$).

the band gap of ATO is larger than SnO_2 by the amount of charge carrier in conduction band¹⁰⁰. However, the dipole created by the collective motion of free electron gas in nanocrystalline metal and semiconductor, surface plasmon¹⁰¹, can effectively interact with donor molecular dipole¹⁰². The frequency of surface plasmon of metal¹⁰³⁻¹⁰⁵ or semiconductor¹⁰³ ranges usually visible and IR depending on the concentration of free electron¹⁰³ and the refractive index of medium¹⁰⁵. It has been observed and published that the ATO nanocrystalline film has non-negligible absorption in the visible region that was assigned to the plasmon band^{33,91,106} as shown in Figure 4.31. The finite absorbance in the visible region is the short-wavelength-side wing of strong surface plasmon band centered at IR ($\sim 3\mu\text{m}^{33}$). The energy transfer from the excited RB and surface plasmon might have led to the decrease of fluorescence lifetime and quantum yield simultaneously. In the previous paragraph about Figure 4.28, we imagined that the surface plasmon might have influenced on the distribution measured with the high (1200 cps) threshold resulting in

the deviation of the distribution from the curve of fully microscopic model. It is certain that the mechanism of the quenching of majority of excited RB molecules adsorbed on ATO was electron transfer from bulk pump-probe study. However, the existence of energy transfer in the observed SMFL distribution and its contribution to the quenching of RB adsorbates on ATO is still worth questioning.

In conclusion, SMFL distributions of the electron injecting but visible molecules were measured and showed low-lifetime-bound distribution. The local field correction and effective medium approximation were applied to the interpretation of SMFL distribution higher than 0.8 ns. However, further experimental and theoretical studies should be sought for complete understanding of the phenomena; e.g. a diagnostic experiment that can measure the oxidation state of the quenched but visible molecule may be helpful for us to explain the distribution below 1 ns more clearly.

IV. Conclusion

The single molecule observations of RB dye adsorbed on the nanocrystalline ATO film were performed. The bulk studies showed clear deviations from single exponential decay dynamics that is intrinsic in single molecule fluorescence decay. The decay dynamics of most single molecules on ATO were single exponential. Electron transfer process on ATO reduced SMFL down to 50 ps. The SMFL distribution of RB on ATO was clearly shifted to shorter lifetime from that of RB on ZrO_2 which was considered as a reference in terms of ET. The major characteristic time of electron injection into the conduction band of ATO would have been from a few to one hundred picosecond time scale, so should the SMFLs. However, the average SMFLs was 700 ps. Such a large discrepancy

was attributed to the limited signal to background ratio of SMD that was lower than other tests for the scattered light from ATO. The lifetime distribution was sensitive to the sampling threshold. The distribution measured with high threshold showed the broad lifetime dispersion without dependence on quantum yield. It was interpreted with a purely dielectric effect: the convolution of local field correction and effective medium approximation.

Appendix A: Polarization Dependence of Fluorescence Intensity

We describe the $\boldsymbol{\mu}$ and \mathbf{E}_0 explicitly in both the lab frame and a frame defined in regard to the laser beam right before the objective lens, and their relation is shown in Figure 4.32 to figure out the polarization dependence of the fluorescence intensity:

$$\boldsymbol{\mu}(\mathbf{r}) = (\sin \theta \cos \phi \hat{\mathbf{x}} + \sin \theta \sin \phi \hat{\mathbf{y}} + \cos \theta \hat{\mathbf{z}}) \delta(\mathbf{r} - \mathbf{r}_0) \quad (4.A1)$$

$$\mathbf{E}_0(\mathbf{R}) = E_x(\mathbf{R}) \hat{\mathbf{X}} + E_y(\mathbf{R}) \hat{\mathbf{Y}} + E_z(\mathbf{R}) \hat{\mathbf{Z}} \quad (4.A2)$$

$$\mathbf{r} = x \hat{\mathbf{x}} + y \hat{\mathbf{y}} + z \hat{\mathbf{z}} \quad (4.A3)$$

$$\mathbf{R} = X \hat{\mathbf{X}} + Y \hat{\mathbf{Y}} + Z \hat{\mathbf{Z}} \quad (4.A4)$$

$$\mathbf{r} = T(\Theta) \mathbf{R} \quad (4.A5)$$

$$T(\Theta) = \begin{bmatrix} \cos \Theta & \sin \Theta & 0 \\ -\sin \Theta & \cos \Theta & 0 \\ 0 & 0 & 1 \end{bmatrix} \quad (4.A6)$$

where $\hat{\mathbf{x}}$, $\hat{\mathbf{y}}$, and $\hat{\mathbf{z}}$ are the unit vectors of the lab frame, and $\hat{\mathbf{X}}$, $\hat{\mathbf{Y}}$, and $\hat{\mathbf{Z}}$ are the unit vectors of the laser beam frame. θ and ϕ are the polar and azimuthal angle of the dipole moment with respect to $\hat{\mathbf{x}}$ and $\hat{\mathbf{y}}$, respectively. Θ is the rotation angle of laser beam frame with respect to the lab frame. \mathbf{r} and \mathbf{R} are the position vector in lab frame and laser beam frame with its origin defined at the crossing point between the substrate surface and optic axis of microscope. \mathbf{r}_0 is the position vector of the dipole moment in lab frame. The dipole moment is assumed to be a point due to the relative sizes of single molecule ($\sim 1\text{nm}$) and laser focus (450nm in diameter). $E_x(\mathbf{R})$, $E_y(\mathbf{R})$, and $E_z(\mathbf{R})$ are three electric

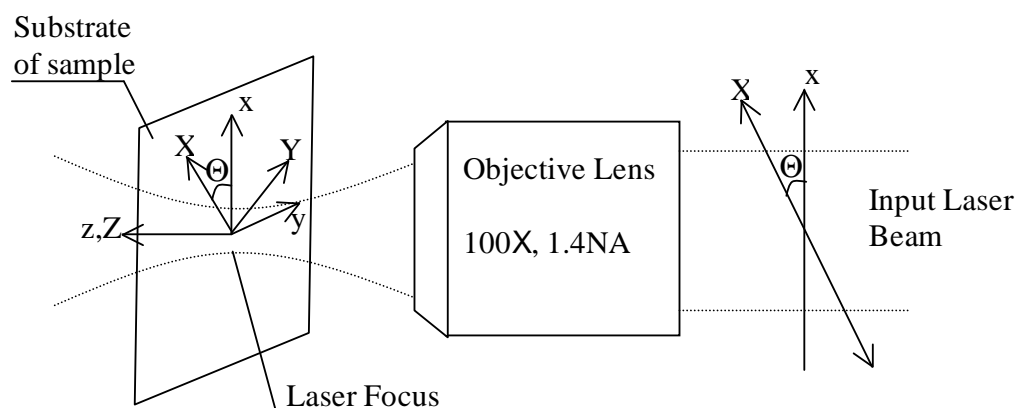


Figure 4.32. Schematic diagram of the coordinates in lab frame (small letter) and laser beam frame (capital letter) in microscope. The laser beam frame has rotated by Θ counterclockwise.

field amplitude components at position \mathbf{R} in the laser beam frame. The magnitude of μ and \mathbf{E}_0 are set to 1. The gist of the above definitions is that the relative magnitudes of the $E_x(\mathbf{R})$, $E_y(\mathbf{R})$, and $E_z(\mathbf{R})$ is not homogeneous at the focal plane: they are homogeneous at a normal cross-section of collimated beam before the objective lens. The profile of the magnitude of each electric field component, $E_x(\mathbf{R})$, $E_y(\mathbf{R})$, or $E_z(\mathbf{R})$ on a focal plane is shown in Figure 2(c) in the published work by Sick et al.⁶⁰. The plane of polarization before the back aperture of input laser beam was along X axis. The objective lens that was used by the authors (100X, 1.3NA, ~ 0.2 mm working distance) was a similar type of one used in this study (100X, 1.4NA, 0.2mm working distance). The theoretical and experimental results of Sick et al.⁶⁰ show that the electric field at the focus, which has the same direction of polarization (along X axis) as the laser beam before the back aperture of objective lens has, decays radially from the center of the focus to about 190nm. The Y-

and Z-components also exist forming four (Y) and two (Z) lobes ranging from 120nm to 370nm away from the center of the focus. If the laser focus is positioned well for the single molecule to be within a circle of 120nm radius concentric with the laser beam, the only effective electric field is linearly polarized along X axis. In this case, when the plane of polarization of the input beam rotates by Θ , the total electric field amplitude $E_0(\mathbf{r}_0)$ in lab frame is:

$$\mathbf{E}_0(\mathbf{r}) = T(\Theta)\mathbf{E}_0(\mathbf{R}_0) = \cos \Theta \hat{x} - \sin \Theta \hat{y} \quad (4.A7)$$

where $\mathbf{E}_0(\mathbf{R}_0)$ is $(1, 0, 0)^T$. The response of fluorescence to the rotation of input beam polarization represented by $|\boldsymbol{\mu} \cdot \mathbf{E}_0|^2$ becomes^{59,67}:

$$|\boldsymbol{\mu} \cdot \mathbf{E}_0|^2 = \sin^2 \theta \cos^2(\phi + \Theta) \quad (4.A8)$$

where the θ and ϕ are fixed, and Θ changes. For arbitrary values of θ and ϕ :

$$|\boldsymbol{\mu} \cdot \mathbf{E}_0|^2 \propto \cos^2 \Theta \quad (4.A9)$$

For two-photon excitation, excitation efficiency is determined by two-photon tensor. Many strongly emitting laser dyes such as RB tend to have the tensor of only one diagonal element¹⁰⁷:

$$|\mathbf{T} : \mathbf{E}_0 \mathbf{E}_0|^2 \propto \cos^4 \Theta \quad (4.A10)$$

$$\mathbf{T} = \begin{pmatrix} 1 & 0 & 0 \\ 0 & 0 & 0 \\ 0 & 0 & 0 \end{pmatrix}$$

where, T is the two-photon absorption tensor.

Appendix B: Solubility of Oxygen in Water and Alcohol

In ideally diluted solution, the mole fraction of solute and its vapor pressure are related by Henry's law¹⁰⁸.

$$p = xK \quad (4.A11)$$

where p is the vapor pressure, x is mole fraction, and K is the Henry's law constant. When the solute is oxygen and solvent is water, K is $4.3 \times 10^4 \text{ atm}^{108}$. The p of oxygen in the air is 0.21 atm, then mole fraction, x , is 4.9×10^{-6} . The molarity of oxygen solution in water can be approximated to that of pure water, 55.5 M. The concentration of oxygen in water is $2.7 \times 10^{-4} \text{ M}$.

The molar volume of air is 22.4L/mol under ideal gas assumption. The number of moles of oxygen in the air per liter is, $0.21 \div 22.4 \text{ mole/L} = 9.4 \times 10^{-3} \text{ M}$. Therefore, the concentration of oxygen in water is about 35 times lower than in the air. The concentration of oxygen in methyl alcohol can estimated to be 2mM using the Henry's law constant for oxygen-Methyl alcohol¹⁰⁹. It is 4.7 times lower than $[\text{O}_2]$ in the air.

References

- (1) Anderson, N. A.; Lian, T. *Annu. Rev. Phys. Chem.* **2005**, *56*, 491.
- (2) Asbury, J. B.; Hao, E.; Wang, Y.; Ghosh, H. N.; Lian, T. *Journal of Physical Chemistry B* **2001**, *105*, 4545.
- (3) Liu, D.; Hug, G. L.; Kamat, P. V. *J. Phys. Chem.* **1995**, *99*, 16768.
- (4) Gaal, D. A.; Hupp, J. T. *J. Am. Chem. Soc.* **2000**, *122*, 10956.
- (5) Nitzan, A.; Ratner, M. A. *Science* **2003**, *300*, 1384-1389.
- (6) Nitzan, A. *Annu. Rev. Phys. Chem.* **2001**, *52*, 681.
- (7) O'Regan, B.; Gratzel, M. *Nature* **1991**, *353*, 737-740.
- (8) Hara, K.; Sato, T.; Katoh, R.; Furube, A.; Ohga, Y.; Shinpo, A.; Suga, S.; Sayama, K.; Sugihara, H.; Arakawa, H. *J. Phys. Chem. B* **2003**, *107*, 597.
- (9) Piotrowiak, P.; Galoppini, E.; Wei, Q.; Meyer, G. J.; Wiewior, P. *J. Am. Chem. Soc.* **2003**, *125*, 5278-5279.
- (10) Asbury, J. B.; Hao, E.; Wang, Y.; Ghosh, H. N.; Lian, T. *J. Phys. Chem. B* **2001**, *105*, 4545-4557.
- (11) Anderson, N. A.; Lian, T. *Ann. Rev. Phys. Chem.* **2005**, *submitted*.
- (12) Benko, G.; Myllyperkio, P.; Pan, J.; Yartsev, A. P.; Sundstrom, V. *J. Am. Chem. Soc.* **2003**, *125*, 1118-1119.
- (13) Zimmermann, C.; Willig, F.; Ramakrishna, S.; Burfeindt, B.; Pettinger, B.; Eichberger, R.; Storck, W. *Journal of Physical Chemistry B* **2001**, *105*, 9245-9253.
- (14) Palomares, E.; Clifford, J. N.; Haque, S. A.; Lutz, T.; Durrant, J. R. *Journal of the American Chemical Society* **2003**, *125*, 475-482.

- (15) Smalley, J. F.; Finklea, H. O.; Chidsey, C. E. D.; Linford, M. R.; Creager, S. E.; Ferraris, J. P.; Chalfant, K.; Zawodzinsk, T.; Feldberg, S. W.; Newton, M. D. *J. Am. Chem. Soc.* **2003**, *125*, 2004-2013.
- (16) Nitzan, A.; Ratner, M. A. *Science* **2003**, *300*, 1384.
- (17) Ramachandran, G. K.; Hopson, T. J.; Rawlett, A. M.; Nagahara, L. A.; Primak, A.; Lindsay, S. M. *science* **2003**, *300*, 1413.
- (18) Xu, B.; Tao, N. J. *Science* **2003**, *301*, 1221.
- (19) Piotrowiak, P.; Galoppini, E.; Wei, Q.; Meyer, G. J.; Wiewior, P. *J. Am. Chem. Soc.* **2003**, *125*, 5278.
- (20) Benko, G.; Myllyperkio, P.; Pan, J.; Yartsev, A. P.; Sundstrom, V. *J. Am. Chem. Soc.* **2003**, *125*, 1118.
- (21) Zimmermann, C.; Willig, F.; Ramakrishna, S.; Burfeindt, B.; Pettinger, B.; Eichberger, R.; Storck, W. *J. Phys. Chem. B* **2001**, *105*, 9245.
- (22) Palomares, E.; Clifford, J. N.; Haque, S. A.; Lutz, T.; Durrant, J. R. *J. Am. Chem. Soc.* **2003**, *125*, 475.
- (23) Rigler, R.; Orrit, M.; Basche, T. *Single molecule spectroscopy: nobel conferencelectures*; Springer: Berlin; New York, 2001; Vol. 67.
- (24) Lu, H. P.; Xie, X. S. *J. Phys. Chem. B* **1997**, *101*, 2753.
- (25) Holman, M. W.; Liu, R.; Adams, D. M. *J. Am. Chem. Soc.* **2003**, *125*, 12649.
- (26) Biju, V.; Micic, M.; Hu, D.; Lu, H. P. *J. Am. Chem. Soc.* **2004**, *126*, 9374.
- (27) Thangaraju, B. *Thin Solid Films* **2002**, *402*, 71.
- (28) Kim, H.; Pique, A. *Applied Physics Letters* **2004**, *84*, 218.

- (29) Kung, H. H.; Jarrett, H. S.; Sleight, A. W.; Ferretti, A. *Journal of Applied Physics* **1977**, *48*, 2463.
- (30) Pant, D.; Levinger, N. E. *Chem. Phys. Lett.* **1998**, *292*, 200.
- (31) Hagfeldt, A.; Gratzel, M. *Chem. Rev.* **1995**, *95*, 49.
- (32) Hashimoto, K.; Hiramoto, M.; Sakata, T. *The Journal of Physical Chemistry* **1988**, *92*, 4272.
- (33) Guo, J.; She, C.; Lian, T. *Journal of Physical Chemistry B* **2005**, *109*, 7095.
- (34) Sakata, T.; Hashimoto, K.; Hiramoto, M. *J. Phys. Chem.* **1990**, *94*, 3040.
- (35) Menzel, R.; Bornemann, R.; Thiel, E. *Phys. Chem. Chem. Phys.* **1999**, *1*, 2435.
- (36) Korobov, V. E.; Shubin, V. V.; Chibisov, A. K. *Chem. Phys. Lett.* **1977**, *45*, 498.
- (37) Xu, C.; Webb, W. W. *J. Opt. Soc. Am. B* **1996**, *13*, 481.
- (38) Magde, D.; Rojas, G. E.; Seybold, P. G. *Photochemistry and Photobiology* **1999**, *70*, 737.
- (39) Snare, M. J.; Treloar, F. E.; Ghiggino, K. P.; Thistlethwaite, P. J. *Journal of Photochemistry* **1982**, *18*, 335.
- (40) Grabowski, Z. R.; Rotkiewicz, K. *Chem. Rev.* **2003**, *103*, 3899.
- (41) Casey, K. G.; Quitevis, E. L. *J. Phys. Chem.* **1988**, *92*, 6590.
- (42) Karstens, T.; Kobs, K. *The Journal of Physical Chemistry* **1980**, *84*, 1871.
- (43) Bindhu, C. V.; Harilal, S. S.; Varier, G. K.; Issac, R. C.; Nampoori, V. P. N.; Vallabhan, C. P. G. *J. Phys. D: Appl. Phys.* **1996**, *29*, 1074.

- (44) Steinfeld, J. I. In *Molecules and Radiation: An Introduction to Modern Molecular Spectroscopy*; Harper & Row: New York, 1974.
- (45) Zipfel, W. R.; Williams, R. M.; Webb, W. W. *nature biotechnology* **2003**, *21*, 1369.
- (46) Vallee, R. A. L.; Tomczak, N.; Vancso, G. J.; Kuipers, L.; Hulst, N. F. v. *Journal of Chemical Physics* **2005**, *122*, 114704.
- (47) Glauber, R. J.; Lewenstein, M. *Physical Review A* **1991**, *43*, 467.
- (48) Barnett, S. M.; Huttner, B.; Loudon, R. *Physical Review Letters* **1992**, *68*, 3698.
- (49) Meltzer, R. S.; Feofilov, S. P.; Tissue, B.; Yuan, H. B. *Physical Review B* **1999**, *60*, R14012.
- (50) Crenshaw, M. E.; Bowden, C. M. *Physical Review Letters* **2000**, *85*, 1851.
- (51) Wuister, S. F.; Donega, C. d. M.; Meijerink, A. *Journal of Chemical Physics* **2004**, *121*, 4310.
- (52) Hernando, J.; Schaaf, M. v. d.; Dijk, E. M. H. P. v.; Sauer, M.; Garcia-Parajo, M. F.; Hulst, N. F. v. *J. Phys. Chem. A* **2003**, *107*, 43.
- (53) Craig, D. P. In *Physical Processes in Radiation Biology*; Augenstein, L., Mason, R., Rosenberg, B., Eds.; Academic Press: New York and London, 1964, p 1.
- (54) Kasha, M.; Rawls, H. R.; El-Bayoumi, M. A. *Pure and Applied Chemistry* **1965**, *11*, 371.
- (55) Zondervan, R.; Kulzer, F.; Orlinskii, S. B.; Orrit, M. *J. Phys. Chem. A* **2003**, *107*, 6770.

- (56) Hou, Y.; Higgins, D. A. *Journal of Physical Chemistry B* **2002**, *106*, 10306.
- (57) Wang, H.; Bardo, A. M.; Collinson, M. M.; Higgins, D. A. *J. Phys. Chem. B* **1998**, *102*, 7231.
- (58) McHale, J. L. *Molecular Spectroscopy*; Prentice Hall: Upper Saddle River, N.J., 1999.
- (59) Macklin, J. J.; Trautman, J. K.; Harris, T. D.; Brus, L. E. *Science* **1996**, *272*, 255.
- (60) Sick, B.; Hecht, B.; Wild, U. P.; Novotny, L. *Journal of Microscopy* **2001**, *202*, 365.
- (61) Novotny, L.; Beversluis, M. R.; Youngworth, K. S.; Brown, T. G. *Physical Review Letters* **2001**, *86*, 5251.
- (62) Sick, B.; Hecht, B.; Novotny, L. *Physical Review Letters* **2000**, *85*, 4482.
- (63) Ha, T.; Enderle, T.; Chemla, D. S.; Selvin, P. R.; Weiss, S. *Physical Review Letters* **1996**, *77*, 3979.
- (64) Monson, P. R.; McClain, W. M. *Journal of Chemical Physics* **1970**, *53*, 29.
- (65) Allcock, P.; Andrews, D. L. *Journal of Chemical Physics* **1998**, *108*, 3089.
- (66) McClain, W. M. *Journal of Chemical Physics* **972**, *57*, 2264.
- (67) Bopp, M. A.; Jia, Y.; Haran, G.; Morlino, E. A.; Hochstrasser, R. M. *Applied Physics Letters* **1998**, *73*, 7.
- (68) Robbins, R. J.; Fleming, G. R.; Beddard, G. S.; Robinson, G. W.; Thistlethwaite, P. J.; Woolfe, G. J. *J. Am. Chem. Soc.* **1980**, *102*, 6271.

- (69) Venkataraj, S.; Kappertz, O.; Weis, H.; Drese, R.; Jayavel, R.; Wuttig, M. *Journal of Applied Physics* **2002**, *92*, 3599.
- (70) Takeshita, K.; Sasaki, Y.; Kobashi, M.; Tanaka, Y.; Maeda, S.; Yamakata, A.; Ishibashi, T.-a.; Onishi, H. *J. Phys. Chem. B* **2003**, *107*, 4156.
- (71) Katoh, R.; Furube, A.; Hara, K.; Murata, S.; Sugihara, H.; Arakawa, H.; Tachiya, M. *J. Phys. Chem. B* **2002**, *106*, 12957.
- (72) Khazraji, A. C.; Hotchandani, S.; Das, S.; Kamat, P. V. *J. Phys. Chem. B* **1999**, *103*, 4693.
- (73) Barzykin, A. V.; Tachiya, M. *J. Phys. Chem. B* **2002**, *106*, 4356.
- (74) Nasr, C.; Liu, D.; Hotchandani, S.; Kamat, P. V. *J. Phys. Chem.* **1996**, *100*, 11054.
- (75) Liu, D.; Kamat, P. V. *J. Electrochem. Soc.* **1995**, *142*, 835.
- (76) Nishikiori, H.; Fujii, T. *Journal of Physical Chemistry B* **1997**, *101*, 3680.
- (77) Ferrer, M. L.; Monte, F. d.; Levy, D. *Langmuir* **2003**, *19*, 2782.
- (78) Gratzel, M. *Heterogeneous photochemical electron transfer*; CRC Press: Boca Raton, 1988.
- (79) Selwyn, J. E.; Steinfeld, J. I. *The Journal of Physical Chemistry* **1972**, *76*, 762.
- (80) Kuhn, O.; Rupasov, V.; Mukamel, S. *Journal of Chemical Physics* **1996**, *104*, 5821.
- (81) Faraggi, M.; Peretz, P.; Rosenthal, I.; Weinraub, D. *Chem. Phys. Lett.* **1984**, *103*, 310.
- (82) Sadkowsky, P. J.; Fleming, G. R. *Chem. Phys. Lett.* **1978**, *57*, 526.

- (83) Ferguson, J.; Mau, A. W.-H. *Aust. J. Chem.* **1973**, *26*, 1617.
- (84) Sharma, A.; Schulman, S. G. *Introduction to Fluorescence Spectroscopy*; J. Wiley: New York, 1999.
- (85) Johansson, L. B. A.; Niemi, A. *J. Phys. Chem.* **1987**, *91*, 3020.
- (86) Kubin, R. F.; Fletcher, A. N. *Journal of Luminescence* **1982**, *27*, 455.
- (87) Arbeloa, I. L.; Rohatgi-Mukherjee, K. K. *Chem. Phys. Lett.* **1986**, *128*, 474.
- (88) Ha, T.; Chemla, D. S.; Enderle, T.; Weiss, S. *Bioimaging* **1997**, *5*, 99.
- (89) Ha, T.; Enderle, T.; Chemla, D. S.; Selvin, P. R.; Weiss, S. *Chem. Phys. Lett.* **1997**, *271*, 1.
- (90) Aspnes, D. E. *Am. J. Phys.* **1982**, *50*, 704.
- (91) Nutz, T.; Felde, U. z.; Haase, M. *Journal of Chemical Physics* **1999**, *110*, 12142.
- (92) Niklasson, G. A.; Granqvist, C. G.; Hunderi, O. *Applied Optics* **1981**, *20*, 26.
- (93) Granqvist, C. G.; Hunderi, O. *Physical Review B* **1977**, *16*, 3513.
- (94) Lide, D. R. *CRC handbook of chemistry and physics: a ready-reference book of chemical and physical data*; CRC Press: Boca Raton, 2005.
- (95) Chibisov, A. K.; Gorner, H. *Chem. Phys. Lett.* **2002**, *357*, 434.
- (96) Frank, A. J.; Otvos, J. W.; Calvin, M. *The Journal of Physical Chemistry* **1979**, *83*, 716.
- (97) Baumler, W.; Schmalzl, A. X.; Gosl, G.; Penzkoler, A. *Meas. Sci. Technol.* **1992**, *3*, 384.

- (98) Vallee, R. A. L.; Tomczak, N.; Kuipers, L.; Vancso, G. J.; Hulst, N. F. v. *Physical Review Letters* **2003**, *91*, 038301.
- (99) Vallee, R. A. L.; Auweraer, M. V. D.; Schryver, F. C. D.; Beljonne, D.; Orrit, M. *ChemPhysChem* **2005**, *6*, 81.
- (100) Sanon, G.; Rup, R.; Mansingh, A. *Physical Review B* **1991**, *44*, 5672.
- (101) Kreibig, U.; Vollmer, M. *Optical Properties of Metal Clusters*; Springer-Verlag: Berlin, 1994.
- (102) Andrew, P.; Barnes, W. L. *Science* **2004**, *306*, 1002.
- (103) Mulvaney, P. *Langmuir* **1996**, *12*, 788.
- (104) Nolte, D. D. *J. Appl. Phys.* **1994**, *76*, 3740.
- (105) Brongersma, M. L.; Hartman, J. W.; Atwater, H. A. *Physical Review B* **2000**, *62*, R16356.
- (106) Link, S.; El-Sayed, M. A. *Annu. Rev. Phys. Chem.* **2003**, *54*, 331.
- (107) Solaroli, N.; Bjerke, M.; Amiri, M. H.; Johansson, M.; Karlsson, A. *Eur. J. Biochem.* **2003**, *270*, 2879.
- (108) Atkins, P. W. *Physical Chemistry*; 6th ed.; Freeman: New York, 1998.
- (109) Luhring, P.; Schumpe, A. *J. Chem. Eng. Data* **1989**, *34*, 250.

Chapter 5. Surface Induced of Fluorescence Lifetime Distribution of Rhodamine B on Glass Measured by Single Molecule Detection

I. Introduction

A fascinating optical process working in the emission of light from a molecule near a flat dielectric interface is the modification of radiative lifetime of the molecule. It is a function of geometry - molecular dipole orientation and its distance from the interface - and of the refractive index ratio of the two media forming the interface¹⁻⁶. Historically, it dates back to the experiments on the dependence of fluorescence lifetime on the distance between chromophore and metal surface done by Drexhage^{7,8} in the 60s and subsequent theoretical works by Tews⁹ and Chances et al.¹⁰⁻¹² in the framework of classical electrodynamics in the 70s. Since then, the fluorescence lifetime studies of molecules on semiconductor¹³⁻¹⁷ and lossless dielectric surface^{1-3,6,18,19} have also been done. Especially, the classical theoretical work on the radiative lifetime of single dipole near the lossless dielectric medium by Lukosz et al.^{1,2} has presented a useful background for the subsequent theoretical advances^{3,20-22} and the understanding of experiments^{4,6,23,24}. We have seen the aforementioned problems come into play in the SMFL measurement of RB dispersed on glass surface as an inhomogeneous broadening of lifetime. The theoretical work of Lukosz et al. fully implemented our analysis of the SMFL distribution data, and, conversely, SMD may be the only realization of the theoretical model set up in the theory^{1,2}.

In this chapter, the RB on glass will be compared with RB on ATO as an ET-inactive system. In addition to the effect of ET-inactiveness, the SMD of RB on glass has

shown interesting SMFL distributions and intensity trajectory patterns. The SMFL distribution is ascribed to the dipole orientation effect on the fluorescence lifetime: the fluorescence lifetime is equal to the radiative lifetime because the quantum yield of RB on glass was assumed to be 1 for the rigid²⁵ and non-polar^{26,27} properties of the air-glass interface. The analytical expressions of the orientation effect² are applied to our experimental results in predicting the SMFL distribution using a parameter - radiative lifetime in air calculated from the fully microscopic model local field correction^{28,29}: those theories are introduced in Section III of Chapter 2. The SMFL distribution of RB in the air side of the surface of flat, lossless dielectric, and higher refractive index substrate (glass, $n_D = 1.52$ ³⁰) was first observed in this study. Good comparison can be made with previous works on DiIC₁₂⁴ and DiIC₁₈^{5,6} embedded in the PMMA ($n_D = 1.49$ ³¹) side of PMMA-air interface.

Contrary to the intensity trajectory of RB on ATO, that of RB on glass has been observed to fluctuate highly. The unique high fluctuations of the intensity trajectory of single rhodamine dyes in inert polymer matrixes^{32,33} and silicate³⁴ have also been observed in the previous works. To my knowledge, the mechanism of high fluctuation has not been uncovered. In this chapter, the high intensity fluctuation is analyzed simultaneously with lifetime fluctuation using TCSPC data, and previous arguments on it are critically reviewed using our experimental results.

II. Results

II.A. Bulk Fluorescence Lifetime of RB on Glass

3 μL of $5 \times 10^{-8} \text{M}$ RB in MeOH solution was dropped on a cleaned cover glass. MeOH evaporated in 30 second and RB molecules were dispersed homogeneously. The average distance to the closest molecule was roughly 50 nm. The negligible formation of the regions of the effective inter-molecular interaction was confirmed by (1) no clear change of bulk lifetime by lowering the concentration of RB solution, and (2) the coincidence of the bulk lifetime and the average of SM lifetimes (to be shown in later sections). Referring to Section I.C of Chapter 3, the sample prepared here was an example of homogeneous distribution in spite of dropping scheme. The phenomenon is considered to originate in the fast adsorption of RB on glass surface through electrostatic attraction in a stereoselective mode. Zwitterion is a dominant form of RB in neutral solution³⁵ – it is called base form in some places^{26,36}. The RB molecules may adsorb quickly on glass surface having negative surface-partial-charge, through their positive part of the structure. Figure 5.1 shows three important resonance structures stabilizing the positive charge in xanthene ring. It is supported by the routine observations of significantly higher concentration of positively charged and zwitterionic rhodamine dyes at the interface between glass surface and dye solution than a deep point in the dye solution. On the contrary, constant concentration has been observed through the interface into the dye solution when the dye was neutral, negatively charged, or bound to solvated DNA.

A $25 \times 25 \mu\text{m}^2$ -wide two-photon fluorescence image is shown in Figure 5.2. Excitation wavelength and power were 800 nm and 110 kW/cm^2 . Fluorescence counts were not spatially resolved, which made it a bulk test. Figure 5.3 is the decay curves of

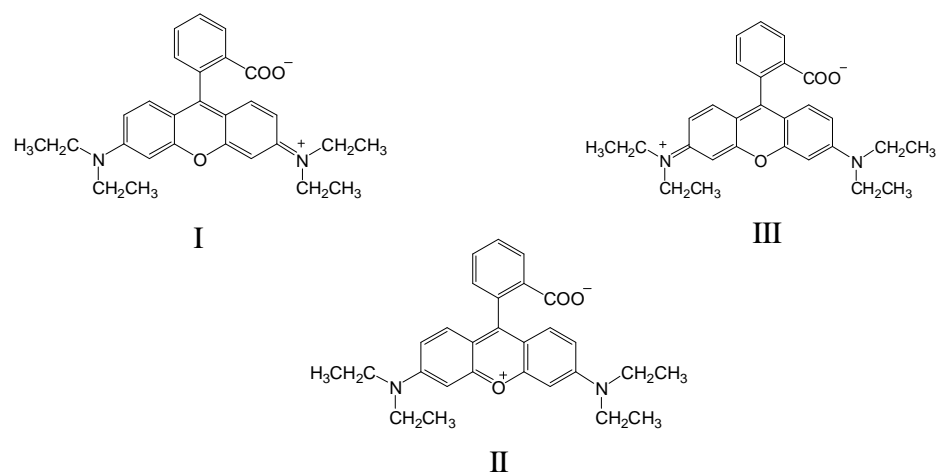


Figure 5.1. Schematic resonance structures of rhodamine B in zwitterion form. Positive charge is distributed in the xanthene ring.

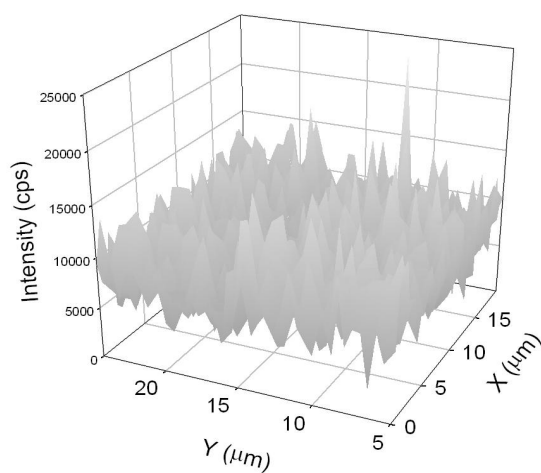


Figure 5.2. Stage-scanned two-photon fluorescence image of RB molecules adsorbed on a glass surface. Total scanned area is $25 \times 25 \mu\text{m}^2$ (40 pixels by 40 pixels).

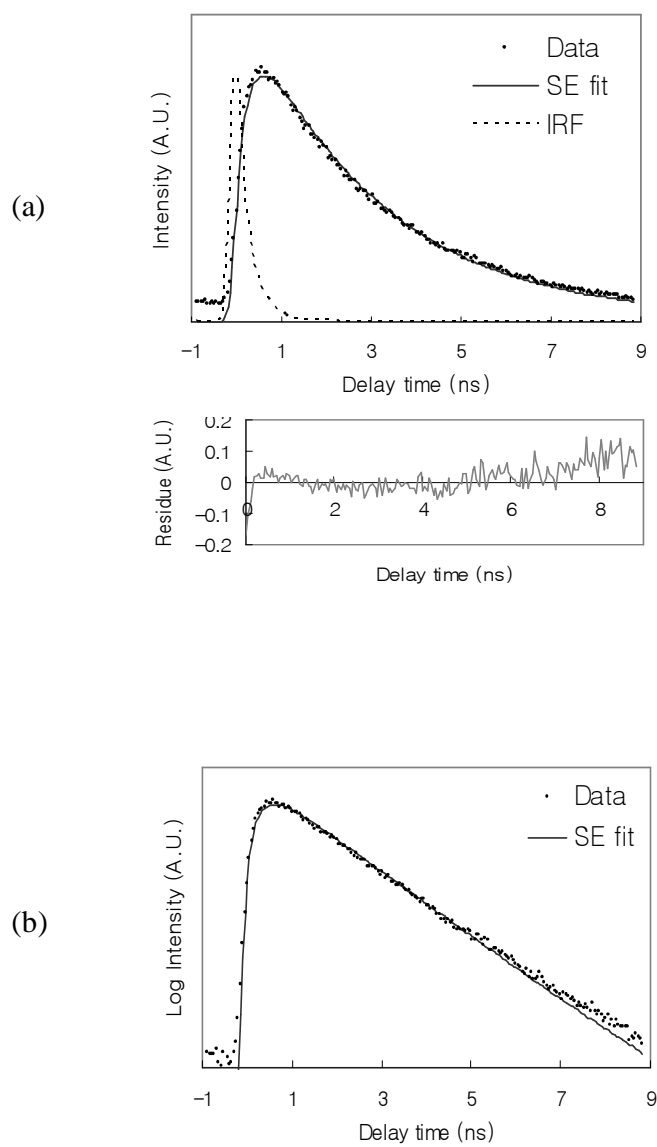


Figure 5.3. Fluorescence decay curve of bulk RB on a cover slip measured in the test shown in Figure 5.2 and fitted to single exponential model. τ and χ^2_r are 3.0 ns and 3.4 respectively. (a) Drawn in linear scale. (b) Drawn in log scale.

the total fluorescence photons detected in the test shown in Figure 5.2. In Figure 5.3, a single exponential model convoluted with an instrument response function is fitted to the measured decay curve. The best fit of lifetime parameter is 3.0 ns with reduced chi square χ^2_r being 3.4. The magnitude of χ^2_r 3.4 suggests that the measured decay curve deviated from a good single exponential decay, but it is closer to single exponential than the bulk fluorescence of RB on ATO of χ^2_r , 11.9. Looking at the fitting result in Figure 5.3a, the measured decay curve could be termed single exponential at a glance. However, the reduced chi square 3.4 is well over 1.5, a conventional criterion of good fitting, and the residue curve shows a signature of multi-exponential dynamics: its sign changes from plus at early time (< 1 ns), to minus in the middle (around 3 ns), and finally to plus (> 5 ns). In Figure 5.3a, we can see the slight deviation around 0.5 ns and 3.0 ns, and deviation from linear line in log scale after 6.5 ns in Figure 5.3b. It is unlikely that any strong heterogeneous quenching effect like the interfacial electron transfer observed in RB-ATO nanoporous film could exist. The origin of slight multi-exponential feature is due to the interfacial electrodynamical effect, which will be explained in Discussion section.

II.B. Single Molecule Fluorescence Lifetime of RB on Glass Surface

The SMD of RB on glass has been performed by the typical two-photon excitation: 800 nm wavelength, 50 fs pulse width, 88 MHz repetition rate laser output from the mode-locked oscillator. The laser power at the focus was about 0.16 MW/cm^2 . A sample with proper number density of RB molecules was loaded on the sample stage in the microscope, and the Search and Record procedures (Section III.A of Chapter 3) found

single molecules and recorded TCSPC data. Optimization procedure was not applied in this SMD of RB on glass test. The threshold for stopping the search procedure was 160 counts/0.1 s.

Figure 5.4 details the information from the TCSPC. Figure 5.4a is an intensity trajectory drawn with standard unit time, 0.1s. Four data point from 2.0 s to 2.4 s is selected in Figure 5.4a and all the pairs of the chronological and delay time associated with detected photons in the point are plotted in Figure 5.4b. In Figure 5.4b, each dot represents a single detected photon and is placed in the plot by its timing data. The number of dots inside the horizontal bar in Figure 5.4b becomes a point of fluorescence decay curve shown in Figure 5.4c with its delay time axis sharing that of Figure 5.4b. The number of dots inside the vertical bar in Figure 5.4b becomes a point of intensity trajectory in Figure 5.4d. The two histograms in Figure 5.4c and 5.4d can be built with arbitrary unit time.

Two pairs of representative fluorescence intensity trajectory and decay of two single molecules on glass are shown in Figure 5.5. The graphs in Figure 5.5a and 5.5b are drawn out of the same single molecule photon counting test by the method described in Figure 5.4, and so are the pair of graphs in Figure 5.5c and 5.5d. Figure 5.5a and 5.5c are intensity trajectories, and 5.5b and 5.5d are the decay curves in log scale. The intensity trajectory of the molecule in Figure 5.5a fluctuated highly while the trajectory shown in Figure 5.5c of the other molecule fluctuated much less than Figure 5.5a. The population of the highly fluctuating molecule was about 90%. The two decay curves were well described by the single exponential decay. The single exponential decay model was fit to the individual fluorescence decay curves to calculate the characteristic decay time. The

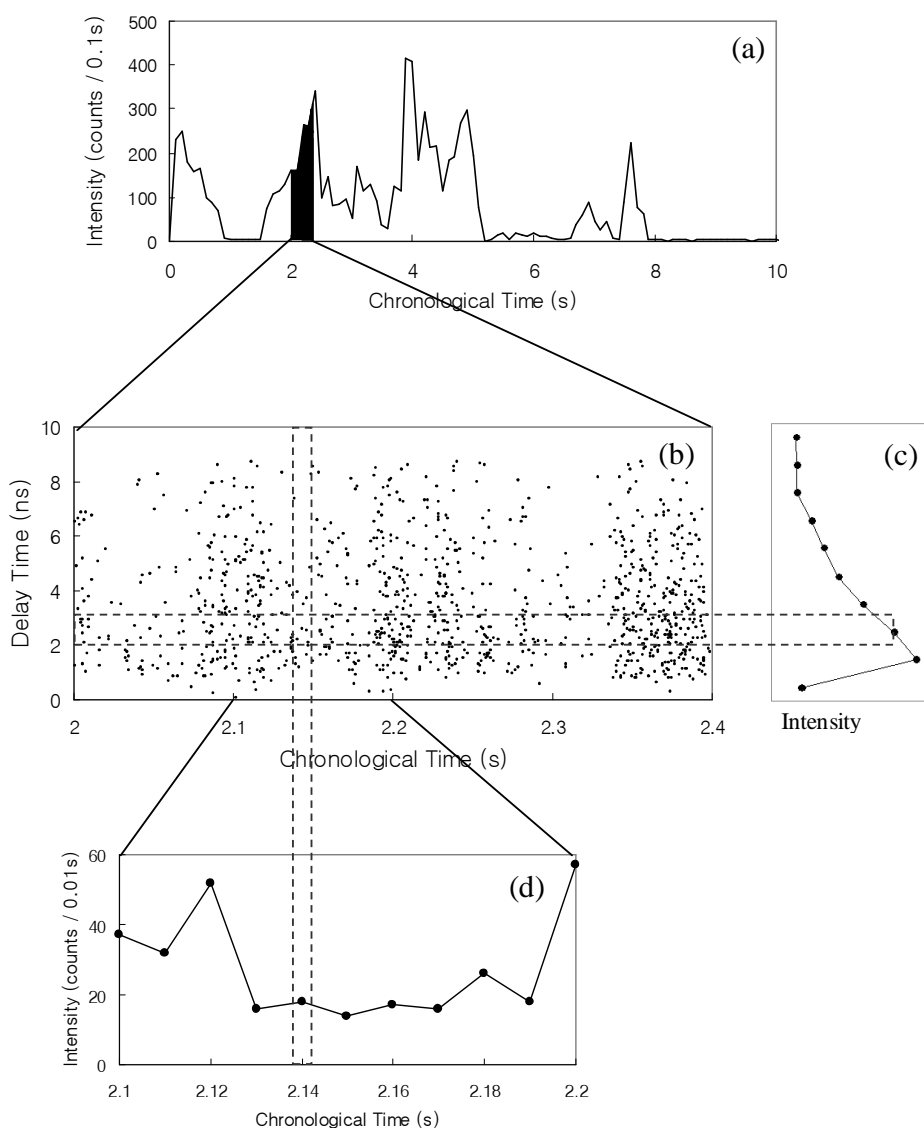


Figure 5.4. Information of single photons of TCSPC data for the construction of decay curve and intensity trajectory. (a) Regular intensity trajectory of a molecule. (b) TCSPC data taken from the part of trajectory in (a) expanded in two coordinates: chronological and decay time. (c) Decay curve by counting the number of photons in the horizontal bar. (d) Intensity trajectory by counting the number of photon in the vertical bar.

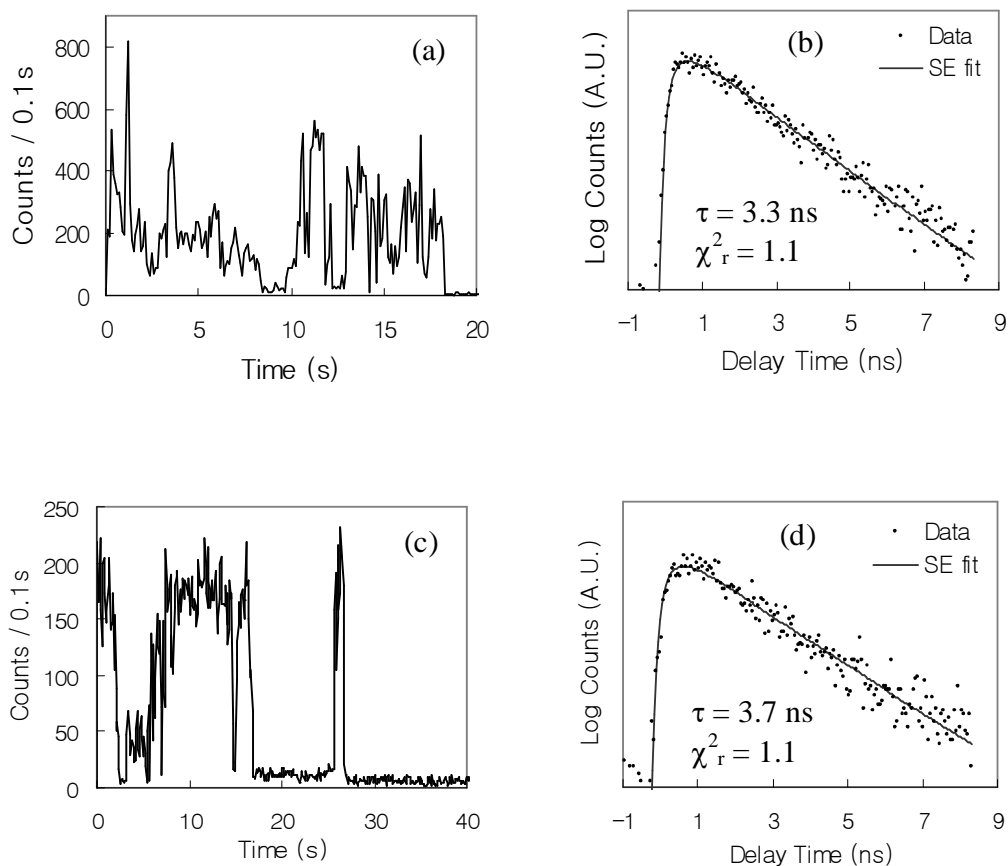


Figure 5.5. Two pairs of representative fluorescence intensity trajectory and decay of single molecules on glass. Excitation power and wavelength are 0.16 MW/cm^2 and 800nm . (a) and (b) are intensity trajectory and decay curve of fluorescence from a molecule. (c) and (d) are from another molecule. The trajectory in (a) fluctuates highly and that in (b) has relatively stable intensity showing the on-off characteristic.

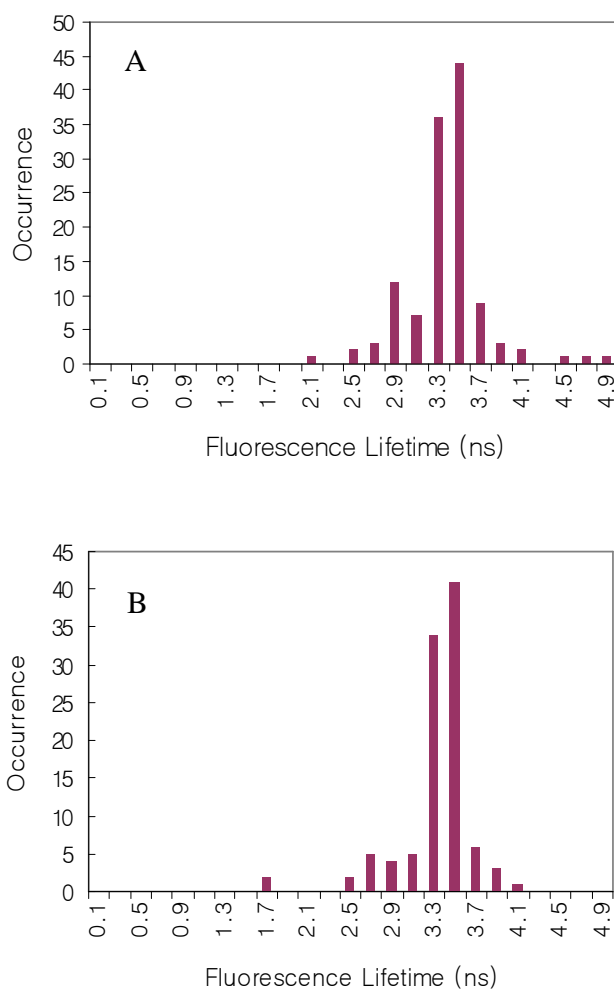


Figure 5.6. Two sets of SMFL experiments of RB on glass. Distribution A has average 3.4 ns and standard deviation 0.37ns. Distribution B has average 3.3 ns and standard deviation 0.35 ns. The SMFL distributions look wider than expected on non-interacting substrate.

SMFL and reduced chi square χ^2_r are put in the right upper corner of each decay graph. Clear relation between the degree of fluctuation and lifetime has not been observed.

Two sets of SMFL experiments were done and their SMFL distributions are shown in Figure 5.6. The distributions A and B consist of 122 and 103 molecules respectively. Each set of SMFL experiment was done in a day and the distribution B was measured one year after A. The distribution A had average lifetime 3.4 ns and standard deviation 0.37 ns. The distribution B had average 3.3 ns and standard deviation 0.35 ns. The SMFLs does not have a definite value although the glass surface is considered as a non-interacting substrate. Both the SMFL distributions ranged roughly from 2.4 ns to 4.2 ns, which is too large to attribute to a measurement error. The verification of the two distributions is necessary. The quantitative estimation of measurement error will be shown in the next section. The possible origin of the wide distribution of SMFL on non-interacting surface will be discussed in the discussion section.

III. Discussion

III.A. Single Molecule Fluorescence Intensity Trajectory

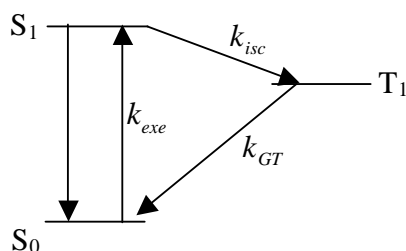
The SMD for the fluorescence intensity trajectory has been a unique observation that provided the insight into the kinetics of photophysical processes³⁷⁻⁴³. Theoretical studies have also been developed using time-correlation function of intensity fluctuation or single photon arrival time as a powerful tool of revealing parameters of molecular or photophysical dynamics associated with the measured dynamic variable, intensity or single photon detection event⁴⁴⁻⁴⁸. In this section, using the SMD technique, we are going to investigate the peculiar high fluctuation of fluorescence intensity from single RB molecule on glass surface. The origin of the phenomenon has eluded previous attempts to

discover and still is in question^{32,34,49}. The objective of this work is to improve the current knowledge on the problem by providing new and supportive experimental results.

The single molecule intensity trajectories of RB on ATO and glass surface were demonstrated showing the clear difference in the fluctuation time scale. About 90% of intensity trajectories on ATO were relatively constant while 90% of trajectories on glass were highly fluctuating in millisecond time scale. The feature of fluctuation depends on the unit time in drawing the intensity plot, and so autocorrelation function, $C(T)$, of intensity is used to quantify the time scale of fluctuation^{39,50-53}:

$$C(T) = \frac{\langle I(t+T)I(t) \rangle}{\langle I(t) \rangle^2} \quad (5.1)$$

where $C(T)$ is the time average of the multiplication of intensities at time t and $t+T$ scaled by the square of intensity average. The $C(T)$ is calculated with t running through the whole trajectory while the T fixed. It can be interpreted as the extent to which the intensities with the time difference T are correlated. The $C(T)$ function of random variable usually has higher value than 1 and decreases to 1 at longer time. That is, the $C(T)$ has value 1 when there is no correlation between the intensities with time difference T . Pair distribution function can be derived from the autocorrelation function in a three state model⁴⁵ of molecular photophysical process :



$$C(T) = 1 + \frac{\alpha_{isc} k_{exe}}{k_{GT}} \exp[-(\alpha_{isc} k_{exe} + k_{GT})T] \quad (5.2)$$

where, α_{isc} , k_{exe} , and k_{GT} are the triplet yield, excitation rate, and the de-excitation rate of $T_1 \rightarrow S_0$ of RB, respectively. The k_{GT} is several orders higher than $\alpha_{isc} k_{exe}$ term for RB in inert environment, so the decay rate of autocorrelation is governed by the triplet decay rate unless other bottleneck channel is involved.

The autocorrelation curves of a single RB molecule on glass surface are shown in Figure 5.7. They are constructed out of the same photon counting data but their unit time of T is 5 ms (a) and 2 μ s (b). According to the graphs, it could be said that the decrease of the intensity correlation has fast and slow components. The fast one is sub-millisecond

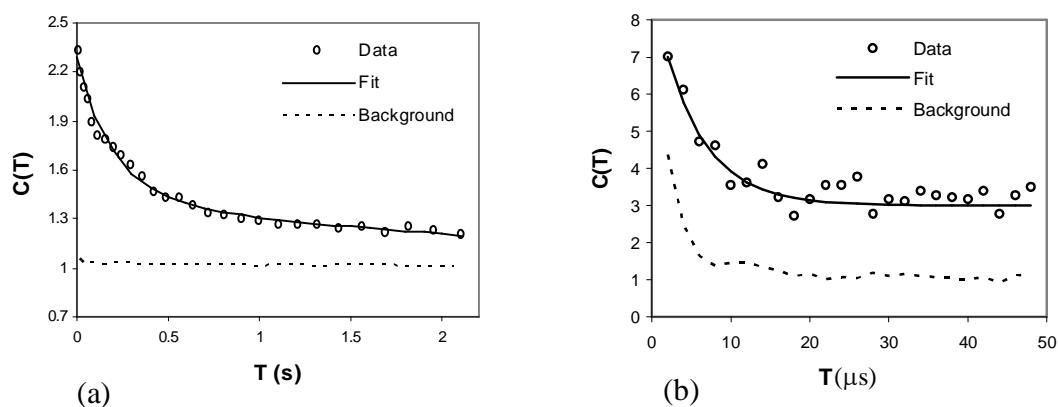


Figure 5.7. Measured intensity autocorrelation function of single RB on glass drawn in two different unit times, 5 ms (a) and 2 μ s (b). They were fitted with double (a) and single (b) exponential decay models. The characteristic decay times in (a) were 200 ms and 2.6 s. The characteristic decay time of (b) was 5 μ s with baseline 3.

time scale and the slow one still has correlation up to 2 s. The $C(T)$ curve of 5 ms unit time reflects the characteristic high intensity fluctuation of RB on glass that is apparent in the intensity fluctuation of ~ 100 ms unit time shown in Figure 5.4, 5.5, etc. To find the decay time, the measured $C(T)$ in Figure 5.7a was fitted with double exponential decay model even though the true dynamics of the intensity fluctuation of fluorescence from RB on glass is not known: it looks fluctuating randomly and we may be able to fit the $C(T)$ decay curve with exponential function because the time correlation function of random process is usually exponential form^{33,54,55}.

The two characteristic decay times τ_c were 200 ms and 2.6s with amplitude 0.84 and 0.45, respectively. The correlation in Figure 5.7b in much faster time scale, 2 μ s unit time, stabilizes to about 3 in 20 μ s. The autocorrelation decay is fitted to single exponential with baseline 3 and its τ_c , 5 μ s. Multi-component autocorrelation functions similar to the one in Figure 5.7a had been observed in the intensity fluctuation of single DiIC₁₂ molecule on cover glass⁴², of which interpretation will be discussed in the later paragraphs.

The dotted lines in Figure 5.7a and 5.7b are the $C(T)$ curves of background. As it should be, the background $C(T)$ does not have correlation with 5 ms unit time of T through the entire T range in the Figure 5.7a, which means the background signal is fully randomized in 5 ms, the first bin of the plot. The slight offset above 1 in Figure 5.7a is due to the limited amount of photon counting data, and unknown slow correlation from device or dark noise. The background cannot be complete white noise with $\delta(0)$ autocorrelation function, and so there naturally appears residual correlation at early time such as in Figure 5.7b. The dead time of photon counting board is 0.2 μ s, which is not the

reason for the residual correlation. Whatever the origin of background correlation near $T=0$ is, the fast decay with τ_c of $5\mu\text{s}$ is not pure photophysical effect but the sum of background autocorrelation and the dark time correlation due to shelving on triplet state having a few μs lifetime⁵⁵⁻⁵⁷.

An intensity autocorrelation function of a single RB on ATO is shown in Figure 5.8. In contrast to those of RB on glass in Figure 5.7, it does not have the slow fluctuation and decays to 1 in $20\mu\text{s}$. The characteristic decay time, τ_c , is $5\mu\text{s}$ that is the same as RB on glass. It means that any structure of intensity fluctuation will not appear even if the intensity trajectory such as Figure 4.12 is plotted in other unit time. Both the fast component of $C(T)$ decay of single RB on glass and the only decay component of $C(T)$ of single RB on ATO are background correlation limited. It means all the other photophysical processes including back electron transfer are faster than the μs time scale, except for the slow intensity fluctuation of the single RB molecule on glass.

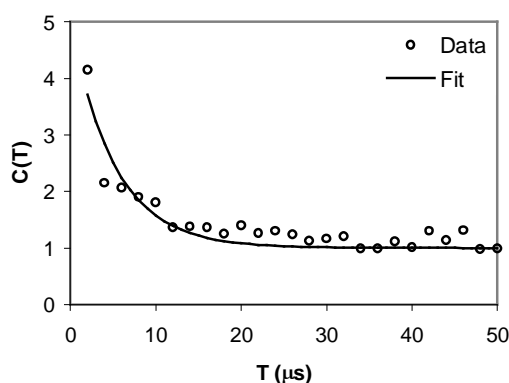


Figure 5.8. Measured intensity autocorrelation function of single RB on ATO drawn in $2\mu\text{s}$ unit time. It was fitted with single exponential decay. The characteristic decay time was $5\mu\text{s}$ with baseline 1.

As shown in Figure 4.8b and 5.4, the single molecule fluorescence intensity trajectory of RB on glass fluctuates highly from millisecond to second time scale. It is dependent on the property of substrate because intensity is relatively constant on ATO surface. Lots of mechanisms have been proposed including photo-induced metastable state formation⁵⁸, interaction with other molecules^{49,58}, conformational changes^{33,59}, rotation^{33,58}, spectral diffusion^{49,58}, dynamic variation of local environment^{34,58}, and radical dark state formation³²; but the origin of the intensity fluctuation of RB on glass has not been elucidated. In the following paragraphs, the proposed mechanisms will be reviewed critically using our experimental data.

Dark triplet state (T_1) has orders of magnitude longer lifetime than any other intrinsic photophysical state lifetime⁶⁰. Rhodamine dyes typically have microsecond time scale triplet lifetime in solution⁵⁶ but have even shorter triplet lifetime in the air where oxygen is more abundant than in solution (see Appendix B). Oxygen is a well known quencher of T_1 state⁶¹ and the above intensity trajectories were recorded on glass-air interface. Therefore, the triplet blinking is excluded from the origin of observed intensity fluctuation³³.

The glass surface is considered as an inactive substrate and is not likely to form photo-induced metastable state where electron is trapped after the ionization of RB through electron transfer. For the reason, the formation of photo-induced metastable state seems not to be the origin of intensity fluctuation.

Because the sample prepared for single molecule observation has a very low number density of dye molecules (~ 0.07 molecules on $1\mu\text{m} \times 1\mu\text{m}$ area), the probability of interaction between other nearby molecules is negligible. Electron transfer and energy

transfer is generally effective within 1 nm and 10 nm, respectively. Therefore, the interaction with other molecules could not be the origin of fluctuation.

The spectral diffusion was disproved by previous works by observing only 3 nm diffusion range of fluorescence peak maximum of RB in silicate film, which was not enough for the whole scale intensity fluctuation^{34,42}. The substrate in our study was the cover glass for general purpose of microscopy, named water glass or sodium silicate. Sodium was one of the major components of the cover glass but did not exist in the silicate film of Wang et al.'s experiment³⁴. The sodium ion might not be responsible for the fluctuation because the intensity fluctuation in this study was similar to that observed by Wang et al., even though the RB was embedded in silicate film in their experiment. Therefore, the fluctuation of absorption cross section by spectral diffusion was also not responsible for the observed intensity fluctuation.

Next, the conformational change mechanism implies the quantum yield change by the formation of TICT state⁶²⁻⁶⁴ proposed by previous works^{33,59}. As explained in detail in Section III.A, The quantum yield change due to TICT state formation results from the increased non-radiative decay rate when the two diethylamino groups pendent on the xanthene backbone twist during the electronic excited state. Therefore, fluorescence lifetime should change along with the intensity change. In addition, the range of fluorescence lifetime change is expected to be from the value of radiative lifetime (~ 9 ns) down to picosecond regime because the low intensity level during fluctuation is less than 10% of maximum intensity. Motivated by the idea, intensity trajectory of a single molecule observation is divided into two trajectories in just the same way as shown in Figure 4.23: two fluorescence decay curves were obtained from two collections of

TCSPC data pieces over and below a criterion. If the TICT state formation is responsible for the intensity fluctuation, the fluorescence lifetime calculated from the high intensity trajectory has to be clearly lower than that of low intensity trajectory. An example of the analysis is shown in Figure 5.9. The total trajectory is shown in graph (a). The fluorescence decay curves of the two intensity trajectories (b) and (c), which are mutually exclusive in time, are plotted and their lifetimes are calculated in Figure 5.10. The average intensity of high intensity trajectory is about four times higher than the low intensity trajectory. Then, we could expect that the lifetime of the high intensity trajectory was four times longer than the low intensity trajectory (Equation 2.5a), if the TICT state worked. However, the fluorescence lifetime of the high intensity trajectory

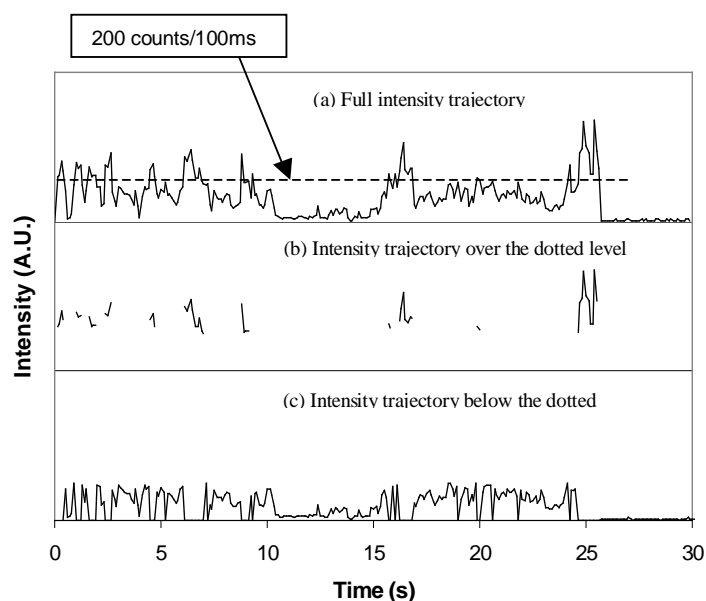


Figure 5.9. Intensity trajectory of RB on glass drawn in 50 ms unit time. The dashed line is a criterion level (200 counts/100ms) for classifying its TCSPC data pieces into high intensity and low intensity groups. Two decay curves were constructed from the two groups.

was 3.3 ns and that of the low intensity trajectory was 3.7 ns. They are not as clearly different from each other as our expectation and we may well say that they are different only by statistical error. Moreover, the trajectory of low intensity must have shorter lifetime in accordance with the above assumption, but it does not. All of seven SMD data analyzed such a way showed similar results and it is concluded that the conformation change forming TICT state was not responsible for the intensity fluctuation of RB on glass. The rotation of single molecule is also excluded because the high fluctuation was observed by both circular and linear polarization of excitation light, which has also been confirmed by Wang et al.³⁴.

The following discussion proposes two possible mechanisms of the intensity fluctuation: slow in-plane translational motion and radical dark state formation³². To watch the translational motion directly, in-plane motion of single RB molecules on a cover slip is demonstrated in Figure 5.11 by a time series of CCD images. Wide field of a single molecule sample is illuminated by TIR (Total Internal Reflection) method and fluorescence is recorded using CCD camera. Details of the detection method and microscopy are described in the previous work of Bartko et al.⁶⁵. In Figure 5.11, each image was taken for 1s exposure time and labeled with time on the left upper corner. The two crosses are placed at the constant positions in each frame of images so that we can clearly see the displacement of bright spots. The size of crosses is 1 μ m long in vertical and horizontal directions. The bright spots near the two crosses moved about 1 μ m for 8s. If the sample had been illuminated with laser focus, not the wide field illumination, there should have been increase and decrease of the fluorescence intensity for about 4s, taking into account the spot size of laser focus, ~500 nm in diameter. For the reason, the slow

second time scale (τ_c ; 2s) change of intensity in Figure 4.8b, and 5.4 may be due to the translational motion. The translational motion is not responsible for the 200 ms time scale intensity fluctuation but could influence on the second time scale intensity change.

The fact that the fluorescence lifetime was constant in spite of the intensity change supports the mechanism of long-lived dark state formation³². In the work of Zondervan et al.³², they proposed that the dark state was a reversible anionic radical formed through triplet state of R6G. If that occurred in our SMD of RB on glass too, the radiative and non-radiative decay rates would not change and only intensity would change as we observed in Figure 5.9 and 5.10. Such experimental evidence and the published work³² provide the justification of the thought that the quantum yield of RB on glass was 1 even if its intensity trajectory fluctuated highly. A photophysical model of

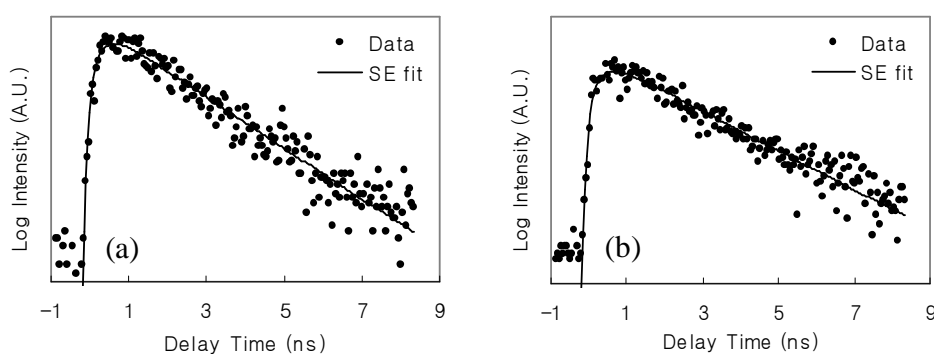


Figure 5.10. Fluorescence decay data of high (a) and low (b) intensity times fitted to single exponential decay model. Their lifetimes were 3.3 ns (a) and 3.7 ns (b). The intensity difference could not originate from the TICT state formation because the lifetime of the high intensity part should be four times longer than that of the low intensity part.

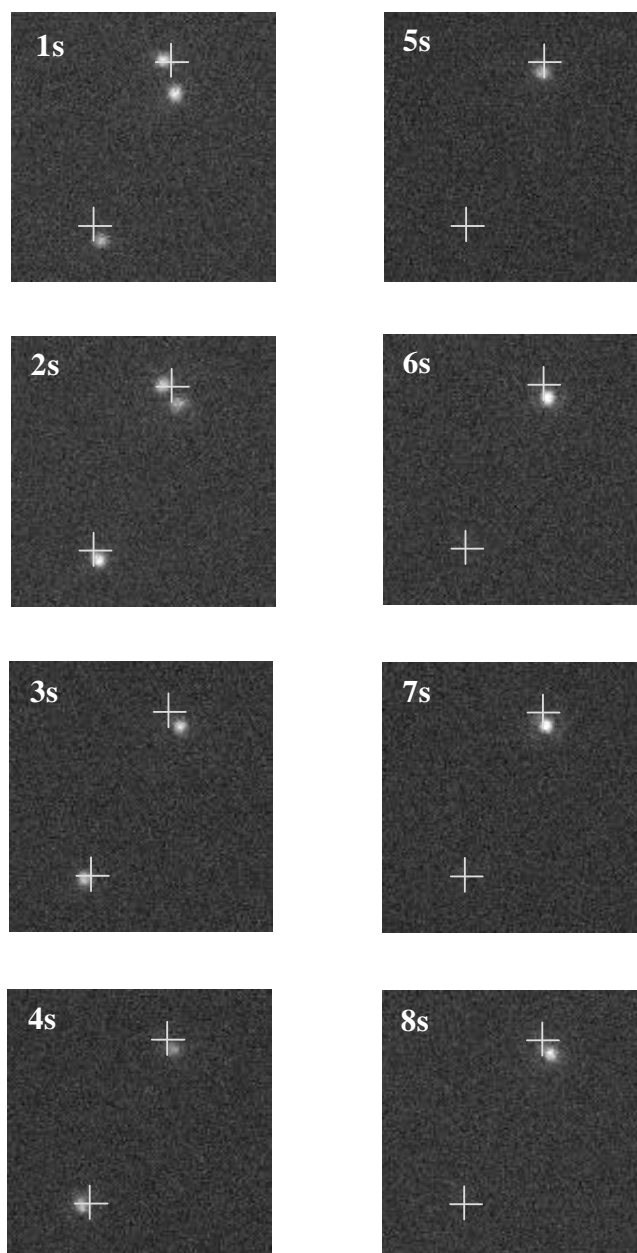


Figure 5.11. Time series of eight fluorescence images of two single RB molecules on glass surface illuminated by TIR method and recorded by CCD camera. Acquisition time, 1 s; size, 8 μm by 8 μm . The single molecules showed translation motion around the two 1 μm sized crosses.

this case should be random interchange among a bright state and multiple dark states. The bright state should be similar to the normal electronic transition cycles in vacuum. There should be multiple number of dark states because the decay dynamics in Figure 5.7a would be single exponential if there were only one dark state^{42,55}, but it was fitted well to double exponential. The double exponential was chosen arbitrarily but it worked well. Similar conclusion was drawn from the SMD of DiIC₁₂ on cover glass by Weston et al. through eliminating several conceivable mechanisms: rotational motion, shelving on triplet state, absorption cross section change by spectral shift^{42,66}. However, the experimental verification of dark radical formation was done on R6G trapped in poly(vinyl alcohol) matrix not on RB on glass. We provisionally attribute the large intensity fluctuation in millisecond time scale to the dynamic formation of radical dark states. In conclusion, it is possible to narrow down the possible mechanisms of intensity fluctuation of RB on glass by measuring lifetime of high and low intensity durations, but the question has not been answered and further study is necessary.

III.B. Single Molecule Fluorescence Lifetime

The SMFL distributions of RB on glass surface shown in Figure 5.6 is sharper than those of RB on ATO shown in Figure 4.14. Taking into account of the inertness of RB's environment in terms of quenching of excited state, we may expect a sharper distribution or rather an almost definite lifetime. However, the measured distributions in Figure 5.6 had reproducible FWHM of about 0.35 ns. Before we investigate the origin of the broadening mechanism, the validity of the presented distribution should be checked. For the method of validity check, we would use the result of the virtual SMFL test introduced

in Section III.C of Chapter 3. There, we demonstrated the statistical fluctuation of the lifetime of the virtual light source of constant lifetime. The standard deviation σ of the statistical lifetime fluctuation turned out to depend on the number of photon counts used in calculating the lifetime (or total counts) and the magnitude of lifetime. Therefore, we can express the credibility of each SMFL value included in the lifetime distribution by the standard deviation, referring to the lifetime and total counts of recorded fluorescence decay. To display the lifetime and total counts, the SMFL distribution graph in Figure 5.6a is re-drawn in total count-lifetime format as shown in Figure 5.12. Each dot stands for the SMD of a molecule. Its x coordinate is SMFL and y coordinate is the total photon counts. Based on the virtual SMFL data shown in Figure 3.22 and 3.23, we could draw the thick gray line representing a border over which the σ of statistical fluctuation of

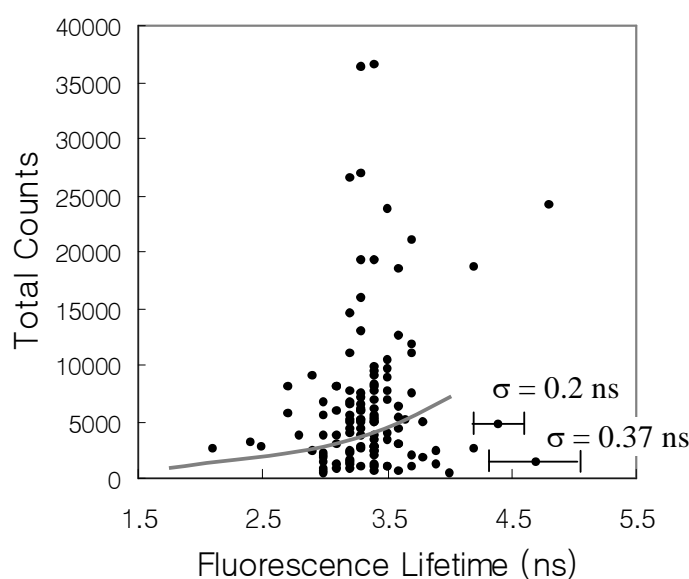


Figure 5.12. Total counts vs. lifetime plot of the data included in the histogram in Figure 5.6a. The thick gray curve divides the population into two groups: SMFL of lifetime fluctuation σ lower than 0.1 (over the curve) and higher than 0.1 (below the curve).

SMFL was less than 0.1 ns and below which higher than 0.1 ns. We postulate that the SMFL data over the gray line did not change true SMFL distribution; and those below the gray line were so uncertain that the possible range of true distribution should be estimated. If we construct, in mind, a distribution of the SMFLs only over the gray line, we can say that their true distribution would range from 2.5 ns to 3.7 ns plus two points over 4 ns in accordance with the postulate. It is similar to the measured total distribution in Figure 5.6a. Let's see the lower limit of the error bars of the two SMFL data in Figure 5.12 because it is doubted that the distribution was fictitiously broad. Their true values were within the ranges marked by the error bars with 68% credibility. Their lower limits are higher than 3.8 ns. In addition, the probabilities of the true values being at the center of distribution (3.4 ns) were 10^3 and 10^7 time lower than the probabilities at 4.4 ns and 4.7 ns, respectively. Briefly speaking, the widths of the distributions over and below the thick gray curve are similar. In conclusion, the probability of the true distribution being much sharper or a definite value is so low that the measured distribution is valid.

Given the fluorescence lifetime distribution, the magnitude and pattern of distribution is intriguing. It is not just a RB SMFL distribution without electron transfer and may not be the best blank test for the SMFL distribution of RB on ATO because their morphologies are completely different from each other. Setting aside the ET process, the nanoporous dielectric environment and the finite dielectric geometry modified the lifetime of adsorbate in different manners while there should be a unified nature in them. To understand the distribution of RB SMFLs on glass surface, we applied the classical optical mechanism described in Section III.B of Chapter 2 for semi-empirical SMFL distribution. An important result of the theory for the analysis of the observed

distributions is Equation 2.21. Because the reciprocal of fluorescence lifetime is a sum of the reciprocals of radiative and non-radiative lifetimes, the full expression for the fluorescence lifetime is:

$$\frac{1}{\tau} = \frac{1}{\tau_{non-rad}} + \frac{1}{\tau_{rad}} \left[\left(\frac{L_{\perp}(z_0)}{L_{\infty}} \right) \cos^2 \theta + \left(\frac{L_{\parallel}(z_0)}{L_{\infty}} \right) \sin^2 \theta \right] \quad (5.3)$$

where, τ is the fluorescence lifetime, τ_{rad} is the radiative decay lifetime when the molecule is in the air far way from the surface. $\tau_{non-rad}$ is the non-radiative decay lifetime. θ is the polar angle of the emission dipole relative to the surface normal. $L_{\parallel}(z_0)$ and $L_{\perp}(z_0)$ are the emission powers of the dipole, at distance $z_0 \sim 5\text{\AA}$, in horizontal and vertical directions to the surface of substrate respectively. L_{∞} is the power when the dipole is far away (\gg emission wavelength) from the surface. The $1/\tau_{non-rad}$ ($=k_{non-rad}$) term is set to 0 because the quantum yield of RB on glass is expected to be 1. The τ_{rad} was either 8.03 ns, 9.50 ns, or 5.43 ns in Section III.A.3 of Chapter 4 depending on the model used in calculating the radiative lifetime in the medium of refractive index 1. We have to choose any one of the three theoretical τ_{rad} values to plot τ as a function of θ using Equation 5.3. The fully microscopic model was supported by the recent experimental study²⁹ (Section III.A of Chapter 2). Similar comparison using published data was done in Figure 4.27 even though the solvent molecules were in contact with solute dye molecules; again, the fully microscopic model fitted to the data best. We chose the 5.43 ns from the fully microscopic model. We plotted the theoretical lifetime curve of Equation 5.3 as a function of θ and compared it with our experimental distributions. They are shown in Figure 5.13. The possible lifetime value curve is in graph C using the 5.43 ns for the τ_{rad} .

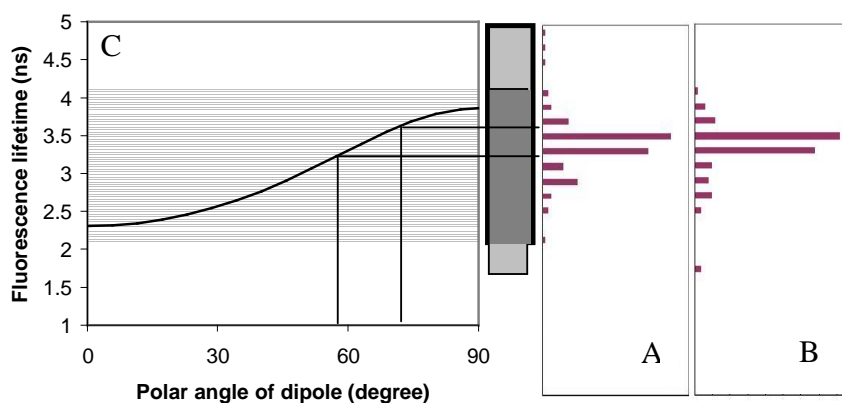


Figure 5.13. Polar angle dependence of fluorescence lifetime. The theoretically expected lifetime range matches well with experimentally observed SMFL distribution. The most probable lifetime range 3.2 ns ~ 3.6 ns corresponds to the polar angle range $57^\circ \sim 74^\circ$.

The two distributions A and B are taken from Figure 5.6: ordinates of them are lifetime axes that share the scales of graph C and abscissas are the occurrences in arbitrary unit. The ranges of distribution of A and B are represented by the gray colored areas with thick and thin border lines, respectively, between the graph C and A. The darker region is the overlapped range of the two distributions. There are 5 molecules outside the overlapped range. Three of the five molecules had the statistical fluctuations of lifetime less than 0.1 ns, which means that the 3 molecules were highly likely a part of true distribution. However, the total number of molecules is 225. The 5 observations out of 225 may be neglected as an impurity, dimer, or unknowns. The overlapped lifetime range is from 2.1 ns to 4.1 ns and marked by the shaded region in plot C. It matches well with the possible lifetime curve, based on (1) the vacuum (or air) radiative lifetime calculated by fully microscopic model local field correction and (2) orientation dependent extra power

emission. The shaded region in plot C overfills the possible lifetime curve by 0.2 ns in the upper limit and 0.15 ns in the bottom limit. The two bars in each graph occupy about 70% of population, which fall within the polar angle range from 57° to 74° . Average lifetime is 3.4 ns and it corresponds to 66° . Surprisingly, it is in good agreement with the reported values measured by other methods. Polarized UV-Vis study showed that RB on Saponite silicates film made 60.7° to surface normal⁶⁷. Using two- and one-photon microscopy, RB on silica was measured to make $49\pm 11^\circ \sim 59\pm 7^\circ$ polar angle⁶⁸. Looking at the AFM image in Figure 3.1, we can explain the polar angle without fancy reasoning by saying that the approximately 1 nm-sized RB single molecule may naturally be tilted appreciably on the about 1 nm-height corrugated glass surface.

IV. Conclusion

The intensity trajectories of single RB molecules turned out to be apparently different depending on the substrates, glass and nanoporous ATO. The previous opinions of the high fluctuation of RB on glass were reviewed and filtered by data acquired in this study. The high fluctuation of intensity is presumably ascribed to the formation of characteristic high yield of dark state on glass surface. The SMFL distribution of RB on glass was explained by classical electrodynamics theory. In combination with the fully microscopic model, the range of SMFL distribution anticipated by those theories was comparable with the measured SMFL distributions.

References

- (1) Lukosz, W.; Kunz, R. E. *J. Opt. Soc. Am.* **1977**, *67*, 1607.
- (2) Lukosz, W.; Kunz, R. E. *Optics Communications* **1977**, *20*, 195.
- (3) Arnoldus, H. F.; Foley, J. T. *OPTICS LETTERS* **2003**, *28*, 1299.
- (4) Macklin, J. J.; Trautman, J. K.; Harris, T. D.; Brus, L. E. *Science* **1996**, *272*, 255.
- (5) Vallee, R.; Tomczak, N.; Gersen, H.; Dijk, E. M. H. P. v.; Garcia-Parajo, M. F.; Vancso, G. J.; Hulst, N. F. v. *Chem. Phys. Lett.* **2001**, *348*, 161.
- (6) Kreiter, M.; Prummer, M.; Hecht, B.; Wild, U. P. *Journal of Chemical Physics* **2002**, *117*, 9430.
- (7) Drexhage, K. H. *J. Lumin.* **1970**, *1/2*, 693.
- (8) Drexhage, K. H. *Sci. Am.* **1970**, *222*, 108.
- (9) Tews, K. H. *Journal of Luminescence* **1974**, *9*, 223.
- (10) Chance, R. R.; Prock, A.; Silbey, R. *The Journal of Chemical Physics* **1975**, *62*, 2245.
- (11) Chance, R. R.; Miller, A. H.; Prock, A.; Silbey, R. *The Journal of Chemical Physics* **1975**, *63*, 1589.
- (12) Chance, R. R.; Prock, A.; Silbey, R. *The Journal of Chemical Physics* **1974**, *60*, 2184.
- (13) Moini, S.; Puri, A.; Das, P. C. *Journal of Chemical Physics* **1993**, *98*, 746.
- (14) Alivisatos, A. P.; Arndt, M. F.; Efrima, S.; Waldeck, D. H.; Harris, C. B. *Journal of Chemical Physics* **1987**, *86*, 6540.

- (15) Whitmore, P. M.; Alivisatos, A. P.; Harris, C. B. *Physical Review Letters* **1983**, *50*, 1092.
- (16) Hayashi, T.; Castner, T. G.; Boyd, R. W. *Chem. Phys. Lett.* **1983**, *94*, 461.
- (17) Sluch, M. I.; Vitukhnovsky, A. G.; Petty, M. C. *Physics Letters A* **1995**, *200*, 61.
- (18) Lukosz, W.; Kunz, R. E. *Optics Communications* **1979**, *31*, 42.
- (19) Lukosz, W.; Kunz, R. E. *J. Opt. Soc. Am.* **1977**, *67*, 1615.
- (20) Parent, G.; Labeke, D. V.; Barchiesi, D. *J. Opt. Soc. Am. A* **1999**, *16*, 896.
- (21) Rahmani, A.; Chaumet, P. C.; Fornel, F. d. *Physical Review A* **2001**, *63*, 023819.
- (22) Hellen, E. H.; Axelrod, D. *J. Opt. Soc. Am. B* **1987**, *4*, 337.
- (23) Lu, H. P.; Xie, X. S. *J. Phys. Chem. B* **1997**, *101*, 2753.
- (24) Lee, M.; Kim, J.; Tang, J.; Hochstrasser, R. M. *Chemical Physics Letters* **2002**, *359*, 412.
- (25) Karstens, T.; Kobs, K. *The Journal of Physical Chemistry* **1980**, *84*, 1871.
- (26) Snare, M. J.; Treloar, F. E.; Ghiggino, K. P.; Thistlethwaite, P. J. *Journal of Photochemistry* **1982**, *18*, 335.
- (27) Ferrer, M. L.; Monte, F. d.; Levy, D. *Langmuir* **2003**, *19*, 2782.
- (28) Crenshaw, M. E.; Bowden, C. M. *Physical Review Letters* **2000**, *85*, 1851.
- (29) Wuister, S. F.; Donega, C. d. M.; Meijerink, A. *Journal of Chemical Physics* **2004**, *121*, 4310.
- (30) Lide, D. R. *CRC handbook of chemistry and physics: a ready-reference book of chemical and physical data*; CRC Press: Boca Raton, 2005.

- (31) *Polymer Handbook*; 4th ed.; Wiley: New York, 1999.
- (32) Zondervan, R.; Kulzer, F.; Orlinskii, S. B.; Orrit, M. *J. Phys. Chem. A* **2003**, *107*, 6770.
- (33) Hou, Y.; Higgins, D. A. *Journal of Physical Chemistry B* **2002**, *106*, 10306.
- (34) Wang, H.; Bardo, A. M.; Collinson, M. M.; Higgins, D. A. *J. Phys. Chem. B* **1998**, *102*, 7231.
- (35) Magde, D.; Rojas, G. E.; Seybold, P. G. *Photochemistry and Photobiology* **1999**, *70*, 737.
- (36) Sadkowski, P. J.; Fleming, G. R. *Chem. Phys. Lett.* **1978**, *57*, 526.
- (37) Shimizu, K. T.; Neuhauser, R. G.; Leatherdale, C. A.; Empedocles, S. A.; Woo, W. K.; Bawendi, M. G. *Physical Review B* **2001**, *63*, 205316.
- (38) Bernard, J.; Fleury, L.; Talon, H.; Orrit, M. *Journal of Chemical Physics* **1993**, *98*, 850.
- (39) Dickson, R. M.; Cubitt, A. B.; Tsien, R. Y.; Moerner, W. E. *Nature* **1997**, *388*, 355.
- (40) Kuno, M.; Fromm, D. P.; Hamann, H. F.; Gallagher, A.; Nesbitt, D. J. *Journal of Chemical Physics* **2000**, *112*, 3117.
- (41) Nirmal, M.; Dabbousi, B. O.; Bawendi, M. G.; Macklin, J. J.; Trautman, J. K.; Harris, T. D.; Brus, L. E. *Nature* **1996**, *383*, 802.
- (42) Weston, K. D.; Carson, P. J.; Metiu, H.; Buratto, S. K. *Journal of Chemical Physics* **1998**, *109*, 7474.

- (43) Kuno, M.; Fromm, D. P.; Hamann, H. F.; Gallagher, A.; Nesbitt, D. J. *Journal of Chemical Physics* **2001**, *115*, 1028.
- (44) Verberk, R.; Orrit, M. *Journal of Chemical Physics* **2003**, *119*, 2214.
- (45) Molski, A.; Hofkens, J.; Gensch, T.; Boens, N.; Schryver, F. D. *Chem. Phys. Lett.* **2000**, *318*, 325.
- (46) Efros, A. L.; Rosen, M. *Physical Review Letters* **1997**, *78*, 1110.
- (47) Novikov, E.; Hofkens, J.; Cotlet, M.; Maus, M.; Schryver, F. C. D.; Boens, N. *Spectrochimica Acta Part A* **2001**, *57*, 2109.
- (48) Jung, Y.; Barkai, E.; Silbey, R. J. *Adv. Chem. Phys.* **2002**, *123*, 199.
- (49) Yip, W.-T.; Hu, D.; Yu, J.; Bout, D. A. V.; Barbara, P. F. *Journal of Physical Chemistry A* **1998**, *102*, 7564.
- (50) McHale, J. L. *Molecular Spectroscopy*; Prentice Hall: Upper Saddle River, N.J., 1999.
- (51) Berne, B. J. *Dynamic Light Scattering*; Wiley: New York, 1976.
- (52) McQuarrie, D. A. *Statistical Mechanics*; University Science Books: Sausalito, Calif., 2000.
- (53) Lu, H. P.; Xie, X. S. *Nature* **1997**, *385*, 143.
- (54) Risken, H. *The Fokker-Planck Equation: Methods of Solution and Applications*; Springer-Verlag: Berlin; New York, 1989.
- (55) Yang, H.; Xie, X. S. *Chemical Physics* **2002**, *284*, 423.
- (56) Menzel, R.; Bornemann, R.; Thiel, E. *Phys. Chem. Chem. Phys.* **1999**, *1*, 2435.

- (57) Martynski, M.; Zydlewicz, J.; Boens, N.; Molski, A. *Journal of Chemical Physics* **2005**, *122*, 134507.
- (58) Ambrose, W. P.; Goodwin, P. M.; Martin, J. C.; Keller, R. A. *Physical Review Letters* **1994**, *72*, 160.
- (59) Ha, T.; Enderle, T.; Chemla, D. S.; Selvin, P. R.; Weiss, S. *Chem. Phys. Lett.* **1997**, *271*, 1.
- (60) English, D. S.; Furube, A.; Barbara, P. F. *Chem. Phys. Lett.* **2000**, *324*, 15.
- (61) Gollnick, K.; Franken, T.; Fouda, M. F. R. *Tetrahedron Letters* **1981**, *22*, 4049.
- (62) Grabowski, Z. R.; Rotkiewicz, K. *Chem. Rev.* **2003**, *103*, 3899.
- (63) Casey, K. G.; Quitevis, E. L. *J. Phys. Chem.* **1988**, *92*, 6590.
- (64) El-Kemary, M.; Rettig, W. *Phys. Chem. Chem. Phys.* **2003**, *5*, 5221.
- (65) Bartko, A. P.; Dickson, R. M. *Journal of Physical Chemistry B* **1999**, *103*, 11237.
- (66) Weston, K. D.; Buratto, S. K. *Journal of Physical Chemistry A* **1998**, *102*, 3635.
- (67) Bujadak, J.; Iyi, N. *J. Phys. Chem. B* **2005**, *109*, 4608.
- (68) Bopp, M. A.; Jia, Y.; Haran, G.; Morlino, E. A.; Hochstrasser, R. M. *Applied Physics Letters* **1998**, *73*, 7.

Chapter 6. Single Molecule Detection of PDI-P1 on Nanocrystalline

Thin films

I. Introduction

Perylene-3,4:9,10-bis(dicarboximide) (PDI) and its derivatives have been intensely studied for their applications to the active element of molecular electronics¹⁻³, organic field effect transistor⁴, and solar cell⁵⁻⁷, optical switching^{8,9}, etc. Integral processes in the applications are interfacial charge transfer through molecular junction^{2,8,9}, charge transport through molecular crystals^{4,6}, charge and energy transfer through excitonic aggregate^{5,7}, etc. The reason for the PDI being shed light on in those studies is its outstanding photochemical properties. The PDI has low triplet yield approximately 0.005¹⁰, quantum yield close to 1¹⁰⁻¹², high photochemical stability^{13,14}, and efficient π -stacking^{5,13}, which made the PDI an ideal material for those studies and for the realization of the devices. Different from conventional solid-state devices, the organic molecule-based electronic and photonic devices can be modified and improved substantially by controlling the molecular properties. That is, the critical process resides in the scale and function of the junction of individual molecule and electrode. As a matter of course, the behavior of individual molecule has become of great importance, and the detection in single molecule level has been valued.

Figure 6.1 is the structure of PDI-P1 derivative used in this study. Octyl and benzoic acid is substituted at the N and N' atoms in the two imide rings, and two *tert*-butylphenoxy groups are substituted at the 1,7-positions of perylene skeleton of PDI. The dipole moment for the electronic transition is along the long axis of the molecule¹⁵. An

advantageous characteristic of the PDI is that its optical property does not change appreciably by substituting functional groups at N and N' positions¹⁵. According to the molecular orbital calculations, its HOMO and LUMO orbitals have nodes at the two nitrogen atoms in the imide rings^{16,17}. This feature enables chemists to design diverse PDI derivatives maintaining its basic optical and electronic property. Figure 6.2 is the absorption and emission spectra of 10^{-5} and 10^{-6} M, respectively, PDI-P1 solution in MeOH. Excitation wavelength 498 nm is marked by arrow. It has been known that the PDI-P1 and other PDI-derivatives similar to the PDI-P1 form H-aggregate and the peak corresponding to the transition $S_0 \rightarrow S_{1,v=1}$ ¹⁴ develops as the concentration of the aggregate increases^{13,18}. The ability of forming aggregate and molecular crystal by the van der Waals interaction through the extended π orbitals is required for some applications^{4,5,19} but has to be inhibited for single molecule detection. The two tert-butylphenoxy groups substituted at the perylene skeleton reduce the tendency of aggregation. The PDI-P1 solution used in this work seems not to form aggregate up to 10^{-5} M or higher concentration based on the irrelevance of fluorescence lifetime with

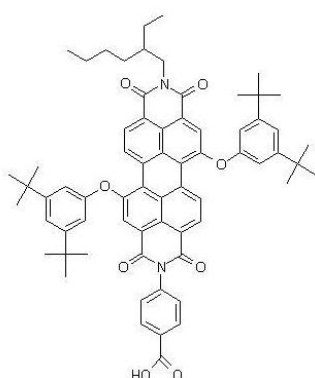


Figure 6.1. Chemical structure of PDI-P1 [*N*-octyl-1,7(3',5' di-*tert*-butylphenoxy)perylene-3,4:4,10-bis(dicarboximide)-benzoic acid].

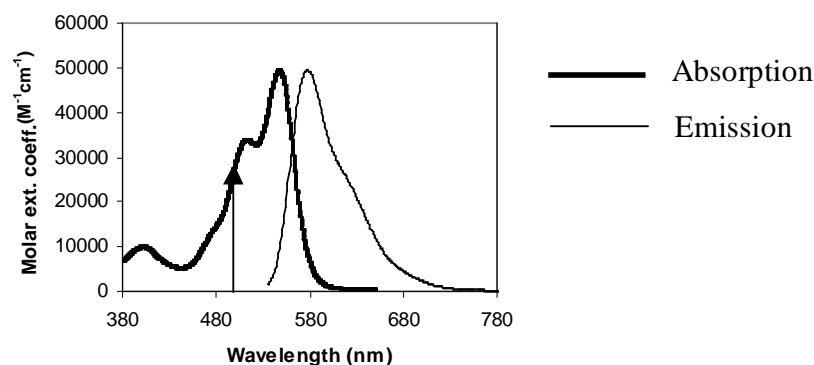


Figure 6.2. Absorption (thick, 10^{-5} M) and emission (thin, 10^{-6} M) spectra of PDI-P1 in MeOH. The wavelength of excitation is marked by the arrow.

concentration assuming that the lifetime of PDI-P1 solution changes when it forms aggregate. The spectroscopic effect of the tert-butylphenoxy groups is a bathochromic shift^{10,20-23}.

In this work, nanoporous ATO thin film was sensitized with the PDI-P1 molecules in a single molecule level surface concentration. Electron transfer at the individual PDI-P1--ATO junction was observed using the confocal microscope described in Chapter 3. Also studied are PDI-P1/ZrO₂ and PDI-P1/glass as a non-interacting case. The energetics of the PDI-P1, ATO, and ZrO₂ system is schematically depicted in Figure 6.3^{5,10,24-27}. Trap states and bottom levels of conduction band of ATO (10% doping level²⁸) was filled with excess electrons by n-type doping, which shift up Fermi level (E_f) by ~ 0.09 eV above the conduction band edge²⁸. Excited state of PDI-P1 is about 0.8 eV higher (1 eV lower) than the conduction band edge of ATO (ZrO₂). An electron is transferred from the discrete level in the electronic excited state of PDI-P1 to the high-density states in the conduction band of ATO. The constant population of electrons in the

trap states and bottom of conduction band secures back electron transfer. Electron transfer to the conduction band of ZrO_2 is not allowed energetically. Similarly to the RB/ATO in Chapter 4, ultrafast electron transfer from the singlet excited state to the conduction band of ATO has been observed using transient IR absorption of electron signal in ATO nanoparticles²⁸. The back electron transfer kinetics $\text{ATO} \rightarrow \text{PDI-P1}$ was also similar to the $\text{ATO} \rightarrow \text{RB}$ and $\text{ATO} \rightarrow \text{Re}(\text{dpbpy})(\text{CO})_3\text{Cl}$ governed by pseudo-first order rate²⁸. The fast quenching due to ultrafast electron transfer also worked in PDI-P1/ATO. It reduced quantum yield of adsorbed PDI-P1, which made large portion of

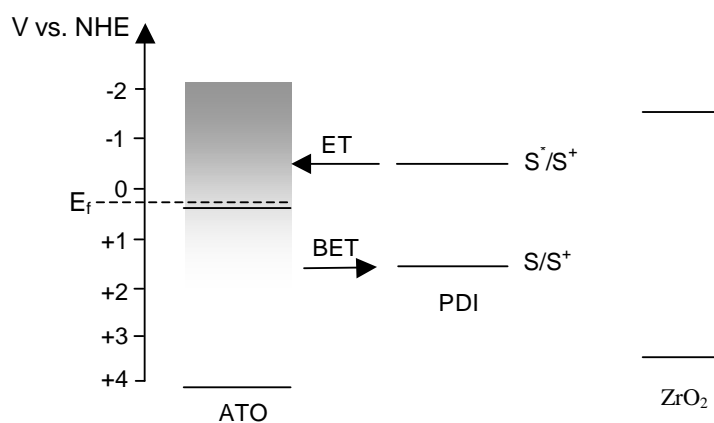


Figure 6.3. Schematic diagram of redox potential energies of valence and conduction bands of ATO, ZrO_2 , and ground and excited states of PDI-P1^{5,10,24-27}. E_f is the Fermi energy level of ATO of 10%²⁸ doping level. Excited state of PDI-P1 is about 0.8 eV higher (1 eV lower) than the conduction band edge of ATO (ZrO_2). An electron is transferred from the discrete level in the electronic excited state of PDI-P1 to the high-density states in the conduction band of ATO. The constant population of electrons in the trap states and bottom of conduction band secures back electron transfer. Electron transfer to the conduction band of ZrO_2 is not allowed energetically.

PDI-P1 molecules not detectable. However, an appreciable number of slowly injecting molecules were detected by using SOR procedure (Section III.A in Chapter 3) with the lowest threshold of sampling. Among the detected molecules, the fastest characteristic time of electron transfer was 210 ps. The irreversible photo-bleach that would work in PDI-P1/SnO₂ was relieved by the electrons abundant in the trap state and conduction band. The electrons played a critical role in the SMD as a constant electron source for the back electron transfer.

For comparison with PDI-P1 on ET-inactive substrate, we investigated PDI-P1/glass and PDI-P1/ZrO₂ following the method of RB/glass and RB/ZrO₂. The unexpected lifetime dispersion of RB/glass was explained by the enhancement of radiative decay due to the power loss through evanescent field near the flat dielectric interface²⁹⁻³¹ (Section III.B in Chapter 2). It was suggested that the intricate dielectric structure of nanoporous film having high conduction band edge like ZrO₂ made the lifetime dispersion due to the spatial heterogeneity of effective refractive index of nanoporous film in Chapter 4. Those mechanisms will be applied to the analysis of experimental data as the postulates. Special observations of dynamical lifetime change were made in PDI-P1/ATO and PDI-P1/glass. It is considered that the dynamic change of lifetime is driven by the conformation fluctuation of PDI-P1 dye pivoted on the oxide surfaces.

This chapter begins with the experimental results of fluorescence detection of bulk PDI-P1 on ATO, glass, and ZrO₂ in Section II.A mainly focusing on the prediction of single molecule lifetime distribution. In Section II.B, the SMD results presented and compared with bulk results. Several pieces of observations of dynamic lifetime

fluctuation will also be presented. In Section III, discussion and additional analysis of the results will be given.

II. Results

II.A. Bulk Test of PDI-P1 on ATO

A nanoporous ATO film was soaked in 10^{-7} M PDI-P1 solution in DMF for 13 min following the method introduced in Section I.C of Chapter 3. The sample was loaded on the microscope introduced in Chapter 3 and the pulsed 498 nm laser was focused on the sample surface with 35 W/cm^2 intensity. Fluorescence images were taken and an example

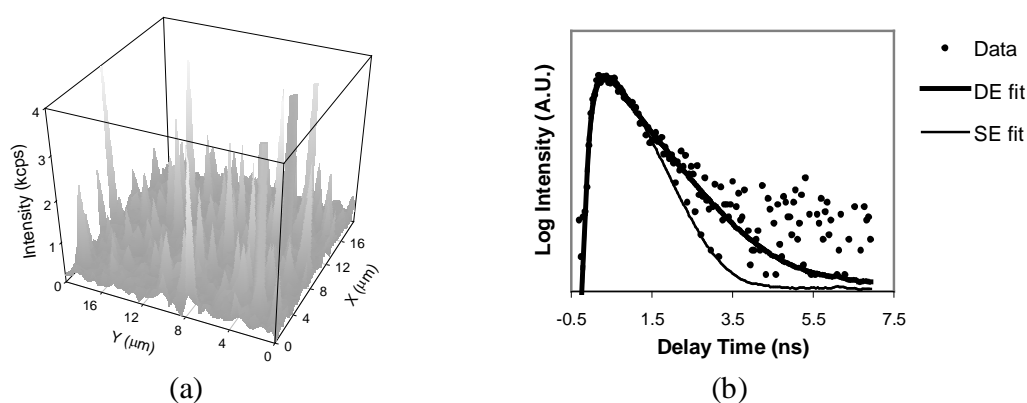


Figure 6.4. (a) Fluorescence image of a bulk PDI-P1 on ATO sample. $20 \mu\text{m} \times 20 \mu\text{m}$ area with 50×50 pixels. A nanoporous ATO film is sensitized with 10^{-7}M PDI-P1 in DMF for 13 min. (b) Single and double exponential fitting of fluorescence decay profile of the sample shown in (a). The fitted lifetimes of double exponential model are (99%) 0.13 ns and (1%) 0.85 ns with reduced chi square 17. The fitted lifetime of single exponential model is 0.4 ns with reduced chi square 40. The double exponential model is fitted to the measured decay better than single exponential.

Model	τ_1 (ns)	A_1 (%)	τ_2 (ns)	A_2 (%)	χ^2_r
Single Exponential	0.4	100			40
Double Exponential	0.13	99	0.85	1	17

Table 6.1. Fitting result of bulk fluorescence lifetime decay shown in Figure 6.4. τ_i and A_i are the lifetime and amplitude of exponential decay model.

is shown in Figure 6.4a. The intensity on the image was not homogeneous due to the spatial heterogeneity of electron transfer efficiency and number density of dye molecules. The fluorescence decay profile of the total recorded TCSPC data is shown in Figure 6.4b. Y axis is drawn in log scale. Single and double exponential models were fitted to the measured decay and the result is summarized in table 6.1. The two reduced chi square χ^2_r values suggest that the double exponential fitted to experimental decay much better than single exponential model. It is apparent graphically in Figure 6.4b. The double exponential does not represent all the decay components present and multi-exponential model of the higher number of single exponential components would fit to the data the better. Figure 6.5 shows the fitting of triple exponential model to a bulk data. The χ^2_r was reduced to 2.6. The multi-exponential characteristic of PDI-P1 on nanocrystalline ATO is similar to the result of RB on ATO shown in Section II.A of Chap. 4.

II.B. Bulk Test of PDI-P1 on Glass

As an ET-inert substrate, glass was chosen and bulk PDI-P1 on a cover glass was tested. 1.0×10^{-8} M PDI-P1 solution in MeOH was dropped on a cover glass by 3 μ L and MeOH

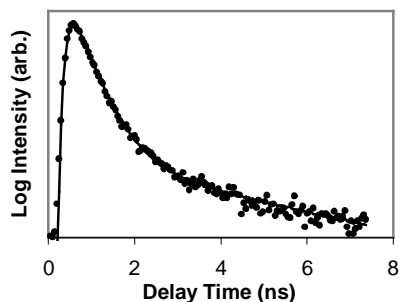


Figure 6.5. Fluorescence decay profile of a bulk PDI-P1/ATO. The fitted lifetimes of triple exponential model are (98.9%) 0.014 ns, (0.9%) 0.48 ns, and (0.2%) 3.9 ns with reduced chi square 2.6.

was evaporated. The pulsed 498 nm laser was focused on the sample surface with 35 W/cm² intensity. Fluorescence intensity map and decay profile are shown in Figure 6.6. Fitting of single exponential model to the measured decay is in (b) and the calculated lifetime is 3.7 ns with $\chi^2_r = 1.6$. The decay profile in (b) is nearly a single exponential based on the magnitude of χ^2_r and the overlap of the data and fitted model curve. However, the χ^2_r is higher than the value usually observed for good bulk decay fitting, 1.0 ~ 1.2, and slight deviation from 7 ns is found. The question is the width of SMFL distribution that could be responsible for the deviation from the single exponential if the deviation is not error but real. At first thought, SMFL distribution might look like just a sharp spike for such a slight deviation. To have a sense of the relation between the deviation of data from single exponential and SMFL distribution, three pairs of artificial gaussian distributions and multi-exponential decays built from the corresponding gaussian distributions are compared in Figure 6.7. The gaussian distribution often models inhomogeneous broadening of a random physical variable³²⁻³⁴. The fluorescence lifetime

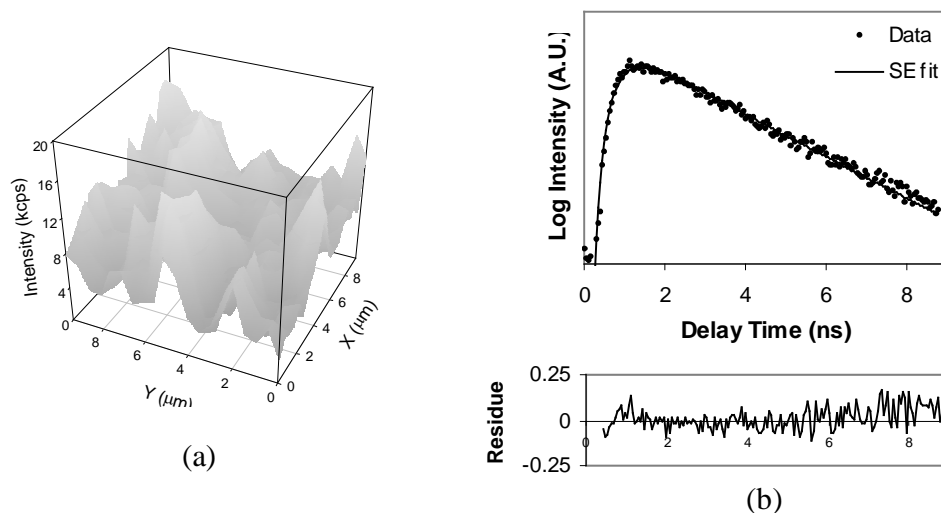


Figure 6.6. Fluorescence measurement of bulk PDI-P1/glass. (a) Intensity map of 10 μm × 10 μm area. (b) Fitting of single exponential model to the decay of fluorescence measured in (a) displayed in Log Y scale. $\tau = 3.7$ ns with $\chi^2_r = 1.6$.

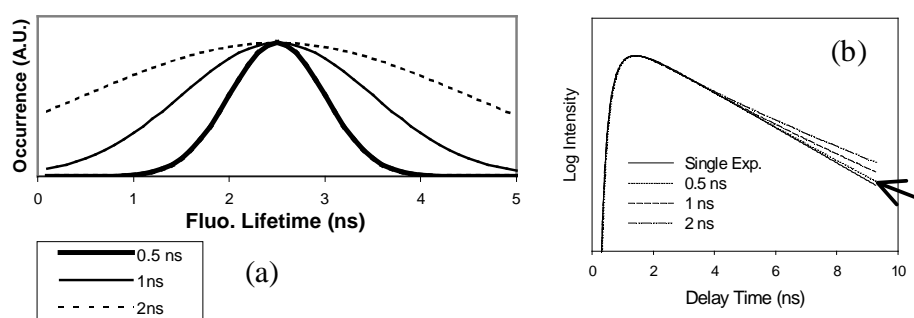


Figure 6.7. (a) Artificial SMFL distributions having different standard deviations σ ; 0.5 ns (thin solid), 1 ns (thick solid), and 2 ns (dashed). (b) Decay curves built from the corresponding distributions in (a). The arrow in (b) marks the similar decay curve to the experimentally measured decay curve in Figure 6.6b.

of PDI-P1 in a disordered dielectric medium would have spatial inhomogeneous broadening. The three artificial distributions are centered at 2.5 ns and have standard deviations 0.5 ns (thick solid), 1 ns (thin solid), and 2 ns (dashed) as drawn in Figure 6.7a. In Figure 6.7b, the artificial decay curves corresponding to the three distributions are drawn using an expression of multi-exponential decay, ME(T):

$$ME(T) = \int_0^{\infty} dt IRF(T-t) \int d\tau e^{-\frac{(\tau-2.5)^2}{2\sigma^2}} \cdot e^{-\frac{t}{\tau}} \quad (6.1)$$

where T is a measurement time; t is the time of signal that contributes to the measured signal at T ; σ is the standard deviation of the gaussian distribution; $IRF()$ is the experimentally recorded instrument response function; and τ is the lifetime that constitutes the lifetime distribution. In Figure 6.7b, the dotted artificial decay curve is pointed by an arrow; it deviated from the single exponential decay (solid line) to a similar degree to the measured one in Figure 6.6b. The corresponding distribution has $\sigma = 0.5$ ns and is plotted in Figure 6.7a (thick solid line). It is surprising that the nearly single exponential decay could have so broad a distribution. The artificial distribution will be compared with experimental SMFL data in later section.

II.C. Bulk Test of PDI-P1 on ZrO₂

By the same motivation as Section II.A of Chap. 4, a blank test using nanoporous ZrO₂ was done. The potential energy of conduction band edge of ZrO₂ is about 1 eV higher than the excited state of PDI-P1 as shown in Figure 6.2 and the electron injection into the ZrO₂ was not energetically allowed. Figure 6.8 shows a result of typical fluorescence test of PDI-P1/ZrO₂. A nanoporous ZrO₂ film was soaked in 10⁻⁷ M PDI-P1 solution in

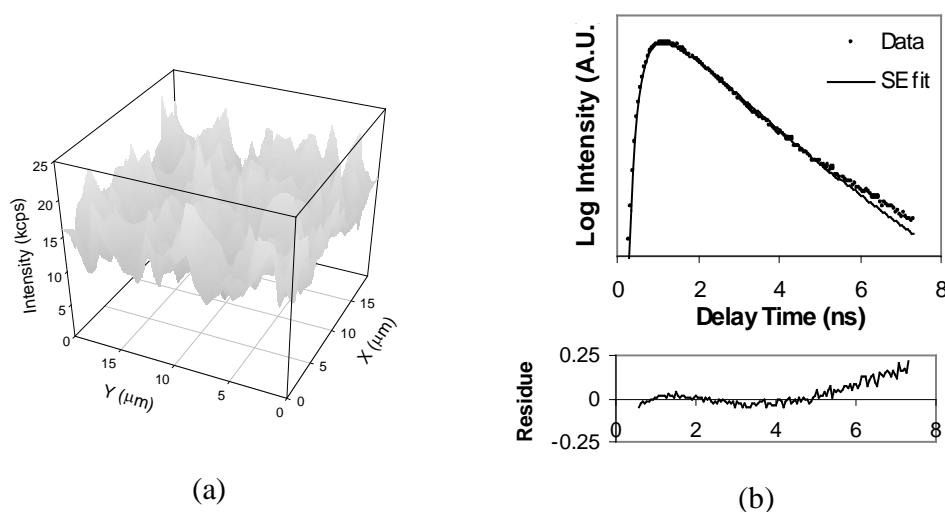


Figure 6.8. Fluorescence measurement of bulk PDI-P1/ZrO₂. (a) Intensity map of 20 μm × 20 μm area. (b) Fitting of single exponential model to the decay of fluorescence measured in (a) displayed in Log Y scale. $\tau = 2.2$ ns with $\chi^2 = 3.4$.

MeOH for 2 min and MeOH was evaporated. The pulsed 498 nm laser was focused on the sample surface with 0.7 W/cm² intensity. The intensity map in Figure 6.8a has similar level of intensity on every pixel, compared to the locale spike-shaped intensity map of the bulk PDI-P1/ATO where significant quenching is going on (Fig. 6.4a). The decay data and its fit of single exponential decay are shown in Figure 6.8b in Log Y scale. Its fluorescence lifetime is 2.2 ns with χ^2 being 3.4. The 2.2 ns is clearly shorter than 3.7 ns of PDI-P1/glass. The shape of the decay curve looks single exponential with slight deviation just as the PDI-P1/glass case. However, the magnitude of χ^2 , noticeable deviation after 5 ns, and the multi-exponential signature of its residue curve in (b) allowed us to predict a finite degree of distribution. Therefore, we take the decay as a multi-exponential and equate the fluorescence decay in Figure 6.8b with the artificial

decay of standard deviation 1.0 ns in Figure 6.7b. The corresponding artificial SMFL distribution in Figure 6.7a looks quite broad for such a little deviation. The artificial distribution will be compared with our experimental SMFL data in later section.

II.D. SMFL Test of PDI-P1 on ATO

Single molecule observation of PDI-P1/ATO has been done by the same method as RB/ATO SMD in Chapter 4. A nanoporous ATO film was soaked in 10^{-7} M PDI-P1 solution in DMF for 13 min following the method introduced in Section I.C of Chapter 3. The pulsed 498 nm laser was focused on the sample surface with 35 W/cm^2 intensity. Figure 6.9 shows that three pairs (A, B, and C) of single molecule fluorescence decay and intensity trajectory. In Figure 6.9a, the three decay data and fitted single exponential curves are plotted. The 0.2 ns decay was one of the fastest one in the PDI-P1/ATO SMFL study. It is clearly separated from the 0.7 ns lifetime decay and the instrument response function (dotted). In Figure 6.9b, the three intensity trajectories paired with the three decay data in (a) are plotted. They were similar to those of RB/ATO: constant and momentary fluctuation. High fluctuation that was dominant in RB/glass (Figure 5.5a) was not observed. There were considerable background signals scattered from ATO. The SMD tests of PDI-P1/ATO have been done four times; each test was done in a day. Figure 6.10 shows the SMFL distributions of the tests. The difference in those tests was the threshold in search procedure for single molecules. The thresholds used are written at the top right corners of the plots. The lower threshold can sample molecules of lower quantum yield better. As a result, the final SMFL distribution measured with the lower threshold has higher portion of molecules quenched by ET. As the threshold increases,

the center of sub-nanosecond population looks shifting to longer lifetime. Molecules having lifetime less than 0.2 ns were not sampled due to their low quantum yield. Short duration of emission was a subsidiary reason for missing molecules. In the experiment (a), the sample stage stopped 150 times when the intensity was higher than 700 cps, but 85 times were not recorded because their durations of emission were too short to make their

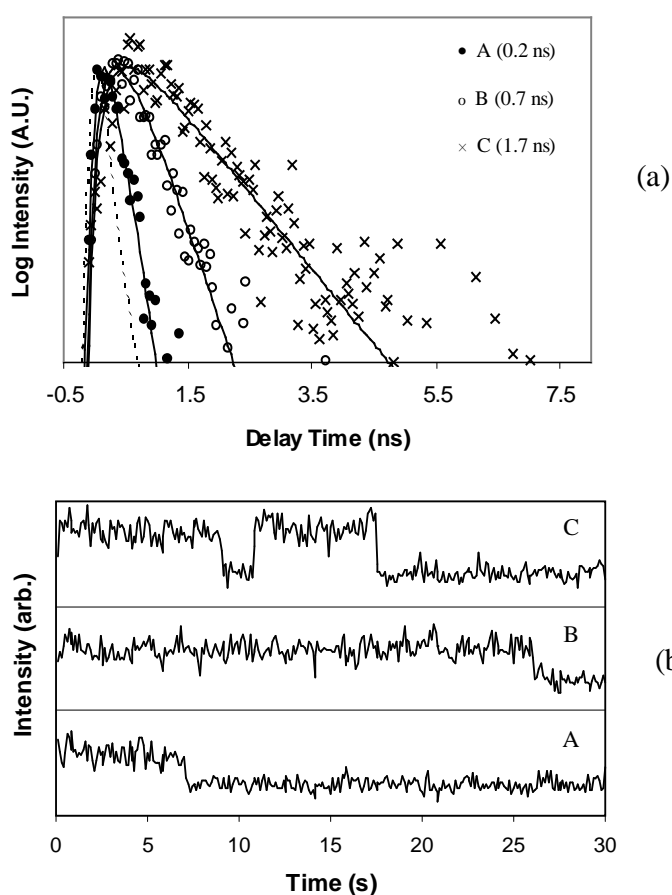


Figure 6.9. (a) Three single molecule fluorescence decays fitted with single exponential decay model. IRF is the dashed curve. Fitted lifetimes are 0.2 ns (•), 0.7 ns (○), and 1.7 ns (×). (b) Intensity trajectories of the three molecules of which fluorescence decays in (a).

decay curves. It is guessed that many of the 85 stops were at the real PDI-P1 molecule and the others were at the impurity and spiky background noise. A clear correlation between the duration of emission and lifetime was not observed. There are appreciable number of molecules over 2 ns that is about the bulk lifetime of PDI-P1/ZrO₂. In Chapter

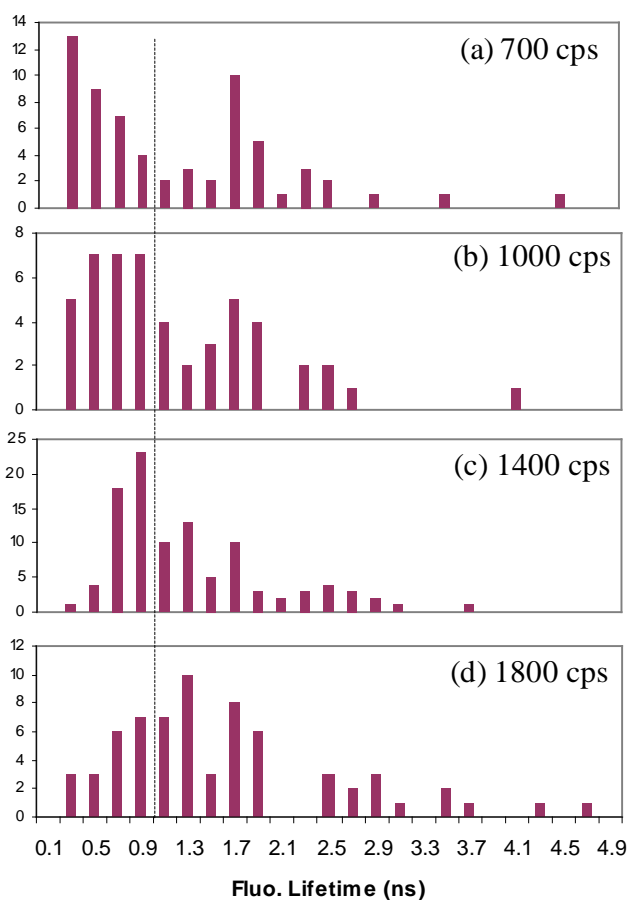


Figure 6.10. Four sets of SMFL distribution measurements done with various sampling threshold. The threshold used in each distribution measurement is written at the top right corner. Total numbers of detected molecules in the tests were 65(a), 50 (b), 103 (c), and 70 (d).

4, the lifetime dispersion in the long lifetime range was ascribed to the local field correction as a function of effective refractive index.

II.E. Single Molecule Fluorescence Lifetime of PDI-P1 on Glass

The bulk lifetime test of PDI-P1/glass in Section II.B was intriguing in its origin that determines the measured value 3.7 ns and the predicted standard deviation of SMFL distribution. To elucidate those problems, single molecule test of PDI-P1 dispersed on a cover glass was performed. 3.3×10^{-9} M PDI-P1 in MeOH solution dropped on a cover glass by $3 \mu\text{L}$ and MeOH was evaporated. The mode-locked 498nm with 35 W/cm^2 intensity. Figure 6.11 shows two fluorescences image before (a) and after (b) the loading of sample solution on the same area. The SMD of PDI-P1/glass seems to be almost free from impurity. The distribution of SMFLs of the sample is shown in Figure 6.12. The average and standard deviation of the distribution are 3.7 ns and 0.6 ns, respectively. The average value coincides with the bulk lifetime fitted to single

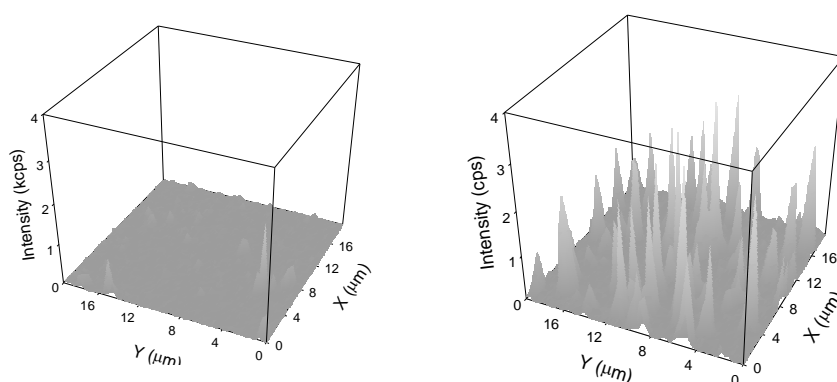


Figure 6.11. Fluorescence images of blank (a) and sample (b) for SMD of PDI-P1/glass.

About 30 peaks are detected on $20 \mu\text{m} \times 20 \mu\text{m}$ area in (b).

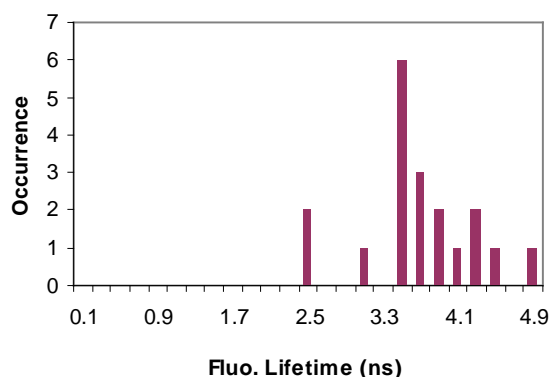


Figure 6.12. SMFL distribution of PDI-P1/glass. Average and standard deviation are 3.7ns and 0.6 ns, respectively.

exponential, 3.7 ns. In section II.B, we expected a SMFL distribution having standard deviation 0.5 ns based on the slight deviation of bulk decay profile from single exponential model decay. The measured standard deviation, 0.6 ns, seems to have satisfied the expected value, 0.5 ns. In conclusion, the bulk and single molecule lifetime measurements were proved to be consistent to each other.

Three pairs of SM fluorescence intensity trajectory and fluorescence lifetime are plotted in Figure 6.13. The fluorescence lifetime trajectories are built by calculating the lifetimes of chunks of TCSPC data of which duration is 2s. The time spacing between adjacent points of the lifetime trajectories is 1s. Each point along the lifetime trajectories is a fitted lifetime of the single exponential decay model to a measured decay built from the 2s TCSPC data. In Figure 6.13a, the intensity trajectory made two clear levels jumping from low to high level. Its fluorescence lifetime trajectory also jumped simultaneously with the intensity trajectory. The fluorescence decay curve of the total trajectory was clearly double exponential (data not shown). Figure 6.13b also shows

positive correlation between intensity and lifetime trajectories. It is interesting that the lifetime trajectory soared up suddenly without any change of intensity right before the irreversible bleach. It has been observed occasionally in SMD of organic dyes. A striking observation is in Figure 6.13c. It shows negative correlation between intensity and

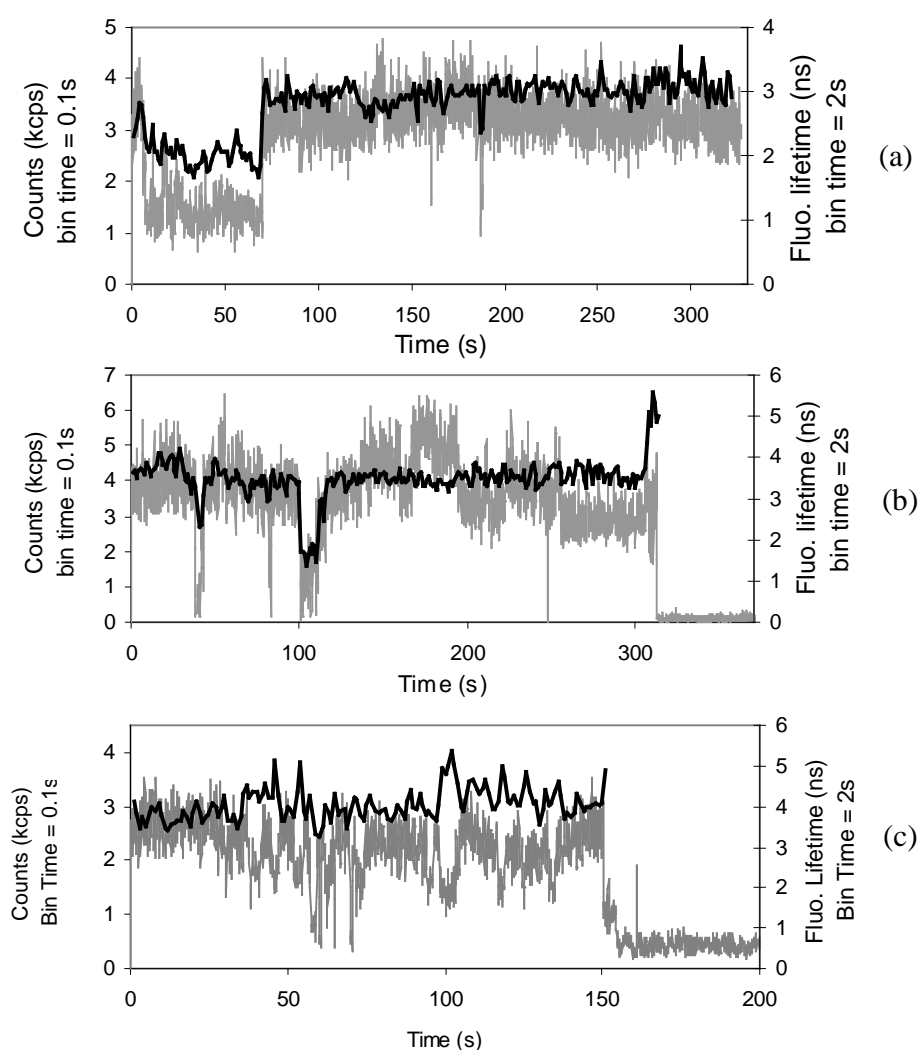


Figure 6.13. Dual plots of fluorescence intensity (thick) and lifetime trajectories (thin) of three SMDs of PDI-P1/glass. Plots (a) and (b) shows positive correlation between intensity and lifetime trajectories while (c) shows clear negative correlation.

lifetime trajectories: the lifetime trajectory changes in the opposite way to the intensity trajectory. Out of total 15 molecules observed, 6 molecules showed positive correlation and 1 molecule showed the negative correlation. The length of intensity trajectories of PDI-P1/glass is dramatically longer than that of PDI-P1/ATO. In Figure 6.14, the distribution of the emission duration of PDI-P1/ATO (gray) and minimum duration of PDI-P1/glass (slashed) are plotted together. The maximum duration of PDI-P1 emission on ATO is similar to the minimum duration on glass. The phenomenon is attributed to the quicker appearance of long dark state of PDI-P1/ATO than the irreversible bleach on glass. As stated in Introduction section, the dark state of PDI-P1/ATO would come much later and last shorter than that of PDI-P1/undoped SnO₂ due to the existence of electrons in trap state and conduction band of PDI-P1/ATO. The implication of the difference in the emission duration is that the electron transfer was certainly involved in the excited state quenching that ended up with the lifetime decrease. The fast bleach of dyes on ATO was attributed to the diffusion of an electron into the nanoporous network of ATO

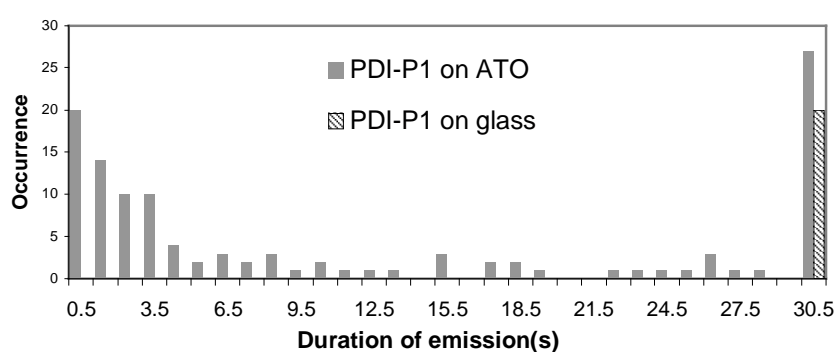


Figure 6.14. Distribution of the SM emission duration of PDI-P1 on ATO and the minimum duration in case of PDI-P1 on glass.

particles after the ET from the excited state of the adsorbed dye in Chapter 4. Another implication is that energy transfer could not be the only mechanism of the excited state quenching because energy transfer does not have a way to transfer electron into the ATO film.

II.F. SMFL of PDI-P1 on ZrO₂

In Section II.C, the fluorescence decay of bulk PDI-P1 on nanoporous ZrO₂ was fitted to a single exponential model with lifetime 2.2 ns and reduced chi square 3.4. The value of lifetime ranged from 2.0 to 2.5 ns depending on the sample. The bulk decay deviated from the single exponential a little and we predicted SMFL distribution of about 1 ns standard deviation based on the decay deviation. The SMFL measurement was done following the typical procedure of SMD. A nanoporous ZrO₂ film was soaked in 10⁻¹² M PDI-P1 solution in DI water for 1 min and washed with 5 ml of water. The pulsed 498 nm laser was focused on the sample surface with 7 W/cm² intensity. Blank test showed insignificant detection of impurity. Figure 6.15 is a resultant distribution of SMFLs of PDI-P1/ZrO₂. The average and standard deviation of the distribution were 2.9 ns and 1.3 ns, respectively. The standard deviation is similar to the expected value 1 ns while the average value is clearly higher than bulk lifetime. Fast components below 0.9 ns were not measured contrary to the distribution of PDI-P1/ATO (Fig. 6.10) because the electron injection into the conduction band of ZrO₂ is not energetically allowed. The distribution looks bell shaped from 0.9 to 4 ns and there are several molecules of long lifetime higher than 4 ns. Taking this PDI-P1/ZrO₂ test as a blank test of PDI-P1/ATO in terms of ET,

we have observed clear lifetime reduction in all four sets of SMD tests of PDI-P1/ATO in Figure 6.10.

III. Discussion

III.A. SM and Bulk Lifetimes of PDI-P1 on ATO

The fastest components of the double and triple exponential decays fitted to the fluorescence decay of the bulk PDI-P1 on ATO were 0.1₃ ns and 0.01₄ ns in Table 1 and Figure 6.5 respectively. Both of them are shorter than the record-shortest SMFL, 0.2 ns, in the SM PDI-P1/ATO study. Below the 0.2 ns, SMFL measurement is difficult because of the low quantum yield resulting from ET. Instrument response function-limited lowest calculable value has been known to be about 5 ps in our detection method. The reasons that made those short lifetime components (0.1₃ ns and 0.01₄ ns) measurable not in single molecule test but in bulk test were as follows: Let's say that there is a molecule that has a lifetime 2ns and emission power 1000 cps on ET-inactive surface. It may have the emission power 50 cps when its lifetime is shortened to 0.1 ns on ATO surface. With the

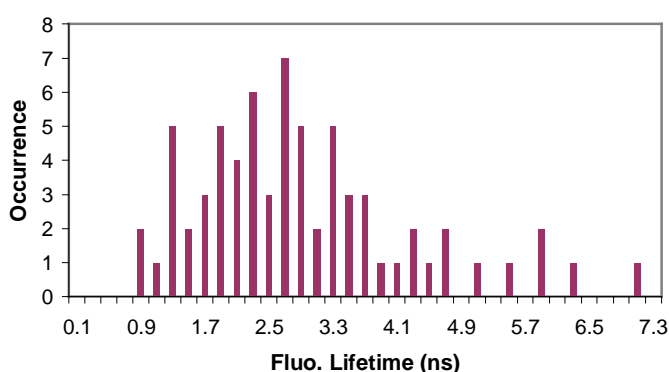


Figure 6.15. SMFL distribution of PDI-P1 on ZrO₂. Average and standard deviation were 2.9 ns and 1.3 ns, respectively.

typical background ~250 cps, the molecule of 50 cps emission power is unlikely to be sampled. Even if the molecule were sampled, we may not be able to collect enough number of photon counts for building decay curve, being limited by the short duration of emission on ET-active surface (Fig. 6.14). In addition, even if the molecule were sampled and survived long enough for building decay curve, the background and 0.1 ns fluorescence decay are hard to be decomposed due to their similar time profile; both of them are nearly instantaneous signal. For those reasons, none of hundreds molecules of 0.1 ns lifetime could be sampled in SMD test and do not appear in SMFL distribution; but all of them could contribute to and appear in bulk decay curve without loss because all the photons emitted by them are included bulk decay curve. The amplitudes in Table 6.1 and Figure 6.5 show that the shorter decay components dominate the total decay dynamics.

Figure 6.16 is the plot of emission power vs. SMFL. The emission power is proportional to the SMFL, which implies that the quenching of excited state was working in the experiment. The threshold dependence of the distribution profile in Figure 6.10 is resultant from the same origin as the emission power dependence on lifetime. The pattern of the plot in Figure 6.16 suggests that even the very slow nanosecond time scale electron transfer seems to be effective in determining the lifetime: 2.9 ns and 1.7 ns corresponds to infinite and 4.1 ns characteristic injection times respectively, simply using the average SMFL of PDI-P1/ZrO₂ 2.9 ns (Section II.F) as the lifetime without ET. Actually, the lifetime without ET was broadly distributed (Figure 6.15). Those slow ET components are not detectable in bulk transient IR absorption test where ET has been measured to finish in 100 ps. As another possible mechanism, heterogeneous energy transfer to the

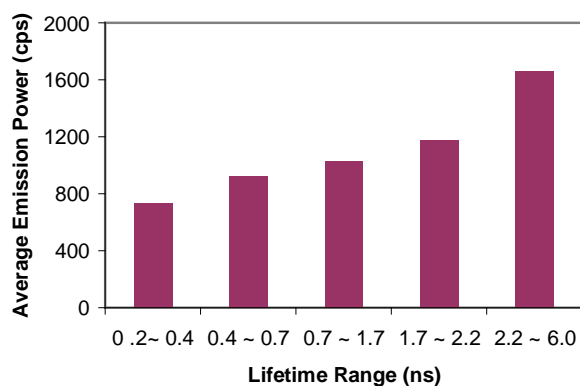


Figure 6.16. Average emission power vs. range of lifetime. The reduction of lifetime accompanied by the reduction of emission power is noticeable.

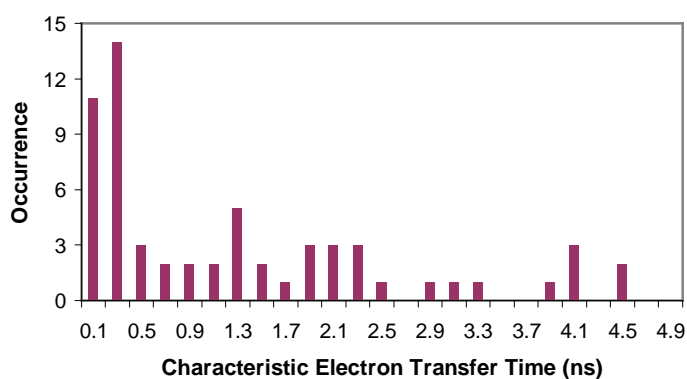


Figure 6.17. Distribution of characteristic electron transfer time of the SMD result shown in Figure 6.10a. The bulk lifetime of PDI-P1/ZrO₂ fitted to single exponential decay 2.2 ns was used as a lifetime of PDI-P1 in an EC-inactive medium.

surface plasmon was suggested in Section III.A.3 of Chapter 3. However, any clear evidence has not been found about the existence of the energy transfer.

The distribution of characteristic ET time is plotted in Figure 6.17 using Equation 2.4. The first two bars are pronounced and the rest of ET times are evenly distributed.

However, the shapes of those distributions in Figure 6.10, 6.16, and 6.17 are subject to change due to the limited number of recorded molecules in SMD.

It is interesting to note that one of the molecules in the SMFL test (Figure 6.10a) showed dynamic lifetime change as shown in Figure 6.18. The intensity and lifetime trajectories are represented by the thin gray solid line and the thick black solid line, respectively. There are two levels of intensity trajectory at 5.5 kcps (< 38 s) and 4 kcps (> 50 s). Between them, intensity changed highly from 0.8 kcps to 6.2 kcps. The surprising thing is that the lifetime also made two levels at 1.6 ns (< 38 s) and 1.2 ns (> 50 s), and fluctuated simultaneously with the intensity from 0.2 ns to 1.7 ns by 8.5 times between the two levels. In addition, the lifetime and intensity gradually and simultaneously changed in the slope marked by the thick arrow, which proves the dynamic observation of lifetime change. The dashed box includes all the changes in those

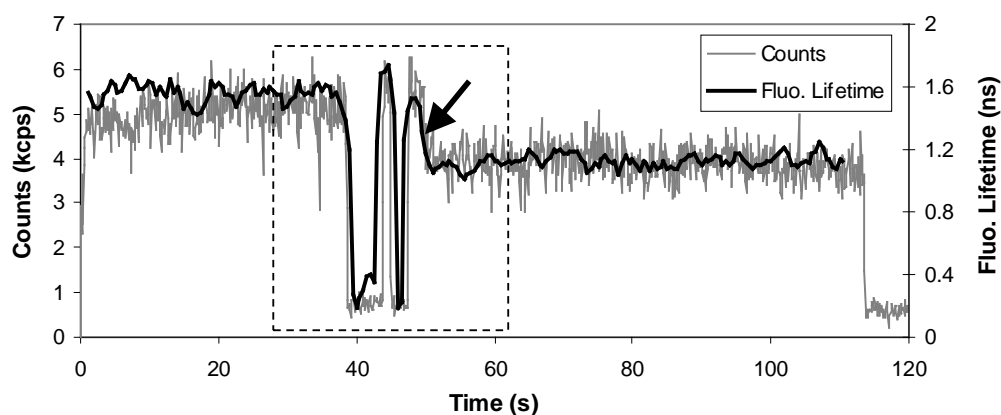


Figure 6.18. Single molecule fluorescence intensity and lifetime trajectories drawn in a graph. The thin gray solid line is the intensity trajectory and the thick black solid line is the lifetime trajectory. The intensity and lifetime changed in positive correlation. The dashed box includes all the changes in those trajectories.

trajectories. Assuming that (1) the PDI-P1 is so photochemically robust that it never have a state in which non-radiative decay rate channel opens and that (2) there is no dipole orientation effect in nanoporous matrix (Section II.B in Chapter 2), such a simultaneous change of intensity and lifetime in positive correlation may have to be attributed to the dynamic electron transfer rate change. The radiative lifetime change seems to be unlikely. Even if it had happened, it would not have changed the intensity. Because all the other physical factors are static and in equilibrium except for the direction of molecular axis of PDI-P1, we could explain that the phenomena resulted from the distance fluctuation between the adsorbed PDI-P1 molecule and ATO nanoparticle. The observed electron transfer rate changed maximum 8.5 times:

$$\frac{k_{fast}}{k_{slow}} = \frac{\tau_{long}}{\tau_{short}} = \frac{1.7 \text{ ns}}{0.2 \text{ ns}} = 8.5 \quad (6.2)$$

where, k_{fast} and k_{slow} are the fast and slow ET rate constants during the fluctuation, respectively. τ_{long} and τ_{short} are long and short fluorescence lifetimes during the fluctuation. The relation between the ET rate ratio in Equation 6.2 and the distance between the π^* orbital and ATO surface d is:

$$\frac{k_{fast}}{k_{slow}} = \exp\left(-\frac{\Delta d}{\beta}\right) = 8.5 \quad (6.3)$$

where, $\Delta d = d(\text{slow}) - d(\text{fast})$. $d(\text{slow})$ and $d(\text{fast})$ are the distances in slow and fast injecting conformation, respectively. β is the exponential decay constant of distance dependent ET rate constant: $k = k_{d=0} \exp(-d/\beta)$. $k_{d=0}$ is the rate constant when $d=0$. The

β is set to 1 here, then Δd is 2.1 Å. We could visualize above discussion as in Figure 6.19. The single PDI-P1 molecule seemed to pivot on the surface of an ATO particle; and it moved intermittently, gradually, and took two constant conformations.

Very similar intensity trajectories to the one in Figure 6.19 have been observed by Liu et al². They attributed the unique trajectory to the intramolecular electron transfer in a specially designed molecule: two PDIs are connected via phenyl spacer. The electron transfer from one PDI to the other PDI made a charge-separated dark state. Different from their observation, the data in Figure 6.18 shows the smooth simultaneous changes marked by the arrow. The formation of charge-separated dark state in the literature may have clear on-off characteristics. Another difference is that the intensity level from 40 s to 47 s in Figure 6.18 is higher than background level, which indicates that the fluorescence is not completely quenched during the time. On the contrary, the off-state in the literature looks completely a dark state.

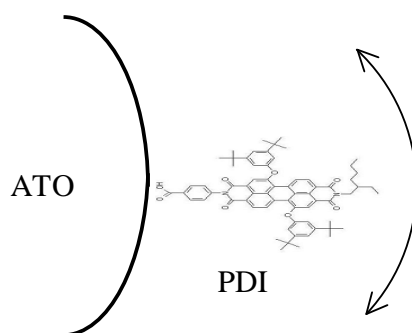


Figure 6.19. Schematic diagram of ATO--PDI-P1 single junction. PDI-P1 swings in a various mode and resultant intensity and lifetime trajectory changes as shown in Figure 6.18.

III.B. Single Molecule and Bulk Lifetime of PDI-P1 on Glass Surface

The average (3.7 ns) SMFL of PDI-P1s on glass matched well with bulk lifetime fitted to single exponential decay model (3.7 ns). The predicted standard deviation (0.5 ns) based on the deviation of measured bulk decay from the single exponential decay matched with measured SMFL standard deviation (0.6 ns) satisfactorily. The distribution in Figure 6.12 is not smooth just because the total number of molecules was only nineteen.

In Section III.B of Chapter 5, we explained the SMFL distribution of RB/glass by the combination of the local field correction and dipole orientation effect on surface. Following the line of the analysis, a possible SMFL range of PDI-P1/glass was investigated. The quantum yield of PDI-P1 in DMF was measured to be 1 using R101 as a standard. The quantum yield of PDI derivative of very similar structure to our PDI-P1 has been reported to be 1, too³⁵. Therefore, we set the measured fluorescence lifetime of PDI-P1 to its radiative lifetime. The fluorescence lifetime of 1 μ M PDI-P1 in DMF was measured to be 4.24 ns, so is the radiative lifetime. We need to know the radiative lifetime of PDI-P1 in the air to find the possible lifetime range on glass surface using the relation in Equation 5.3. The fully microscopic local field correction model (Equation 2.11) are adopted to calculate the radiative lifetime in the air using the refractive index of DMF 1.431³⁶. As a result, the theoretical radiative lifetime in the air was 5.7 ns. The possible lifetime curve as a function of polar angle of emission dipole moment orientation is plotted in Figure 6.20a. The measured SMFL distribution (Fig. 6.20b) is taken from Figure 6.12. Most of SMFLs are populated in the high polar angle region. The range of the possible lifetime curve does not cover the whole measured SMFL distribution. The origin of the discrepancy should be found by continued study. The

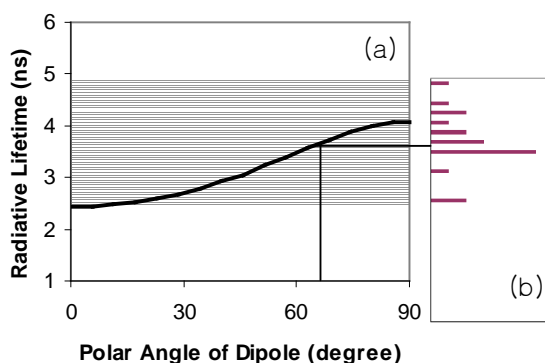


Figure 6.20. Polar angle dependence of radiative lifetime (a) compared with the measured SMFL distribution (b). The polar angle of the highest population is about 64° .

highest population of the polar angle was about 64° that is similar to the RB/glass case, $\sim 66^\circ$.

It is interesting that the intensity and lifetime trajectories made both positive and negative correlations in Figure 6.13. The possibility of the creation of non-radiative decay channel is certainly excluded because of the negative correlation in the plot (c); the change of non-radiative decay rate makes only positive correlation (Equation 2.5a). In addition, the PDI-P1 is believed to have negligible non-radiative decay yield in normal environment¹⁰⁻¹². With its quantum yield fixed to 1, the change of intensity results from the excitation rate change inevitably; and the fluorescence lifetime change must be a change of radiative decay rate. It is considered that the only mechanism that can account for those phenomena is the dipole orientation effect on the radiative lifetime. Figure 6.21 depicts schematically the possible configurations of the dipole orientation changes resulting in the simultaneous lifetime change. Picture A is the case of positive correlation. A dipole (thin single headed arrow) pivots on the flat surface and is excited by the

electric field circularly polarized on the XY plane (thick double headed arrow); when its polar angle increases, its excitation efficiency and intensity increases, accompanied by the simultaneous increase of lifetime. Picture B is the case of negative correlation. The dipole pivots on the tilted surface and is excited by the electric field circularly polarized on the XY plane. The tilted surface used to be observed by AFM. When the dipole's polar angle increases, its excitation efficiency and intensity decrease, while its lifetime increases. Picture C is another case of negative correlation. The dipole pivots on the flat surface. In this case, the molecule is not well positioned at the center of the laser focus (Appendix A in Chapter 4) and falls in a region where Z component of the electric field is dominant⁴⁰; when its polar angle increases, its excitation efficiency and intensity decrease, while its lifetime increases. The measured range of the lifetime changes in Figure 6.13

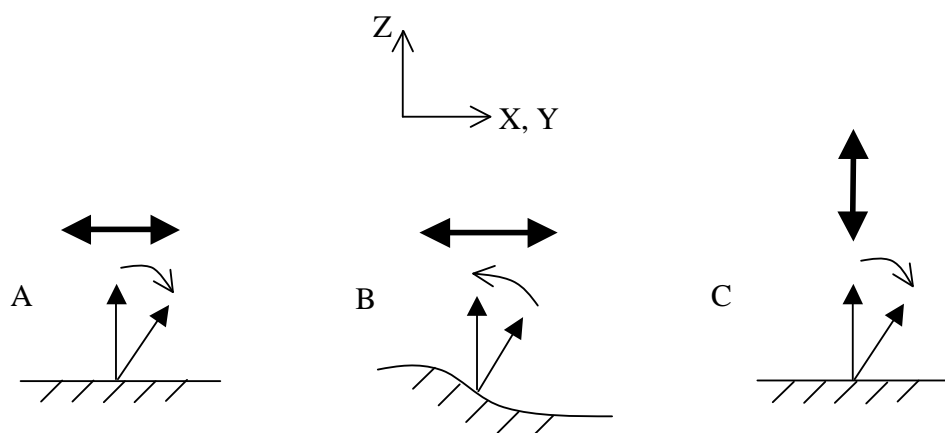


Figure 6.21. Schematic diagrams of the possible configurations of dipole orientation changes resulting in the simultaneous lifetime change. Coordinate system is shown above. In the picture A, B, and C, thick double-headed arrows are electric field polarized along the direction of arrows. Thin single headed arrows represent dipoles pivoting on the glass surfaces. A, positive correlation; B, negative correlation; C, negative correlation.

were within the span of SMFL distribution (Figure 6.12), not so much as the drastic change in PDI-P1/ATO in Figure 6.18. The more frequent observations of the lifetime fluctuation of PDI-P1 on glass than RB is ascribed to PDI-P1's less affinity to the surface than RB's.

In Figure 6.13b, the sudden increase of lifetime at the end of the trajectory is in question. Such phenomenon has been observed occasionally. Spectral diffusion and oscillator strength change might not be responsible for it because the intensity did not show a noticeable change before the bleach. For the same reason, dipole orientation effect is also not likely. A tentative explanation is that the molecule experienced a change of nuclear configuration for a couple of second before photo-bleach. The different state had proper photophysical parameters (radiative and non-radiative decay rates and absorption cross-section) for the constant intensity and increased lifetime.

III.C. Single Molecule and Bulk Lifetime of PDI-P1 on ZrO₂

The bulk lifetime fitted to 2.2 ns lifetime of single exponential decay model and we predicted ~ 1 ns standard deviation of SMFL distribution. The measured average SMFLs was 2.9 ns with its standard deviation 1.3 ns. The inherently multi-component bulk lifetime seemed to lose its slow components by fitting with single exponential model. The lifetime vs. filling factor curve of PDI-P1/ZrO₂ is shown in Figure 6.22. The curves are the convolutions of empty-cavity (dotted), virtual-cavity (thick solid), and fully microscopic (thin solid) models, with the Bruggeman effective medium approximation⁴¹. The light gray area represents the full range of SMFL distribution shown in Figure 6.15. The dark gray area represents the part of the SMFL distribution, which had sound bell

shaped distribution. The reason for defining the bell shaped range is to consider the possibility of treating the long lifetimes (> 4 ns) as the exceptional ones that might be governed by other theoretical model. The filling factor inferred from the bell-shaped part ranged from 0.48 to 1, which is similar to the range in Figure 4.28. According to the reasoning in Section III.A.3 of Chapter 4, a single PDI-P1 molecule is considered to have felt the heterogeneous effective refractive index and the local filling factor of the space, where the molecule was adsorbed, should always be higher than the bulk filling factor ~ 0.2 . Comparing Figure 4.20 and Figure 6.15, the distribution of PDI-P1/ ZrO_2 is clearly shifted to shorter lifetime from that of RB/ ZrO_2 . It is not known why the optically almost

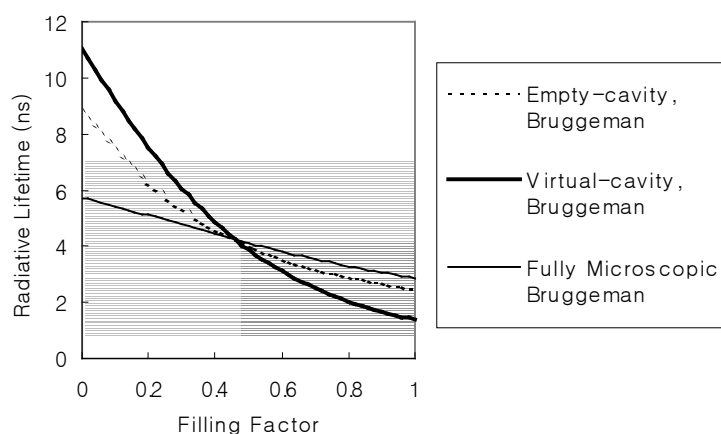


Figure 6.22. Plot of radiative lifetime as a function of filling factor based on the three combinations of effective medium approximation and local field correction. Dotted line, empty-cavity and Bruggeman model; Thick solid line, virtual-cavity and Bruggeman model; thin solid line, fully microscopic and Bruggeman model. The light gray area represents the full span of measured SMFL distribution shown in Figure 6.15. The dark gray represents the part of the SMFL distribution that had sound bell shaped distribution.

equivalent systems had the different distributions. It is also in question why the fully microscopic model could not explain the SMFLs less than 2.5 ns. One conceivable explanation is that the excited state of PDI-P1 injected an electron to the trap states of ZrO_2 . The long SMFLs over 4 ns may be resultant from the fortuitous formation of local structure that induced long lifetime, or just impurities from solvent. To check the existence of quenching mechanism, the relation between emission power and lifetime is inspected in Figure 6.23. Obviously, there was no clear quenching signature.

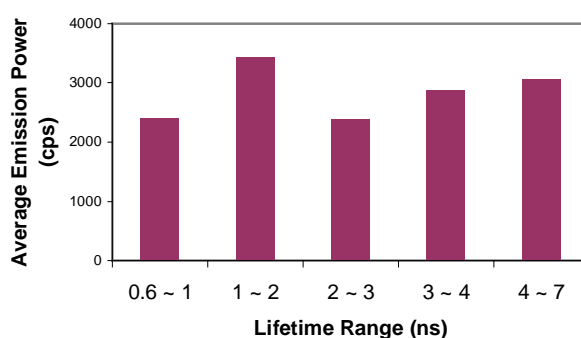


Figure 6.23. Average emission power vs. range of lifetime without any proportionality between them.

IV. Conclusion

The interfacial fluorescence lifetimes of PDI-P1 on ATO, glass, and ZrO_2 were measured in the surface concentrations of bulk and single molecule levels. Consistency in the bulk and the single molecule observations were confirmed. The multi-exponential bulk decay of PDI-P1/ATO was resolved by SMFL distribution while the faster components than 210ps were not recorded. Under the sampling limit, strong lifetime reduction effect has

been observed as shown in Figure 6.24 that is a collection of plots shown already. The plot A, B, and C are PDI-P1/ATO sampled with 700 cps (Figure 6.10a), PDI-P1/glass (Figure 6.12), PDI-P1/ZrO₂ (Figure 6.15), respectively. The distribution A is clearly displaced to shorter lifetime from B and C. Both the distributions B and C are ET-inactive but their positions in lifetime axis and standard deviations are different. The origins of the phenomena are attributed to the dipole orientation effect (B) and heterogeneous effective medium approximation (C). Dynamic lifetime fluctuations were observed in the PDI-P1/ATO and PDI-P1/glass. Their mechanisms suggested in this work are case by case depending on the energetics and optical geometry at the PDI-P1/ATO

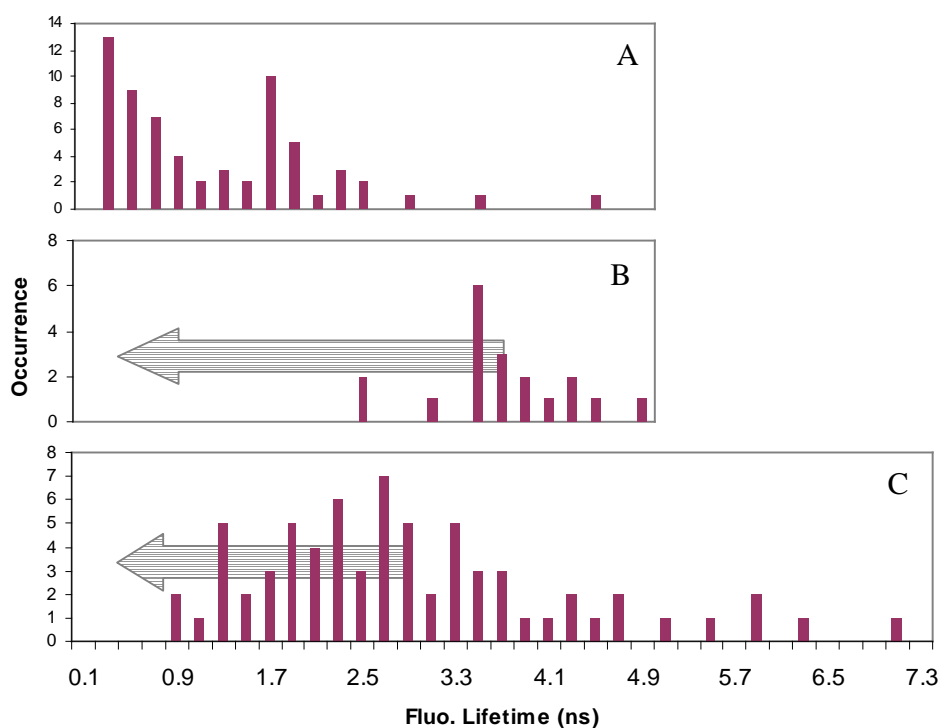


Figure 6.24. SMFL distribution of PDI-P1 on ATO (A), glass (B), and ZrO₂ (C). Clear lifetime shortening is shown in PDI-P1/ATO compared to the PDI-P1 on ET-inactive substrates glass and ZrO₂.

and PDI-P1/glass junctions. They are summarized in Figure 6.25. All the observed fluctuations are originated from the fluctuation of PDI-P1 conformation pivoted on the surface of ATO and glass. ET rate change by the conformation fluctuation is a function of the distance between the HOMO of PDI-P1 and ATO surface; and dipole orientation effect is a function of the polar angle of the dipole with respect to surface normal. The

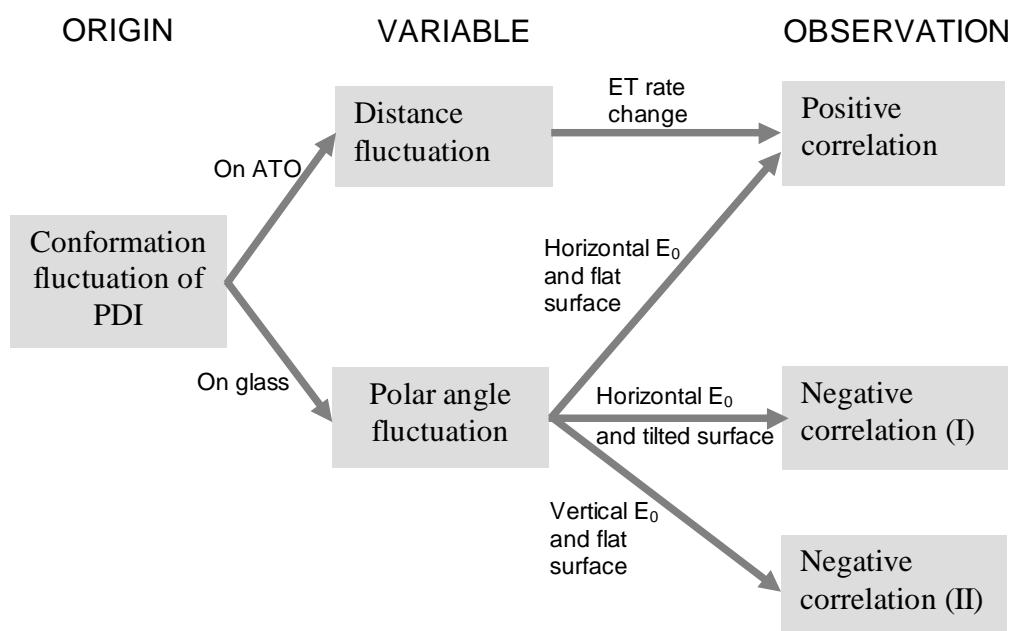


Figure 6.25. Diagram of lifetime fluctuation mechanisms suggested in this work. ET rate changed as a function of the distance between HOMO and ATO surface, resulting in positive correlation between intensity and lifetime. Power loss at the glass interface changed as a function of the polar angle of emission dipole, resulting in positive or negative correlation; the negative correlation were explained in two different ways and labeled I and II.

orientation effect could be divided to the positive and negative correlations between the lifetime and intensity trajectories. The positive correlations are ascribed to the molecules that are well-positioned on horizontal surface, while the negative correlation might result from one of extraordinary configurations.

References

- (1) Holman, M. W.; Adams, D. M. *CHEMPHYSCHEM* **2004**, *5*, 1831.
- (2) Liu, R.; Holman, M. W.; Zang, L.; Adams, D. M. *J. Phys. Chem. A* **2003**, *107*, 6522.
- (3) Haas, U.; Thalacker, C.; Adams, J.; Fuhrmann, J.; Riethmuller, S.; Beginn, U.; Ziener, U.; Moller, M.; Dobrawa, R.; Wurthner, F. *J. Mater. Chem.* **2003**, *13*, 767.
- (4) Wurthner, F. *Angew. Chem. Int. Ed.* **2001**, *40*, 1037.
- (5) Boom, T. v. d.; Hayes, R. T.; Zhao, Y.; Bushard, P. J.; Weiss, E. A.; Wasielewski, M. R. *J. Am. Chem. Soc.*, *124*, 9582.
- (6) Schmidt-Mende, L.; Fechtenkötter, A.; Mullen, K.; Moons, E.; Friend, R. H.; Mackenzie, J. D. *Science* **2001**, *293*, 1119.
- (7) Li, X.; Sinks, L. E.; Rybtchinski, B.; Wasielewski, M. R. *J. Am. Chem. Soc.* **2004**, *126*, 10810.
- (8) Lukas, A. S.; Miller, S. E.; Wasielewski, M. R. *Journal of Physical Chemistry B* **2000**, *104*, 931.
- (9) O'Neil, M. P.; Niemczyk, M. P.; Svec, W. A.; Gosztola, D.; III, G. L. G.; Wasielewski, M. R. *Science* **1992**, *257*, 63.
- (10) Kircher, T.; Lohmannsroben, H.-G. *Phys. Chem. Chem. Phys.* **1999**, *1*, 3987.
- (11) Lee, S. K.; Zu, Y.; Herrmann, A.; Geerts, Y.; Mullen, K.; Bard, A. J. *J. Am. Chem. Soc.* **1999**, *121*, 3513.
- (12) Weiss, E. A.; Tauber, M. J.; Kelley, R. F.; Ahrens, M. J.; Ratner, M. A.; Wasielewski, M. R. *J. Am. Chem. Soc.* **2005**, *127*, 11842.

- (13) Rybtchinski, B.; Sinks, L. E.; Wasielewski, M. R. *Journal of Physical Chemistry A* **2004**, *108*, 7497.
- (14) Gvishi, R.; Reisfeld, R.; Burshtein, Z. *Chemical Physics Letters* **1993**, *213*, 338.
- (15) Wurthner, F.; Thalacker, C.; Sautter, A.; scharl, W.; Ibach, W.; Hollricher, O. *Chem. Eur. J.* **2000**, *6*, 3871.
- (16) Langhals, H.; Demming, S.; Huber, H. *Spectrochimica Acta Part A* **1988**, *44A*, 1189.
- (17) Mercadante, R.; Trsic, M.; Duff, J.; Aroca, R. *Journal of Molecular Structure(Theochem)* **1997**, *394*, 215.
- (18) Tauber, M. J.; Kelley, R. F.; Giaimo, J. M.; Rybtchinski, B.; Wasielewski, M. R. *J. Am. Chem. Soc.* **2006**, *128*, 1782.
- (19) Schenning, A. P. H. J.; Herrikhuyzen, J. v.; Jonkheijm, P.; Chen, Z.; Wurthner, F.; Meijer, E. W. *J. Am. Chem. Soc.* **2002**, *124*, 10252.
- (20) Quante, H.; Geerts, Y.; Mullen, K. *Chem. Mater.* **1997**, *9*, 495.
- (21) Wurthner, F.; Thalacker, C.; Diele, S.; Tschierske, C. *Chem. Eur. J.* **2001**, *7*, 2245.
- (22) Zhao, Y.; Wasielewski, M. R. *Tetrahedron Letters* **1999**, *40*, 7047.
- (23) Lukas, A. S.; Zhao, Y.; Miller, S. E.; Wasielewski, M. R. *Journal of Physical Chemistry B* **2002**, *106*, 1299.
- (24) Schurr, J. M. *Chemical Physics* **1984**, *84*, 71.
- (25) Kim, H.; Pique, A. *Applied Physics Letters* **2004**, *84*, 218.

- (26) Kung, H. H.; Jarrett, H. S.; Sleight, A. W.; Ferretti, A. *Journal of Applied Physics* **1977**, *48*, 2463.
- (27) Hagfeldt, A.; Gratzel, M. *Chem. Rev.* **1995**, *95*, 49.
- (28) Guo, J.; She, C.; Lian, T. *Journal of Physical Chemistry B* **2005**, *109*, 7095.
- (29) Lukosz, W.; Kunz, R. E. *J. Opt. Soc. Am.* **1977**, *67*, 1607.
- (30) Lukosz, W.; Kunz, R. E. *Optics Communications* **1977**, *20*, 195.
- (31) Arnoldus, H. F.; Foley, J. T. *OPTICS LETTERS* **2003**, *28*, 1299.
- (32) Zumofen, G.; Klafter, J. *Chem. Phys. Lett.* **1994**, *219*, 303.
- (33) Lawless, M. K.; Mathies, R. A. *Journal of Chemical Physics* **1992**, *96*, 8037.
- (34) Todd, M. D.; Nitzan, A.; Ratner, M. A.; Hupp, J. T. *Journal of Photochemistry and Photobiology A: Chemistry* **1994**, *82*, 87.
- (35) Weiss, E. A.; Ahrens, M. J.; Sinks, L. E.; Gusev, A. V.; Ratner, M. A.; Wasielewski, M. R. *J. Am. Chem. Soc.* **2003**, *126*, 5577.
- (36) Lide, D. R. *CRC handbook of chemistry and physics: a ready-reference book of chemical and physical data*; CRC Press: Boca Raton, 2005.
- (37) Glauber, R. J.; Lewenstein, M. *Physical Review A* **1991**, *43*, 467.
- (38) Barnett, S. M.; Huttner, B.; Loudon, R. *Physical Review Letters* **1992**, *68*, 3698.
- (39) Wuister, S. F.; Donega, C. d. M.; Meijerink, A. *Journal of Chemical Physics* **2004**, *121*, 4310.

- (40) Sick, B.; Hecht, B.; Wild, U. P.; Novotny, L. *Journal of Microscopy* **2001**, 202, 365.
- (41) Aspnes, D. E. *Am. J. Phys.* **1982**, 50, 704.